Visualising the local single-channel underpinnings of calcium sparks in excitable cells

Miriam Elizabeth Hurley

Submitted in accordance with the requirements for the degree of
Doctor of Philosophy

The University of Leeds
School of Biomedical Science

September 2020

The candidate confirms that the work submitted is her own, except where work which has formed part of jointly-authored publications has been included. The contribution of the candidate and the other authors to this work has been explicitly indicated below. The candidate confirms that appropriate credit has been given within the thesis where reference has been made to the work of others.

Acknowledgements

I owe a great thanks to my supervisor Dr Izzy Jayasinghe for welcoming me into her group at The University of Leeds. Throughout the PhD she has provided support and encouragement, but ultimately has given me the confidence to establish myself as a researcher and for that I am most thankful. I would also like to thank my co-supervisor Professor Derek Steele for his door always being open and for his expertise and assistance with the calcium signalling experiments.

A thank you to the whole cellular cardiology group, past and present, for creating such an enjoyable and collaborative place to study. In particular, thank you to Professor Ed White, who 8 years ago, introduced me to the concept of scientific research as a career. I thank him for the support inside and outside of the laboratory in establishing the model of heart failure and I look forward to another 3 years working together. Thank you also to Dr Eleftheria Pervolaraki who taught me such great lessons and who was always available to answer any question, regardless. Thank you to Dr Hannah Kirton for your generosity and company. I am beyond grateful for the hours which you spent teaching me the best practices in cell isolation and your support, along with Dr Zhaokang Yang, in supplying cardiomyocytes across the years. Thank you to Thomas Sheard for your camaraderie on the early starts and long weekends as we worked together in the laboratory. A specific thank you to Ashlea Rowley for the many collaborative discussions about the development of DNA-PAINT, I look forward to them continuing long into the future. A special thanks to Dr Ruth Norman, who for 4 years has been championing me as a researcher and who has made this PhD experience unforgettable. And of course, thank you to my very good friend Dr Robert Walmsley who continues to always be there to provide perspective.

Thank you to Professor Nikita Gamper for taking such interest in the research and providing the opportunity to venture into the world of neuroscience. Thank you to Dr Shihab Shah for his welcome and his

willingness to provide me with dorsal root ganglion neurones whilst I shadowed and learnt the process myself. Thank you to Dr Eleni Kyriakopoulou who was a joy to be with in the laboratory and whose laughter was infectious. Thank you also to The University of Leeds for providing me the opportunity and funding for such an unforgettable 4 years.

It remains for me to thank those friends outside of the laboratory who have been with me across the many stages of the PhD. You know who you are, and you have all helped in various ways to motivate, encourage and rationalise as required. If you're reading this then I thank you for letting me talk all things 'science' more times than is healthy. To my family, thank you. Thank you for being interested in every experiment, even when there was nothing to say. Thank you for the unconditional love, for the phone calls, for the perspective and for the distraction. Here's to the next chapter.

Abstract

The elementary release of calcium (Ca^{2+}) from a cell's internal store is known as a Ca^{2+} spark. The spatiotemporal summation of a cell's Ca^{2+} signalling underpins its function. The junctional membrane complex (JMC) is a structural unit which contains clusters of the ryanodine receptor (RyR) or inositol triphosphate receptor (IP3R) responsible for Ca^{2+} spark generation. The impact of a cell's Ca^{2+} signalling due to single protein orientation has only been studied experimentally in isolation. This thesis outlines the development of a correlative imaging protocol that has allowed Ca^{2+} signalling within primary cells to be visualised in relation to the local nanoscale structure of the JMC. This was achieved by combining total internal reflection fluorescence imaging of Ca^{2+} sparks, with protein distribution using DNA-PAINT and dSTORM super-resolution microscopies.

Examining Ca^{2+} sparks and RyR arrays in ventricular myocytes taken from the monocrotaline-induced rat model of right ventricular heart failure (RV HF) revealed a relationship between RyR orientation and spark mass. Remodelling of the RyR cluster pattern was observed within RV HF. Specifically, a fragmentation of the RyR cluster pattern, represented by an increased distance between puncta, was accompanied by a decreased spark mass. Therefore, at a local level the structural remodelling of the JMC has an impact upon functional Ca^{2+} signalling within the failing heart.

Versatility of the correlative imaging protocol was evidenced by its application to the dorsal root ganglion sensory neurones to evaluate the role of IP3R and RyR in Ca^{2+} spark generation. Application of the protocol revealed that both IP3R1 and RyR3 were present in regions where Ca^{2+} sparks occur. However, the IP3R1 was considered to have a more fragmented pattern compared to RyR3 in regions where Ca^{2+} sparks were generated.

Overall, the project highlights the importance of studying local Ca^{2+} signalling in relation to a cell's ultrastructure.

Table of Contents

List of Tables

List of Figures

List of Appendix

Abbreviations

ACE	angiotensin-converting enzyme
AFM	atomic Force Microscopy
ANO1	anoctamin channel
AP	action potential
BSA	bovine serum albumin
cAMP	cyclic adenosine monophosphate
CICR	calcium-induced calcium release
CLEM	correlative light and electron microscopy
CO	cardiac output
Control-RV	right ventricular cardiomyocytes from control animals
CRU	calcium release unit
DAG	diaglycerol
DNA-PAINT	DNA points accumulation for imaging in nanoscale topography
DRG	dorsal root ganglia
dSTORM	direct stochastic optical reconstruction microscopy
ECC	excitation-contraction coupling
ER	endoplasmic reticulum
Fail-RV	right ventricular cardiomyocytes from fail animals
FRET	Förster resonance energy transfer
FWHM	full width at half-maximum
GFP	green fluorescent protein
GPCR	G-protein coupled receptor
HBSS	Hanks' balanced salt solution
HF	heart failure
IP3	inositol triphosphate
IP3R	inositol triphosphate receptor
IS	isolation solution
JMC	junctional membrane complex
JPH	junctophilin
jSR	junctional sarcoplasmic reticulum
K_{On}	association rate
K_{Off}	dissociation rate

K_D	dissociation constant
LV	left ventricular
MCT	monocrotaline
mRNA	messenger ribonucleic acid
NCX	sodium/calcium exchanger
NGS	normal goat serum
NND	nearest neighbour
PAH	pulmonary arterial hypertension
PALM	photoactivated localisation microscopy
PBS	phosphate-buffered saline
PFA	paraformaldehyde
PIP_2	phosphatidylinositol 4,5-biphosphate
PKC	protein kinase C
PLA	proximity ligation assay
PLB	phospholamban
PSF	point spread function
PyME	Python Microscopy Environment
ROS	reactive oxygen species
RT	room temperature
RV HF	right ventricular heart failure
RV	right ventricular
RyR	ryanodine receptor
SD	standard deviation
SEM	standard error of mean
SERCA	sarco-endoplasmic reticulum Ca^{2+} ATPase
SMLM	single molecule localisation microscopy
SOCE	store operated Ca^{2+} entry
SPR	surface plasmon resonance
SR	sarcoplasmic reticulum
STED	stimulated emission depletion
SV	stroke volume
TAB	thoracic aortic banded
TIRF	total internal reflection fluorescence
T-tubules	transverse tubules

2-APB	2-amino-ethoxydiphenyl borate
10xEMM	10x enhanced expansion microscopy

Chapter 1. Introduction

Light microscopy has been widely used to visualise cellular structures beyond the capabilities of the human eye. Based on Abbe's law, it was initially believed that the wavelength of light itself placed an absolute limit on the resolving power of optical microscopy (Abbe, 1873). However, the development of 'super-resolution' microscopy techniques has enabled visualisation of structures below this theoretical limit.

Specifically, the development of single molecule localisation microscopy (SMLM) has enabled biological structures to be visualised at an unprecedented level of detail. This use of nanoscopy has revealed to the world the intricate architecture of cellular structures at a spatial scale which is <10 nm (Jayasinghe et al., 2018a). Due to technical complexity, expense and availability, the use of SMLM has been largely limited to the microscopy community. Consequently, to the author's knowledge, the use of SMLM in parallel with the functional characterisation of primary cells has been largely neglected.

One function of great importance within cellular biology is calcium (Ca^{2+}) signalling. Previously, the structure of Ca^{2+} release channels and their Ca^{2+} signalling function has been widely studied in isolation (Cosi et al., 2019; Kolstad et al., 2018). The use of a green fluorescent protein (GFP) model has enabled a cell's structural and functional properties to be investigated in tandem. However, these studies were diffraction limited and required the use of expensive genetic models (Hiess et al., 2018). As a result, there is a requirement for an adaptable and affordable correlative imaging protocol which has the ability to combine the functional assessment of Ca^{2+} signalling with visualisation of a cell's nanoscale protein structure. Such a protocol would benefit the biologist by providing a platform to study protein distribution in regard to cellular function whilst aiding the biophysicist in their study of cellular mechanisms which relate to this same function. The fulfilment of a correlative imaging protocol would therefore bridge the gap between SMLM and functional application, with the potential to study pharmacological and biophysical protein-protein coupling. The research that

follows explores one approach by which SMLM could be adapted to enable functional correlative studies.

1.1 Calcium signalling

1.1.1 Overview of calcium

Ca^{2+} is a ubiquitous second messenger. Within the body, Ca^{2+} has an extracellular concentration of 1-2 mM (Breitwieser, 2008) and an intracellular concentration of around 100 nM. Intracellularly there are a host of proteins and channels responsible for the movement and buffering of Ca^{2+} in a process known as signal transduction, with an excitable cell having the capacity to be 'activated' upon the rise of intracellular Ca^{2+} to 500 – 1000 nM. It is important that a homeostatic Ca^{2+} concentration is maintained across a cell to prevent the dysregulation of Ca^{2+} signalling which can lead to eventual necrosis or apoptosis (Berridge et al., 2000; Clapham, 1995).

1.1.2 Role of calcium within excitable cells

Neurones within the peripheral nervous system utilise the Ca^{2+} signalling second messenger pathway and are one class of excitable cell. Dorsal root ganglia (DRG) are sensory neurones which use Ca^{2+} to propagate a somatosensory signal from the peripheral to the central nervous system. They are a heterogenous group of neuronal cell bodies (somata) which transduce thermoception, nociception, mechanoception and proprioception information (Nascimento et al., 2018). Upon the arrival of an electrical signal from the periphery, somata within the DRG can be depolarised from the activation of voltage-gated channels, which are located within the neurone's plasma membrane. A resultant Ca^{2+} influx can initiate a signalling cascade and eventual exocytosis of neurotransmitters from intracellular vesicles (Haberberger et al., 2019; Park and Luo, 2010).

Smooth, skeletal, and cardiac muscle are classified as excitable cells. Consequently, all three muscle types rely upon Ca^{2+} as a second messenger to ensure synchronised and efficient muscle contraction (Rüegg, 1986). A myocyte has the ability to transform an electrical signal in the form of a depolarising current into a contractile response; a process known as

excitation-contraction coupling (ECC). The arrival of this electrical current triggers the opening of voltage-gated Ca^{2+} channels and a consequent Ca^{2+} influx. Physiologically, Ca^{2+} is partly responsible for the degree of contractile force produced as the ion binds to and activates the muscle's myofilament structures (Bers, 2008). This process is known as actin-myosin crossbridge cycling. Cytoplasmic Ca^{2+} can bind to troponin-C and cause a conformational change in the troponin complex which shifts tropomyosin from its positioning between the actin filaments. In turn, the myosin head is then able to bind to actin to elicit a contractile response (Klabunde, 2012; Martini et al., 2012).

1.1.3 Mechanism of calcium-induced calcium release

Extracellular Ca^{2+} is not the only Ca^{2+} pool that excitable cells can utilise in the process of signal transduction. The initial Ca^{2+} influx caused by a change in electrical potential across a cell's membrane as denoted above can be amplified in a process known as calcium-induced calcium release (CICR). This is where a cell's internal Ca^{2+} store can be mobilised by Ca^{2+} itself. Within an excitable cell, Ca^{2+} is sequestered and stored within either the endoplasmic reticulum (ER) or in muscle, the sarcoplasmic reticulum (SR). The uptake of Ca^{2+} into this store from the intracellular space occurs via SERCA (sarco-endoplasmic reticulum Ca^{2+} ATPase), a specialised Ca^{2+} re-uptake pump. The release of Ca^{2+} from a cell's internal store is mainly via the Ca^{2+} mediated activation of the ryanodine receptor (RyR) or via inositol triphosphate receptor (IP3R) Ca^{2+} channels (Berridge et al., 2000; Bootman et al., 2002; Putney, 1999).

Fabiato and Fabiato first reported that a small but rapid increase in Ca^{2+} at the surface of the SR membrane could initiate a much larger release of Ca^{2+}. (Endo, 2009; Fabiato, 1983; Fabiato and Fabiato, 1972). The process of CICR was summarised as the mechanism by which an increase of Ca^{2+} at the plasma membrane of a cell can induce a release of Ca^{2+} from the cell's internal Ca^{2+} store. This response to Ca^{2+} was found to be biphasic, with the presence of high levels of Ca^{2+} eventually becoming inhibitory to further ion release (Endo, 2009).

The process of CICR was discovered within skeletal muscle. However, unlike the role of CICR within cardiomyocytes, interaction of the L-type Ca^{2+} channel with the RyR protein is suggested to be the main mechanism by which the Ca^{2+} release from the SR is mediated (Endo, 2009). Within a cardiomyocyte the influx of Ca^{2+} can be mediated primarily through the L-type Ca^{2+} channel and to a lesser extent the sodium/calcium exchanger (NCX), both of which are within the cell's sarcolemma. The efficiency of CICR is dependent upon the size of the 'fuzzy space' between the cell's plasma membrane and it's Ca^{2+} store. (Cannell and Soeller, 1997; Lederer et al., 1990). Cannell et al. (1994) suggested that within a cardiomyocyte, CICR had a structural unit which consisted of an L-type Ca^{2+} channel in juxtaposition with a cluster, namely four, RyR channels. This structure is commonly referred to as a calcium release unit (CRU) or junctional membrane complex (JMC). Maintenance of this JMC within a cardiomyocyte ensures that Ca^{2+} release from the SR can occur in < 2 ms from the initiation of sarcolemmal Ca^{2+} influx via CICR (Cannell et al., 1994).

The mechanism of CICR has been reported within multiple neuronal cell types (Llano et al., 1994; Sandler and Barbara, 1999), including DRGs (Shmigol et al., 1995). Within a DRG the process of CICR is dependent upon the activation of the ER-bound RyR3 and to a lesser extent IP3R (Ouyang et al., 2005b). The majority of research has evaluated the role of CICR within DRGs using pharmacological agents to target the Ca^{2+} handling proteins. However, the Ca^{2+} buffers present within a cell and the neurone's ultrastructure ideally needs to be studied in relation to CICR functionality (McDonough et al., 2000; Ouyang et al., 2005b).

1.1.4 Calcium sparks

Cytoplasmic Ca^{2+} signalling is the principal determinant of contractility within cardiac muscle. Additionally, Ca^{2+} signalling can aid the transduction of afferent signalling pathways from the secretion of neurotransmitters and neuropeptides from the somata of DRG sensory neurones. Ca^{2+} is stored within a cardiomyocyte's SR or a DRGs ER. The elementary release of Ca^{2+} from its Ca^{2+} store is in the form of a 'Ca^{2+} spark'. Within rodents, Cheng et al.

(1993) first characterised a stereotypical Ca^{2+} spark within the ventricular cardiomyocyte to have a 1.5 μm spatial footprint which takes 25 ms to decay by half of its amplitude and consists of 170 nM Ca^{2+}. Because of their small size, Ca^{2+} sparks were not visualised until the development of confocal microscopy, due to its enhanced 250 nm xy spatial resolution and faster frame rate (Cheng et al., 1993).

The open probability of the RyR channel is dependent upon Ca^{2+} concentration within the cytosol and the SR/ER and the binding of additional physiological and pharmacological modulators (Sato and Bers, 2011). Ca^{2+} can leak out of a cell's internal store to maintain Ca^{2+} homeostasis. It is the spark fidelity, the probability by which an RyR channel will spontaneously open, which determines whether Ca^{2+} leak can elicit a Ca^{2+} spark and how large that Ca^{2+} spark will be (Walker et al., 2014). Otherwise, a smaller volume of Ca^{2+} leak is known as a Ca^{2+} quark (Brochet et al., 2011).

Walker et al. (2014) developed a three-dimensional CRU model based upon stimulated emission depletion microscopy to determine the influence of RyR cluster size upon Ca^{2+} spark fidelity. They concluded that Ca^{2+} spark fidelity increased when RyR clusters were greater in size, due to a higher number of neighbouring RyRs being present to allow for inter-RyR coupling. Sato and Bers (2011) similarly suggest that RyRs which are not as tightly coupled can lead to the failure in Ca^{2+} spark generation.

The release of Ca^{2+} from its internal storage pool can be visualised in microscopy with the use of a Ca^{2+} indicator dye (Cheng et al., 1993; Prasad and Inesi, 2012). For a Ca^{2+} spark to develop, Baddeley et al. (2009b) suggested that several RyR clusters need to be activated and function as a 'supercluster' as determined by local cytosolic and SR Ca^{2+} concentration. However, estimation of the number of RyRs activated in the generation of a unitary Ca^{2+} spark has widely varied across research. Within ventricular cardiomyocytes of rodents, this ranges from 4-6 RyRs (Wang et al., 2001) to 25 RyRs (Baddeley et al., 2009b).

Structural heterogeneity at the level of the JMC has been suggested to underlie variations in Ca^{2+} spark amplitude, with Ca^{2+} sparks having a polymorphic nature (Bridge et al., 1999). This forms the hypothesis that heterogeneous Ca^{2+} spark behaviour is dependent upon the structural properties of an RyR cluster and the extent to which the Ca^{2+} release channels are modulated. The number of RyRs involved within Ca^{2+} spark generation and the functional significance of a single RyR cluster is still unclear. There is a requirement, therefore, to study local Ca^{2+} functionality in relation to JMC structure (Baddeley et al., 2009b; Bridge et al., 1999; Chen-Izu et al., 2006; Hou et al., 2015). Under physiological conditions, an action potential (AP) can trigger the opening of multiple RyR channels which act as Ca^{2+} spark sites. The summation of multiple Ca^{2+} sparks can lead to the propagation of Ca^{2+} across a cell, known as a Ca^{2+} transient (Cheng and Lederer, 2008; Fearnley et al., 2011; Song et al., 2005). There are reported changes to Ca^{2+} signalling within disease, namely heart failure (HF), and this can lead to arrhythmogenic Ca^{2+} handling (Fearnley et al., 2011). The following work will focus upon the role of Ca^{2+} within ventricular cardiomyocytes and DRG sensory neurones in relation to their underlying Ca^{2+} release machinery.

1.2 Ventricular cardiomyocyte

1.2.1 Cellular structure

Within the heart, cardiomyocytes have various forms depending upon their function and are characterised based upon location; nodal, conduction, atrial and ventricular (Kane and Terracciano, 2017). Due to their abundance and contractile role, the primary cell-type of interest within this research is the ventricular cardiomyocyte and it will therefore be the focus herein.

A ventricular cardiomyocyte is multi-nucleated and has a characteristic rod-shape which is 50-100 μm long and 10-20 μm in diameter (Figure 1.1A). Specifically, within rodents a ventricular cardiomyocyte has two nuclei. Throughout a ventricular cardiomyocyte there are myofibrils which in turn contain myofilaments. Myofilaments occupy 45-60% of the cell volume and are important in the cell's ability to contract. They are grouped together in a repeating unit known as a sarcomere (Figure 1.1B). Within optical microscopy

(Figure 1.1A), the striated pattern of a cardiomyocyte is representative of the 1.6-2.2 μm length of a sarcomere (Bers, 2001; Klabunde, 2012; Martini et al., 2012).

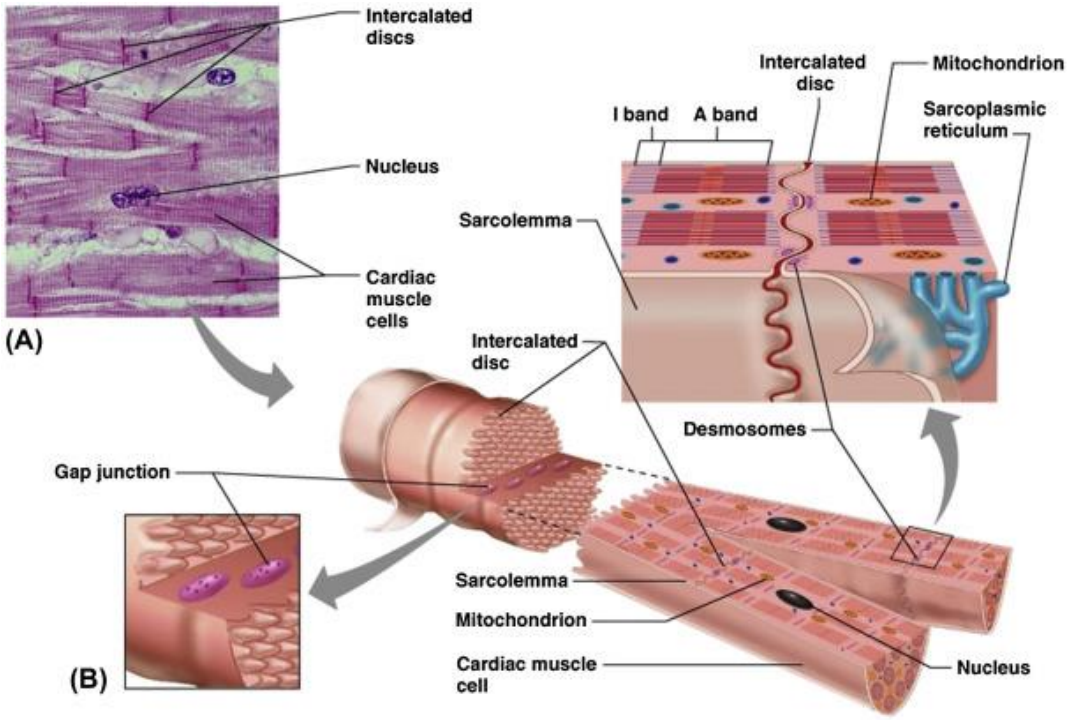

Figure 1.1: Ventricular cardiomyocyte structure. (A) Histochemistry staining of ventricular cardiomyocytes to show the tightly packed orientation of each cells rod-shaped structure with its multiple nuclei, striated sarcomeric pattern and intercalated discs which aid cell-to-cell adhesion. (B) Schematic of a ventricular cardiomyocyte which shows the ordered sarcomeric array of myofilaments across the length of the cell, the tight packing of mitochondria, the internal SR Ca^{2+} store and the interconnections between cells which allows the heart to function efficiently. Adapted directly from Wilmot et al. (2017).

1.2.2 Excitation-contraction coupling

Within ventricular cardiomyocytes, Ca^{2+} is integral to the mechanism of ECC. Excitation-contraction coupling (Figure 1.2) defines the series of events which underlie the depolarising current of an AP being translated to mechanical contraction at the sarcomere, the stages of which are detailed above (Bers, 2001). To ensure that a cardiomyocyte is excited in an efficient and uniform manner, the spread of depolarisation is maximised by the organisation and morphology of transverse tubules (T-tubules) (Crossman et al., 2011; Ibrahim et al., 2011).

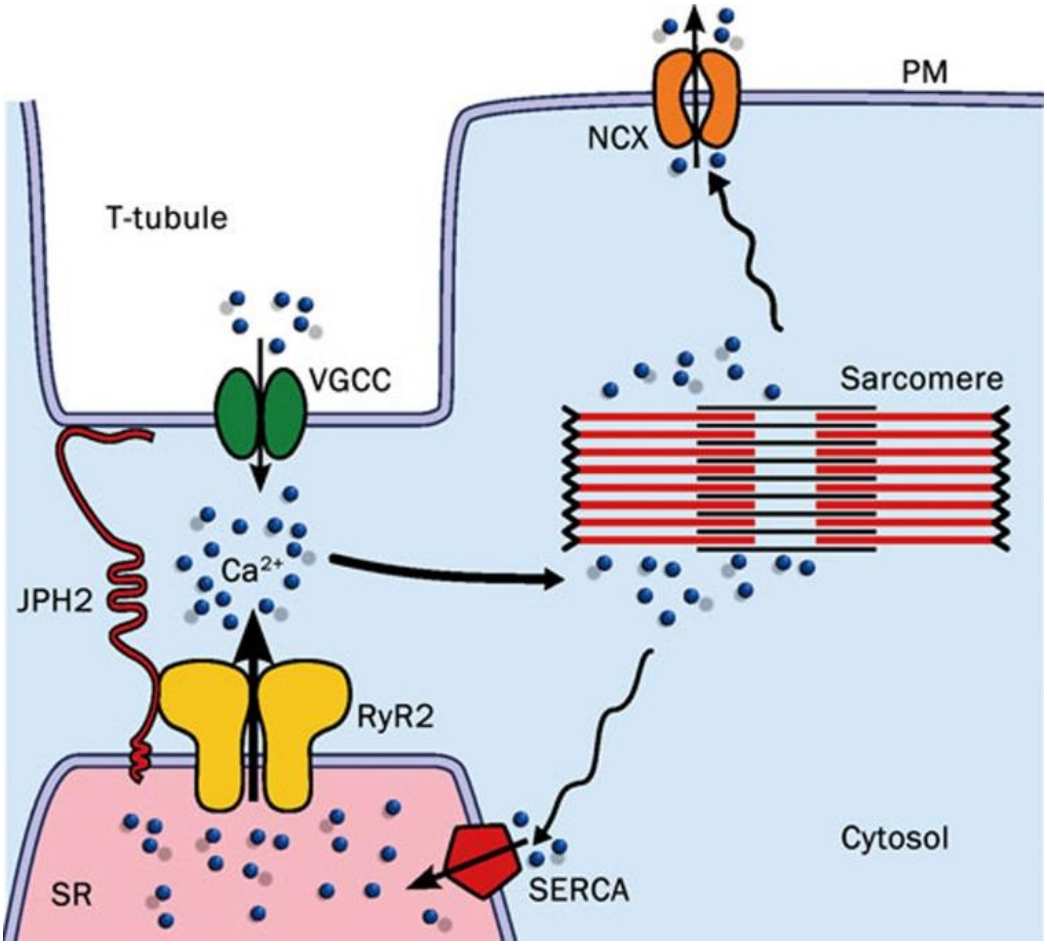

Figure 1.2: Excitation-contraction coupling. Schematic detailing the process of excitation-contraction coupling in a ventricular cardiomyocyte. Adapted directly from Garbino and Wehrens, (2010).

1.2.3 Transverse-tubule structure

In 1956, Lindner first discovered the presence of T-tubules within mammalian ventricular cardiomyocytes through the use of electron microscopy (Lindner, 1957). T-tubules are invaginations of the sarcolemma (Crossman et al., 2011; Ibrahim et al., 2011). Within a cell, 60% of the T-tubule structure lies along the Z-line. Use of the Di-8-ANNEPS lipophilic sarcolemma stain revealed T-tubules to have a striated 1.8-2.0 μm pattern, similar to the location of the L-type Ca^{2+} channel and RyR (Smyrnias et al., 2010). However, their orientation (Figure 1.3) is not just transverse with axial sarcolemmal invaginations also visible (Soeller and Cannell., 1999). The repeated structure of the T-tubule enables the synchronised spread of a depolarising current throughout the cell's length and depth, having a critical role for the function of ECC (Ibrahim et al., 2011; Orchard et al., 2009). The morphology of a T-tubule is species

dependent. 3D reconstruction of the rabbit T-tubule system revealed a mean± SD (standard deviation) diameter of 448±172 nm (Savio-Galimberti et al., 2008). This is compared to a rat's T-tubule mean± SEM (standard error of mean) diameter of 255±0.85 nm (Soeller and Cannell, 1999). When comparing these data, it is important to note the differing measures of error, with SD a measure of variability from the mean whilst SEM accounts for the deviation from the mean population, taking into account sampling size.

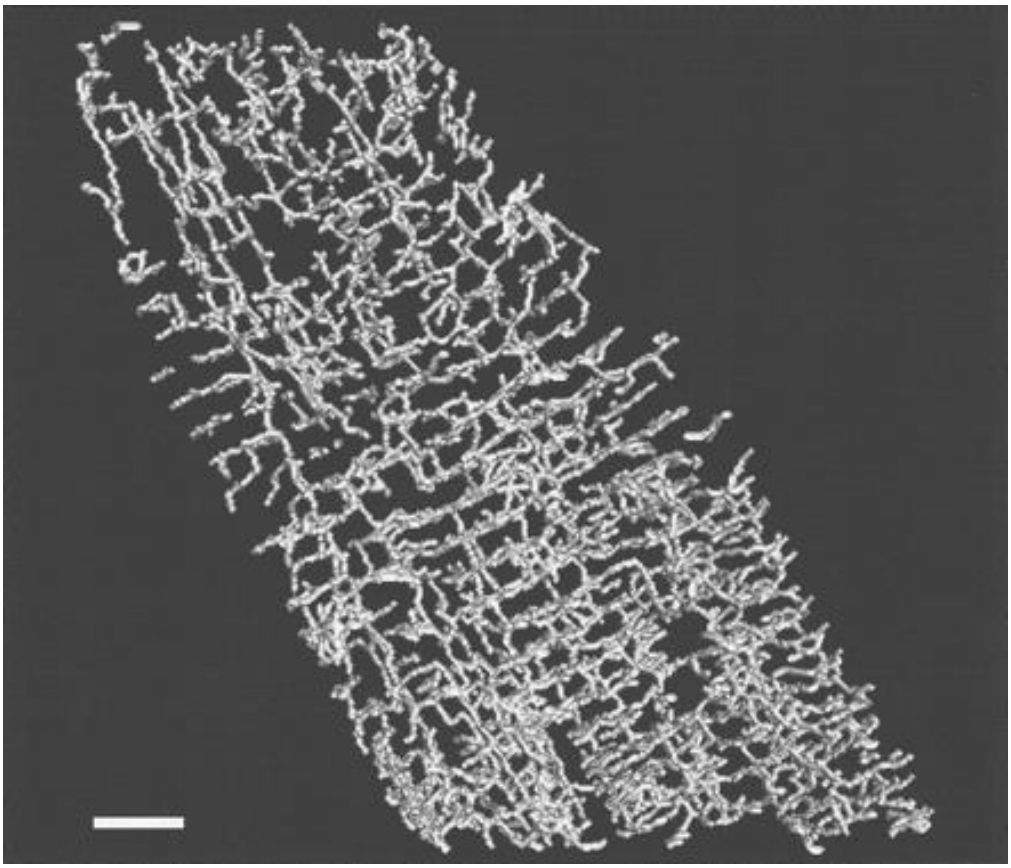

Figure 1.3: Ventricular cardiomyocyte transverse-tubule. Three-dimensional reconstruction of the T-tubule architecture within a rat ventricular cardiomyocyte revealing its transverse and axial morphology. Adapted directly from Soeller and Cannell (1999). Scale bar: 5 μm.

Within the T-tubule membrane there are an abundance of Ca^{2+} handling proteins. This finding reflects the importance of the T-tubule architecture in Ca^{2+} signalling (Smyrnias et al., 2010) as an array of ion channels and pumps within the T-tubule are critical for the function of ECC (Ibrahim et al., 2011; Orchard and Brette, 2008). They include the L-type Ca^{2+} channel, the electrogenic NCX pump, the Na^{+}/H^{+} exchanger, Na^{+}/K^{+} ATPase pump and a

variety of Na^+ and K^+ channels. The T-tubule architecture is therefore not only critical for Ca^{2+} influx to mediate CICR but also in Ca^{2+} extrusion from the cell to enable relaxation of the cardiomyocyte (Brette and Orchard, 2003; Orchard et al., 2009). The roles of these Ca^{2+} channels and pumps are of great importance within cells, such as atrial myocytes, that have a limited and sometimes non-existent, T-tubule network (Smyrnias et al., 2010).

A reduction in T-tubule density is known to affect the synchrony of Ca^{2+} release from the SR (Louch et al., 2004). As previously described, within a ventricular cardiomyocyte CICR describes the amplification of the L-type Ca^{2+} channel mediated Ca^{2+} influx during ECC. The efficiency of ECC is dependent upon cardiomyocyte structure. In particular, the L-type Ca^{2+} channel located upon the T-tubule is in close apposition with the cardiac specific Ca^{2+} release channel known as the RyR2 within the SR membrane. This co-clustering of the L-type Ca^{2+} channel and RyR2 was evidenced by Sun et al. (1995) and forms part of the JMC. In a healthy cardiomyocyte, the structural unit of the JMC spans an average distance of 12 nm (Garbino et al., 2009; Takeshima et al., 2000).

Porcine ventricular cardiomyocytes were cultured in a manner which induced T-tubule atrophy (Louch et al., 2004). They noted that alongside the reduced T-tubule architecture was a noticed increase in Ca^{2+} desynchrony. Furthermore, de-tubulation of rat ventricular cardiomyocytes with formamide solution during osmotic shock was associated with a 75.5% reduction in Ca^{2+} current and dyssynchronous CICR, potentially due to the disruption of the tightly coupled JMC structure (Kawai et al., 1999; Smyrnias et al., 2010). Similar changes were recorded in human HF, with a distortion and remodelling of the T-tubule architecture being visualised in the disease (Brette and Orchard, 2003; Crossman et al., 2011). It has been suggested that altered cardiomyocyte structure could impair cardiac function in regard to Ca^{2+} handling. Specifically, alteration in the mechanism of ECC due to structural changes between the sarcolemma and SR are thought to be associated with and potentially lead to HF (Franzini-Armstrong et al., 1999; Gómez et al., 1997; Wu et al., 2014).

1.2.4 Sarcoplasmic reticulum

The SR is a specialised form of smooth endoplasmic reticulum that stores Ca^{2+} ions within a cell (Martini et al., 2012). Within a ventricular cardiomyocyte, T-tubules are separated by the junctional sarcoplasmic reticulum (jSR). The jSR is connected to the wider longitudinal SR structure which runs across the length of a sarcomere (Song et al., 2006). The RyR2 is a Ca^{2+} release channel which spans the SR membrane (Song et al., 2006). Opening of RyR2 occurs in the presence of Ca^{2+}, with the channel being activated when local Ca^{2+} is >10 μM (Bers, 2002; Soeller and Cannell, 2002). Calcium release from the SR is thought to be responsible for 92% of the Ca^{2+} involved in a Ca^{2+} transient within rat ventricular cardiomyocytes and therefore is critical to the phenomenon of ECC (Bers, 2001).

For cardiac muscle relaxation to occur, the removal of Ca^{2+} from the cytosol is required to return intracellular Ca^{2+} concentration to basal levels. Ca^{2+} removal occurs via NCX, the Ca^{2+}-ATPase, the mitochondrial Ca^{2+} uniporter and SERCA (Bers, 2002). Of these, the greatest contributor to cardiac muscle relaxation is SERCA (Periasamy et al., 2008). Within a ventricular cardiomyocyte, the isoform SERCA2a is located within the SR membrane and is primarily regulated by phospholamban (PLB). Specifically, PLB mediates β-adrenergic responses, due to cyclic adenosine monophosphate (cAMP) dependent and calmodulin dependent phosphorylation of PLB; the latter mechanism is sensitive to local Ca^{2+} concentration. Overall, the phosphorylation of PLB can increase SERCA2a pump activity (Periasamy et al., 2008; Tada et al., 1983).

1.2.5 Membrane tethers

Membrane tethers are proteins responsible for maintaining the distance between two membranes (Gallo et al., 2016; Henne et al., 2015). For a protein to be classified as a membrane tether, its upregulation should increase the association between two membrane contact sites and a down-regulation should have the opposite effect (Gallo et al., 2016). The protein junctophilin (JPH) is part of the family of JMC membrane tethers (Figure 1.4). Within a cell, JPH has a two-fold role; to provide structural support at the location of

the JMC, and to aid cellular Ca^{2+} signalling. The structure of JPH enables it to function as a membrane tether. For example, the membrane occupation and recognition nexus (MORN) motifs at the N-terminus aid the protein to bind to the sarcolemma, whilst the hydrophobic carboxy-terminal aids binding to the SR (Garbino et al., 2009; Takeshima et al., 2000).

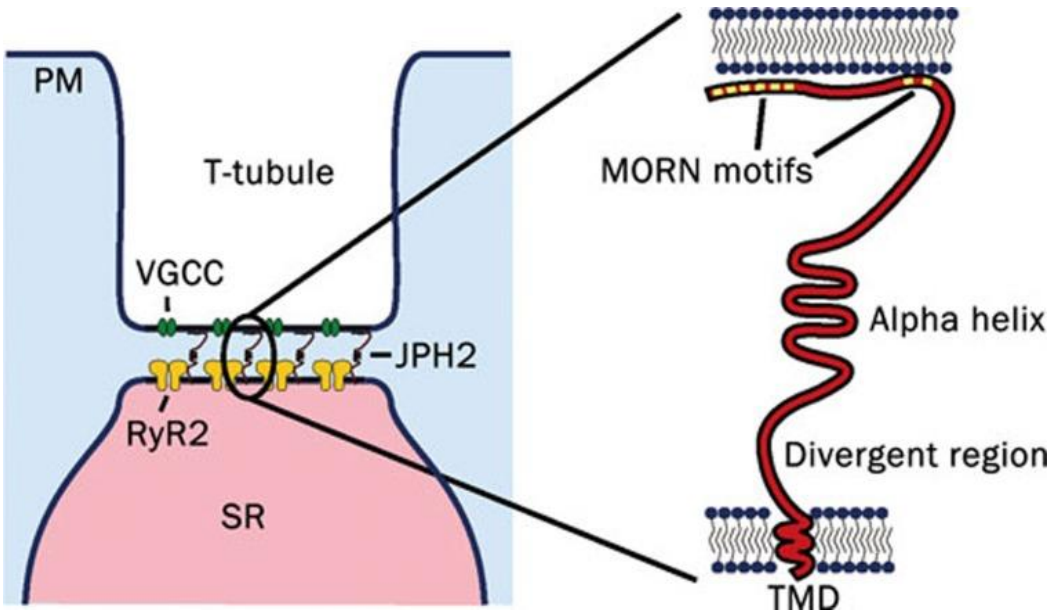

Figure 1.4: The junctional membrane complex. Schematic depicting the structure of junctophilin-2 in respect to the JMC of a ventricular cardiomyocyte. Adapted directly from Garbino and Wehrens (2010).

The isoforms of JPH have developed to become tissue specific, with JPH2 located within cardiac muscle (Garbino et al., 2009; Takeshima et al., 2000). Junctophilin-2 has a role in recruiting L-type Ca^{2+} channels to the T-tubule membrane as evidenced by an increased density when the membrane tether was overexpressed (Poulet et al., 2020). The Ca^{2+} handling proteins RyR2 and L-type Ca^{2+} channel have a ratio of 7.3 within rat cardiomyocytes (Bers and Stiffel, 1993), with the two proteins in association at the JMC. It is unclear the extent by which L-type Ca^{2+} channel and RyR co-localisation is influenced by T-tubule morphology. Formamide de-tubulation does not significantly alter their co-localisation (Smyrnias et al., 2010). This differs from the reported reduction in co-localisation from T-tubule disruption in HF (Crossman et al., 2011).

Junctophilin-2 cluster pattern is suggested to be tightly coupled to the cluster pattern of RyR2, with 90% of JPH2 labelling being within a 30 nm distance of RyR2 clustering in rat ventricular cardiomyocytes when visualised with super-resolution microscopy. The precise physical interaction between RyR2 and JPH2 is unknown (Jayasinghe et al., 2012). Despite this, JPH2 is suggested to have the capability to bind to and regulate RyR2 gating (Wang et al., 2014). In particular, the tamoxifen-induced knock-down of JPH2 within mice led to a 4-fold increase in RyR2 channel open probability, which was accompanied by a 15-fold increase in SR Ca^{2+} leak (Wang et al., 2014). Decreased JPH2 and RyR2 co-localisation in multiple JPH2 knock-down models has shown a decrease in RyR2 stability and consequent Ca^{2+} handling dysfunction that can lead to arrhythmia generation. This reveals JPH2's role as an allosteric modulator for RyR2 channel gating (Beavers et al., 2013; van Oort et al., 2011). Overall, JPH2 is suggested to have three roles within a cardiomyocyte. Through its structural role as a membrane tether, JPH2 is believed to mediate the functional role of RyR2 by having an inhibitory effect upon the Ca^{2+} pore, aid T-tubule development and influence RyR2 cluster organisation (Munro et al., 2016).

1.3 Ryanodine receptor cluster pattern

The RyR at 2.2 kDa is the largest known ion channel within mammals (Franzini-Armstrong, 1994; Lanner et al., 2010). There are three RyR isoforms (numbered 1-3) which all have a homotetrameric composition. Each tetramer within an RyR isoform is identical. Together they form a pore for the conductance of Ca^{2+} from the ER or SR to the cytoplasmic region of a cell (Lanner et al., 2010; Peng et al., 2016). The channel is 29x29x12 nm in size (Asghari et al., 2014). Within a ventricular cardiomyocyte RyR2 is the abundant isoform, with a conformational change in RyR2 itself believed to underlie the movement of Ca^{2+} (Peng et al., 2016).

Within a ventricular cardiomyocyte, the cytoplasmic domain of RyR2 is arranged in clusters within the surface of the SR. The size and orientation of these clusters has been greatly researched, enabled by the application of developing optical microscopy techniques (Jayasinghe et al., 2018b). Using

the diffraction-limited technique of confocal microscopy, a double-banded RyR2 pattern was identified which followed the orientation of the Z-line. The size of these clusters ranged from 80-140 RyR2 in density with minimal differentiation in RyR2 patterning at the periphery compared to deeper within a cell (Baddeley et al., 2009b). Similarly, Chen-Izu et al. (2006) calculated clusters to contain an average of 100 RyR2. The spacing between clusters was quantified by Soeller et al. (2007). They determined that the distance between one RyR2 cluster and its nearest neighbour (NND) was 0.78± 0.07 μm (mean ± SD) within human cardiomyocytes (Soeller et al., 2007). However, Jayasinghe et al. (2009) revealed that within rodents, 16% of RyR2s do not align with the T-tubule system and Z-line spacing, with a proportion of clusters being >250 nm from the T-tubule structure. These differing reports suggest that there is more complexity to RyR2 placement than confocal microscopy has the capability to resolve.

Single molecule (super-resolution) microscopy and tomographic electron microscopy have enabled the JMC to be visualised at an unprecedented level of detail. Specifically, the orientation of single RyR2 proteins can now be mapped within the JMC. The ability to quantify the RyR2 cluster pattern has been reviewed by Jayasinghe et al. (2018b).

The advent of super-resolution microscopy revealed that the size of RyR2 clusters within rat ventricular cardiomyocytes is different at the periphery compared to deeper within the cell. At the periphery, RyR2 cluster patterning is considered less dense, with the NND between RyR clusters being 472±5 nm compared to 135±15 nm at the intracellular jSR (mean ± SEM; Franzini-Armstrong et al., 1999). Additionally, Hou et al. (2015) visualised clusters within a cell to be nearly 4 times greater in size than sub-sarcolemmal RyR clusters at the periphery. Furthermore, with the use of SMLM, RyR2 clusters were found to contain 14 receptors at the periphery and 63 receptors internally (Baddeley et al., 2009b; Hou et al., 2015) compared with the previous conclusions based on confocal microscopy (Jayasinghe et al., 2018b). It is important to note that Baddeley et al. (2009b) used a SMLM that had a 40-60 nm lateral spatial resolution to obtain the reduced cluster sizes. However, the

ability to resolve structures is still poorer than the size of an individual RyR2. Therefore, a quasi-crystalline lattice had to be applied to their data which made the assumption that an RyR2 cluster was densely packed with proteins (Jayasinghe et al., 2018a).

The use of dual-tilt tomograms, however, revealed that the organisation of RyR2 within rat ventricular cardiomyocytes was non-ordered (Asghari et al., 2014). Electron tomography studies further revealed that the dyadic structure has a high degree of non-uniformity across a cell (Hayashi et al., 2009). A further advancement in optical microscopy verified this finding due to the ability to obtain a <10 nm spatial localisation. This enabled true molecular resolution of single RyR2 puncta to be studied. It was concluded that Baddeley et al. (2009b) had over-estimated RyR2 cluster size with sub-plasmalemmal clusters at the cell's periphery containing 8.8±0.86 RyR2 per cluster with an NND of 40.1±0.9 nm between clusters containing two or more RyR2 puncta (mean ± SD). Compared to the RyR2 cluster size derived by Baddeley et al. (2009b), this RyR2 cluster density at the cell's periphery is 64% lower (Jayasinghe et al., 2018a). It was recently reported by Jayasinghe et al. (2018a) that the majority of peripheral RyR2 clusters contain <5 receptors.

The arrangement of RyR2 can resemble a checkerboard or side-by-side array. Each cluster can exhibit both orientations, with cluster morphology being transient. The phosphorylation of an RyR2 has been suggested to trigger a change in the RyR2 cluster array (Asghari et al., 2014). The orientation of RyR2 tetramers and their clusters can have an impact upon Ca^{2+} signalling, a concept reviewed by Williams et al. (2018). Local control theory, known commonly as CICR, states that in a healthy cell, the clustered pattern of RyR2 enables Ca^{2+} release from the SR to occur in a controlled and localised manner.

Only a subset of RyR2 channels are thought to be activated at once from a localised Ca^{2+} influx during ECC (Williams et al., 2018). Patch-clamp studies of rat ventricular cardiomyocytes suggested that whole RyR2 clusters are never activated simultaneously. Instead, the release of Ca^{2+} from an open

RyR2 can trigger further Ca^{2+} release from neighbouring clusters (Baddeley et al., 2009b; Wang et al., 2004). This mechanism of positive feedback within CICR was suggested by Chen-Izu et al. (2006) due to the ordered 1.87±0.18 μm (mean ± SD) longitudinal spacing of RyR2 along the Z-line. Changes to the ultrastructure of the JMC could therefore disrupt the mechanism of CICR and the propagation of a Ca^{2+} throughout the cell (Chen-Izu et al., 2006). The importance of RyR2's cellular location was evidenced by Kolstad et al. (2018). In their post-infarct rat model of HF, they noted a dispersion of RyR2 with an increased density of smaller RyR2 clusters. This corresponded with a disruption in SR Ca^{2+} release marked by an increased spontaneous Ca^{2+} leak.

Within a cluster, RyR2s are considered to be functionally coupled together in a process known as 'coupled gating'. This mechanism is thought to ensure the co-ordinated activation and inactivation of RyR2 across a cell. This process is facilitated by the FKBP12.6 binding protein. When bound, FKBP12.6 increases an RyR2's open probability to make it more sensitive to local Ca^{2+} changes within the JMC (Marx et al., 2001). However, it is important to note that coupled gating of RyR2s is not required for the activation and opening of RyR2 channels during CICR (McCall et al., 1996).

1.4 Heart failure

Globally, 26 million people are diagnosed with HF. The mean age for diagnosis is 70-75 years of age (Ambrosy et al., 2014). HF is defined as the inability of the heart's cardiac output (CO) to meet the metabolic demands of the body. Heart failure is a progressive disease that can begin with a hypertrophic response to compensate for; an overloading of pressure or volume, damage as a result of a specific cardiac event such as ischaemia, or in response to genetic factors. The heart's hypertrophic response involves remodelling and growth of existing cardiomyocytes to assemble more sarcomeres and recruit more contractile units. Eventually, this response can result in 'decompensation'. When the heart is in a state of decompensation the capacity for Ca^{2+} signalling is reduced and consequently the heart's CO is reduced, leading to HF and cardiac death (Cohn et al., 2000; Fearnley et al.,

2011; ; Houser and Margulies, 2003; Kemp and Conte, 2012; Levy et al., 1990).

In general, remodelling of the heart as a form of compensation can occur at the whole organ, cellular and molecular level (Cohn et al., 2000). The focus of this research will be upon the structural and functional implications of Ca^{2+} handling within a failing cardiomyocyte at the level of the JMC. Disruption to the Ca^{2+} signalling pathways has been suggested to have a role in the development of hypertrophy and eventual HF (Molkentin, 2006). Specifically, the cycling of Ca^{2+} from the SR has been suggested to underlie the progression of HF with Ca^{2+} re-uptake into the SR via SERCA and Ca^{2+} release from the SR via RyR2 being the focus (Hoshijima et al., 2006).

At present, treatments include angiotensin-converting enzyme (ACE) inhibitors and β-blockers to target the haemodynamic and neurohormonal drivers that can aid remodelling (Cohn et al., 2000). However, research and therefore treatments in general have focussed upon the heart's LV function (Harjola et al., 2016). This does not account for the role that both the left and right ventricle have in maintaining CO (Friedberg and Redington, 2014).

The most common underlying cause of right ventricular (RV) HF is an increased pressure or volume overload, with the majority of RV HF incidences being linked to pulmonary disease (Friedberg and Redington, 2014). Within RV HF there is an increase in right atrial pressure and filling of the RV with blood is impaired (Harjola et al., 2016). However, further research is required to understand the mechanisms underlying the series of events leading to RV HF so that targeted treatment can be developed (Harjola et al., 2016). There are multiple research models to study the development of left and right ventricular HF. To understand the mechanisms underlying RV HF further, the monocrotaline-induced model of RV HF is favoured for its reproducible, simple and inexpensive method (Gomez-Arroyo et al., 2012; Wilson et al., 1992).

Administration of monocrotaline (MCT), creates a model of acute pulmonary arterial hypertension (PAH) characteristic of the MCT syndrome. As

compensation from PAH, RV hypertrophy can be induced and lead to the development of RV HF (Benoist et al., 2014; Gomez-Arroyo et al., 2012; Kay and Heath, 1966). Monocrotaline is an alkaloid substance originating from the *Crotalaria spectabilis* plant (Kay and Heath, 1966). The mechanism by which MCT acts is not fully understood. Recently, it has been suggested that MCT binds to the extracellular region of the extracellular Ca^{2+} sensing receptor which is located within the endothelial cells of the pulmonary artery. When bound, MCT can activate the receptor to initiate a signalling cascade which results in endothelial damage and consequential PAH (Xiao et al., 2017).

Research using the MCT model has revealed numerous cardiac changes from healthy physiology. Animal models with MCT-induced RV HF have a noted increase in RV wall thickness accompanied by a decrease in HR and stroke volume (SV) which results in a decreased CO. End-systolic and end-diastolic volume within the LV are also reduced (Rocchetti et al., 2014).

Disruption to ECC within the MCT model is suggested to result from changes in Ca^{2+} handling proteins, e.g. a 35% decrease in JPH2 was accompanied by a decrease in NCX, SERCA2 and Cav1.2 L-type Ca^{2+} channel expression. No changes, however, were detected in RyR2 or PLB expression (Xie et al., 2012). On the contrary, Kögler et al. (2003) revealed a decreased RV mRNA (messenger ribonucleic acid) expression of RyR2 and PLB with no change in sarcolemmal NCX. Furthermore, Rocchetti et al. (2014) suggested that RyR2 had an unstable function. A reduction in the SERCA2 pump was recorded by Benoist et al. (2014) which was compartmentalised by Kögler et al. (2003) to the RV. This complements an earlier study (Benoist et al. 2011) which detailed a non-significant and significant reduction in the L-type Ca^{2+} channels' LV and RV mRNA expression respectively. Regardless of the specific protein changes within the heart, it has been suggested that these changes are a result of an increased mechanical load from PAH which can affect CICR and consequently lead to ECC dysfunction (Kögler et al., 2003). It should be noted, however, that mRNA expression cannot reveal information regarding altered channel density at one cellular location, such as the JMC.

There is a lack of clarity regarding how known changes in Ca^{2+} signalling within RV HF pair with changes in Ca^{2+} handling proteins. This in part is due to previous research not taking into account the heterogeneity of remodelling (Benoist et al., 2014; Kögler et al., 2003; Xie et al., 2012). The diffusion of Ca^{2+} is in part determined by cellular components and therefore remodelling of the couplon in RV HF should be studied (Bers, 2001; Sobie et al., 2006). Within the MCT model there is a known overload of Ca^{2+} within the SR (Fowler et al., 2018). This is contrary to the statement made by Bers et al. (2003) that SR Ca^{2+} content is generally decreased in HF. However, when specifically looking at RV HF, the increased SR Ca^{2+} content could explain the recorded change in Ca^{2+} handling properties. Specifically, the presence of smaller, slower and desynchronised Ca^{2+} transients has been noted (Xie et al., 2012). Fowler et al. (2018) recorded changes in spontaneous Ca^{2+} spark profiles. Within the MCT model the mean Ca^{2+} spark frequency was significantly greater than control. There was also a trend towards increased spark width, amplitude and duration within the failing cardiomyocytes. Kolstad et al. (2018) similarly recorded changes in Ca^{2+} handling within their post-infarct HF model. A slowing of Ca^{2+} handling kinetics was evident with a significant increase in Ca^{2+} spark duration and time taken to reach peak amplitude. However, unlike Fowler et al. (2018) a reduced Ca^{2+} spark frequency was recorded with an increased spark mass. Earlier research led to the suggestion that within the MCT model, changes were independent of Ca^{2+}, with a decrease in the rate-limiting enzyme creatine kinase being the main contributor to the developed diastolic dysfunction (Fowler et al., 2015).

T-tubule disorganisation is a characteristic of HF (Guo et al., 2014). The degree of change within T-tubule orientation is greater within human failing cardiomyocytes than HF animal models (Crossman et al., 2011). However, this statement should take into consideration the differing T-tubule architecture across species as discussed previously (Crossman et al., 2011; Savio-Galimberti et al., 2008; Soeller and Cannell., 1999). Within the failing human heart, there was a decrease in RyR2 and L-type Ca^{2+} channel co-localisation observed at the level of the T-tubule (Crossman et al., 2011). A similar trend was observed by Song et al. (2006), with L-type Ca^{2+} channel

altered localisation reflecting T-tubule system disorganisation, leaving the RyR2 ‘orphaned’ at the Z-line. This change in ECC-related proteins and resultant ECC dysfunction is suggested to be due to transformation of the T-tubule system from its radial orientation to one that is longitudinal and oblique (Crossman et al., 2011). The change in T-tubule morphology visualised within a trans-aortic banded mice model of HF was prevented by an over-expression of JPH2. This suggests that JPH2 at the level of the JMC can have a protective effect against pressure overload by maintaining the ultrastructure of the CRU (Guo et al., 2014). The extent of JPH2’s role was evidenced in a knock-down model which resulted in a 40% decrease in JMC density, T-tubule disorganisation and eventual ECC dysfunction (van Oort et al., 2011).

Within HF there is a known change to the RyR2 cluster pattern at the level of the JMC. Crossman et al. (2011) recorded a reduced RyR2 cluster density within failing human ventricular tissue. However, within cardiomyocytes from a pacing-induced canine model of HF Yano et al. (2000) recorded a conformational change within RyR2 itself alongside a simultaneous Ca^{2+} leak from the SR. Super-resolution techniques were also used to analyse RyR2 distribution. Within RV cardiomyocytes from the MCT model, a 40% reduction in RyR2 cluster size was detected across the depth of the cell. Importantly, the spatial orientation of RyR2 is altered within a cell and not just RyR2 cluster size, with a dispersion and fragmentation visualised within RV HF (Sheard et al., 2019). With an xy spatial resolution of 21±3 nm (mean ± SD) Kolstad et al. (2018) similarly revealed a re-organisation of RyR2 at the level of the JMC. Within their post-infarct rodent model of HF they visualised an increased density of smaller clusters and a decrease in distance between clusters, representing a fragmented reorganisation.

Alongside the structural remodelling of the RyR2 cluster pattern, a degree of biochemical remodelling was also recorded within the MCT model. A rightward shift in RyR2 phosphorylation state for the Ser2808 residue was visualised, revealing a hyperphosphorylation gradient from the edge to the centre of the RyR2 cluster. It was suggested that this increased phosphorylation state across the JMC could limit the propagation of Ca^{2+}

signals across the cell (Sheard et al., 2019). However, the degree by which RyR2 phosphorylation can occur is thought to be influenced by local signalling, with the effect of isoprenaline being reduced in regions of T-tubule disruption where JMC ultrastructure is altered (Orchard and Brette, 2008)

1.5 The relationship between a cell's structure and function

Until now, research has generally focussed upon the structure of the JMC in isolation to its local Ca^{2+} signalling function. Therefore, when studying the relationship between local structure and function there has been a reliance upon computational simulations. The following section will discuss areas of research which have focused upon adopting a correlative imaging approach in regard to cellular structure and function.

Within cardiomyocytes, Kolstad et al. (2018) modelled the unitary release of Ca^{2+} at the level of the JMC. They concluded that Ca^{2+} spark fidelity, the likelihood by which a Ca^{2+} spark was elicited, was dependent upon the morphology of RyR2 clusters due to their role as a Ca^{2+} release channel. Specifically, when RyR2 clusters were reduced in size and dispersed across the JMC they recorded reduced Ca^{2+} spark fidelity with an increased silent SR Ca^{2+} leak. This chosen RyR2 pattern reflected experimental data from their post-infarct model of HF (Kolstad et al., 2018). Similarly, simulations have been developed to understand the relationship of RyR2 placement to AP propagation and Ca^{2+} signalling. A multiscale model simulated various RyR2 placements at the dyad and concluded that the positioning of RyR2 within a cluster can influence Ca^{2+} spark parameters. Specifically, elongated RyR2 clusters weakened the signalling between the L-type Ca^{2+} channel and RyR2 compared to clusters which have an array of 40 nm spaced RyR2 puncta (Cosi et al., 2019).

A number of experimental approaches have attempted to evaluate the local relationship between structure and function at the level of the JMC. The development of a GFP tagged RyR2 mouse model enabled RyR2 to be studied within live cells (Hiess et al., 2018). Using 3D confocal microscopy and total internal reflection fluorescence (TIRF) imaging, RyR2 arrangement

was aligned with local Ca^{2+} handling. It was determined that Ca^{2+} signalling was unaltered across the depth of a cell despite RyR2 cluster arrangement at the periphery being irregular in comparison to the striated and ordered array of RyR2 within the cell. It is important to note, however, that xy spatial resolution of this experimental technique is limited to 250 nm. Therefore, the GFP-tagged RyR2 arrays could be representative of multiple underling RyR2 clusters, creating an inability to locally ascertain Ca^{2+} spark generation at the level of a single cluster (Hiess et al., 2018). Line-scan confocal microscopy is the gold-standard technique for imaging Ca^{2+} sparks. However, it lacks spatial information regarding the unitarity release of Ca^{2+}. The technique was adopted by Asghari et al. (2020) to study Ca^{2+} handling within rat ventricular cardiomyocytes. Within a 200-300 nm thick section of the same cells, the Ca^{2+} spark activity was aligned with dual tilt electron tomography studies to understand RyR2 orientation. Whilst electron tomography provides the ability to visualise single RyR2 proteins, this study was not truly correlative by design as Ca^{2+} signalling cannot be studied in relation to local JMC structure due to the loss of spatial information. More recently, Hou et al. (2020) released a conference abstract describing the application of a super-resolution microscopy technique to quantify RyR2 cluster morphology within a transgenic mouse that had a photo-activated tagRFP targeted to the RyR2 protein. The scope of this research is as of yet unclear. No research, as far as the author is aware, has explored the physiological or pathophysiological relationship between local JMC structure at the level of a single protein and Ca^{2+} spark signalling in a correlative manner within primary cells. However, the conclusions drawn from the explored literature suggest that there is a relationship between Ca^{2+} signalling and a cell's underlying structure which requires further study.

1.6 Dorsal root ganglion sensory neurones

The mechanism of CICR has been well established within cardiac muscle as previously explored. However, there are a growing number of excitable cells that are believed to also exhibit the Ca^{2+} signalling mechanism of CICR to aid their cellular function. One of these cell types is the somata of sensory neurones (Figure 1.5) located within DRG.

1.6.1 Overview

Within the human body there are 31 pairs of spinal nerves. Each spinal nerve has a DRG located at the level of the vertebrae. The size of an individual DRG is dependent upon its positioning along the spinal column (Haberberger et al., 2019). The DRGs themselves are located proximal to the dorsal root of the spinal cord (Hanani, 2005). Each DRG contains connective tissue, vasculature and other non-neuronal cells amongst the somata of sensory neurones. Satellite cells are also present. Satellite cells are a specialised glial cell that are known to support the function of DRG sensory neurones (Haberberger et al., 2019; Hanani, 2005).

Sensory neurones within the DRG have a unique structure. From the somata, they have a single stem axon which bifurcates into a periphery and central axonal branch (Nascimento et al., 2018). The periphery branch extends to sensory endings at the periphery and the central branch extends to the spinal cord whereby it transmits a neuronal signal to the central nervous system. Therefore, the DRG has been suggested to be the beginning of all somatosensory pathways due to its specialised role in relaying nociceptive, mechanoreceptive and proprioceptive information from the peripheral nervous system to the central nervous system (Hanani, 2005; Nascimento et al., 2018).

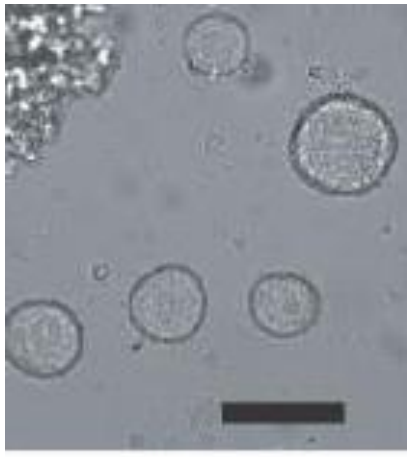

Figure 1.5: Structure of the dorsal root ganglion. Brightfield images of the somata of sensory neurones located in the dorsal root ganglion. Somata within dorsal root ganglia are of various cell diameters. Modified from Lu et al. (2006). Scale bar: 50 μm

Within the DRG, there is a diverse neuronal population, with somata ranging from 20-100 μm in diameter (Haberberger et al., 2019; Nascimento et al., 2018). A classification system for DRG sensory neurones has therefore been established. In general, there are two classes of DRG sensory neurones; large light and small dark as classified by size. However, the study of neurochemical markers has more recently enabled further sub-classification of neurones to understand better the role of DRGs (Haberberger et al., 2019; Lawson, 1992; Sommer et al., 1985).

1.6.2 Calcium signalling

The function of Ca^{2+} signalling is considered to be heterogenous across the population of sensory neurones within a DRG. For example, larger somata which have a non-nociceptive role are suggested to have a higher level of Ca^{2+} activity compared to somata from the smaller nociceptive afferents. In turn, the density of Ca^{2+} handling proteins is known to be heterogenous (Lu et al., 2006). The role of Ca^{2+} in neuronal function is widely disputed (Haberberger et al., 2019; Park and Luo, 2010). In the transmission of afferent signals, specifically nociceptive inputs, Ca^{2+} is known to trigger the exocytosis of vesicles from the somata of DRGs. These vesicles contain neurotransmitters and peptides (Cheng and Lederer, 2008). Specifically, an increased intracellular Ca^{2+} concentration, for example from ER-mediated Ca^{2+} release, can trigger the release of the neuropeptide substance P which is widely responsible for mediating pain signalling (Huang and Neher, 1996). When released, substance P binds to a G-protein coupled receptor (GPCR) complex within a neighbouring neurone to trigger a second messenger cascade and propagate nociceptive signalling (Graefe and Mohiuddin, 2020).

Sensory neurones within the DRG are considered a form of excitable cell. Their degree of neuronal excitability and therefore the likelihood that an AP will propagate across a neurone is determined by the ease with which ions can be conducted across their plasma membrane. Ca^{2+} has been suggested to have a crucial role in AP propagation, with intracellular Ca^{2+} concentration known to alter a neurone's level of excitability (Henzi and MacDermott, 1992). The absence of extracellular Ca^{2+} inhibited the generation of spontaneous

APs and the inhibition of the Ca^{2+}-ATPase pump within the neuronal ER store of the ion resulted in a slowed signal transduction throughout the cell (Markram et al., 1995; Mathers and Barker, 1984). The concentration of Ca^{2+} within the ER can determine how responsive a neurone is to the arrival of a depolarising current (Friel and Tsien, 1992). One suggestion for this functional reliance upon Ca^{2+} could be due to the mechanism of CICR within the neurone. The activation of voltage gated Ca^{2+} channels within the plasma membrane can initiate CICR from a local increase in cytosolic Ca^{2+}. This feed-forward amplification of the Ca^{2+} signal is considered to contribute towards 80% of the Ca^{2+} signalling which occurs as a result of an AP (Usachev and Thayer, 1997).

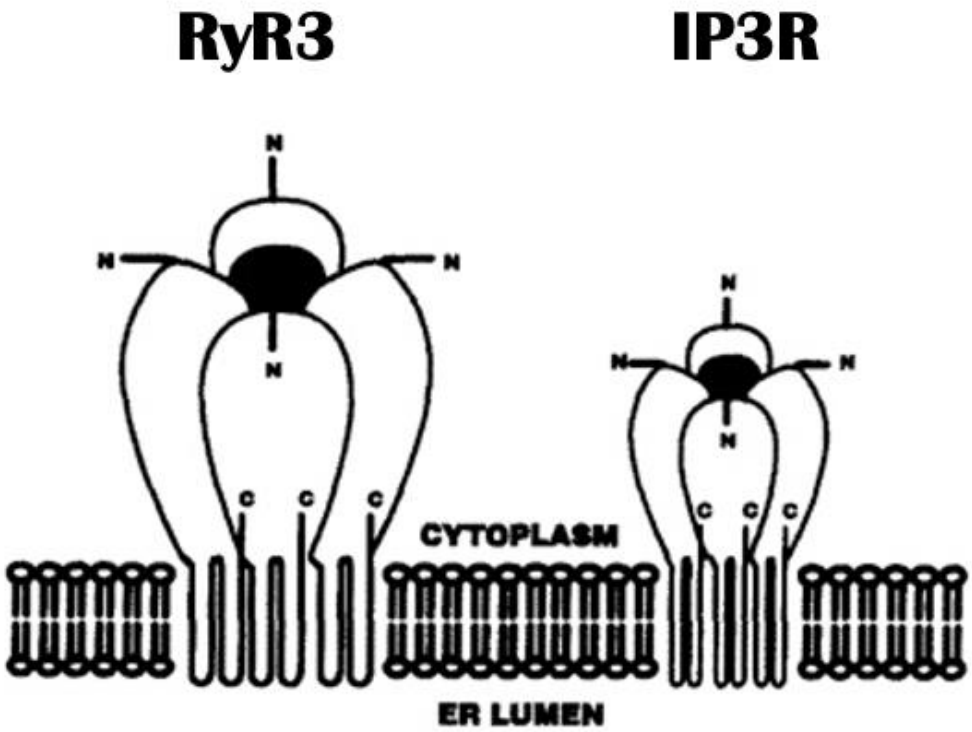

Figure 1.6: Calcium release channels within the dorsal root ganglion. Schematic detailing the overall tetrameric structure of the RyR and IP3R pore forming Ca^{2+} channels within the surface the ER. Adapted directly from Henzi and MacDermott, (1992).

The ER within a sensory neurone is located throughout the somata and axonal regions of the cell. Electron microscopy visualised the ER to be in close apposition with a neurone's outer plasma membrane, with the two membranes suggested to be anchored 20-80 nm apart. The region of the ER closest to the plasma membrane is known as the subsurface cisternae, representing the

JMC described within ventricular cardiomyocytes (Berridge, 1998; Rosenbluth, 1962). Located on the surface of the ER are two Ca^{2+} release channels; RyR3 and IP3R (Figure 1.6). Unlike ventricular cardiomyocytes, the RyR3 isoform is the only RyR present within sensory neurones. The ER also has the Ca^{2+} re-uptake pump SERCA (Berridge, 1998; Lokuta et al., 2002). SERCA enables restoration of the ER Ca^{2+} concentration, to ensure that the neurone is primed for the arrival of the next depolarising current. The sensitivity of RyR3 and IP3R has been suggested to be partially dependent upon the ER's Ca^{2+} concentration (Berridge, 1998; Khomula and Voitenko, 2006). Overall, Ca^{2+} signalling within sensory neurones of the DRG is controlled by a binary membrane system, with the plasma membrane and ER acting cohesively to regulate neuronal excitability, neurotransmitter release, associativity, neuronal plasticity and the function of gene transcription (Berridge, 1998).

The structure and function of the RyR has already been discussed. The RyR3 isoform shares the role of RyR2 which is abundant in cardiac muscle. Within the somata of DRG sensory neurones, RyR3 has a density of 0.33 puncta per μm^2 (Ouyang et al., 2005a). Similar to RyR3, the IP3R is a homotetramer, with the IP3R1 isoform being most abundant within the central nervous system. The primary mechanism by which IP3R is activated is through a second messenger cascade. Within the plasma membrane, metabotropic GPCRs are located (Henzi and MacDermott, 1992; Simpson et al., 1995). The activation of GPCRs can be by hormones or neurotransmitters, one example being bradykinin. Once activated, the enzyme phospholipase C can in turn be activated to hydrolyse the plasma membrane-bound phosphatidylinositol 4,5-biphosphate (PIP_2) phospholipid. Once hydrolysed, the phospholipid forms diaglycerol (DAG) which can activate protein kinase C (PKC) and inositol triphosphate (IP3). The latter IP3 can bind to and activate IP3R to enable the release of Ca^{2+} from the ER (Henzi and MacDermott, 1992; Thayer et al., 1988).

The extent by which Ca^{2+} alone can activate the IP3R is unclear. However, Ca^{2+} can bind directly to the IP3R to enhance the receptor's activity (Henzi

and MacDermott, 1992). This was demonstrated by Finch et al. (1991). They concluded that Ca^{2+} can bind to the IP3R and when IP3 concentration was unchanged. In turn, they noticed that an increased cytoplasmic Ca^{2+} concentration had the ability to enhance IP3R mediated Ca^{2+} release. Optimal IP3R activity was observed when local cytoplasmic Ca^{2+} concentration was 300 nM. Notably, a concentration of 10-100 μM Ca^{2+} was shown to potentiate any further response, demonstrating a limit to the modulatory role of Ca^{2+} (Finch et al., 1991; Simpson et al., 1995). Upon the IP3R, Ca^{2+} and IP3 are therefore considered to act as co-agonists within the DRG (Berridge, 1998).

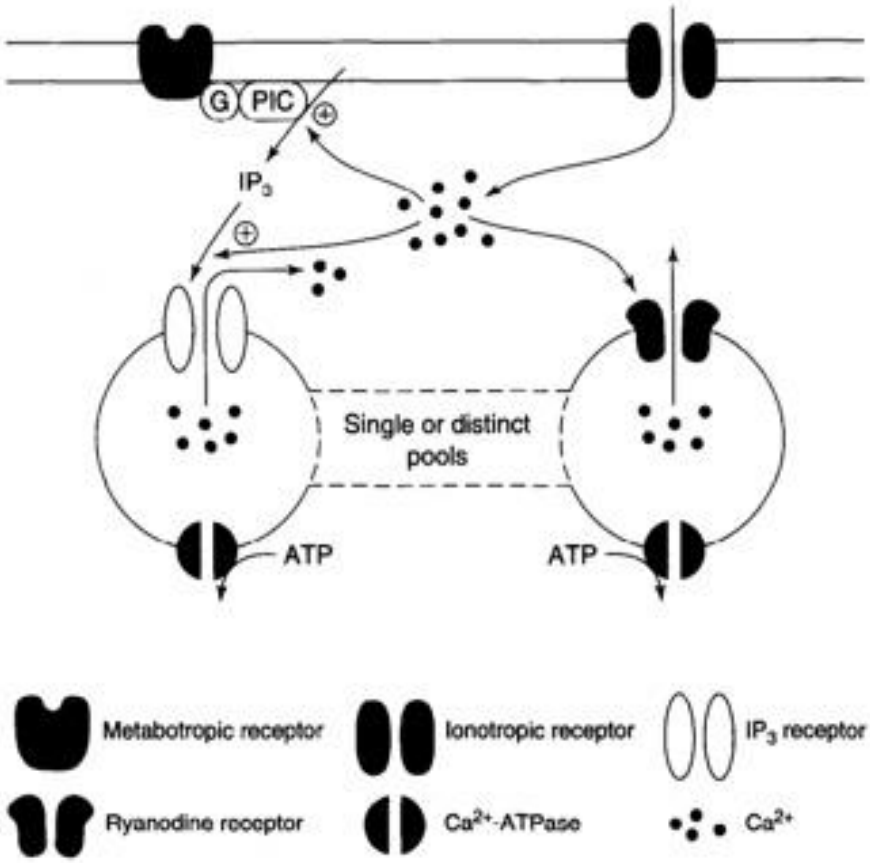

Figure 1.7: Schematic detailing the binary membrane system within the somata of DRG sensory neurones. The process of CICR is mediated by the entry of Ca^{2+} from the extracellular space into the intracellular region of the neurone. Further rise in cytosolic Ca^{2+} concentration is from the efflux of Ca^{2+} from the ER either via IP3R or RyR3. The activation of IP3R is by IP3 and to an unknown extent Ca^{2+} itself, whereby Ca^{2+} alone activates the RyR3 channel. The question of whether IP3R and RyR3 share the same ER store is still unanswered. Adapted directly from Simpson et al. (1995).

There has been debate within the literature as to whether RyR3 and IP3R have the same unified Ca^{2+} store within a sensory neurone. Within bovine adrenal chromaffin cells, the addition of RyR3 and IP3R sensitive

pharmacological agents to the same Ca^{2+} store led Liu et al. (1991) to the conclusion that both Ca^{2+} release channels are located within the same ER. However, Thayer et al. (1988) reported two separate stores within DRG sensory neurones, a caffeine-sensitive store whereby RyR3 is activated and a bradykinin-sensitive store whereby IP3R is located (Figure 1.7). Furthermore, RyR3 abundant ER stores were suggested to be mainly within the somata, with IP3R ER stores located throughout the somata and axonal regions (Thayer et al., 1988). However, another consideration is that Ca^{2+} release mediated by IP3R can lead to RyR3 activation through an alternate mechanism of CICR (Henzi and MacDermott, 1992). Uncertainty still remains regarding the individual roles of IP3R and RyR3 within CICR and overall Ca^{2+} signalling within the DRG collection of neurones (Simpson et al., 1995).

The unitary release of Ca^{2+} from the ER, either through the RyR3 or IP3R channel is classified as a Ca^{2+} spark, similar to that within ventricular cardiomyocytes. These co-ordinated release events of Ca^{2+} from ER channels within neuronal cells were originally characterised as Ca^{2+} puffs. A comparison has been suggested between the release of Ca^{2+} from a single channel in the form of a Ca^{2+} blip within neurones and the recording of Ca^{2+} quarks within cardiomyocytes (Lipp and Niggli, 1996). In relation to DRGs, the role of Ca^{2+} sparks within the somata of sensory neurones was to evoke vesicular secretion and signal propagation. The mechanism of CICR was therefore suggested to account for 60% of Ca^{2+} dependent exocytosis (Ouyang et al., 2005a).

Using confocal microscopy, Ca^{2+} spark events were primarily recorded at the subsurface of the somata, with 75% of Ca^{2+} spark activity being within 1 μm of the cell membrane. These Ca^{2+} sparks exhibited a more prolonged morphology with a smaller amplitude compared to Ca^{2+} sparks from ventricular cardiomyocytes. Specifically, spontaneous Ca^{2+} spark release from the ER within the somata have a F/F0 spark amplitude of 0.27±0.05, with a full width at half-maximum (FWHM) spatial dispersion of 2.03±0.29 μm and 37.9±6.3 ms duration (mean ± SEM). Overall, the morphology of a Ca^{2+} spark within the DRGs is smaller than within cardiac muscle. Unlike cardiomyocytes,

Ca^{2+} sparks have an inability to form a propagating Ca^{2+} wave across the cell, with Ca^{2+} release being spatially distinctive (Ouyang et al., 2005a). These spatially distinctive Ca^{2+} release sites were detected 1.7 μm apart, which is synonymous with the RyR3 cluster spacing of 1.84±0.10 μm (mean ± SEM) within the subsurface cisternae. The role of RyR3 in Ca^{2+} spark generation was further exemplified by the application of 5 mM caffeine which activated RyR3 in relation with an increase in Ca^{2+} spark frequency. It is important to note that Ca^{2+} spark activity was only inhibited upon the addition of an RyR3 antagonist (10 μM ryanodine or 1 mM tetracaine), with an IP3R antagonist (20 μM 2-aminoethoxydiphenyl borate or 10 μM xestospongin C) having no significant change upon Ca^{2+} spark recordings. This finding provides the rationale for further research to explore the role of RyR3 and IP3R within CICR and Ca^{2+} spark generation (Ouyang et al., 2005a; Ouyang et al., 2005b).

1.6.3 Additional targets of interest

The isoform JPH4 has been suggested to maintain the 20-80 nm distance between the plasma membrane and subsurface cisternae within DRG sensory neurones (Berridge, 1998; Hogea et al., 2019; Lu et al., 2006). Further research is required to understand the extent of JPH4's role as a membrane tether within the DRGs. However, it has been suggested that the protein is vital to Ca^{2+} signalling, with a knock-down of JPH4 reducing the responsiveness of GPCR activation in the IP3 signalling pathway (Hogea et al., 2019; Ouyang et al., 2005a; Ouyang et al., 2005b). Additional to JPH4, the anoctamin channel (ANO1) protein is considered to tether the ER to the PM within DRG sensory neurones (Cabrita et al., 2017; Kunzelmann et al., 2016). The ANO1 channel is part of the cellular store operated Ca^{2+} entry (SOCE) mechanism. Due to channel placement, the ANO1 is thought to interact with the bradykinin (B_2) receptor within the PM and IP3R within the ER. Instead of Ca^{2+} mediated activation of ANO1 from voltage-gated Ca^{2+} channels within the PM, the IP3R release of Ca^{2+} is considered to mediate ANO1 channel activation (Cabrita et al., 2017; Jin et al., 2013; Kunzelmann et al., 2016). Specifically, ANO1 forms a complex with the Ca^{2+} permeable channel TRVP1. The use of a proximity ligation assay (PLA) enables the close association of two targets to be detected. Within DRGs, PLA spatially resolved

the ANO1/TRVP1 complex within 30-40 nm of IP3R1. Due to its close association, Ca^{2+} release from the ER via IP3R1 has been suggested to activate the TRVP1 channel which can indirectly enhance ANO1 activation and exacerbate the SOCE mechanism (Shah et al., 2020). These findings suggest that despite the earlier suggestion that RyR3 has a larger role within CICR, local structure of the JMC can still influence local Ca^{2+} signalling.

1.7 Super-resolution and novel tools for visualising calcium handling machineries

The scale of a cell's ultrastructure requires the application of a high-resolution imaging technique to accurately study the location of Ca^{2+} handling proteins. For example, within a cardiomyocyte the distance between the SR bound RyR2 channel and the T-tubule is 12 nm (Garbino et al., 2009; Takeshima et al., 2000). Early electron microscopy studies were limited in their ability to resolve multiple targets in relation to each other at the level of the JMC (Elbaz and Schuldiner, 2011; Helle et al., 2013). Optical microscopy has also been used as a tool to ascertain the structural morphology of Ca^{2+} handling proteins. However, widefield microscopy is limited to an axial resolution of 800 nm. The addition of a pinhole within confocal microscopy, as reviewed by Stemmer et al. (2008) improved resolution to 250 nm. Regardless, this resolution is still over 8-fold poorer than the spatial localisation required to visualise the assumed 30 nm size of RyR2 (Chen-Izu et al., 2006). When choosing a microscopy technique, cell-to-cell variability and imaging depth should be considered alongside optical resolution. For example, confocal microscopy despite its 250 nm resolution has the ability to image beyond the TIRF-field 100 nm depth that techniques such as DNA-PAINT are limited by (Fish, 2009). This factor becomes pertinent in studying cardiomyocytes when the interspaced nature of peripheral RyR2 clusters between the Z-lines are to be considered in relation to the ordered 1.87±0.18 μm (mean ± SD) RyR2 spacing deeper within the cell (Chen-Izu et al., 2006; Hou et al., 2015).

Super-resolution microscopy is a form of high-resolution fluorescence microscopy, otherwise known as nanoscopy. Two methods of nanoscopy have been developed; SMLM and stimulated emission depletion (STED)

microscopy. Both techniques exploit the photo modulation properties of a fluorophore to image light in a spatial and temporal manner (Turkowyd et al., 2016). As a result, the point spread function (PSF) of light is reduced, which in turn improves xy spatial resolution. The PSF is the diffraction pattern of light that is emitted from a focal point (Figure 1.8), for example from the localisation of a fluorophore-emitted light within immunofluorescence studies (Cole et al., 2011).

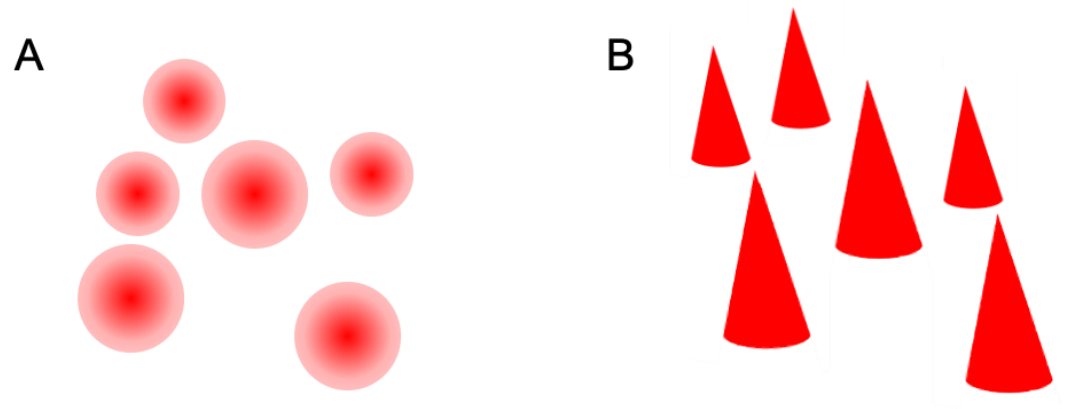

Figure 1.8 Point spread function. Schematic to represent the point spread function within microscopy. When fluorescence is emitted, light is collected. The ability to collect the diffraction pattern of emitted light can vary. This variation is displayed as the point spread function and it determines how spatially close two points of fluorescence can simultaneously be emitted whilst still being individually resolved. (A) Points of emitted fluorescence (B) and their 3D diffraction pattern, known as the point spread function, according the microscopy technique applied.

The principle of SMLM is reliant upon the ability to visualise single fluorescent molecules individually by turning them on and off (Moerner and Kador, 1989). This principle within a fluorophore was characterised at room-temperature when Dickson et al. (1997) described optical switching within a mutant GFP (Möckl et al., 2014). Betzig et al. (2006) applied the photophysical switching characteristics of a fluorophore to an optical microscopy technique known as photoactivated localisation microscopy (PALM), which has the ability to resolve structures to 20 nm (Betzig et al., 2006; Möckl et al., 2014). Development of SMLM based upon optical switching has led to the development of numerous microscopy techniques. Two single-molecule imaging techniques known as direct Stochastic Optical Reconstruction Microscopy (dSTORM) and DNA – Points Accumulation for Imaging in Nanoscale Topography (DNA-PAINT) are able to achieve an xy spatial

resolution of 20 nm and <10 nm respectively (Heilemann et al., 2008; Jungmann et al., 2014).

There is continual development of SMLM within the field of microscopy. Specifically, the application of DNA-PAINT was a development from the redox photoswitching approach of dSTORM to provide an imaging approach resistant to photobleaching, with improved temporal resolution (Jungmann et al., 2010). The concept of DNA-PAINT has been further developed to account for the visualisation of multiple proteins of interest and termed Exchange-PAINT (Jungmann et al., 2014). One limitation of DNA-PAINT which has limited its use within tissue samples was background fluorescence from an excess of unbound imager strand. To address this limitation, Auer et al., (2017) developed a Förster resonance energy transfer (FRET) PAINT method. The use of a FRET-based imager strand reduced background fluorescence by altering the conditions by which an imager strand would emit fluorescence. The occurrence of a stochastic event was therefore dependent upon two imager strands binding to a docking strand, and their FRET-pair to emit fluorescence. An alternative approach was developed by Lutz et al., (2018) known as quencher DNA-PAINT. It is this approach which will be utilised within the research that follows. Quencher-PAINT relies upon the use of a short oligonucleotide strand which can transiently bind to any ‘free’ imager strand within solution and ‘quench’ the background fluorescence to enable an improved xy spatial resolution and use within tissue sections.

Since the initiation of this research project, Clowsley et al., (2020) have published the repeat DNA-PAINT technique. This imaging tool relies upon a docking strand with a repeated nucleotide sequence to allow for multiple imager strands to bind in an attempt to increase binding specificity and decrease background fluorescence. All of these developed methods can adopt the analysis technique of quantification PAINT, which is an alternative analysis tool to identify individual proteins of interest (Jungmann et al., 2016). There is still a requirement for DNA-PAINT to be developed further. Within the following research, the aim was to quantify the 2D spatial patterning of Ca^{2+} handling proteins. Therefore, the use of dSTORM and DNA-PAINT were

selected due to their ability to spatially resolve individual Ca^{2+} handling structures with increased clarity, specifically in relation to the study of RyR in the xy spatial plane (Baddeley et al., 2009b; Jayasinghe et al., 2018a). The reliance of both of these SMLM techniques upon TIRF enable a robust comparative with live cell Ca^{2+} imaging in the TIRF-plane. Combined, this allows for a novel approach to be undertaken with SMLM, through its combination with live cell functional imaging techniques to develop a correlative imaging protocol. However, it should be noted that microscopy techniques that do not rely upon the use of TIRF microscopy can visualise Ca^{2+} handling proteins within the z plane. For example, 10x enhanced expansion microscopy (10xEEM) has been utilised to quantify RyR2 within cardiomyocytes with a 15 nm in-plane and 35 nm axial spatial resolution (Sheard et al., 2019).

1.8 Aims of study

For the heart to contract as a functional syncytium, the movement of Ca^{2+} needs to be tightly controlled. In RV HF, there is a disruption in Ca^{2+} handling which results in an inability of the heart to meet the body's metabolic demands. Ca^{2+} movement is mediated by the RyR channel. Remodelling of the RyR cluster pattern occurs within RV HF. However, the local impact that this structural change has upon local Ca^{2+} handling is unknown. The development of a correlative imaging protocol is required to enable local Ca^{2+} function to be studied in relation to a cardiomyocyte's local structure. Uncovering how this relationship changes in RV HF is critical for the proportion of the population affected by the disease, for which there is no curative treatment. The development of a correlative imaging protocol to examine local Ca^{2+} function in relation to a cell's Ca^{2+} handling ultrastructure would provide a greater understanding as to the importance of Ca^{2+} in other cells. One example is the DRG sensory neurones which have shown to exhibit CICR. The functional role of their JMC is still unclear, with the contribution between RyR3 and IP3R unknown and proteins such as JPH4 only now being studied.

This study aims to test the hypothesis that local ultrastructure of the JMC within an excitable cell can impact local Ca^{2+} signalling and overall cell

function. The specific aims are three-fold. The first aim is to develop a correlative imaging protocol for primary cells to understand the local relationship between structure and function. Specifically, Ca^{2+} signalling will be studied in regard to spontaneous Ca^{2+} spark generation and evaluated in regard to a cell's underlying Ca^{2+} handling protein structure at the level of the JMC. The second aim is to apply the correlative imaging protocol to determine whether pathological changes in Ca^{2+} signalling within RV HF are related to a structural change within the JMC, specifically at the level of the RyR2 Ca^{2+} release channel. Finally, the third aim is to understand the role of RyR3 and IP3R Ca^{2+} release channels within the somata of DRG sensory neurones in relation to their local Ca^{2+} signalling by using the correlative imaging protocol.

Achievement of the above study aims would enable the dissemination of a protocol that would facilitate the study of a cell's local structure in relation to Ca^{2+} signalling, a feature that is questioned within pathophysiology.

Chapter 2. Methods

All experiments were undertaken according to the UK Animals (Scientific Procedures) Act of 1986 under the EU Directive 2010/63/EU with UK Home Office and local ethical approval (PPL 70/8399). All animals were obtained from Central Biomedical Services, University of Leeds. Animals were housed at 20-22 °C at 50% humidity on a 12-hour light/dark cycle with *ab libitum* access to food and water. Animals were euthanised in the morning, unless otherwise dictated by the presentation of HF.

2.1 Heart failure model

Adult male Wistar rats (180-215 g) had an intraperitoneal injection using a 26G needle of either 60 mg/kg MCT (Sigma-Aldrich, USA) to induce acute RV HF or an equivalent volume of 140 mM NaCl saline as a control. These two animal groupings will be referred to as Fail and Control respectively. As described previously, the alkaloid MCT can result in endothelial damage within the vascular bed of the pulmonary arterial system. Administration can result in acute PAH and consequent development of RV hypertrophy and eventual RV HF (Kay and Heath, 1966; Xiao et al., 2017). The 60 mg/kg MCT solution, within a 140 mM NaCl buffer, was prepared fresh on the day of injection. Initially, MCT was dissolved in 1 M HCl before being corrected to pH 7.4 within the NaCl buffer. Post-injection, animals were weighed and observed three times weekly for three weeks before being weighed and observed daily. Throughout this time, animals were monitored for visual signs of RV HF with an end-point established upon a; 10 g weight loss within a 24 hour period, weight loss over two consecutive days or an overall weight loss of 20 g. Signs of a cold extremity, lethargy, dyspnoea and piloerection were also monitored to denote the severity of RV HF development. Upon the presentation of RV HF, animals were euthanised by concussion followed by cervical dislocation. Control animals were age-matched in regard to the number of days post-injection in which the Fail animals reached their pre-described end point. The described MCT model of RV HF follows those previously described within the literature (Benoist et al., 2011; Fowler et al., 2015; Sheard et al., 2019).

2.2 Sample preparation

2.2.1 Ventricular cardiomyocyte cell isolation

The whole heart was quickly excised upon the animal reaching its end point and cannulated at the aorta to a Langendorff apparatus (Figure 2.1). A retrograde perfusion of isolation solution (IS) consisting of (in mM): 130 NaCl, 1.4 $MgCl_2$, 5.4 KCl, 0.4 NaH_2PO_4, 5 HEPES, 10 Glucose, 20 Taurine, 10 Creatine at pH 7.4; 37°C with added 0.75 mM $CaCl_2$ was started at a steady 7 mL/min to clear the heart's coronary circulation.

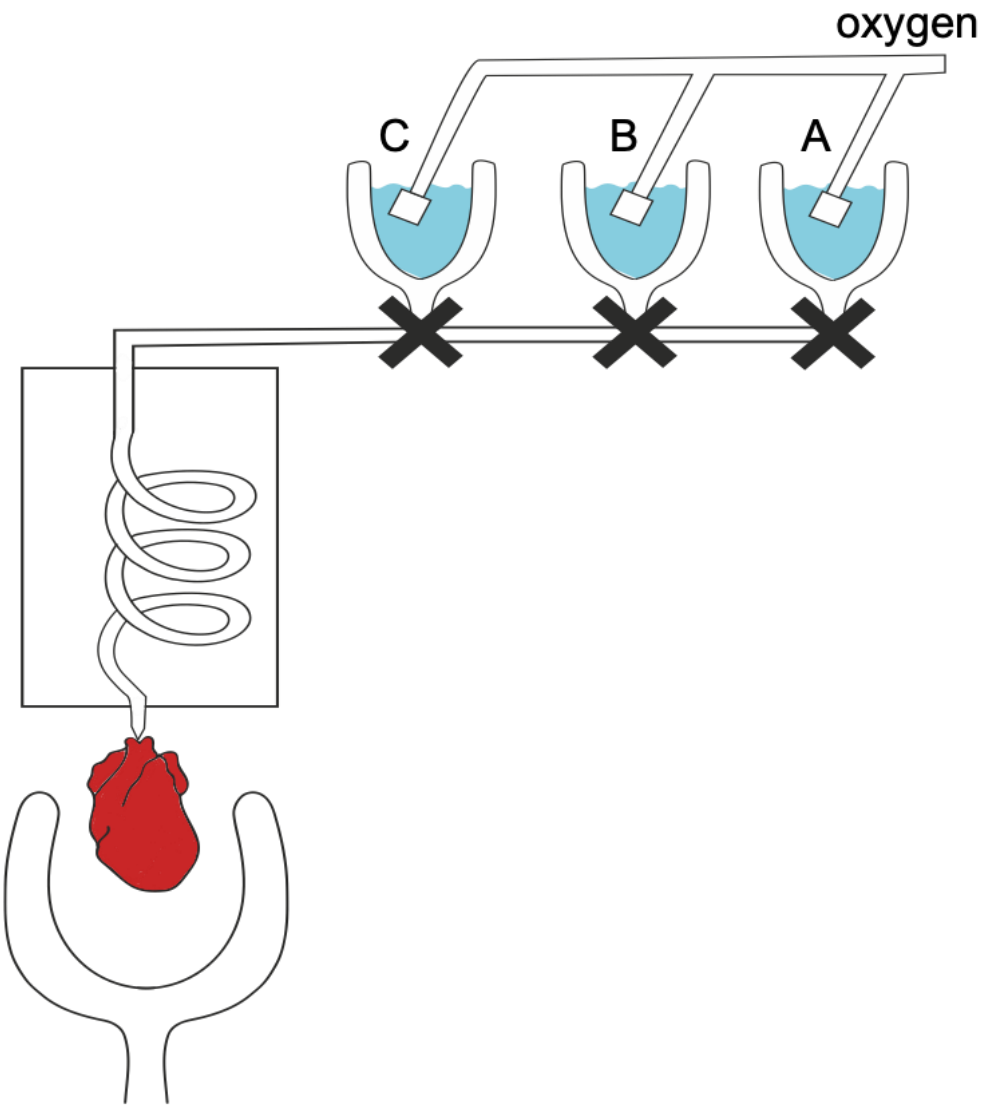

Figure 2.1: Schematic of the Langendorff Apparatus. Heart was cannulated at the aorta and perfused at 7 mL/min with (A) IS to initially clear the coronary circulation, (B) prior to a 4 minute perfusion of IS with 0 mM $CaCl_2$ and added 0.1 mM EGTA and (C) 7 minute perfusion of enzyme solution with 0 mM $CaCl_2$ and added 1 mg/mL Collagenase Type II and 0.8 mg/mL protease. Solutions were oxygenated and passed through a 37°C heated water jacket and reservoir placed for collection after perfusion through the heart.

The following protocol was then implemented to enzymatically isolate left and right ventricular cardiomyocytes. For 4 minutes, IS with added 0.1 mM EGTA (Sigma-Aldrich, USA) and 0 mM $CaCl_2$ was perfused to remove Ca^{2+} from the heart. Next, a 7-minute perfusion of IS with 0 mM $CaCl_2$, 1 mg/mL Collagenase Type II (Worthington Biochemicals, USA) and 0.8 mg/mL protease (Sigma-Aldrich, USA) occurred to enzymatically digest the heart. The whole heart was removed from the Langendorff apparatus and weighed. Atria and vasculature were dissected away, and heart weighed again prior to the dissection and weighing of the left and right ventricle. The RV and LV tissue were placed in separate conical flasks with collagenase solution. Using a rotary shaker, for 5 minutes, the conical flasks were shaken within a 37°C water bath prior to the filtering of enzyme solution through a 200 μm^2 nylon mesh gauze. Collected cardiomyocytes were centrifuged (50 rpm; 45 s), supernatant removed, and cardiomyocytes resuspended within 750 μM $CaCl_2$ containing IS. Remaining tissue was shaken again for 5 minutes with the above steps repeated until no cell-rich tissue remained. LV and RV cardiomyocytes were separately re-suspended with Tyrode's solution which constituted of (in mM): 140 NaCl, 4 $MgCl_2$, 1 KCl, 10 HEPES, 10 Glucose, 0.75 $CaCl_2$ at pH 7.4 and kept at room temperature (RT) until required for experiments.

2.2.2 Primary culture of dorsal root ganglion neurones

Neonatal male Wistar rats (aged 6-10 days) were euthanised by an overdose of the inhalational anaesthetic isoflurane followed by cervical dislocation. The spine was removed and divided in two along the sagittal plane before being placed on ice in Mg^{2+} and Ca^{2+} free Hanks' balanced salt solution (HBSS). For one half of the spine, the spinal cord was removed and using fine forceps the DRGs from each vertebrae level were removed and placed on ice in a separate Mg^{2+} and Ca^{2+} free HBSS containing dish. This was repeated for the other half of the spine. Under sterile conditions, the DRGs were placed into 2 mL of dissection solution which contained 10 mg/mL dispase and 1 mg/mL Type 1A collagenase in Mg^{2+} and Ca^{2+} free HBSS. The DRGs were incubated for 15 minutes (humidified incubator at 37°C, air supplemented with 5% CO_2). DRGs were triturated gently to avoid

mechanical stress prior to adding 10 mL of ice-cold DMEM pre-supplemented with GlutaMAX, 10% foetal bovine serum, 5% penicillin, and 50 μg/mL of streptomycin to inactivate the dispase and collagenase enzymes. Cells were centrifuged (800 g; 5 mins; 4°C), supernatant removed, and cells resuspended in 10 mL DMEM solution. Centrifugation was repeated and cells resuspended in a reduced volume of DMEM solution. A 200 μL volume of cell solution was added to the middle of a 50 μg/μL laminin and 0.001% poly-D-lysine coated 500 μm square gridded imaging dish, with #1.5H glass coverslip (Ibidi, USA). With care not to break the meniscus, dishes were placed in a humidified incubator for 4 hours. Dishes were flooded with 2mL of 37°C heated DMEM and kept within the humidified incubator for 24 hours (Kirton et al., 2013). On the day of use, DMEM solution was removed and replaced with DRG-specific Tyrode's which constituted of (in mM): 160 NaCl, 1 $MgCl_2$, 2.5 KCl, 10 HEPES, 10 Glucose, 0.75 $CaCl_2$ at pH 7.4 and cells kept at 37°C until use.

2.3 Live-cell calcium imaging

Cardiomyocyte and DRG 0.75 mM $CaCl_2$ containing Tyrode's solution was removed and replaced with 5 mM $CaCl_2$ containing Tyrode's. Cells were incubated with a greater $CaCl_2$ concentration to increase the propensity by which spontaneous Ca^{2+} activity occurred. A final 5 mM $CaCl_2$ containing Tyrode's was chosen based upon a qualitative assessment of a 0.1 mM to 10 mM range of $CaCl_2$ concentrations. At 10 mM $CaCl_2$, Ca^{2+} spark frequency was minimal with a high number of cyclic Ca^{2+} waves detected that were followed by cell death. At 5 mM $CaCl_2$, a moderate Ca^{2+} spark frequency was detected across the imaged cells, and these same cells remained intact throughout the fixation protocol. Minimal Ca^{2+} sparks were detected at $CaCl_2$ concentrations ranging between 0.5 mM and 3 mM $CaCl_2$. A high frequency of Ca^{2+} sparks were detected at 0.1 mM $CaCl_2$ and cells remained intact throughout the fixation protocol. However, a final 5 mM $CaCl_2$ was chosen due to its mechanism of increased Ca^{2+} spark activity being through Ca^{2+} overload of the cell's internal store rather than a cell's internal Ca^{2+} store being depleted in the presence of 0.1 mM $CaCl_2$.

Cells were foil-wrapped to limit light exposure and loaded with 5 μM Fluo-4 AM (ThermoFisher Scientific, UK) for 15 minutes at RT upon a low-speed rocker. Fluo-4 AM loading for DRG preparations was done with added 0.01% Pluronic acid (10% w/v; Sigma-Aldrich, USA). Excess Ca^{2+} indicator dye was removed, and cells were re-suspended in 5 mM $CaCl_2$ containing Tyrode's prior to a 30-minute de-esterification period at 4°C (Steele and Steele, 2014). After 30 minutes, DRG dishes were washed with fresh 5 mM $CaCl_2$ Tyrode's and 0.1 μm sized TetraSpeck microsphere (ThermoFisher Scientific, UK) fiducial markers were added prior to imaging. Cardiomyocytes were further incubated for 90 minutes at RT in fresh 5 mM $CaCl_2$ Tyrode's (Bridge et al., 1999) on a 11.9 μg/mL laminin (ThermoFisher Scientific, UK) coated 500 μm square gridded imaging dish, with #1.5H glass coverslip (Ibidi, USA). After 90 minutes, unattached cells were removed and the 0.1 μm sized TetraSpeck microspheres added prior to imaging. Ca^{2+} imaging was undertaken upon cells which showed spontaneous Ca^{2+} spark activity.

2.3.1 Tools for visualising calcium sparks

Despite the development of microscopy techniques for immunofluorescence staining, live cell Ca^{2+} imaging remains diffraction limited. Within the literature, there is uncertainty regarding the methodology of choice to visualise Ca^{2+} spark activity. This uncertainty arises from a high signal-to-noise ratio (Bridge et al., 1999). Background noise can lead to optical blurring and the formation of artefacts, a phenomenon exacerbated by the concentration and potential saturation of Ca^{2+} indicator dye. In turn, this can lead to an overestimation of Ca^{2+} spark parameters (Bridge et al., 1999; Thompson et al., 2002).

2.3.1.1 Total internal reflection fluorescence microscopy

TIRF microscopy is limited to imaging the periphery of a cell. By illuminating a visual field only 100 nm from the coverslip it reduces background fluorescence whilst retaining a high temporal resolution (Mattheyses et al., 2010). As a result, the amount of out of focus light from Ca^{2+} sparks occurring deeper within the cell is reduced. This enables the detection of smaller Ca^{2+} sparks at the near surface.

Within the research, fiducial markers were used to evaluate imaging depth within the TIRF field. A 488 nm laser (Cobolt Jive DPSS, Sweden) with 800 mW power output was positioned upon a modified Nikon TE2000 microscope (Nikon; Japan) with 60x 1.49NA TIRF objective. Power output was controlled by a motorised neutral density filter wheel (Thorlabs, Germany; FW102C). An ultraflat dichroic mirror (Chroma T495lpxr 1 mm dichroic) with ET525/50m (Chroma) emission filter were present to direct the light path, with emitted light detected by a Zyla 5.5 USB scientific CMOS camera (Andor Zyla 5.5; Andor, Belfast). A 100 ms/frame integration time was applied to visualise Fluo-4 AM fluorescence. The open-source Python Microscopy Environment (PyME) Acquire software, developed primarily by Dr David Baddeley (Yale University) was used for image acquisition. The light path of the TIRF microscope is detailed in Figure 2.2.

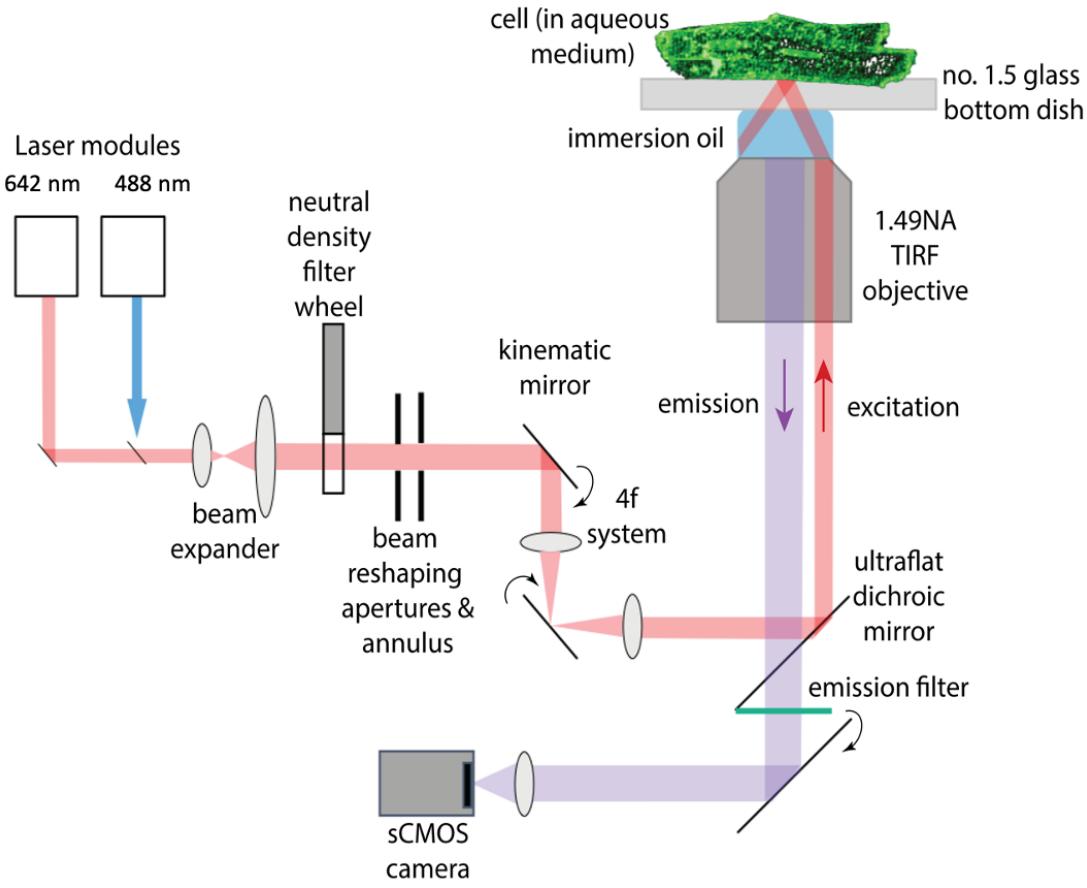

Figure 2.2: Total internal reflection fluorescence microscope light path. A modified Nikon microscope was utilised for live-cell Ca^{2+} imaging and single molecule localisation microscopy. All imaging modalities followed the same light path which originated from the 488 nm or 642 nm laser modules respectively. Schematic designed by Dr Izzy Jayasinghe and modified with permission.

2.3.1.2 Confocal spinning disk microscopy

The spontaneous Ca^{2+} spark activity at a cell's surface or within was recorded upon a confocal spinning disk microscope. A 488 nm laser passes through a Yokogawa-designed and Nipkow disk. These disks have a spiral arrangement of microlenses and pinholes respectively. Together, the spinning disks ensure light hits the sample at multiple points, unlike traditional confocal microscopy. Emitted light is passed through a photomultiplier tube to ensure minimal background fluorescence (Stehbens et al., 2012; Tanaami et al., 2002; Wang et al., 2005). Alternatively, within this system, an Andor EMCCD camera was installed which has a higher quantum efficiency. In turn, the ability to reject out of focus light enables the study of Ca^{2+} activity deeper into the cell, compared to TIRF microscopy. However, confocal microscopy is not optimised for use in thick samples due to crosstalk from the adjacent pinholes located across the spinning disk. This can lead to variability within the fluorescence signal and an increase in background noise regardless of z-depth (Pawley, 1991; Shimozawa et al., 2013; Stehbens et al., 2012). The system was mounted upon a modified Nikon microscope with 60x water-immersed 1.4 NA objective. PyME Acquire was utilised to record the Fluo-4 AM fluorescence signal with a frame rate of 100 ms/frame.

2.4 Immunofluorescence staining

2.4.1 Cell fixation

After live-cell Ca^{2+} imaging, cells were fixed *in situ* with 2% paraformaldehyde (PFA; Sigma-Aldrich, USA) for 10 minutes at RT prior to 4 washes of 10 minutes in phosphate-buffered saline (PBS) at RT. Twenty-four hours after extraction, DRG neurones for immunofluorescence staining were likewise fixed in 2% PFA for 10 minutes at RT prior to 4 washes of 10 minutes in PBS at RT. Cells were kept in PBS at 4°C until use, typically within 4 weeks.

Cardiomyocytes for immunofluorescence staining were incubated for 2 hours at 37°C upon a 11.9 μg/mL laminin coated coverslip (#1.5) prior to fixation *in situ* as above with 2% PFA followed by PBS washes. Alternatively, excess

LV and RV cardiomyocytes that were not imaged upon the day of enzymatic cell isolation were separately fixed with 2% PFA in suspension for 10 minutes on a rocker at RT. Cells were centrifuged (700 rpm, 2 minutes), supernatant removed and cells re-suspended within PBS for 10 minutes at RT. Cells were centrifuged again (1100 rpm, 2 minutes) and re-suspended in storage solution containing (w/v or v/v); 2% bovine serum albumin (BSA) and 0.1% NaN_3 dissolved in PBS. Cells were kept at 4°C until use, typically within 4 weeks.

2.4.2 Antibody application

Cardiomyocytes and DRGs were permeabilised with 0.1% Triton X-100 (Sigma-Aldrich, USA) in PBS for 10 minutes at RT. Subsequently, cells were blocked for 60 minutes at RT in PBS with 10% normal goat serum (NGS; ThermoFisher Scientific, UK). A primary antibody was used to label the protein of interest (Table 3). The primary antibody was diluted in incubation solution to its required working concentration. Incubation solution consists of the following (w/v or v/v); 0.05% NaN_3, 2% BSA, 2% NGS and 0.05% Triton X-100 dissolved in PBS. Cells were incubated overnight at 4°C and then washed 3 times in PBS for 20 minutes each. Depending upon the microscopy technique to be utilised, a secondary antibody was applied that has the ability to specifically target the primary antibody already *in situ*. The required secondary antibody working dilution was made fresh with incubation solution and applied to the cells for 2 hours at RT. The cells were washed a final 3 times in PBS for 20 minutes each, prior to storage at 4°C until imaged (Sheard et al., 2019). This protocol was followed for attached cells within an imaging dish (500 μm square gridded imaging dish, with #1.5H glass coverslip; Ibidi, USA), or cells in suspension. For cells in suspension, cells were stored within an Eppendorf and solution was exchanged by centrifugation (2000 rpm; 2 minutes), with supernatant removed and new solution used to re-suspend the cell pellet.

2.5 Microscopy techniques

2.5.1 Confocal microscopy

Standard Alexa fluorophore dyes (Table 3) were used to undertake diffraction-limited confocal microscopy (Soeller et al., 2009). Confocal microscopy was utilised due to its fast method of imaging and larger field of view compared to TIRF microscopy. Cells were imaged in PBS after completion of the immunofluorescence staining protocol. Images were obtained using a Zeiss LSM880 Inverted microscope, with an approximate 0.7 airy unit pinhole, 63x oil objective with 1.4 NA. The following 633 nm or 488 nm laser were used based upon the Alexa dyes of choice. Images were acquired using ZEN software. The use of an Airyscan detector within the Zeiss LSM880 Inverted microscope adopts a movable pinhole and a linear deconvolution stage as detailed by Huff et al. (2017). This improves spatial resolution by 1.7-fold to achieve an *xy* spatial resolution of 140 nm compared to the 250 nm acquired using traditional confocal microscopy methods (Huff, 2015).

2.5.2 dSTORM microscopy

Similarly, the single-molecule localisation microscopy technique of dSTORM is also dependent upon the use of Alexa dyes due to their ability to move between their stable ground state and excited state of fluorescence (Klein et al., 2014; van de Linde et al., 2011; Xu et al., 2017). When a fluorophore is excited by light in its ‘on-state’ it can emit fluorescence. The presence of a reducing agent within dSTORM can chemically modulate the fluorophore and encourage it to move from its ‘on-state’ into a ‘dark state’ of variable length whereby no fluorescence is emitted. This concept is known as stochastic photoswitching and is depicted by the Jablonski diagram (Figure 2.3). As a result, a series of single photoswitching events (Figure 2.4) are localised over the image duration to map the underlying staining pattern of the sample imaged. Before imaging, a mounting medium is made fresh. The mounting medium (pH 7.0) is made within a glycerol-based buffer to ensure cells are minimally exposed to O_2 to aid photochemical switching. With glycerol as the solvent, the mounting medium consists of 10-20 mM cysteamine, 1.5 mM Na_2SO_4 and 10x PBS. Cysteamine acts as the thiol-

containing reducing agent upon the fluorophore (van de Linde et al., 2008; Baddeley et al., 2009a).

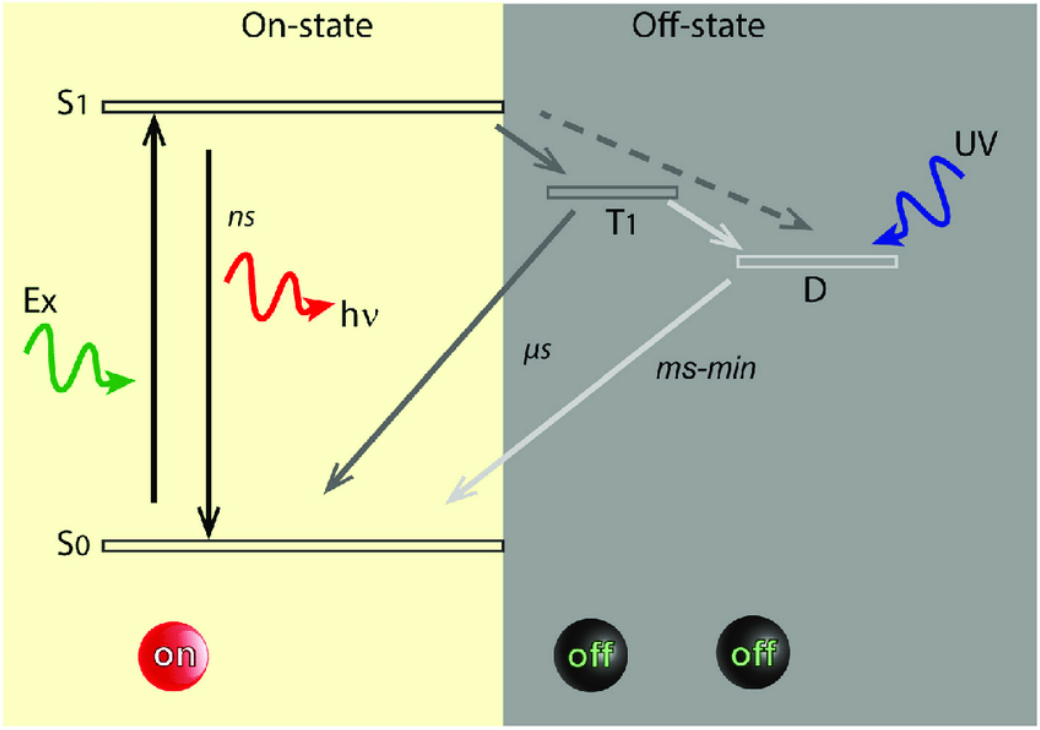

Figure 2.3: Jablonski diagram. Schematic detailing the cyclic nature in which a fluorophore can emit single photoswitching events. From its ground state (S_0) a fluorophore whilst in its 'on-state' can be excited by light (S_1) and consequently emit fluorescence. However, from its excited state a fluorophore can be moved into a dark triplet (T_1) 'off-state' or into a longer-lasting dark state (D) before returning to its ground state to be excited once again. A fluorophore can remain within its 'off-state' for microseconds to minutes. Adapted from Nahidiazar et al., (2016).

Specifically, Alexa 660 and Alexa 647 secondary antibodies were utilised within dSTORM (Table 3). This was due to their ability to be excited by the same 642 nm CW diode laser (Viasho, China), which enabled two proteins of interest to be visualised within the same sample in association with each other. The 642 nm laser has an output power of 800 mW and was located on the same modified Nikon TE2000 (Nikon; Japan) microscope as used previously in live-cell Ca^{2+} imaging (Figure 2.2), its pathway directed by a Chroma T685lpxr 1 mm ultraflat dichroic mirror into the Nikon 1.49NA TIRF objective. Laser power was controlled by the motorised neutral density filter wheel (Thorlabs, Germany; FW102C). The addition of a purpose-built beam splitter (Cairn Research Optosplit-II containing T710LPXXR-UF3 Chroma dichroic mirror) enabled emitted light from the Alexa 660 and 647 dyes to

pass through the ET720/60m (Chroma) emission filter and each be detected by half of the Andor Zyla 5.5 chip, with the constructed images being a mirror of each other. The sample was illuminated using HILO microscopy. Prior to image acquisition, the sample was pre-bleached using the laser's full power capacity to initiate photochemical switching of the Alexa fluorophores. This was followed by a 20,000 to 30,000 frame image acquisition, using PyME Acquire to record single molecule events with a frame rate of 50 ms/frame and localisation accuracy of 20 nm, as determined by the acquisition software.

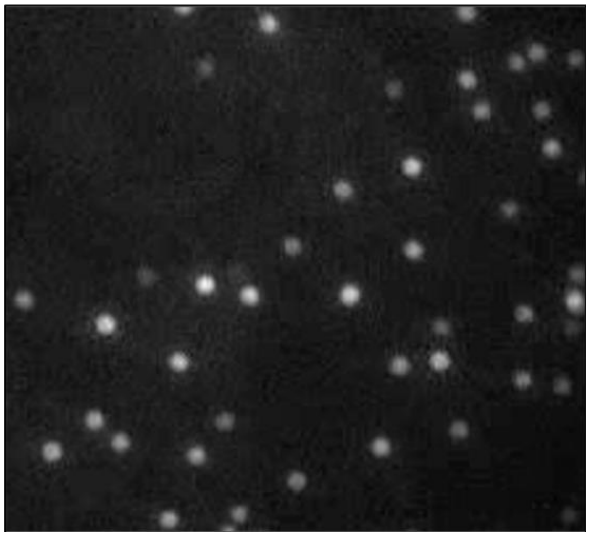

Figure 2.4: Stochastic photoswitching events. Raw data showing single molecule events or 'blinking' of multiple fluorophores in their on-state within dSTORM or as a result of the transient hybridisation of the docking and imager strand within DNA-PAINT. The rate of these events is 50 ms/frame within dSTORM and 100 ms/frame within DNA-PAINT acquisition.

2.5.3 DNA-PAINT microscopy

To undertake DNA-PAINT, a custom oligonucleotide strand (Integrated DNA Technologies, USA) conjugated to an AffiniPure goat or donkey IgG (Jackson Immunoresearch Europe Ltd, UK) is required in place of a secondary antibody. This is known as a 'docking' strand. Within the imaging buffer, there is a complementary oligonucleotide strand known as an 'imager' strand which is modified to have a fluorophore upon one end. The docking and imager strands transiently hybridise (Figure 2.5) to elicit single molecule events (Figure 2.4) with an xy spatial resolution of <10 nm (Jungmann et al., 2010; Jungmann et al., 2014; Jungmann et al., 2016).

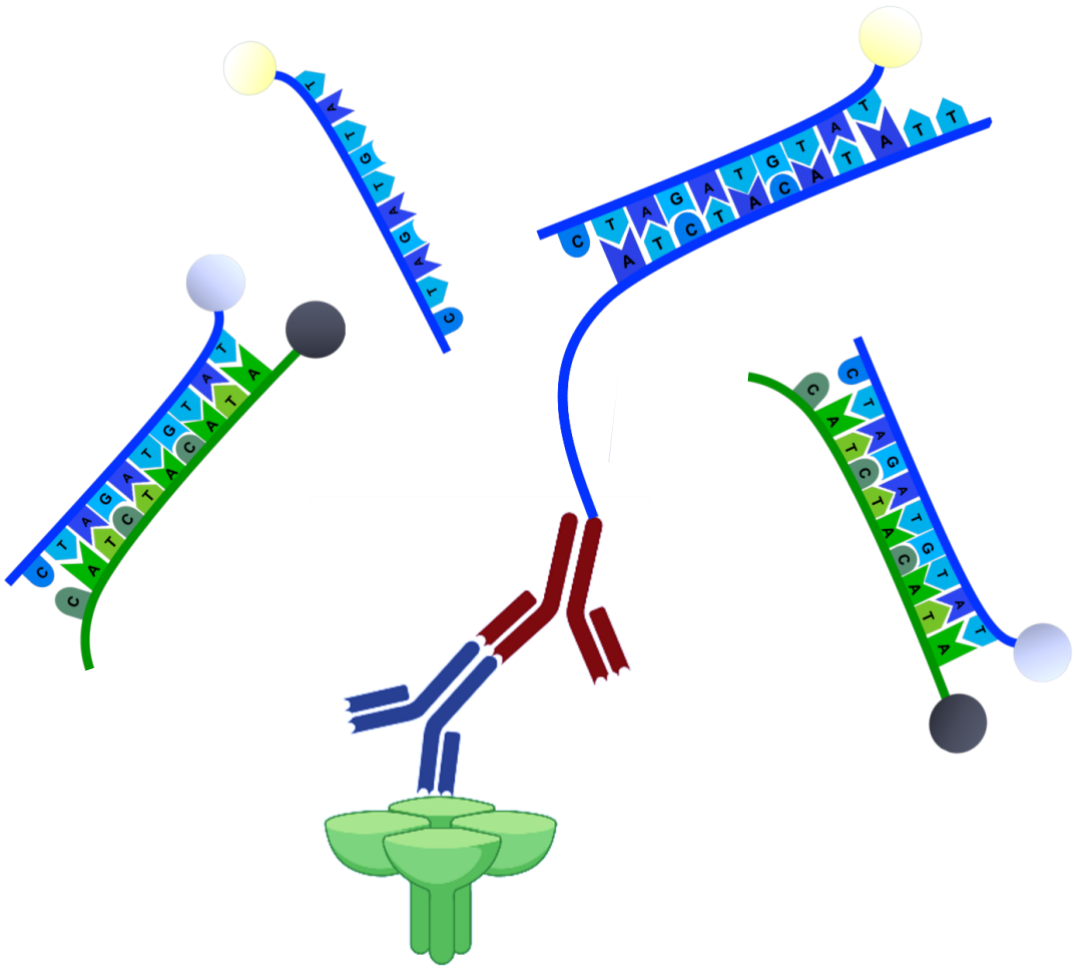

Figure 2.5: Schematic of DNA-PAINT. A target protein is detected using the standard antibody immunofluorescent staining technique. With the primary antibody (navy) bound to a secondary antibody (red), which is conjugated to a docking strand (blue). The docking strand has a complementary oligonucleotide sequence to the imager strand (blue) which is in solution. The imager strand has an Atto 655 fluorophore which emits increased fluorescence upon the transient hybridisation of the imager and docking strands. Addition of a quencher strand (green) with covalent bound Iowa Black RQ quencher can quench fluorescence from unbound imager strands to reduce background fluorescence and improve localisation accuracy (made using BioRender).

2.5.3.1 Conjugation process

Together, the docking strand and IgG antibody are known as the ‘conjugate’. Originally, a biotin-streptavidin linker was used to affix the docking strand to an antibody. However, this method has a linkage error and streptavidin’s tetrameric structure hindered calculation of the docking strand to antibody ratio when quantifying protein structures of interest. Therefore, this research uses a modified conjugation technique, whereby the docking strand and antibody are covalently bound through the use of a thiol-modified oligonucleotide strand (Agasti et al., 2017; Jayasinghe et al., 2018a).

Name	Oligonucleotide sequence (5' to 3')	Nucleotide length	5' modification	3' modification
P1 docking	TTA TAC ATC TA	11	Cy5	Amino Modifier C6 dT
P2 docking	TTA TCT ACA TA	11	Cy5	Amino Modifier C6 dT
P3 docking	TTT CTT CAT TA	11	Cy5.5	Amino Modifier C6 dT
P9 docking	TTT AAT AAG GT	11	Cy5	Amino Modifier C6 dT
P1 imager	CTA GAT GTA T	10	-	Atto655
P2 imager	TAT GTA GAT C	10	-	Atto655
P3 imager	GTA ATG AAG A	10	-	Atto655
P9 imager	CAC CTT ATT A	10	-	Atto655
P1 quencher	ATA CAT CTA C	10	Iowa Black RQ	-
P3 quencher	TCT TCA TTA C	10	Iowa Black RQ	-
P3P1 docking	TCA TTA CTT CTT TTT TAT ACA TCT A	25	Amino Modifier C6 dT	Cy5
P9P2 docking	TCT GGA ATA ATT TTT TAT CTA CAT A	25	Amino Modifier C6 dT	Cy5

Table 2.1: Oligonucleotide sequences. Table of oligonucleotide sequences that constitute the docking, imager and quencher strands, alongside their denoted name and any modifications.

Oligonucleotides were modified at the 3’ end with a 6-carbon spacer followed by a primary amine group. They had a Cy5.5 or Cy5 fluorophore modified to their 5’ end and underwent HPLC purification. Oligonucleotide sequences (Table 1) were adapted from Jungmann et al. (2016). The docking strand (70-100 μM, diluted with 1 mM EDTA containing PBS) was conjugated to either a 1 mg/mL (diluted from stock with PBS) goat anti-rabbit, goat anti-mouse or donkey anti-mouse IgG using a Thunder-link oligonucleotide-antibody conjugation kit (Innova Biosciences, USA). A 1:10 ratio of antibody to oligonucleotide was selected and protocol followed for the activation, conjugation, incubation and purification steps. The process of

conjugating an oligonucleotide to chosen antibody varied in success, with the structural integrity of the antibody being a limiting factor. Therefore, a successful conjugation was ultimately determined by the ability to undertake DNA-PAINT.

2.5.4 DNA-PAINT image acquisition

Cells were stained for specific protein targets following the immunofluorescence staining protocol as described above. In place of the secondary antibody the conjugate was applied with a 1:100 dilution. All washes after the application of the secondary antibody were with PBS containing 1 mM EDTA to preserve the conjugate's covalent attachment of the antibody to the docking strand through its ability to chelate excess minerals. On the day of image acquisition, 0.1 μm sized TetraSpeck microspheres were added to the coverslip. Imaging buffer, known as Buffer C (PBS with final 500 mM NaCl; pH8.0) was applied to the imaging chamber to regulate the reaction kinetics between the docking and imager strands (Jungmann et al., 2010; Jungmann et al., 2014). The sequence-specific imager strand (1.2 nM) was added (Table 2.1), which has an Atto 655 dye modified to the oligonucleotide's 3' end (Eurofins Ltd, Luxembourg). Within DNA-PAINT there is an excess of imager strand within the imaging buffer. This is advantageous as it ensures no photobleaching and minimises the likelihood of a docking strand being unbound for a prolonged period across the imaging duration. As a result, the efficiency of the DNA-PAINT probes to transiently hybridise and elicit stochastic events was postulated to be 95% by the Jungmann group. However, the excess imager strand required for this high efficiency can lead to background fluorescence, even with TIRF microscopy limiting the field of illumination to a 100 nm depth in the *z* plane (Fish, 2009; Jungmann et al., 2014; Jungmann et al., 2010; Takeshima et al., 2015). We therefore adopted the use of 'quencher' strand (Lutz et al., 2018). The quencher strand (Table 2.1) is an oligonucleotide strand (Integrated DNA Technologies, USA), which has partial complementary binding with the imager strand but is shorter in length, to ensure that stronger binding affinity remains between the docking and imager strand. A quencher strand has a modified Iowa Black fluorophore upon its 5' end

which quenches the Atto 655 emitted fluorescence upon the 3' end of any unbound imager strand within solution.

Similar to dSTORM, the same modified Nikon TE2000 microscope (Nikon; Japan) with 642 nm laser set up was utilised for DNA-PAINT acquisition (Figure 2.2), with a Nikon 60x 1.49 NA TIRF objective. However, in TIRF illumination a frame rate of 100 ms/frame was used due to the stochastic events being longer in duration within DNA-PAINT compared to dSTORM. Image acquisition was with PyME Acquire to collate 20,000-40,000 frames with a localisation accuracy of 12 nm or less.

2.6 Image processing

Within PyME Acquire, single molecule events were detected within dSTORM and DNA-PAINT acquisition, forming a 12-bit HDF time series image file (.h5) which could be opened within the PyME based dh5view software for image processing (Jayasinghe et al., 2018a). The co-ordinates of each single molecule event were stored within a compact .h5r file and opened using the PyME based *VisGUI* software. Within *VisGUI*, the single molecule events were drift corrected according to Baddeley et al. (2011), using a piecewise linear algorithm. Within *VisGUI*, the localisation accuracy in the *xy* plane was filtered to 20 nm and 12 nm for dSTORM and DNA-PAINT data respectively. Events were rendered onto a super-resolution 32-bit, 5 nm pixel grid using Delaunay triangulation. This method of image processing within PyME has been described previously within the literature (Baddeley et al., 2011; Baddeley et al., 2009a; Baddeley et al., 2009b; Jayasinghe et al., 2012).

2.6.1 Puncta detection analysis

For SMLM rendered images, a puncta detection analysis was applied to identify co-ordinates of a specific protein staining pattern (Figure 2.6), similar to Jayasinghe et al. (2018a). Using the dh5view puncta detection plugin, a single protein (i.e. puncta) was identified and its co-ordinates mapped depending upon the set puncta threshold (1.5-3.5) and blur size (3.0-4.0). A binary mask was created of the original image, based upon a threshold (0.7-

0.9) of the signal intensity. This enabled the clustered property of the protein to be visualised. A custom IDL v 8.0 code (written by Dr Izzy Jayasinghe and accessible in a GitHub repository at https://github.com/ijayas/imagealigning alongside a step-by-step guide) calculated the protein patterns spatial measurements in regard to density and nearest neighbour distance (Hurley et al., 2020).

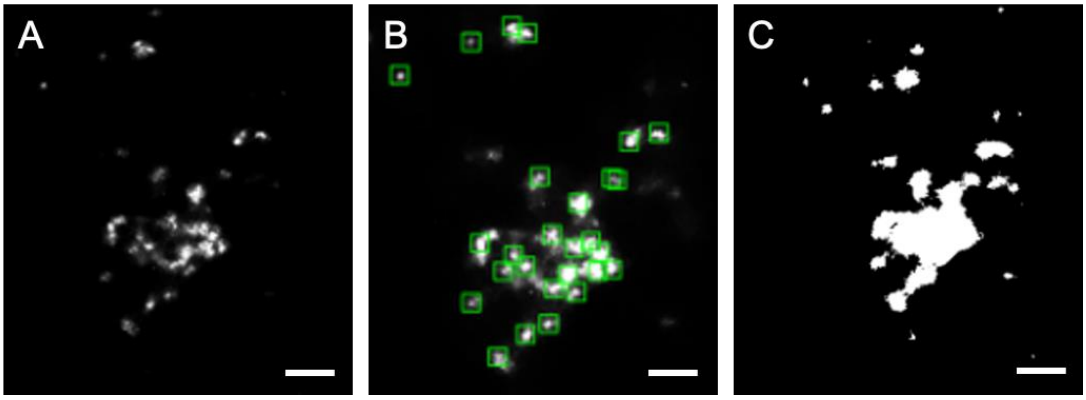

Figure 2.6: Cluster analysis of single-molecule localisation microscopy data. (A) A punctate protein pattern obtained with dSTORM or DNA-PAINT microscopy, rendered using PyME Acquire. (B) Individual puncta are selected, using dh5view software, and their co-ordinates identified based upon a pre-set puncta threshold and blur size. (C) Data points undergo a signal threshold function in dh5view (0.7-0.9 of signal fraction) to form a binary mask and enable quantification of punctate protein pattern. Scale bar; A: 100 nm.

2.6.2 Calcium spark analysis

Within ImageJ (Fiji), Ca^{2+} waves were removed and a 15-pixel sliding paraboloid was applied to subtract background fluorescence. The *xySpark* plug-in (Steele and Steele, 2014) was used to analyse Ca^{2+} spark data. A 2D Gaussian fit was applied to the increased fluorescence detected from a rise in local Ca^{2+} concentration. For each Ca^{2+} spark its FWHM, spark mass, and coefficient of determination r^2 was calculated in relation to the baseline florescence level (Figure 2.7). FWHM is a 2D measure of Ca^{2+} sparks spatial footprint. The coefficient of determination r^2 is a measure of how well a detected increase in fluorescence from a rise in local Ca^{2+} concentration fits a standardised gaussian profile of a Ca^{2+} spark at its point of greatest amplitude (Steele and Steele, 2014). Spark mass was a product of spark amplitude, $FWHM^3$ and coefficient 1.206 (Hollingworth et al., 2001).

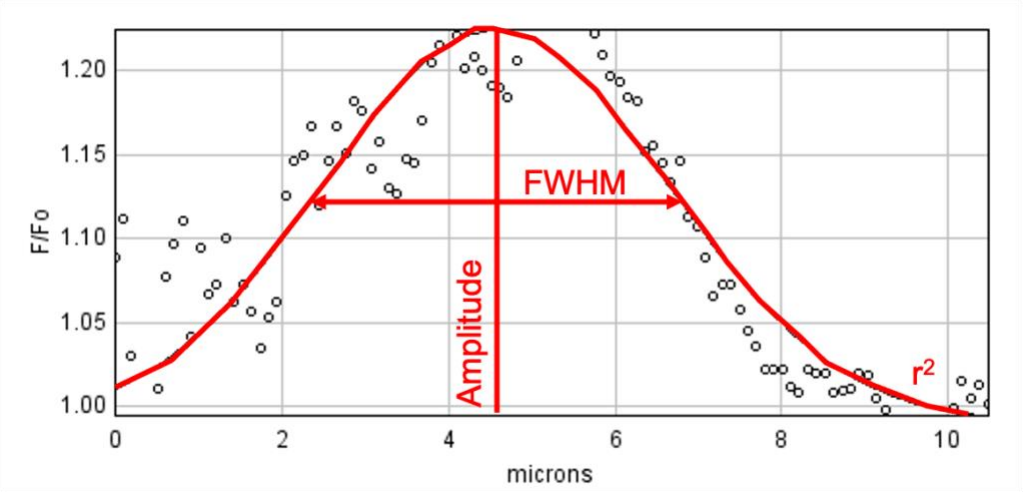

Figure 2.7: Calcium spark analysis. Exemplar output of a Ca^{2+} spark according to *xySpark* plug-in (Steele and Steele, 2014). The amplitude (F/F_0), full width at half maximum (FWHM) and coefficient of determination (r^2) to denote how well the increased fluorescence from a Ca^{2+} spark (circles) fit to a standardised gaussian profile of a Ca^{2+} spark at its point of greatest amplitude.

A frame rate, otherwise known as integration time, of 100 ms was applied for both TIRF and confocal Ca^{2+} spark imaging. It is acknowledged that this longer frame rate can result in a Ca^{2+} spark being resolved within a single frame which may limit the temporal resolution of Ca^{2+} imaging. The 100 ms frame rate was optimally chosen for TIRF microscopy to ensure that Ca^{2+} sparks were detected with minimal background fluorescence to maintain a xy spatial resolution close to the diffraction-limit for each technique. This is important as the Ca^{2+} spark analysis is focussed upon the spatial properties of a Ca^{2+} spark, namely FWHM and spark mass. TIRF microscopy was favoured within this project due to its ability to detect small Ca^{2+} sparks rather than confocal microscopy which has to integrate a Ca^{2+} signal over a thicker cell volume. Detected events were accepted or rejected based on a set of Ca^{2+} spark parameters (Table 2.2).

	FWHM (μm)	Spark mass (AU)	r^2
Cardiomyocytes	$\geq 1\ but\ \leq 6$	≤ 50	≤ 5
DRG Neurones	≤ 5	≤ 50	≤ 2

Table 2.2: Calcium spark parameters. Parameters by which Ca^{2+} sparks within DRG and cardiomyocytes were filtered.

2.7 Statistical analysis

Statistical analysis was performed using Excel and SPSS. All data are presented as mean ± SEM with *n* referring to number of animals or number of cells as denoted. When data were normally distributed, the significant difference between two dependent groups was calculated using a paired Student's t-test and a non-paired Student's t-test was applied when the difference was analysed between two independent groups. A one-way ANOVA with Tukey's post-hoc analysis was undertaken for the analysis of three or more independent groups. Statistical significance is considered when $p<0.05$ for all analysis undertaken.

Host	Target	Company	Dilution	Catalogue Number
Mouse	SERCA	Abcam	1:200	AB2861
Mouse	RyR2	ThermoFisher	1:200	MA3916
Rabbit	RyR2	Sigma-Aldrich	1:250	HPA020028
Rabbit	RyR3	Sigma-Aldrich	1:200	AB9082
Rabbit	IP3R1	ThermoFisher	1:200	PA1-901
Mouse	NCX	Swant	1:200	R3F1
Mouse	Cav3	BD Transduction Lab	1:200	610420
Rabbit	Cav3	Abcam	1:200	AB2912
Mouse	α-actinin	GeneTex	1:200	GTX29465
Rabbit	JPH2	ThermoFisher	1:250	40-5300
Rabbit	JPH4	Sigma-Aldrich	1:200	PRS4923
Anti-Rabbit	Alexa 660	Invitrogen	1:200	A21073
Anti-Mouse	Alexa 660	Invitrogen	1:200	A21054
Anti-Rabbit	Alexa 488	Invitrogen	1:200	A11008
Anti-Mouse	Alexa 488	Invitrogen	1:200	A11001
Anti-Mouse	Alexa 647	Invitrogen	1:200	A21235
Anti-Rabbit	Alexa 647	Invitrogen	1:200	A21244

Table 2.3: Antibodies. List of antibodies used within immunofluorescence staining.

Chapter 3. Towards correlative imaging

3.1 Introduction

The optical limitations of light established within Abbe's law (Abbe, 1873) were considered to limit the visualisation of cellular structures. However, the development of super-resolution microscopy overcame the diffraction-limited barrier of light. The ability of a fluorophore to undergo optical switching has enabled light to be imaged in a spatial and temporal manner to obtain resolutions at <200 nm. SMLM techniques rely upon this phenomenon (Moerner and Kador, 1989; Turkowyd et al., 2016).

The value of super-resolution microscopy within the literature can be identified by the manner in which it has re-directed physiological understanding. For example, organisation of the RyR2 Ca^{2+} release channel has been studied for many years. Confocal microscopy revealed that RyR2 are clustered on the surface of the SR. The diffraction-limited technique, however, is restricted in its ability to resolve a single 30 nm^2 RyR2 protein (Chen-Izu et al., 2006). The 30 nm^2 size of RyR2 is over 8-fold smaller than the 250 nm resolution of confocal microscopy. As a result, the 80-140 RyR2 commonly identified within each cluster has been an over-estimate (Asghari et al., 2014; Baddeley et al., 2009b).

Jungmann et al. first introduced the SMLM method of DNA-PAINT in 2010. The technique relies upon DNA hybridisation to elicit single molecule events that can be collated over time with an xy spatial resolution equivalent to 12 nm or less (Jungmann et al., 2010; Jungmann et al., 2014). As a result, the technique revealed that peripheral RyR2 clusters within cardiomyocytes contain 8.8±0.86 RyR2 (mean ± SD) (Jayasinghe et al., 2018a; Jayasinghe et al., 2018b). This finding demonstrates the requirement within research to ensure that the correct imaging modality is utilised when observing cellular structures.

The extent by which the ultrastructure of a cell can infer its cellular function is unclear. Specifically, computational simulations have attempted to understand how the structural morphology of Ca^{2+} handling proteins, such

as RyR2 within a cardiomyocyte, can impact the functional Ca^{2+} release at the level of the JMC (Cosi et al., 2019; Kolstad et al., 2018). However, simulations have inherent limitations and require experimental validation. An experimental method is therefore required which allows the functional properties of Ca^{2+} signalling to be studied in relation to the nanoscale cellular ultrastructure. Indeed, this development is fundamental to understanding the physiological role of Ca^{2+} in controlling cellular function and the consequences of dysregulation, which can lead to numerous pathological outcomes including apoptosis or necrosis (Berridge et al., 2000; Clapham, 1995).

This chapter investigates the importance of choosing the correct imaging modality within research and explores how to establish and optimise an SMLM approach, namely DNA-PAINT. Furthermore, the chapter reveals the development of a correlative imaging protocol. The protocol's aim is to combine the advantages of SMLM with the study of Ca^{2+} signalling to observe the functional and structural properties of a cell.

3.2 Method

3.2.1 Conjugate development

The development of a conjugate was undertaken using a ThunderLink kit as detailed in the Methods Chapter (Section 2.5.3). The kit enables an oligonucleotide sequence-specific strand to covalently bind to a secondary antibody for use within DNA-PAINT acquisition (Figure 3.1). As previously mentioned, the success of this conjugation process was ultimately determined by the use of the conjugated docking strand within DNA-PAINT. However, other methods of validation were undertaken because the exact chemistry within the conjugation kit is unknown.

3.2.1.1 Physical validation of conjugation stage

A Nanodrop was utilised on its 'proteins and labels' function with the dye set to Cy5.5 or Cy5. Using the wash buffer, supplied within the conjugation kit, blank absorbance measurements were obtained. Measurements for each of the following; activated oligonucleotide, activated antibody, supernatant and

conjugate were then quantified. These measurements were used as a guide to determine the ratio of oligonucleotide to antibody based upon their concentration within the supernatant and conjugate. At a 100% yield, the ratio of oligonucleotide docking strands and antibody should be equal in regards to the molarity.

According to the ThunderLink kit, the docking strand is known to bind to the heavy chain of the antibody. The success of conjugation can therefore be visualised by a shift in the heavy chain's molecular weight when the oligonucleotide is conjugated. The degree of this shift is dependent upon the molecular weight of the docking strand. Samples were denatured by heating at 95°C for 5 minutes in 1x sample buffer (62.5 mM Tris; pH 6.8, 10% glycerol, 2% SDS, 5% β-mercaptoethanol, bromophenol blue). Protein samples were run alongside a 10-250 kDa protein ladder (Precison Plus Protein Dual Colour Standards; Bio-Rad, USA) and separated by electrophoreses in SDS-PAGE gels (7-12% acrylamide) in SDS-PAGE running buffer (0.01% SDS in 25 mM Tris, 192 mM glycine). Gels were stained overnight at RT in InstantBlue Coomassie protein stain (Abcam, UK) before imaging (Syngene, G:BOX). It is known that the IgG antibody has a 150 kDa molecular weight, with two 50 kDa heavy chains and two 25 kDa light chains (Janeway et al., 2001). The protein ladder was used as a guide to qualitatively analyse the protein samples present (Figure 3.2).

3.2.1.2 Microscopy

Confocal microscopy was undertaken to evaluate binding specificity by detection of the Cy5.5 or Cy5 fluorophore located upon the 5' end of the docking strand. The standard immunofluorescence staining protocol was followed as described in the Methods Chapter (Section 2.4) and the conjugate was applied as a secondary antibody with a 1:100 dilution. Then, upon a modified Nikon microscope, DNA-PAINT image acquisition was undertaken to verify conjugate success. Image acquisition was undertaken as discussed within the Methods Chapter, with the use of a complementary imager and quencher strand (Figure 3.1).

3.2.2 Immunofluorescence staining

A standard immunofluorescence protocol was utilised for each microscopy technique; confocal, airyscan, dSTORM and DNA-PAINT. Either a 1:200 dilution of α-actinin mouse antibody was applied or a 1:250 dilution of RyR2 rabbit antibody. This was paired with a standard Alexa fluorophore (Table 2.3) which was utilised at a 1:200 working dilution. Image acquisition was undertaken upon a Zeiss LSM880 Inverted microscope, in either confocal or Airyscan mode. The addition of an airyscan detector and the integration of a linear deconvolution process enabled a 140 nm xy spatial resolution compared to the 250 nm xy spatial resolution achieved by confocal microscopy.

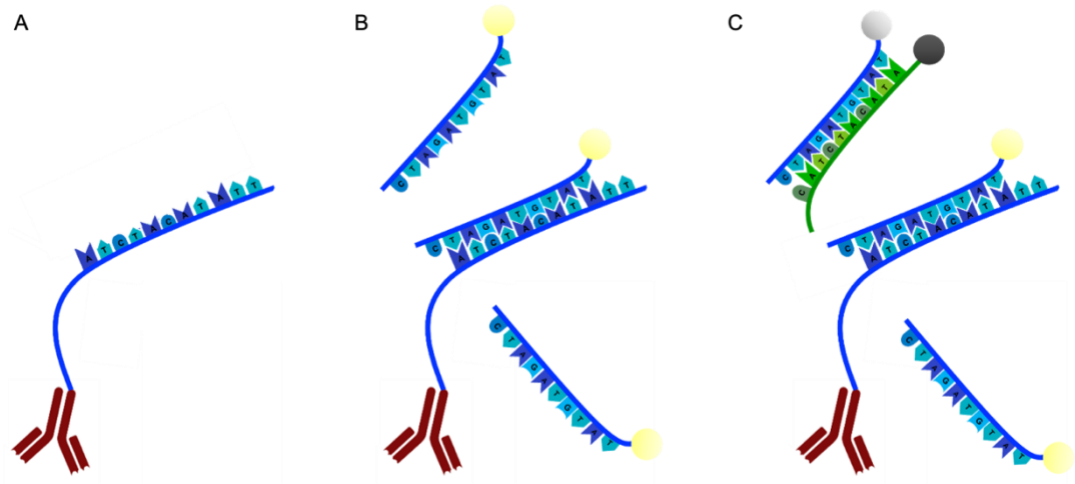

Figure 3.1: Components of DNA-PAINT microscopy. (A) Conjugate as a product of the ThunderLink kit, comprising a sequence-specific oligonucleotide strand covalently bound to an IgG antibody. (B) Addition of an imager strand, with Atto 655 3' modification to the Buffer C imaging solution. The imager strand transiently hybridises with a complementary docking strand to elicit stochastic optical switching. (C) Addition of a quencher strand (green) to the imaging solution. The quencher strand has a 5' Iowa Black RQ modification. When bound to a 'free' complementary imager strand within solution the Atto 655 fluorophore upon the imager strand is quenched and background fluorescence reduced (made using BioRender).

A standard Alexa fluorophore was utilised with the SMLM technique of dSTORM. However, as described in detail within the Methods Chapter (Section 3.5.2), the use of mounting media enabled single molecules to be detected. The stochastic blinking activity was recorded using PyME Acquire software. This is similar to how stochastic events within DNA-PAINT were

recorded from the addition of an essential 1.2 nM imager strand and optional 1.2 nM quencher strand (Figure 3.1) within an imaging solution of Buffer C. Imager strand concentration was optimised through observation of background fluorescence and rate of stochastic events across a 0.5 nM – 5 nM range of imager and quencher strand concentrations. A detailed description of DNA-PAINT has been outlined within the Methods Chapter (Section 2.5.3).

3.2.3 Kymograph

The sequence-specific oligonucleotides used within DNA-PAINT were chosen from previous studies by Jungmann et al. (2014). Following the nomenclature outlined in Table 2.1, four sequence-specific oligonucleotide strands were adopted within this research; P1, P2, P3 and P9. To evaluate the binding kinetics of each specific docking strand, a kymograph was formed, using ImageJ. The kymograph was of the transient binding between docking and imager strands in solution, with and without the presence of a quencher strand. For each kymograph, a randomised 1000 frame period from an acquired image was used. For each dataset, the integration time was a standardised at 100 ms/frame. For all kymographs, the underlying immunofluorescence staining was of a Caveolin-3 staining pattern within ventricular cardiomyocytes.

3.2.4 Image analysis

Prior to image analysis, data acquired with confocal or airyscan microscopy underwent a gaussian blur subtraction (sigma radius 8) to remove background fluorescence.

The width of an α-actinin band within a ventricular cardiomyocyte was obtained by undertaking a plot profile in ImageJ. This plot profile visualised signal intensity across a rendered image of the microtubule stain. The region of increased signal intensity was identified as the α-actinin band. When the spatial scale within the xy plane was known for each image modality, the width of the α-actinin band could be quantified dependent upon the width of the plot profile.

The cluster size of RyR2 was quantified for confocal or airyscan acquired data using ImageJ. A local threshold was applied and a binary mask formed. Then, using the analyse particles function, the area of each RyR2 cluster was analysed with ellipses applied when circularity was 0.0-1.0 and pixel size set from 30 nm to infinity. This ensured that regions within the data that accounted for an area smaller than one RyR2 puncta were ignored. The correct xy spatial scale was applied to each dataset, to enable calculation of RyR2 cluster area. An array of methodologies have developed to analyse diffraction-limited RyR2 distribution. Following the assumption that the protein is tightly packed together, akin to a checkerboard, the RyR2 density was approximated based upon cluster area being divided by 30 nm^2. For the SMLM techniques of dSTORM and DNA-PAINT, RyR2 puncta were identified using the dh5view puncta detection analysis. Cluster size calculated from a binary mask; a technique described previously in the Methods Chapter (Section 2.6.1).

3.2.5 Calcium imaging

The preparation of cells for live-cell Ca^{2+} imaging was identical regardless of the TIRF microscopy or confocal spinning disk imaging modality applied. The detailed method for Fluo-4 AM loading is described within the Methods Chapter (Section 2.3). Fiducial markers are fluorescent beads applied to the coverslip and used as marker of z-depth to ensure the near surface of a cell was observed where applicable. For confocal spinning disk microscopy, the Ca^{2+} spark analysis within the cell was undertaken at a depth where fiducial markers were out of focus and cell nuclei were visible. The stage was not motorised and therefore the exact z plane could not be recorded. For both live-cell imaging methods, Ca^{2+} spark activity was quantified using the ImageJ *xySpark* plug-in (Steele and Steele, 2014). Ca^{2+} sparks were filtered according to the cell-specific parameters previously detailed (Table 2.2).

3.3 Results

3.3.1 Development of conjugate for DNA-PAINT

Conjugation efficiency was evaluated experimentally. The P3P1 docking strand was conjugated to an anti-rabbit IgG using the ThunderLink conjugation kit. A 1:10 ratio of antibody to oligonucleotide was utilised.

The ratio of oligonucleotide to antibody within the conjugate sample was 0.41 (Figure 3.2A). There was an unequal concentration of antibody and oligonucleotide present within the sample, which questions the specificity and efficiency of DNA-PAINT acquisition due to less than half of the antibody present within the conjugate sample being bound to an oligonucleotide sequence. Conversely, there was a 1.1 ratio of antibody to oligonucleotide within the supernatant. This suggests a similar concentration of each unbound reagent was removed in the clean-up stage of the conjugation. The degree of bound oligonucleotide to antibody could affect the stoichiometry of the conjugate which should be considered when quantifying the efficiency of image acquisition due to the number of imager strands that could bind to one antibody target.

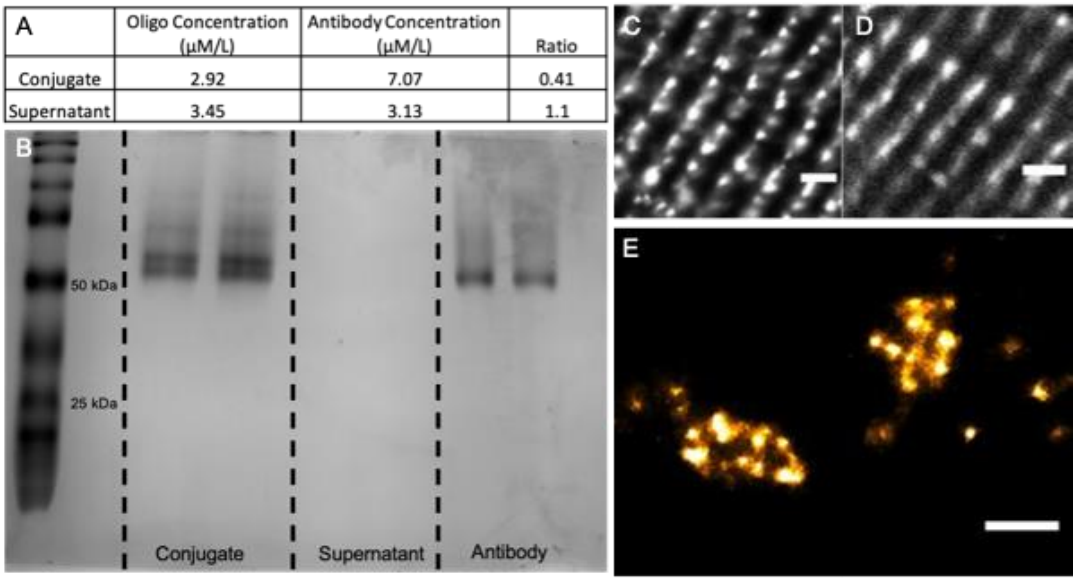

Figure 3.2: Development of conjugate probe for DNA-PAINT acquisition. Validation of the P3P1 oligonucleotide strand conjugated to an anti-rabbit IgG. (A) Nanodrop measurements of the oligonucleotide and antibody concentration within the conjugate and supernatant solution and their respective ratio of bound oligonucleotide/antibody, with a 1.0 ratio representing a successful yield. (B) Successful conjugation was confirmed, however, by a 6.37 kDa molecular weight shift detected within the conjugate sample alone compared to the 50 kDa antibody heavy chain. A comparison was made using confocal microscopy to visualise the

RyR2 staining pattern within ventricular cardiomyocytes. A clear RyR2 striated pattern was evident when both the (C) standard Alexa 488 fluorophore and (D) P3P1 docking strand were applied. (E) A successful conjugation was reported when the P3P1 conjugate could be used to successfully undertake DNA-PAINT with a localisation accuracy comparative to the <10 nm previously reported. Scale bars, C-D: 2 μm; E: 200 nm.

Through electrophoresis, denatured imaging probes from the conjugate and supernatant samples were separated based upon their molecular weight. The samples were run alongside a known molecular weight ladder which was used as a guide (Figure 3.2B). Within the conjugate sample, the antibody's heavy chain was detected at 56.4 kDa, it known to be 50 kDa within an IgG antibody. Furthermore, there was a protein band detected which had a 6.37 kDa molecular weight shift. This heavier protein represented the successful conjugation of the 8.37 kDa oligonucleotide P3P1 strand (Table 2.1) with the heavy chain of an IgG antibody. This band was not present in a sample of activated antibody alone. It is important to note that the expected 25 kDa light chain of IgG was not visible within the conjugate sample. No protein was detected within the supernatant sample, suggesting that a minimal amount of antibody was removed during the purification stage of conjugation, despite the nanodrop measurements.
The Cy5 fluorophore upon the docking strand was exploited within confocal microscopy to qualitatively assess the specificity of immunofluorescence staining. An Alexa 488 fluorophore was used as a comparative secondary antibody to visualise RyR2 striations within a ventricular cardiomyocyte (Figure 3.2). The characteristic pattern of RyR2 clusters along the Z-line was visible with the use of an Alexa 488 fluorophore and the P3P1 conjugate. The signal intensity of the Cy5 fluorophore was reduced in comparison to the Alexa 488 control. However, the specificity of the staining pattern was comparable between the two cardiomyocytes imaged, suggesting a successful conjugation. When immunofluorescence staining was repeated for DNA-PAINT acquisition, a specific RyR2 pattern was still visible in the final rendered image (Figure 3.2E). A 1.2 nM P1-Atto 655 imager strand concentration was present within the imaging buffer, which enabled the characteristic transient optical switching events of SMLM. There was minimal background fluorescence and non-specific binding, resulting in a

localisation accuracy of 12 nm or less. This is synonymous with the technique of DNA-PAINT and suggestive of a successful conjugation.

3.3.2 Choice of oligonucleotide sequence

A kymograph was created for each of the oligonucleotide sequences adopted within DNA-PAINT acquisition. This has enabled qualitative assessment of the single-molecule events across the varying docking strands (Figure 3.3). Visually the P1 docking strand had the greatest number of events across a 1000 frame period. The P3 oligonucleotide strand also had an abundant number of single molecule events that occurred throughout the width of the sample and for the duration of image acquisition. However, this higher event density for both the P1 and P3 sequences, compared to the P2 and P9 sequences, potentially led to a greater degree of background signal which can diminish localisation accuracy (Jayasinghe et al., 2015). Increased background signal could be from a spatial overlap of fluorescence due to a greater proportion of Atto 655 fluorophores being in their excited ‘on-state’ upon the transient binding of the imager to docking strand.

Application of a sequence-specific quencher strand visually reduced background fluorescence. This in turn improved the localisation accuracy of the rendered DNA-PAINT image which is quantified upon the immunofluorescence staining of the Cav3 protein within a cardiomyocyte. Furthermore, a reduction in background fluorescence can be visualised by a reduced number of non-specific structures within the Cav3 staining pattern for both the P1 and P3 conjugates. The application of a quencher strand reduced the number of single molecule events which occurred over a 1000 frame time course. The use of 1.2 nM quencher strand within the imaging buffer therefore required an increased image duration to acquire the same number of single molecule events compared to the imaging buffer containing 1.2 nM of imager strand alone. Qualitatively, the use of the P1 and P3 oligonucleotide strands was not dissimilar. Both sequences have the ability to acquire a protein-specific stain with a localisation accuracy of 12 nm or less when a quencher strand is utilised (Figure 3.3), as determined by the use of a biological calibration tool (Figure 3.4).

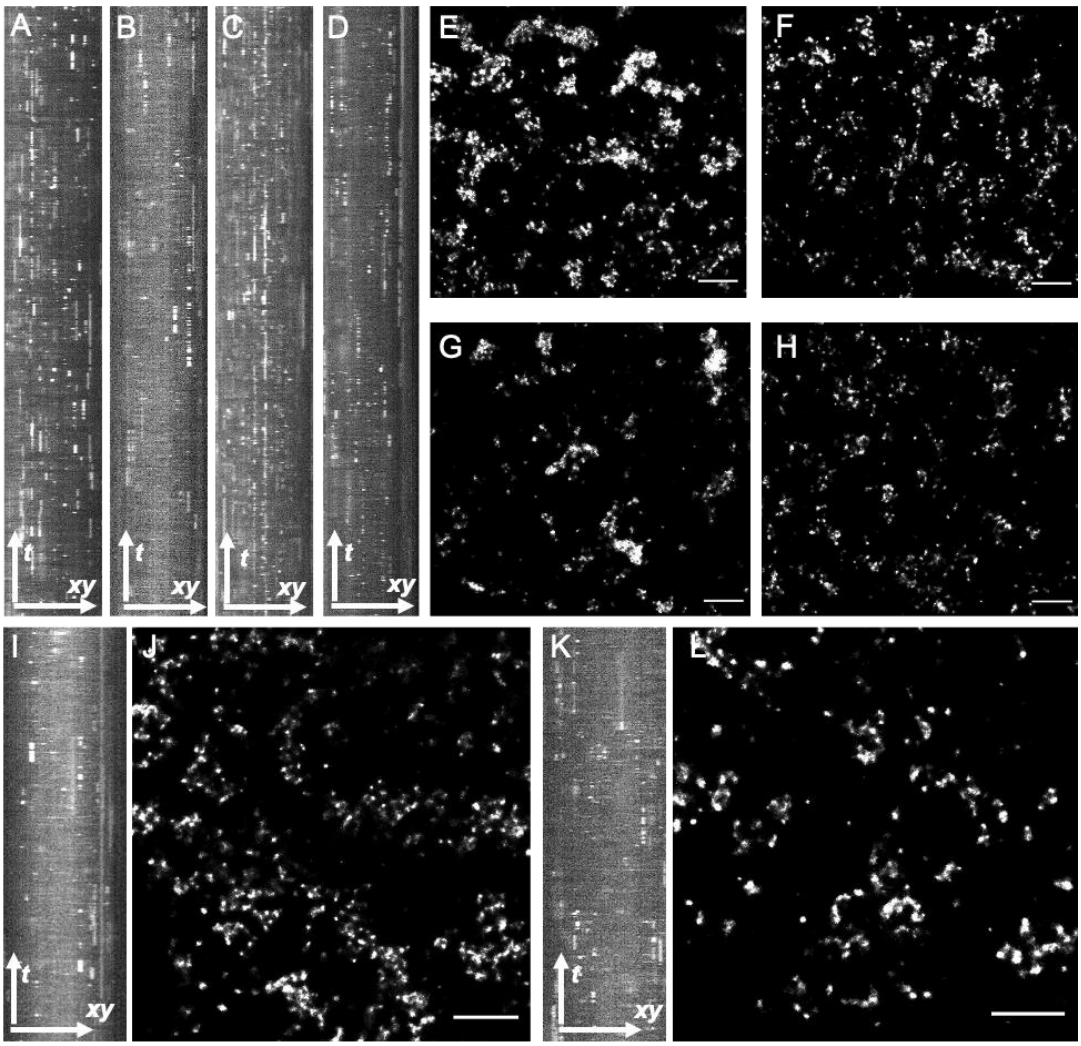

Figure 3.3: Evaluation of DNA-PAINT imaging efficiency based upon oligonucleotide sequence. A 1000 frame (1.67 minute) kymograph for each oligonucleotide sequence utilised within DNA-PAINT microscopy was obtained. The top of each kymograph represents the beginning of the 1000 frame time period. Four sequences were studied (A-D); P1, P2, P3, P9 respectively. (E-H) For each respective sequence, imaging efficiency was qualitatively assessed according to the ability to image caveolin-3. Quencher strands were applied, and their kymograph and caveolin-3 stain acquired. For both, P1 with added quencher (I-J) and P3 with added quencher (K-L), there was a reduced event density accompanied by reduced background fluorescence and improved localisation accuracy according to PyMe Acquire. Scale bars, A-D; I, K: time 100,000 ms; xy 500 nm; E-H; J, L: 500 μm.

The P9 oligonucleotide strand had a low level of background fluorescence with a high contrast evident between the cell sample and fluorescent single molecule events (Figure 3.3). Compared to the P1 and P3 oligonucleotide kymographs, the events were longer in their duration, lasting across multiple 100 ms frames. This is a disadvantage within DNA-PAINT which relies upon transient binding of the imager and docking strand sequences. Such a

characteristic of the P9 docking strand within DNA-PAINT could contribute to a sub-optimal localisation accuracy than the 12 nm which is typical as the stochastic nature of the technique is impaired. The events also appear to be recorded from similar regions of the sample. This could lead to an incomplete Cav3 staining pattern being acquired. Similarly, single molecule events visualised with the P2 docking strand are limited to a reduced region of the sample. Of note, there is a decreased intensity of single molecule events over time which suggests photo-bleaching of the Atto 655 fluorophore. Such a phenomenon could limit the acquisition of a Cav3 immunofluorescence stain with the P2 docking strand (Figure 3.3).

3.3.3 Choosing a microscopy technique

The application of varying optical microscopy techniques was undertaken to determine the optimal technique to use in visualising structures within cardiomyocytes. The significance of a microscopy technique's xy spatial resolution upon imaging cellular structures was quantified by the observation of the microfilament α-actinin binding protein using; confocal microscopy, airyscan microscopy, dSTORM and DNA-PAINT (Figure 3.4).

The diffraction-limited microscopy techniques of confocal and airyscan microscopy visualised α-actinin as a 743.75$\pm$43.22 nm (Figure 3.4F) and 592.25$\pm$13.75 nm (Figure 3.4G) wide band respectively. The width of the α-actinin stain is reduced to 162.5$\pm$13.62 nm upon the application of dSTORM (Figure 3.4H). However, the characteristic double-banded nature of α-actinin was only visible when DNA-PAINT was utilised. Upon DNA-PAINT acquisition, an α-actinin band was 54.38$\pm$2.90 nm in width, with a 92.5$\pm$1.44 nm separation (Figure 3.4I).

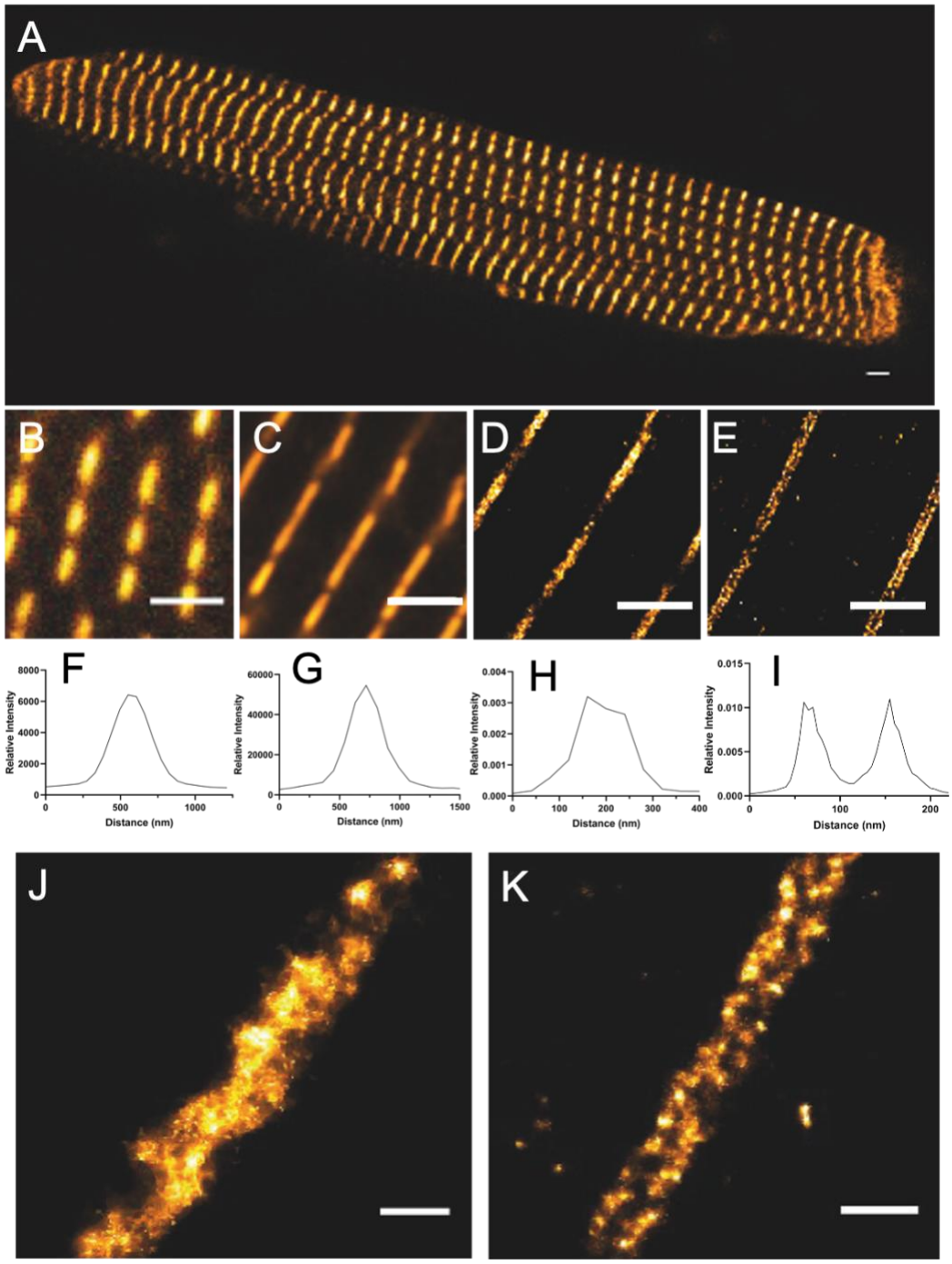

Figure 3.4: Evaluation of microscopy technique for imaging cell ultrastructure. The microtubule α-actinin was used as a biological calibration tool within ventricular cardiomyocytes obtained from Adult male Wistar rats. (A) The α-actinin stain visible across a cardiomyocyte with confocal microscopy, (B) with the banded nature apparent at a close-up scale. (C) Airyscan microscopy acquisition of α-actinin. (D; inset J) The α-actinin banding pattern when dSTORM was utilised. (E; inset K) The double-banded α-actinin staining pattern visible with DNA-PAINT. (F-I) The plot profile for each microscopy technique demonstrates the spatial resolution of; confocal, Airyscan, dSTORM and DNA-PAINT respectively. The double-banded morphology of α-actinin was only visible as two peaks when DNA-PAINT was utilised. Scale bars, A-E: 2 μm; J-K: 200 nm.

3.3.3.1 Imaging and analysing calcium handling proteins

The use of SMLM compared to diffraction-limited optical microscopy was evaluated for imaging peripheral Ca^{2+} handling proteins, such as RyR2 (Figure 3.5). The density of RyR2 per cluster was calculated based upon the 30 nm^2 size of the protein (Chen-Izu et al., 2006). Using the diffraction-limited techniques of confocal and airyscan microscopy, the number of peripheral RyR2 puncta per cluster were 110±19 RyR2 and 131±15 RyR2 respectively. The adoption of dSTORM led to 10±2 RyR2 puncta per cluster being calculated. With DNA-PAINT, 4±1 RyR2 puncta per cluster was calculated when individual RyR2 proteins could be visualised.

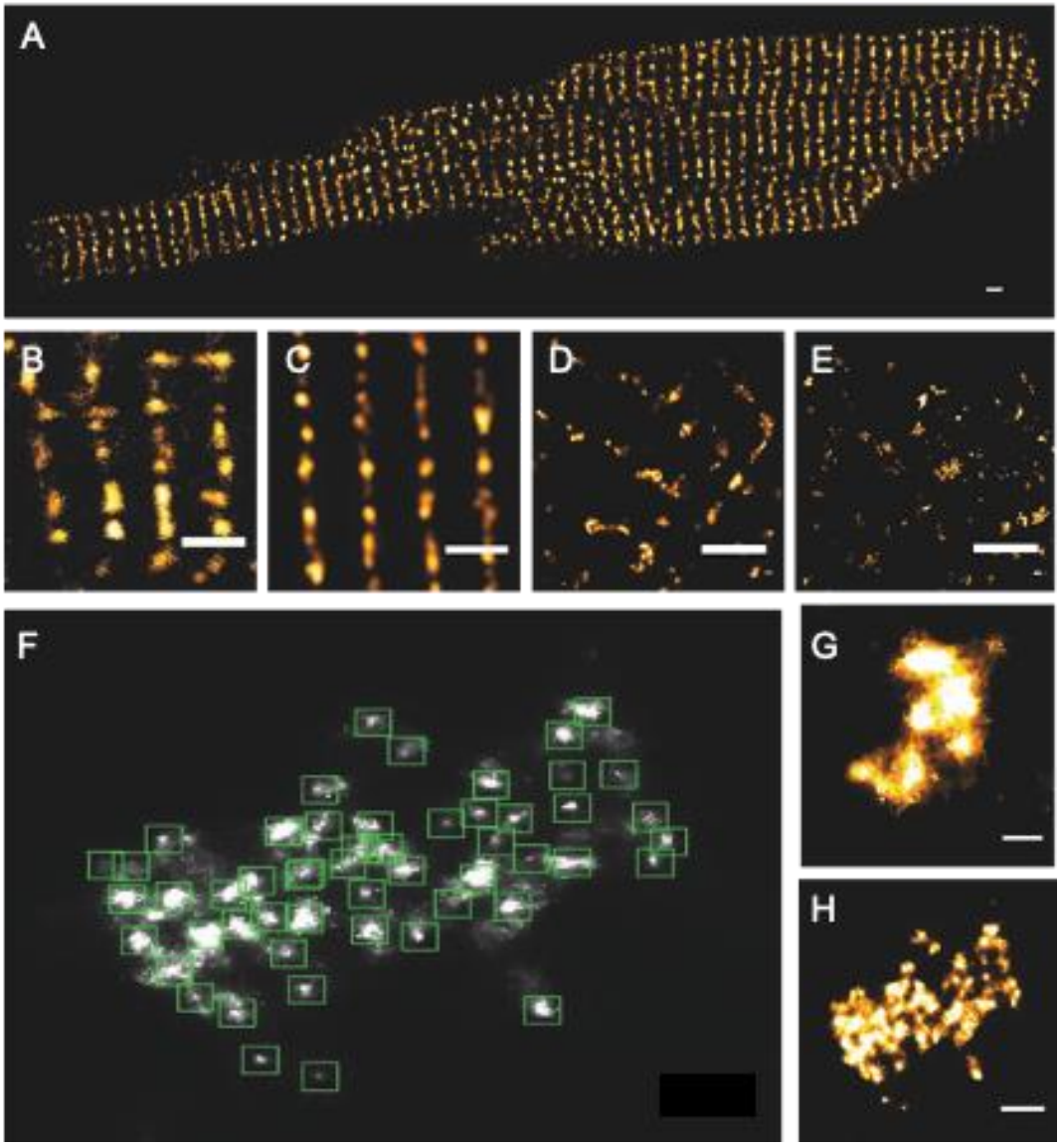

Figure 3.5: Evaluation of microscopy technique for imaging calcium handling. All microscopy techniques visualised anti-rabbit RyR2 within ventricular cardiomyocytes from Adult male Wistar rats. (A) Striated pattern of RyR2 across

the width and length of a cardiomyocyte obtained with confocal microscopy, (B) with an inset to reveal protein clustering. (C) RyR2 cluster pattern obtained with diffraction-limited Airyscan microscopy. (D) Sub-sarcolemmal cluster pattern of RyR2 is more distinct with use of dSTORM due to the 20 nm spatial resolution, (G) with heterogeneous cluster morphology becoming apparent. (E) Use of DNA-PAINT with <10 nm spatial resolution enabled for individual RyR2 puncta to be resolved. (H) Visualisation of the RyR2 cluster pattern reveals the heterogenous morphology across a cell, with clusters having holes and a non-uniform shape. (F) The method for RyR2 quantification for single-molecule localisation microscopy techniques is through puncta detection analysis. Alteration of the puncta threshold and blur size ensure each RyR2 puncta is identified, as denoted by a green box. Values are mean±SEM; n= 4 cells. Scale bars, A-E: 2 μm; G-H: 200 nm.

3.3.3.2 Imaging and analysing calcium sparks

Spontaneous Ca^{2+} sparks were observed within RV cardiomyocytes following the protocol detailed in the Methods Chapter. The spontaneous formation of Ca^{2+} sparks was aided by the use of a 5 mM Ca^{2+} containing Tyrode's solution to overload the SR and initiate RyR2 channel opening. Multiple variables were measured using *xySpark* (Steele and Steele, 2014) for Ca^{2+} spark profiles obtained within TIRF and confocal microscopy (Figure 3.6).

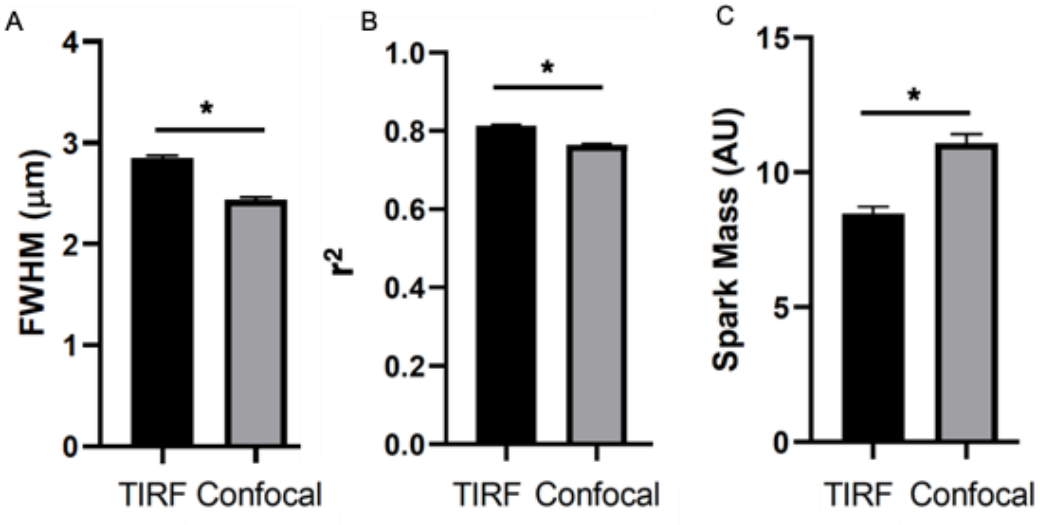

Figure 3.6: Comparison of live-cell calcium imaging technique at the near-periphery of a ventricular cardiomyocyte. Ventricular cardiomyocytes from Adult male Wistar rats were analysed for their Ca^{2+} spark signalling using TIRF and confocal spinning disk microscopy. Ca^{2+} spark kinetics were analysed with xySpark. (A) Within TIRF microscopy, FWHM was significantly increased demonstrating a larger spatial footprint across the cell. (B) Ca^{2+} spark morphology had a significantly greater fit to a Gaussian profile according to r^2 value when TIRF microscopy was used. (C) The spark mass was significantly reduced in TIRF microscopy, with confocal spinning disk recording on average a larger Ca^{2+} spark profile. Values are mean±SEM; confocal n= 3 animals, n= 1168 Ca^{2+} sparks; TIRF n= 6 animals, n= 1675 Ca^{2+} sparks.

There was a significant observation made within the variables; FWHM, r^2 value and spark mass. The spatial spread of a Ca^{2+} spark was 14.47% less within confocal observations, with a mean FWHM of 2.44±0.03 μm compared to TIRF measurements (t-test; $p=9.54x10^{-22}$). The change in r^2 was not as great, with Ca^{2+} spark profiles having a 6.03% greater Gaussian fit, with a 0.81±0.00 r^2 value within TIRF microscopy (t-test; $p=3.29x10^{-25}$). An increased r^2 value is reflective of a Ca^{2+} spark's profile having greater alignment to a standardised gaussian profile of a Ca^{2+} sparks rise in fluorescence. A 23.62% significantly greater Ca^{2+} spark mass was recorded on average within confocal measurements (Confocal 11.09±0.33 AU; TIRF 8.47±0.26 AU, (t-test; $p=3.13x10^{-10}$)).

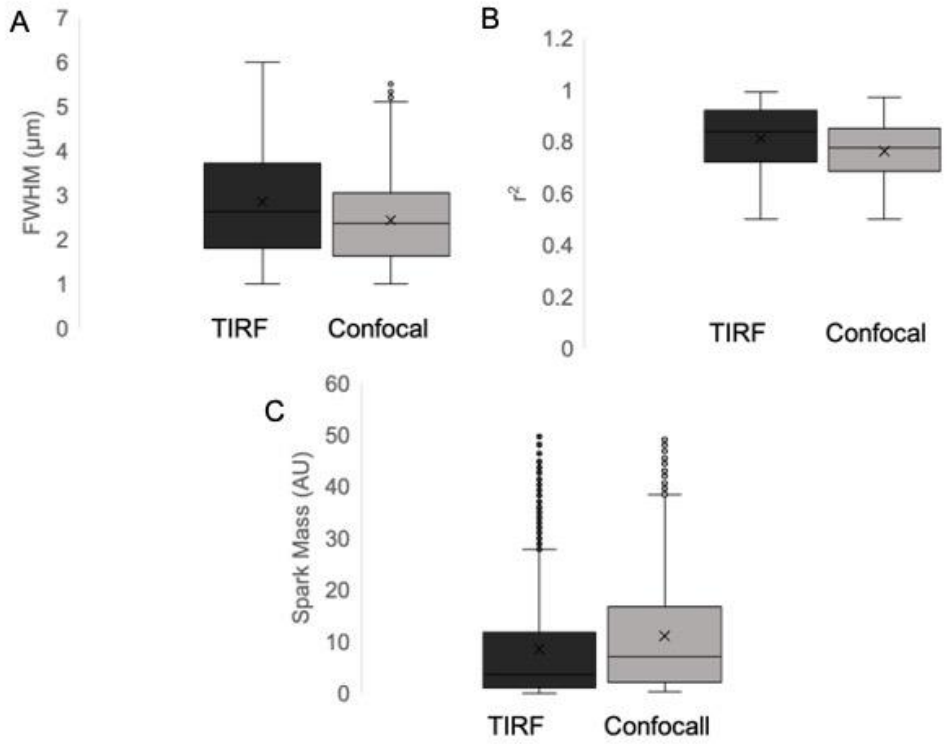

Figure 3.7: Heterogeneity across live-cell calcium imaging techniques at the near-periphery of a ventricular cardiomyocyte. Ventricular cardiomyocytes from Adult male Wistar rats were analysed for their Ca^{2+} spark signalling using TIRF and confocal spinning disk microscopy. Ca^{2+} spark kinetics were analysed with xySpark. (A) Within TIRF microscopy there was an increased median FWHM. (B) Ca^{2+} sparks acquired using TIRF microscopy had a better alignment with a standardised Gaussian distribution, with an increased median r^2 value. (C) Smaller Ca^{2+} sparks were detected with TIRF microscopy compared to confocal microscopy in regard to spark mass. Values are median; confocal n= 3 animals, n= 1168 Ca^{2+} sparks; TIRF n= 6 animals, n= 1675 Ca^{2+} sparks.

Data was grouped together to account for the heterogeneity that exists within Ca^{2+} spark signalling (Figure 3.7). There was minimal difference in the range of values acquired between microscopy techniques for FWHM (Confocal 4.57 μm; TIRF 5.0 μm), r^2 (Confocal 0.47; TIRF 0.49) and spark mass (Confocal 49.61 AU; TIRF 49.68 AU). However, TIRF microscopy had an increased level of sensitivity, with the ability to detect small sparks on a repeated basis. This sensitivity is represented by a median 3.67 AU spark mass within TIRF acquisition compared to 7.06 AU within confocal datasets and less so by a median 2.63 μm FWHM within TIRF microscopy compared to a median 2.37 μm FWHM within confocal microscopy. This increased sensitivity to Ca^{2+} spark morphology is highlighted by a median 0.84 r^2 within TIRF microscopy, which was 0.06 greater than within confocal microscopy representing a greater alignment to a standardised gaussian profile of a Ca^{2+} sparks rise in fluorescence.

3.3.4 Calcium spark morphology according to cell depth

Spontaneous Ca^{2+} sparks were imaged within RV cardiomyocytes exposed to 5 mM Ca^{2+} containing Tyrode's solution. Ca^{2+} sparks were measured at the near surface and deeper within the cell (Figure 3.8).

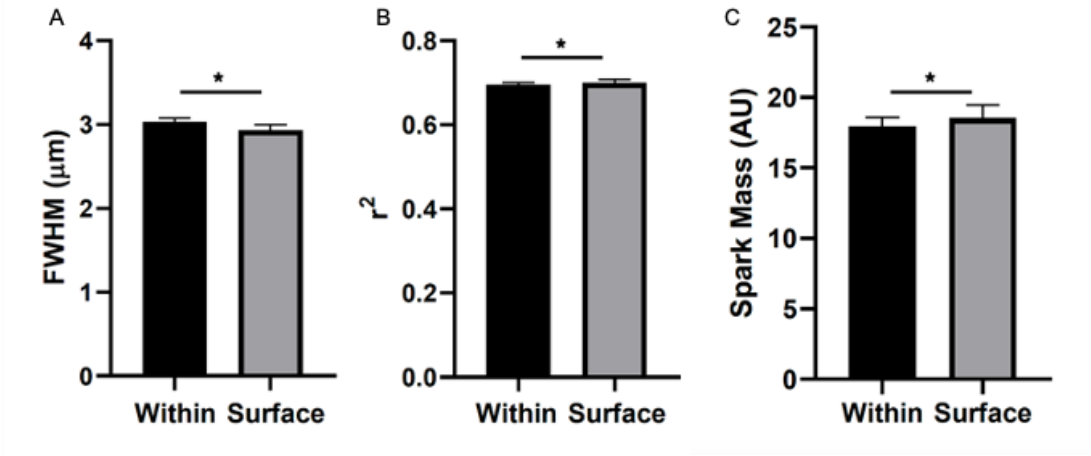

Figure 3.8: Comparison of calcium spark morphology at the near periphery and deep within a cell. Live cell Ca^{2+} imaging undertaken in ventricular cardiomyocytes from Adult male Wistar rats using spinning disk confocal microscopy. Near-periphery was determined by use of fiducial markers. Ca^{2+} spark kinetics were analysed with xySpark. (A) FWHM was significantly smaller at the near periphery. (B) According to the r^2 value, the fit of a Ca^{2+} spark to a Gaussian profile was significantly better at the near periphery. (C) The spark mass was significantly increased when measurements were taken at the near periphery. Values are mean±SEM; Within n= 11 cells, n= 430 Ca^{2+} sparks; Surface n= 11 cells, n= 237 Ca^{2+} sparks.

There was a significantly 3.27% greater FWHM recorded for Ca^{2+} sparks within the cell at 3.03±0.05 μm compared to Ca^{2+} sparks at the surface (paired t-test; $p=1.60x10^{-24}$). However, Ca^{2+} sparks at the near surface had a better gaussian fit, with a significant increase in r^2 value compared to Ca^{2+} sparks from within the cell (Surface 0.70±0.01; Within 0.69±0.01 (paired t-test; $p=1.16x10^{-7}$)). Conversely, spark mass from Ca^{2+} sparks within a cell was 17.94±0.66 AU. This was significantly smaller than the 18.54±0.94 AU spark mass recorded at the surface, suggesting that the spatial spread of a Ca^{2+} spark within the cell compared to at the periphery was greater in the xy plane than in amplitude (paired t-test; $p=5.85x10^{-43}$).

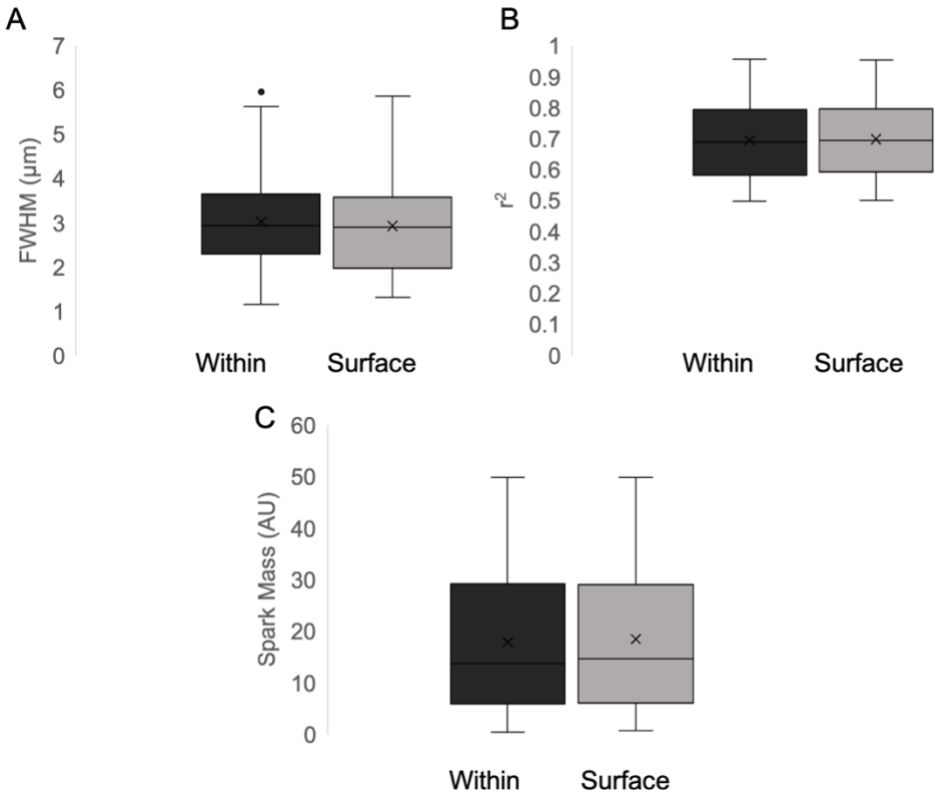

Figure 3.9: Heterogeneity across calcium spark morphology at the near periphery and deep within a cell. Live cell Ca^{2+} imaging undertaken in ventricular cardiomyocytes from Adult male Wistar rats using spinning disk confocal microscopy. Near-periphery was determined by use of fiducial markers. Ca^{2+} spark kinetics were analysed with xySpark. (A) FWHM was significantly smaller at the near periphery. (B) According to the r^2 value, the fit of a Ca^{2+} spark to a Gaussian profile was significantly better at the near periphery. (C) The spark mass was significantly increased when measurements were taken at the near periphery. Values are median; Within n= 11 cells, n= 430 Ca^{2+} sparks; Surface n= 11 cells, n= 237 Ca^{2+} sparks.

Data was grouped together to account for the heterogeneity that exists within Ca^{2+} spark signalling. No outliers had an impact upon a dataset, as suggested by a similar range in variables regardless of imaging depth. Specifically, the range of values for FWHM (Surface 5.56 μm; Within 4.81 μm), r^2 (Surface 0.45; Within 0.46) and spark mass (Surface 49.07 AU; Within 49.36 AU) were analysed (Figure 3.9). Ca^{2+} spark morphology was comparable according to FWHM, with a median width of 2.9 μm at the surface of a cardiomyocyte being only 0.05 μm smaller than deeper within the cell. Of note, the median variability in regard to r^2 value was 0.70 at the surface and 0.69 within a cell. A 0.90 greater median spark mass value of 14.70 at the surface was analysed, reflective of the significant increase analysed across the mean data.

3.3.5 Correlative imaging protocol

A protocol was established (Figure 3.10) which enabled the sequential imaging of spontaneous Ca^{2+} activity followed by the SMLM visualisation of Ca^{2+} handling proteins at the level of a JMC. Primary cells were prepared as described previously (Section 2.2). To enable individual cells to be tracked throughout the duration of the protocol a 500 μm square gridded imaging dish with #1.5H glass coverslip was used.

Initially, cells were loaded with a Ca^{2+} indicator dye, in this case 5 μM Fluo-4 AM (Section 2.3). Live-cell Ca^{2+} imaging was undertaken using a 488 nm excitation wavelength. The cell surface location of imaging was confirmed by the use of fiducial markers upon the coverslip. Near-surface Ca^{2+} sparks were promoted by imaging the cells in 5 mM Ca^{2+} extracellular Tyrode's solution. The gridded dish was placed upon the microscope stage, with the grid lines parallel and perpendicular to the camera's visual field. For each cell imaged for its Ca^{2+} signalling properties, the gross morphology of the cell was recorded using brightfield microscopy and its grid position recorded. Furthermore, the location of the Ca^{2+} spark activity in relation to nearby fiducial markers and in relation to the cell edge was recorded.

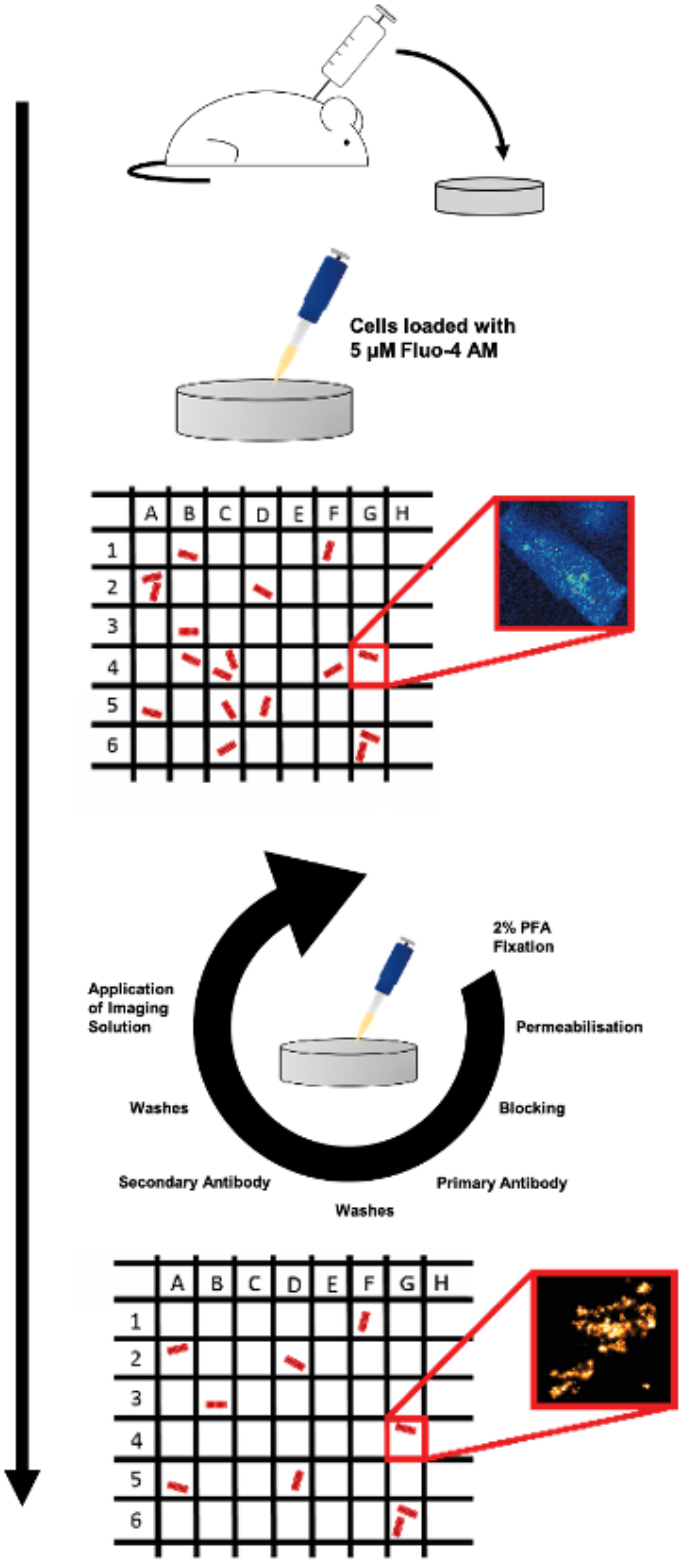

Figure 3.10: Schematic of developed correlative imaging protocol. The stages of the protocol are as follows, according to the direction of the arrow. Primary cells are extracted prior to loading with 5 µM Fluo-4 AM. Cell position within the grid is recorded and calcium spark image acquisition undertaken. All cells undergo fixation and immunofluorescence staining. Cells which were previously imaged for their calcium activity are re-located and their Ca^{2+} handling proteins visualised using single-molecule localisation microscopy.

Immediately post live-cell Ca^{2+} imaging, the cells were fixed and underwent immunofluorescence staining for the required Ca^{2+} handling proteins. The proteins of interest were imaged using either the SMLM technique of dSTORM or DNA-PAINT. The required imaging solution for the respective imaging technique was applied to the dish prior to imaging, as detailed in the Methods Chapter (Section 2.5). The gridded dish was placed upon the microscope stage, with grid lines once again parallel and perpendicular to the camera's visual field to minimise rotational error across the protocol. Cells which had been previously imaged for their functional Ca^{2+} spark activity were located using the grid function. Using the brightfield image of a cell's gross morphology, the cell identity was verified. Cell outline and the positioning of fiducial markers was used to locate the specific region of a cell where Ca^{2+} imaging had occurred. Image acquisition was then undertaken within this same region following the SMLM protocol (Section 2.5) for dSTORM or DNA-PAINT.

Functional Ca^{2+} spark data was analysed as described in the Methods Chapter (Section 2.6.2) and identified Ca^{2+} sparks were filtered as appropriate depending on cell type (Table 2.2). Data for structural Ca^{2+} handling proteins were rendered as previously described, with 1 pixel equating to 5 nm.

3.3.6 Image alignment protocol

The Nysquist sampling criteria were met for the Ca^{2+} spark functional data and the structural single-molecule data acquired during the correlative imaging protocol. The Ca^{2+} spark co-ordinates were quantified using the *xySpark* ImageJ plug-in (Figure 3.11). The co-ordinates of each Ca^{2+} handling protein was identified using the PyME Acquire puncta detection method (Figure 3.11). The location of each data point was undertaken to a pixel level of accuracy. A custom IDL code (written by Dr Izzy Jayasinghe) which is available at the GitHub repository https://github.com/ijayas/imagealigning alongside a user guide (Hurley et al., 2020) was utilised to rescale (Figure 3.11), correlate and analyse the functional and structural datasets (Figure 3.12).

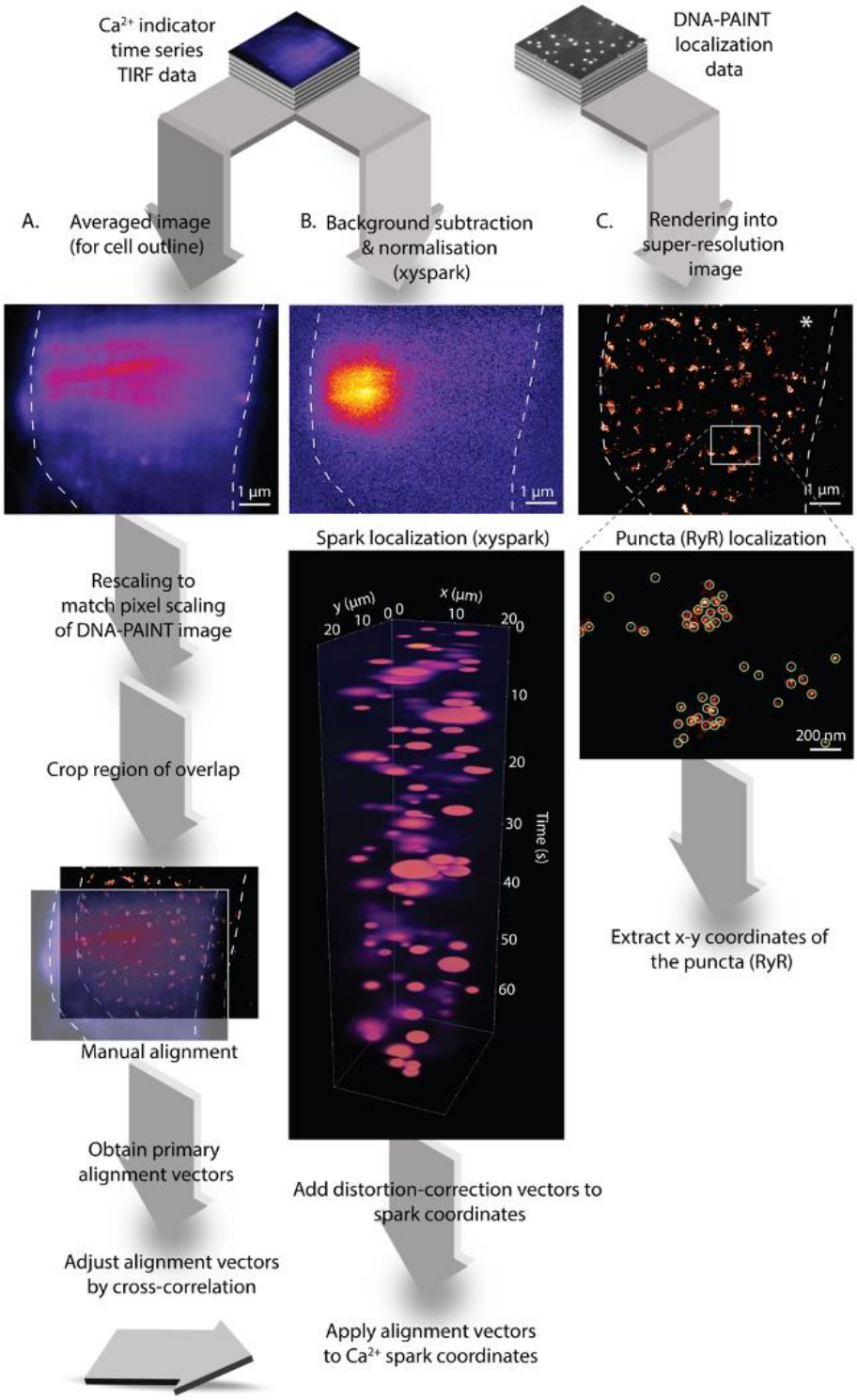

Figure 3.11: Workflow of image alignment. (A) Construction of a low-noise average image from a time series Ca^{2+} spark dataset. Using the cell geometry as a guide, alignment vectors could be determined in regard to the Ca^{2+} data. (B) Detection of Ca^{2+} sparks co-ordinated using 'xySpark', with previously calculated alignment vectors applied. (C) Localisation of RyR single proteins using a puncta detection threshold method. Schematic designed by Dr Izzy Jayasinghe and used with permission.

The Ca^{2+} signalling data were re-scaled to match the 5 nm/pixel value of the SMLM dataset (Hurley et al., 2020). Both datasets were cropped to ensure each image had the same dimensions prior to alignment. The alignment of the functional and structural dataset was a two-step process. Initially, the cell outline and any fiducial markers present within the datasets were used to align the two images manually in the xy plane. Shift vectors, known as 'primary alignment vectors' in the x and y plane were recorded, with no rotational factor applied. A second fine alignment was undertaken through a cross-correlation of the two datasets in Fourier space. This stage was automated and relied upon a 2D cross-correlation whereby the deviation of each dataset from the peak correction value was assessed. A fine adjustment was undertaken to align peak correlation values for each dataset. When the fine alignment vector was adjusted >300 nm the primary alignment vectors were applied.

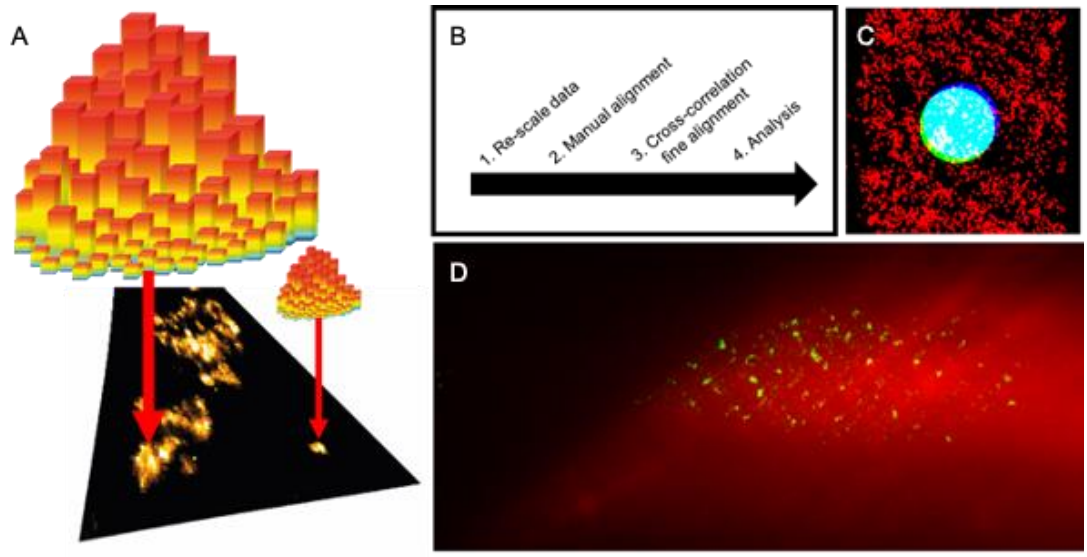

Figure 3.12: Schematic detailing the analysis process within the correlative imaging protocol. (A) Simulation to demonstrate how single-molecule localisation microscopy data of a cell's ultrastructure is aligned with a Ca^{2+} spark profile, with the use of fiducial markers as a guide for alignment. (B) Sequence of events which detail the cross-correlation process within the correlative imaging protocol. (C) In the analysis stage, structural data (red) will be evaluated underneath the footprint of a single Ca^{2+} spark, calculated according to the calcium sparks FWHM (cyan). (D) Example of how the functional and structural datasets are overlaid.

A PSFcheck reference slide (Product ADC0001; PSFCheck Slides, University of Exeter) was used to ensure the alignment of the 488 nm and

642 nm TIRF illumination spot. During analysis, a distortion-correction vector map was applied to adjust the Ca^{2+} and SMLM dataset according to any variability in alignment based upon microscope set-up. The distortion-correction vector map was formed from the analysis of the same 100 nm fiducial markers using the 488 nm channel compared to the 642 nm channel. Correction values were applied to each dataset to account for the presence of in-plane shift between the two laser channels.

The design of the correlative imaging protocol was based upon the investigation of local cellular regions specific to the 2D area in which Ca^{2+} spark activity was recorded. For each Ca^{2+} spark, the FWHM was applied to its known co-ordinate (Figure 3.12C). The spatial footprint of a Ca^{2+} spark was formed equal to its FWHM. This spatial footprint outlined a region in which the Ca^{2+} handling proteins were identified which were likely to be involved in the activation of the Ca^{2+} spark (Figure 3.13). The protocol therefore enables the grouped density of Ca^{2+} release proteins underneath a Ca^{2+} spark's footprint to be quantified.

The diffraction-limited nature of live-cell Ca^{2+} imaging provides a degree of uncertainty regarding cytosolic Ca^{2+} concentration. Therefore, the single RyR puncta from which Ca^{2+} is released is unknown due to the diffusion of Ca^{2+}, diffusion of the Ca^{2+} indicator dye and the extent to which Ca^{2+} is buffered within the cytosol being unknown. The use of FWHM to define the spatial footprint of a Ca^{2+} spark therefore provides a window of confidence within the correlative imaging approach to which the total density of RyR within this region can be studied (Hurley et al., 2020). Furthermore, once the spatial footprint of a Ca^{2+} spark is identified, the NND and average NND of the Ca^{2+} handling protein can also be quantified. The limiting factor within the alignment of the Ca^{2+} spark co-ordinates with those of the Ca^{2+} handling protein is the diffraction-limited nature of TIRF microscopy for imaging Ca^{2+} signalling. Therefore, the *xy* accuracy of the alignment process is half of the diffraction limit.

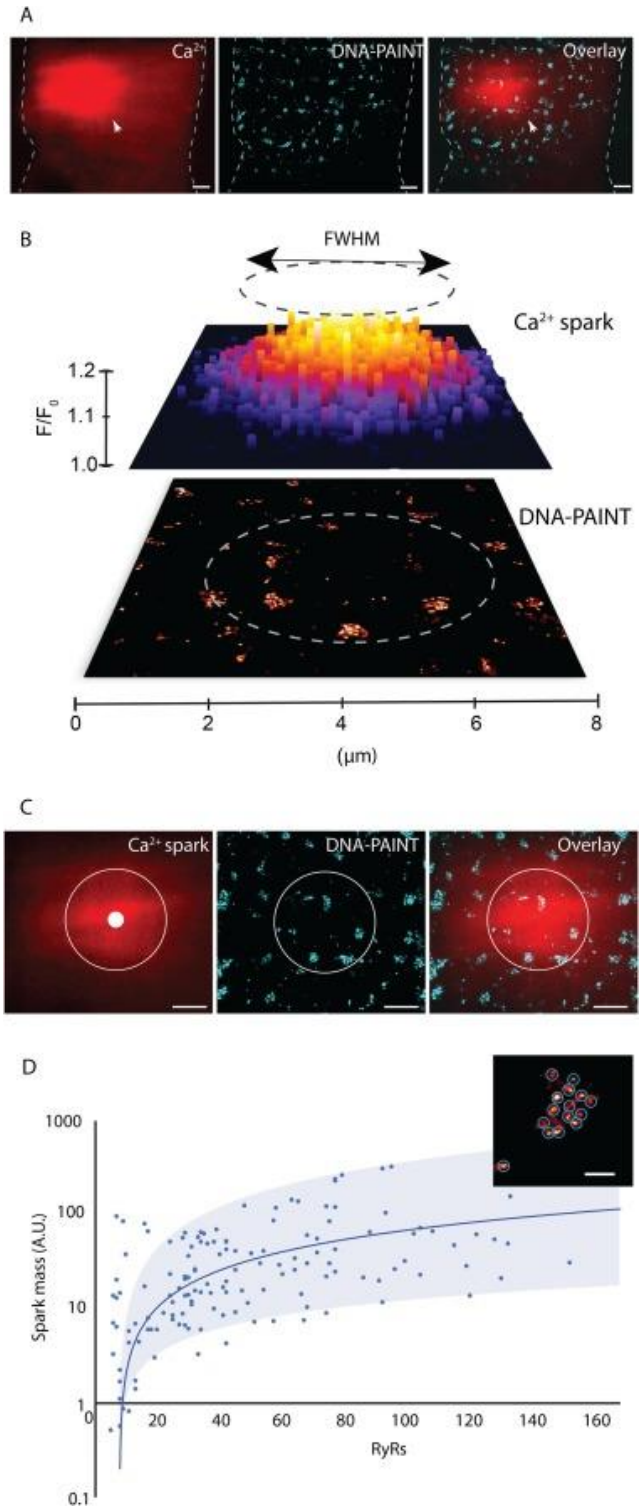

Figure 3.13: Analysis of local RyR organisation underneath a single calcium spark. (A) Cell alignment of functional Ca^{2+} spark acquisition with structural RyR organisation according to cell outline (dashed line). (B) FWHM of a Ca^{2+} spark's profile is used as a 2D spatial indicator to determine the underlying cell region in which the RyR structural pattern is quantified. (C) The spatial footprint of a Ca^{2+} spark (white dot) is analysed in relation to the underlying RyR puncta pattern. (D) The relationship between a single Ca^{2+} spark mass in regard to its spark mass and the underlying RyR density as determined by the FWHM of the Ca^{2+} in question. A logarithmic trendline is plotted, with the shaded region representing a 90% confidence interval. RyR puncta are individually resolved (inset; circled blue). Scale bars, A: 1 µm, C: 2 µm, D: 100 nm. Adapted directly from Hurley et al. (2020).

A scattergram can reveal the relationship between RyR density and the corresponding spark mass (Figure 3.13D). It concluded that 95% of Ca^{2+} sparks arose from regions within the cell that had 8-105 RyR puncta (Hurley et al., 2020), however understandable deviation from the trend observed can occur. For all analysis, spark mass was a product of spark amplitude, $FWHM^3$ and coefficient 1.206 (Hollingworth et al., 2001), as depicted within the *xySpark* ImageJ plug-in. Analysis was undertaken for each Ca^{2+} spark co-ordinate in a sequential manner.

3.4 Discussion

3.4.1 Conjugation success

The success of an oligonucleotide-antibody conjugation for use in DNA-PAINT was determined through multiple experimental methodologies, as explained above. The 6.37 kDa molecular weight shift suggests a successful conjugation, despite the Nanodrop analysis calculating a <1.0 oligonucleotide to antibody ratio. The Nanodrop analysis is based upon the assumption that all present antibody and oligonucleotide are bound. However, despite the clean-up stage within the protocol, the ThunderLink kit does not expect a 100% yield. Nanodrop analysis can therefore not be considered an indicator of conjugation success. This is exemplified by the supernatant with 1.1 ratio failing to specifically stain a cardiomyocyte within immunofluorescence studies. Instead, SDS-PAGE is a more reliable marker for conjugate success. However, a greater sample concentration would be worthwhile to ensure antibody light chain detection. To gain a better understanding of conjugation yield, mass spectrophotometry could be undertaken (Agasti et al., 2017).

Confocal immunofluorescence studies revealed a double-banded RyR2 stain (Chen-Izu et al., 2006). Conjugation success was further evidenced by DNA-PAINT studies revealing an RyR2 staining pattern comparable with Jayasinghe et al. (2018a), with a localisation accuracy not dissimilar from Jungmann et al. (2014). The photophysical properties of the dye used needs to be taken into account. The choice of Atto 655, Cy5 and Cy5.5 reflected that used previously within DNA-PAINT (Jungmann et al. 2010). However,

Alexa dyes have a greater degree of photostability. This could explain why the Alexa 488 confocal data had less background fluorescence than the Cy5 labelled DNA-PAINT probe, with differences not necessarily indicative of conjugate success. Furthermore, when bound to a protein, Cy5 is known to aggregate and act in a self-quenching manner to reduce fluorescence intensity (Berlier et al., 2003).

Any further understanding regarding the efficacy of the conjugation process is limited by the unknown chemistry within the ThunderLink kit. Unlike the original biotin-streptavidin linker (Jungmann et al., 2010), it is concluded that an NHS ester link covalently binds the antibody and oligonucleotide (Jayasinghe et al., 2018a; Jungmann et al., 2016; Schnitzbauer et al., 2017). Discussions have led to the suggestion that the activation stage of the conjugation process can break the antibody disulphide bonds. This is defined by the manufacturer Expedion as a sulfhydryl conjugation whereby the oligonucleotide strand can bind to the hinge region of the antibody at exposed thiol sites. Future studies could adopt an alternate conjugation methodology, such as click chemistry (Gong et al., 2016). The use of heteroatom links through carbon-carbon bonds (Kolb et al., 2001) would provide versatility within the conjugation process.

3.4.2 Choosing an oligonucleotide sequence

The oligonucleotide sequences utilised within this project were originally published by Jungmann et al. (2014). They have since been used by a variety of research groups and have formed a template for further sequence development (Agasti et al., 2017; Jayasinghe et al., 2018a; Lutz et al., 2018).

The association and dissociation rate of hybridisation between the imager and docking strand is dependent not only upon the concentration of imager strand within solution but also the length of the oligonucleotide sequence and its sequence of base pairings. For the 9 base pair oligonucleotide strands the dissociation rate is calculated as 1.6 s^{-1}. However, the kymographs within this study revealed that reaction kinetics are also

dependent upon DNA sequence (Jungmann et al., 2010). Within DNA-PAINT, two or three base pairs are required to initially hybridise prior to complete docking and imager strand hybridisation. It is known that GC base pairs form three hydrogen bonds, whilst AT base pairs only form two. Therefore, reaction kinetics are faster and hybridisation more stable in the presence of GC base pairings (Ouldridge et al., 2013; Zhang et al., 2018). In this study, all sequences have the same number of GC base pairs. However, the placement of the AT and CG base pairings along the P1, P2, P3 and P9 sequences differs slightly which could vary hybridisation kinetics. Specifically, the P9 sequence has GC base pairs located only at the 3' end, with the remaining strand being AT rich. This could explain the appearance of longer lasting events within the P9 kymograph compared to the other sequences.

The less stable P2 and P9 kymographs revealed a reduction in fluorescence intensity across time, suggesting dye phototoxicity. However, an excess of imager strand ensures that DNA-PAINT does not undergo photobleaching (Jungmann et al., 2010). Despite this, it has been suggested that spatial localisation may not always be identified due to a dye bleaching whilst transiently hybridised to the docking strand (Jungmann et al., 2016). A repeated or variable interaction between the imager and docking strand could therefore lead to the bleaching of dyes in-situ during a single binding event. Specifically, Blumhardt et al. (2018) suggests that fluorophore excitation can lead to reactive oxygen species (ROS) production, which over prolonged image acquisition has the capacity to damage DNA. When damaged, the docking strand has limited capacity to bind to complementary imager strand, resulting in a progressive inability of the imager probes to elicit any stochastic events.

Detailed assessment of the binding affinity for each DNA-PAINT probe is required to fully understand the underlying differences exhibited between kymographs. The work of Ashlea Rowley at The University of Leeds has utilised our imager strands within surface plasmon resonance (SPR) studies to analyse the binding kinetics in reference to biotinylated docking strands

that are bound to a streptavidin sensory chip (Appendix A.1). This quantitative assessment of the oligonucleotide sequences used within this study revealed that the P1 and P3 sequences have a comparable dissociation constant (K_D) as reflected in their similar association (K_{on}) and dissociation (K_{off}) rate. This is reflected in our qualitative assessment of the P1 and P3 kymographs, which revealed a high event density and detailed Cav3 staining pattern compared to the P2 and P9 sequences. SPR studies were not undertaken upon the P9 strand. However, the P2 sequence had a notable slower K_{on} and faster K_{off} compared to the P1 and P3 sequences. This was reflected by a decreased K_D and therefore a reduced binding affinity between the P2 imager and docking strand. Such a notion is reflected within our qualitative assessment of the P2 probe, which suggested variable fluorophore excitability across the sample and a resultant incomplete Cav3 stain. These comparisons suggest a desirable dissociation constant being required within DNA-PAINT image acquisition to ensure stochastic events occur at a rate which is optimal for detection whilst maintaining a minimal background fluorescence and consequently a minimal spatial localisation error.

Single molecule events are difficult to control. This is evidenced across the kymographs produced. To minimise variability, the Atto 655 dye was utilised and imaging buffer conditions characterised by Jungmann et al. (2014). This study of RyR2, similar to Jayasinghe et al. (2018a) ensured sufficient labelling density and the ability to produce a <10 nm localisation accuracy. The use of the P1 and P3 sequences in the following chapters reflects the DNA-PAINT probes primarily used by other research groups (Jayasinghe et al., 2018a).

The application of an Iowa Black RQ quencher strand is known to decrease fluorescence by 98% (Lutz et al., 2018). Background fluorescence can negatively impact localisation accuracy (Thompson et al., 2002). Kymograph studies of P1 and P3 sequences with added quencher strand revealed a reduced background fluorescence due to a decreased density of single

molecule events per frame (Lutz et al., 2018). However, there is still capacity for DNA-PAINT to be developed further.

Future research should consider repeat DNA-PAINT. This recently published technique relies upon a docking strand with repeated oligonucleotide sequence to enable the binding of multiple imager strands. Compared to the method of DNA-PAINT used within this study, the repeat method can decrease non-specific events 10-fold and reduce background fluorescence 5-fold to improve image acquisition (Clowsley et al., 2020). Beyond this, further developments of DNA-PAINT could include direct binding of the oligonucleotide to a primary antibody (Agasti et al., 2017). Alternatively, the use of affimers, aptamers or nanobodies would reduce the linkage error from the 10 nm defined with standard 150 kDa IgG antibodies (Janeway et al., 2001; Opazo et al., 2012; Ries et al., 2012; Schnitzbauer et al., 2017). However, care is needed regarding the specificity of these antibody alternatives (Opazo et al., 2012).

3.4.3 Choosing a microscopy technique

The microfilament α-actinin spans the width of a cardiomyocyte, enabling it to be used as a biological calibration tool (Sheard et al., 2019). Within biological research the diffraction-limited technique of confocal microscopy is commonly used. This is partly due to the removal of out of focus light from the addition of a pinhole complemented by the ability to image at various z-depths in a simplistic and reproducible manner (Croix et al., 2005; Huff, 2015). Regardless, the technique remains diffraction-limited as demonstrated by the large α-actinin bandwidth analysed. The level of background fluorescence can impair a fluorophore's PSF which in turn can limit resolution (Mortensen et al., 2010). The Airyscan method has an improved signal to noise ratio. As a consequence, resolution is improved to 140 nm. However, due to the complex geometry of biological systems, the bandwidth of α-actinin is still overestimated (Huff, 2015).

The adoption of SMLM reduced the width of the α-actinin band. This was noticeable with a narrower α-actinin calculated with dSTORM microscopy.

However, dSTORM is liable to over and undercounting due to its reliance upon photoswitchable dyes which have a narrow window of optimisation based upon oxygen removal and cysteamine concentration. As a result, the density and duration of single molecule events can vary across image acquisition. Furthermore, a dye has a fluorescence lifetime, known as a photon budget, which can lead to photobleaching and limit imaging efficiency (Blumhardt et al., 2018; Nieuwenhuizen et al., 2015; Vogelsang et al., 2008). Comparable with the findings of Sheard et al. (2019), it was not until DNA-PAINT was applied that the double-banded morphology of α-actinin was identifiable. The adoption of TIRF microscopy within DNA-PAINT enabled an improved signal to noise ratio beyond that of dSTORM (Tokunaga et al., 2008). Agasti et al. (2017) revealed a similar finding in their use of DNA-PAINT to study the microtubule tubulin. It was suggested that the double-banded structure of α-actinin was from antibodies binding to the outermost layer of the microtubule structure, forming a tube-like appearance (Sheard et al., 2019). This finding provided a rational to explore the use SMLM, specifically DNA-PAINT, for the study of Ca^{2+} handling proteins within the following research.

3.4.4 Imaging calcium handling proteins

The use of diffraction-limited techniques, such as confocal and airyscan microscopy, have the inability to resolve individual RyR puncta. Results within this study revealed the characteristic double-banded striation of RyR internally, with a more irregular pattern at the surface, as evidenced previously (Chen-Izu et al., 2006; Hiess et al., 2018; Scriven et al., 2000). Within diffraction-limited microscopy, the RyR cluster size ranges from 212-960 nm in diameter, containing 120-260 RyRs (Chen-Izu et al., 2006; Soeller et al., 2007). This is similar to the calculations within this study, based upon cluster area. The use of dSTORM detailed RyR clusters to have an elongated morphology. Their 13.6 RyR/cluster was based upon a quasi-crystalline array (Baddeley et al., 2009b). This was comparable with this study, which calculated 10$\pm$2 RyR/cluster. Any variation was due to the ability to account for holes within the cluster pattern from use of the puncta threshold algorithm.

The 10 nm xy spatial resolution of DNA-PAINT led to a 6-fold improved localisation accuracy compared to dSTORM. At the periphery, RyR puncta were distinctly resolved and the cluster size 8.8±0.86 RyR puncta/cluster (mean ± SD) (Jayasinghe et al., 2018a). This finding was supported by Sheard et al. (2019) who used 10xEEM to resolve single RyR puncta, calculating an average 8.98 RyR/cluster at the periphery. This decreased trend in RyR cluster size as xy spatial resolution improved was evidenced within this study where 4±1 RyR/cluster was calculated. One explanation for the smaller average cluster size, compared to Jayasinghe et al. (2018a), could be from the addition of quencher strands which have the capacity to improve localisation accuracy within DNA-PAINT acquisition by reducing background fluorescence.

One claim for the decreased cluster size within DNA-PAINT could be changes in the local RyR environment at the level of the JMC (Asghari et al., 2020). However, no data yet supports these claims and electron tomography is unable to localise individual RyR puncta (Jayasinghe et al., 2018b). An alternate reasoning for the smaller RyR cluster size could be heterogeneity across the cell in regard to RyR cluster patterning (Xie et al., 2010). Another reason could be the differences in immunofluorescence staining, with antibody labelling efficiency for RyR2 being only 42% (Soeller et al., 2007). It should be noted that RyR2 as a tetramer has multiple antibody binding sites, however, due to the resolving power of DNA-PAINT each stochastic event can be spatially resolved and only attributed to one RyR2 within the analysis due to RyRs 30 nm diameter and neighbouring spacing (Peng et al., 2016; Jayasinghe et al., 2018a). Perhaps the most likely suggestion is due to 35% of RyRs not being linked to a couplon (Scriven et al., 2010), with puncta being orphaned from the JMC (Sobie et al., 2006; Song et al., 2006). A high prevalence of orphan RyRs within this study could be causing a leftward shift in average RyR cluster size. This suggestion could be verified by the clusters detected having a range of 1 to 30 RyR. Further research is warranted to study RyR2 in relation to additional JMC proteins or T-tubule structure to understand the extent by which the protein may be orphaned. Ultimately, the versatility of DNA-PAINT and its documented use within

cardiomyocytes led to the primary use of this SMLM technique within the following research.

3.4.5 Calcium spark imaging

The use of confocal spinning disk and TIRF microscopy were evaluated for visualising Ca^{2+} sparks. The thin light sheet of TIRF microscopy enables out of focus light to be discarded. Consequently, background fluorescence is minimised and optical blurring or the presence of artefacts is reduced (Bridge et al., 1999). At the near surface, confocal microscopy has the capacity to overestimate the measurements of a Ca^{2+} spark. This could explain why Ca^{2+} spark mass was significantly smaller under TIRF imaging conditions. This suggestion is supported by Ca^{2+} sparks having a significantly greater fit to a gaussian profile within TIRF conditions and further evidenced when the median values are analysed. Specifically, TIRF's increased ability to differentiate signal to noise was exemplified by the 3.39 AU difference within median spark mass values, accounting for the ability that TIRF has in quantifying smaller Ca^{2+} sparks. The use of TIRF microscopy therefore enables a greater representation of the Ca^{2+} spark population that is generated within a cell and in turn enables a clearer understanding of the local control mechanisms at the CRU. It is the sensitivity of TIRF microscopy, along with its ability to be undertaken under the same microscopy parameters as DNA-PAINT, which promoted its choice within the following research. However, a limitation still persists within TIRF microscopy regarding xy spatial resolution. This could lead to multiple Ca^{2+} sparks being grouped together which could explain the difference in FWHM between confocal and TIRF microscopy. Despite this, to examine near surface activity TIRF microscopy was chosen as the technique of preference. Looking ahead, it is important to note that the two-dimensional approach within this study also negated the diffusion of Ca^{2+} within the three-dimensional subspace which is the JMC. Future studies would benefit from the analysis of a Ca^{2+} sparks diffusional properties within the xyz plane to understand the role of cellular structures in regard to the propagation of a Ca^{2+} signal.

3.4.6 Evaluating calcium spark morphology at various z-planes

The confocal spinning disk technique was used to evaluate whether Ca^{2+} spark morphology varied across cell depth. In alignment with previous literature it was noted that the diffusional profile of a Ca^{2+} spark was different within a cell compared to at a cell's periphery (Jayasinghe et al., 2009). Notably, according to Fick's first law, the diffusion of Ca^{2+} was dependent upon the diffusional gradient and the area of diffusion (Soeller et al., 2007). Additionally, the size of RyR clusters is considered to be 4 times greater than at a cell's periphery (Hou et al., 2015), with a cell suggested to have a larger CRU internally. The density of RyR in determining Ca^{2+} spark generation is important. This is evidenced by Ca^{2+} spark sites being primarily located along the transverse orientation of a cell, specifically along the Z-line where there is a known clustering of RyR (Jayasinghe et al., 2009; Lukyanenko et al., 2009; Parker et al., 1996b). The diffusion of Ca^{2+} is isotropic. However, the transverse contractile structures within a cell can limit and slow the diffusion of Ca^{2+}. Conversely, a ventricular cardiomyocyte's periphery has a simplified structure with the movement of Ca^{2+} less inhibited (Subramanian et al., 2001). Accounting for a cell's variation in ultrastructure based upon cell depth, for example the presence of mitochondria sub-structures deeper within the cell, could begin to explain the diffusional differences in Ca^{2+} spark profiles within this study. This explanation is appropriate in regard to the greater median and mean spark mass recorded across the surface of a cell compared to deeper within. Furthermore, the variation in r^2, albeit minimal, is reflective of the limitations that live-cell Ca^{2+} imaging has in regard to acquiring Ca^{2+} spark recording beyond the periphery of a cell. This knowledge supports the focus of the following research upon near-periphery Ca^{2+} sparks.

3.4.7 Correlative imaging

The requirement to study a cell's signalling nanodomain in relation to its structure and function arises from the known dependency that Ca^{2+} spark generation has upon RyR arrangement (Hiess et al., 2018; Walker et al., 2015). The extent of this relationship is unclear. Multiple parameters, both structural and regulatory, are therefore likely to modulate Ca^{2+} signalling (Xie

et al., 2010). For example, the cluster size of Ca^{2+} release proteins, their orientation and their biochemical modulation is believed to impact Ca^{2+} spark fidelity (Asghari et al., 2014, Asghari et al., 2020; Galice et al., 2018; Walker et al., 2014). The precise number of RyR channels which are required to generate a Ca^{2+} spark is also disputed (Baddeley et al., 2009b; Wang et al., 2001, Wang et al., 2004). Ca^{2+} spark generation from single RyR channels has been proposed. Wang et al. (2004) suggested, for example, that 12% of Ca^{2+} sparks can originate from single RyR channels. However, an increased density of orphaned RyR channels, as evidenced in HF, are thought to contribute towards dyssynchronous Ca^{2+} activity (Song et al., 2006).

The developed correlative imaging protocol has enabled Ca^{2+} signalling within live cells to be analysed in relation to the Ca^{2+} handling proteins that directly underpin calcium's functional release. Application of this protocol can enable the shape of a Ca^{2+} signal (i.e. Ca^{2+} spark) to be studied in response to cellular remodelling within disease or in response to pharmacological agents. As a result, protein-protein interactions and a Ca^{2+} signal's response to biochemical modifications can be experimentally observed. To the author's knowledge, this correlative imaging protocol allows the first direct study of a signalling nanodomain's function and structure within wild-type live cells.

The concept of correlative imaging has been explored previously across multiple imaging modalities. Correlative Light and Electron Microscopy (CLEM) and Atomic Force Microscopy (AFM) with super-resolution microscopy are two examples of correlative imaging protocols previously published. Both examples are focussed upon visualising cell structure. Techniques such as electron microscopy and AFM provide the mechanical properties of a cell to be studied at an ångström scale of detail but without any differentiation. The added specificity of fluorescence microscopy, therefore, enables context to be applied to the study of a cell's ultrastructure (Chacko et al., 2013; Cosentino et al., 2019; Hampton et al., 2017; Kukulski et al., 2012). So far, a focus of correlative imaging has been the combination of structural imaging techniques to reduce artefacts and improve xy spatial

resolution (Hamel et al., 2014). However, there is a requirement to apply such approaches to study live-cell dynamics (Gómez-Varela et al., 2017).

All of the correlative imaging protocols discussed above have applied super-resolution microscopy to study cellular heterogeneity at the level of a single protein. This study design is reflective of the rationale which applies SMLM to study specific Ca^{2+} handling proteins. In particular, the following chapter discusses the application of DNA-PAINT to the correlative imaging protocol to gain a true molecular scale resolution. Of note, the specificity of each antibody marker should be evaluated before conclusions regarding its staining pattern are reached in case of target saturation or pattern distortion. The following research utilises an anti-RyR antibody that has been previously established within DNA-PAINT (Jayasinghe et al., 2018a) and 10xEEM studies (Sheard et al., 2019). Future work is required to evaluate the validity of all additional antibodies utilised within SMLM.

Before continuing with the application of the newly designed correlative imaging protocol it is important to discuss its current limitations. Akin to all imaging techniques, there are technical limitations. Combining live-cell Ca^{2+} imaging alongside SMLM is labour-intensive and time-consuming. Many AFM and super-resolution microscopy correlative approaches can undertake image acquisition simultaneously for the respective techniques (Hirvonen and Cox, 2018). However, the above protocol requires cells to undergo fixation and immunofluorescence staining between the image acquisition protocols. As a result, there is a possibility of cell movement and rotational error between the functional and structural datasets. The use of a gridded dish and fiducial markers were applied to minimise this limitation. This approach is similar to CLEM which relies upon a gridded dish for image alignment (Hampton et al., 2017). Use of a glass dish with gridded etching was chosen for its suitability for SMLM, due to its minimal background fluorescence. This is important as all imaging modalities were limited to the 100 nm depth of TIRF microscopy. Furthermore, Hampton et al. (2007) relied upon fiducial markers to aid with the alignment of each dataset. When their fluorescence is retained, for example within CLEM, fiducial markers are

an ideal guide for image alignment and can ensure a localisation precision of <100 nm (Gibson et al., 2014; Kukulski et al., 2012).

A third element by which alignment was undertaken was by overlaying the two datasets in regard to a region of interest, such as the cell outline. The applied correlative imaging protocol required multiple buffer exchanges which disturbed or completely removed fiducial markers. This limitation was observed by Crossman et al. (2015) in their confocal and dSTORM correlative technique. The limitation of buffer exchange across AFM and STORM acquisition was eliminated by Hirvonen and Cox (2018) by the removal of oxygen scavengers. However, the ability to minimise this limitation is largely dependent upon the imaging technique applied. Buffer exchange within the correlative imaging protocol was unavoidable, resulting in cell outline being used as the primary guide for alignment, similar to Crossman et al. (2015). Overall, the method of cell alignment according to fiducial markers, cell outline or use of a gridded dish were combined to a varying extent and validated by a calibration system as discussed above and in accordance with the literature (Chacko et al., 2013; Cosentino et al., 2019; Hampton et al., 2017).

The use of an xy spatial alignment can further reduce the likelihood of any rotational aspect. However, it should be noted that the initial alignment stage was user-driven. An upper limit for the xy shift vectors was applied and datasets were discarded if this was exceeded so as to not undermine the fine alignment stage. The degree of error within the z-plane was minimised by using the same microscope setup throughout the whole protocol. To minimise the potential of cell movement across the protocol, the uncoupling drug 2,3-butanedione monoxime could have been applied to prevent contractile motion. However, the decision to exclude such a drug was made due its known ability to reduce intracellular Ca^{2+} concentration and overall Ca^{2+} spark formation (Gwathmey et al., 1991).

The process of fixation is known to alter cellular structure. Hiess et al. (2015) reported an overestimate of RyR density within their fixed cell preparations.

The correlative imaging protocol similarly used an aldehyde-based fixation method but with a less aggressive approach (Munro et al., 2016). This method of fixation is known to retain biochemical information to a greater extent than organic solvents (Hobro and Smith, 2017). Due to the aforementioned limitations, there will always be a degree of error present. However, one method to validate the detected alignment between regions of RyR2 and Ca^{2+} sparks could be the additional analysis of randomised FWHM measurements across the cell in regions where no RyR2 density is present to understand the extent by which the two variables are dependent upon one another.

The developed correlative imaging protocol demonstrates for the first time the relationship between a cell's protein pattern which is directly responsible for a Ca^{2+} signal. In the future, this protocol could be extended further across multiple cell types and encapsulate the study of Ca^{2+} waves.

3.5 Concluding remarks

The data presented within this chapter outlines the use of SMLM to study the Ca^{2+} handling proteins within a cell. It concluded that the xy spatial resolution of DNA-PAINT was required to visualise single RyR puncta and understand cluster morphology. When studying Ca^{2+} signalling within a cell, the use of a TIRF based system to visualise Ca^{2+} spark morphology at a cell's periphery was preferable. Together, these findings enabled the development of a correlative imaging protocol.

Within primary cells, the correlative imaging protocol enables the study of Ca^{2+} spark kinetics in regard to the local arrangement of the JMC. In turn, suggestions can be formed regarding the role that a cell's ultrastructure can have upon the local Ca^{2+} signalling recorded. The ability to study a cell's local function and structure in tandem is revolutionary. It is an experimental tool to study the heterogeneity of RyR clustering across a cell in regard to its local Ca^{2+} release from the SR. Furthermore, the protocol can be utilised to study functional response to the pathological remodelling which is suggested to occur in several disease models. Alternatively, it can be applied to

uncover the role of single channels in Ca^{2+} signalling which has only been alluded to previously from pharmacological interventions.

To understand the relationship between a cell's ultrastructure and Ca^{2+} spark formation at a local level, the correlative imaging protocol will be utilised in the following chapters. Firstly, the protocol will evaluate the degree of remodelling within a model of RV HF. Secondly, the role of differing Ca^{2+} handling proteins will be discussed in light of Ca^{2+} spark generation within DRG sensory neurones. Both of these applications are areas within the literature which would benefit from the study Ca^{2+} signalling and the Ca^{2+} handling structure in relationship to each other.

Chapter 4. Correlative imaging in heart failure

4.1 Introduction

The heart is classified as failing when its CO is unable to meet the metabolic demands of the body (Kemp and Conte, 2012). Heart failure is the outcome of a hypertrophic compensatory response from an initial pathological event, such as volume or pressure overload. Remodelling of the heart during this compensatory response can occur at a whole heart, cellular or molecular level (Cohn et al., 2000).

Decompensation of the heart is driven by changes to Ca^{2+} signalling (Molkentin, 2006; Roderick et al., 2007). In turn, the mechanism of Ca^{2+} release from the SR by RyR2 and its re-uptake by SERCA is affected which can then contribute further to the heart's hypertrophic response (Hoshijima et al., 2006). This suggestion has led to the RyR2 Ca^{2+} release channel being the focus of the following research.

Whilst research has focussed upon LV HF, the development of right-sided HF and the mechanism of remodelling within the RV is still unclear. There is a need for the mechanisms underlying the contractile deficit associated with RV HF to be understood to better focus treatment development. This factor has driven the use of a RV HF model within the following research (Harjola et al., 2016). Previously, remodelling of Ca^{2+} handling proteins in RV HF has been studied in regard to changing mRNA and protein expression at the level of the ventricle. However, research groups using the same MCT-induced RV HF model have reported contrasting results. For example, Xie et al. (2012) reported no change in the global RyR2 expression within the RV, unlike the decreased RyR2 expression observed by Kögler et al. (2003). Such discrepancies highlight the need to study Ca^{2+} handling proteins at the level of the single protein, to visualise the heterogeneous nature of remodelling across the ventricle. Most recently, Sheard et al. (2019) have used SMLM to reveal a nanoscale reduction in RyR2 cluster size and a fragmentation of the channel across the JMC.

Previous research has attempted to study the local relationship between Ca^{2+} spark signalling and JMC remodelling. Most notably, within RV HF there is an increased frequency of spontaneous Ca^{2+} spark activity. However, the mechanism behind this altered Ca^{2+} signalling is unclear (Fowler et al., 2015; Fowler et al., 2018). Computational simulations suggest that Ca^{2+} spark fidelity is partially dependent upon the JMC in regard to RyR2 orientation (Kolstad et al., 2018). To derive the role of the JMC in relation to Ca^{2+} spark fidelity there is a requirement to study experimentally the relationship of local Ca^{2+} signalling and RyR2 structure at the level of the single protein (Hiess et al., 2018; Asghari et al., 2020).

This chapter utilises the developed correlative imaging protocol which was detailed in Chapter 3 to explore the relationship between local Ca^{2+} signalling and RyR2 structure at the level of the JMC. The aim was to investigate the extent of RyR2 remodelling at the level of a single protein within the pathophysiological state of RV HF and the role, if any, this can have upon local Ca^{2+} signalling. To the author's knowledge, no experimental study has so far addressed this relationship in a correlative manner in primary cells.

4.2 Method

Male Wistar rats (180-215g) had an intraperitoneal injection of MCT or saline solution and were grouped into 'Fail' and 'Control' animals respectively. Fail animals developed RV HF due to compensation from pulmonary arterial hypertension, as described in Section 2.1. Control animals were age-matched in regard to the number of days post-injection. Upon reaching their pre-defined end point, hearts were excised and RV and LV cardiomyocytes enzymatically isolated as described in the Methods Chapter (Section 2.2). After the heart was excised, the liver and lungs were harvested by blunt dissection and weighed immediately.

4.2.1 Live cell calcium spark recording

Confocal and TIRF-field microscopy was undertaken to record spontaneous near-surface Ca^{2+} sparks within RV cardiomyocytes. Live-cell Ca^{2+} imaging

was undertaken in the presence of 5 mM $CaCl_2$ containing Tyrode's solution as described previously in the Methods Chapter (Section 2.3). Each Ca^{2+} spark was analysed with *xySpark* (Steele and Steele, 2014) and filtered according to the pre-determined criteria (Table 2.2).

4.2.2 Correlative imaging approach

Live-cell Ca^{2+} imaging of RV cardiomyocytes was carried out as described in the Methods Chapter (Section 2.3). This was the initial imaging stage of the developed correlative imaging protocol which was previously described in Section 3.3.5. For DNA-PAINT image acquisition, RV cardiomyocytes were stained with an RyR2 rabbit primary antibody alongside the P1P3 anti-rabbit conjugate (Section 2.5.4).

Single molecule data was rendered using PyME Acquire, as detailed in the Methods Chapter (Section 2.6), with RyR2 puncta having a spatial localisation accuracy of 12 nm or less. Ca^{2+} spark analysis was undertaken using *xySpark* (Steele and Steele, 2014) and identified Ca^{2+} sparks were filtered according to the inclusion criteria as described in the Methods Chapter (Table 2.2). Identification of RyR2 puncta as individual receptors was undertaken as described by Jayasinghe et al. (2018a) using a puncta detection algorithm. Application of custom IDL code (written by Dr Izzy Jayasinghe) enabled Ca^{2+} spark profiles to be aligned with RyR2 puncta as detailed in Section 3.3.6. This enabled Ca^{2+} spark mass (AU) to be evaluated in relation to RyR2 density and the Ca^{2+} channel's nearest neighbour distance for the area of the cell located underneath the Ca^{2+} spark's spatial footprint.

4.2.3 Dual imaging of calcium signalling proteins

Immunofluorescence staining was undertaken with application of the primary antibodies; RyR2 mouse and JPH2 rabbit primary. DNA-PAINT or two-colour DNA-PAINT, known as Exchange-PAINT, was undertaken through the addition of a P1 mouse and P3 rabbit conjugate in lieu of a secondary antibody. Traditional DNA-PAINT was undertaken as described in the Methods Chapter (Section 2.5.3). To image both docking strands at the

same cellular region, Buffer C was used to wash out and exchange the imaging buffer from the P1 imager and quencher-specific strands for the P3 sequence after 30,000 to 40,000 frames. RyR2 and JPH2 images were individually rendered and image processing was undertaken as described within the Methods Chapter (Section 2.6.1). Co-localisation of the RyR2 and JPH2 stain was calculated as a fraction of one stain in relation to the other using the co-localisation analysis plug-in (Hou et al., 2015; Jayasinghe et al., 2018a).

4.2.4 Immunofluorescence staining of the transverse tubule network

Cardiomyocytes from the RV underwent fixation and immunofluorescence staining in suspension as detailed in the Methods Chapter (Section 2.4). The T-tubule network was stained with the NCX mouse and Cav3 mouse primary antibodies, with the addition of either an Alexa 488 anti-mouse or Alexa 647 anti-mouse secondary antibody (Table 2.3). The combined use of NCX and Cav3 as a sarcolemma marker was validated by Crossman et al. (2011). Confocal microscopy was utilised to visualise the T-tubule system in cardiomyocytes from Fail and Control animals at varying points along the *z*-axis of the cell. Image acquisition using confocal microscopy was undertaken as detailed in the Methods Chapter (Section 2.5.1). Using ImageJ, an Isodata auto threshold (Ridler & Calvard, 1978) was applied to create a binary mask and the T-tubule structure was skeletonised. The skeleton structure was analysed to quantify branch length and directionality when transverse regions of the T-tubule structure are at a 90° orientation and longitudinal regions in a 0° plane (Crossman et al., 2015).

4.3 Results

4.3.1 Right ventricular heart failure time course

Animal weight was monitored after the administration of MCT or saline. The greatest determinant of compensatory hypertrophy and the resultant development of RV HF from PAH is weight loss (Benoist et al., 2011; Fowler et al., 2015). From day 0 to the pre-determined end point, each animal had its weight observed (Figure 4.1). From day 0, the Fail group had a mean weight gain of 69.23±4.21 g compared to the significantly greater

133.30±4.17 g weight gain within the Control group (t-test; $p=5.89x10^{-10}$). Deviation of the Fail group's growth curve is visualised from day 10 post injection. The difference in overall weight gain is therefore a result of animals within the Fail group having less rapid a growth combined with a notable weight loss immediately before each animal's end point.

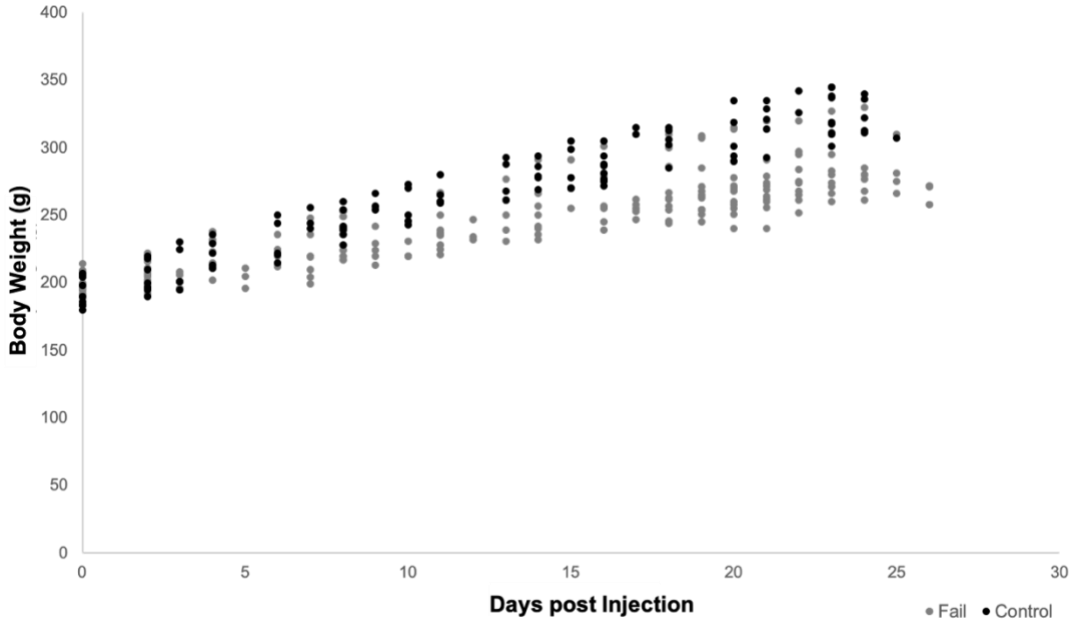

Figure 4.1: Growth curve of saline and monocrotaline injected rodent models. Body weight of Adult male Wistar rats from day 0 post injection until the pre-established end point. Rodents were injected with either 60 mg/kg monocrotaline to induce right ventricular heart failure or were saline injected as a day-matched control. Fail n=13 animals; Control n=10 animals.

Organ weights were immediately weighed upon euthanasia at each animal's end point (Figure 4.2). The Fail group had a mean 10.54±0.57 g liver weight which was significantly lighter than the mean 12.16±0.53 g of the Control group (t-test; *p=0.049*). Conversely, average lung weight was significantly greater within Fail animals compared to the Control (Control 1.43±0.09 g; Fail 2.28±0.08 g (t-test; $p=1.26x10^{-6}$)). There was no significant difference in whole heart weight (t-test; *p=0.57*) or weight of the ventricles (t-test; *p=0.91*) between the two groups. However, there was a significant increase in the heart weight to body weight ratio in Fail animals compared to Control when final body weight was considered (Control 0.0057; Fail 0.0067 (t-test; *p=0.02*)). This suggests that when the animal's weight is considered, hearts

from the Fail animals are heavier. Likewise, Fail animals had a significantly greater lung weight to body weight ratio compared to Control (Control 0.0044; Fail 0.0085 (t-test; $p=2.33x10^{-9}$)).

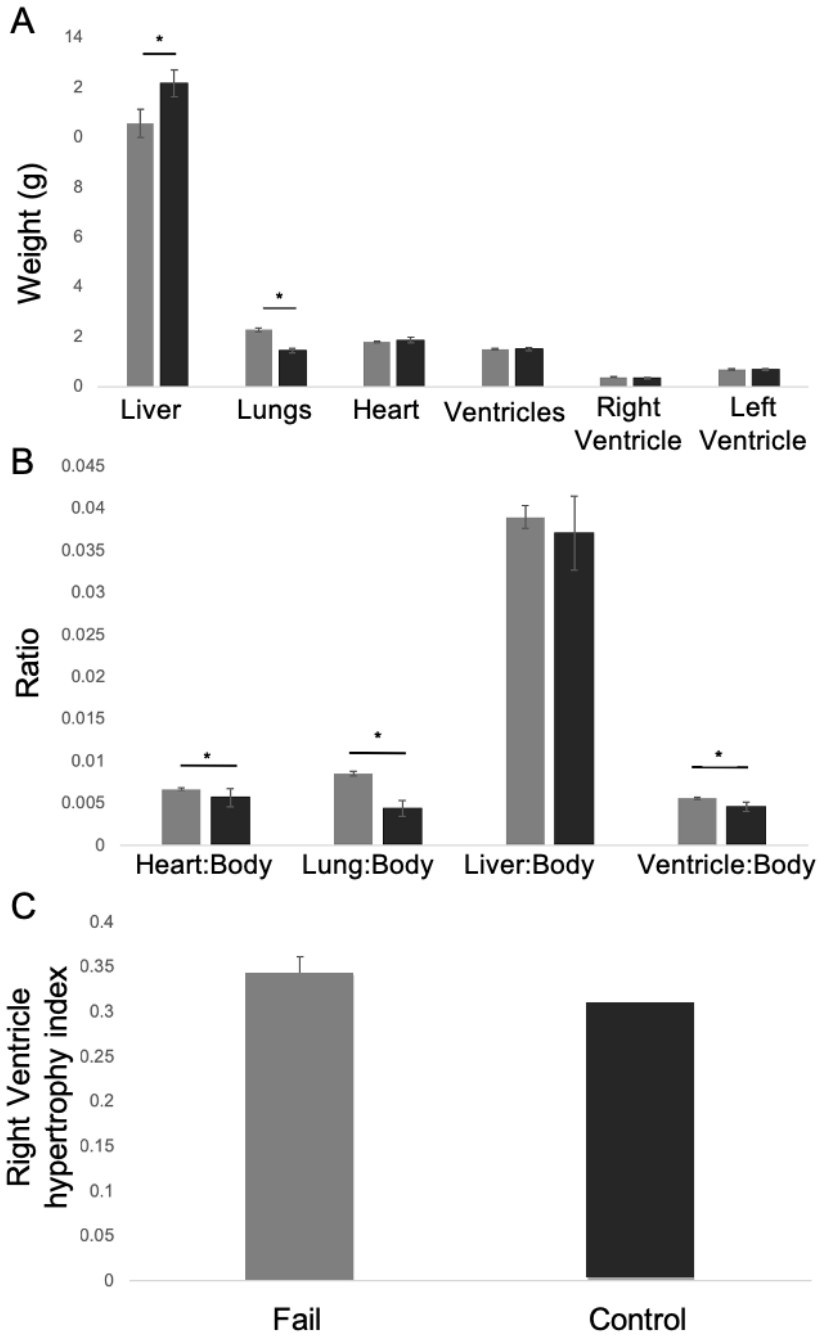

Figure 4.2: Organ weight measurements for monocrotaline-induced model of right ventricular heart failure. At the pre-established end point, the heart, liver and lungs were weighed from Adult male Wistar rats that were injected with either 60 mg/kg monocrotaline to induce right ventricular heart failure (Fail group; grey) or were saline injected as a control (Control group; black). (A) Comparison of organ and ventricular weight between Fail and Control group. (B) Comparison of organ and ventricular weight between Fail and Control group in relation to each animal's respective body weight at the pre-established end point. (C) Comparison of right ventricular hypertrophy index between Fail and Control group as an indicator of HF development. Values are mean±SEM; Fail n=13 animals; Control n=10 animals.

A marker of remodelling within the RV is the degree of hypertrophy, quantified by the RV hypertrophy index (Figure 4.2). This value is calculated from the RV weight divided by the weight of the LV and septum. The Fail group had a greater RV hypertrophy index compared to the Control group; however, this difference was not significant (t-test; *p=0.37*). The degree of hypertrophy within the ventricles was reflected by a significant increase in ventricular weight to body weight ratio within the Fail animals (Control 0.0046; Fail 0.0056 (t-test; $p=2.64x10^{-4}$).

4.3.2 Calcium spark analysis in right ventricular heart failure

Spontaneous Ca^{2+} spark activity was visualised within the near-surface 100 nm depth of TIRF microscopy (Figure 4.3). There was a significant increase in a Ca^{2+} spark's FWHM in RV cardiomyocytes from Fail animals (Fail-RV) compared to RV cardiomyocytes from Control animals (Control-RV) (Control-RV 2.85±0.03 μm; Fail-RV 2.94±0.03 μm (t-test; *p=0.02*)). However, this was accompanied by a shift in r^2 value for Gaussian fit.

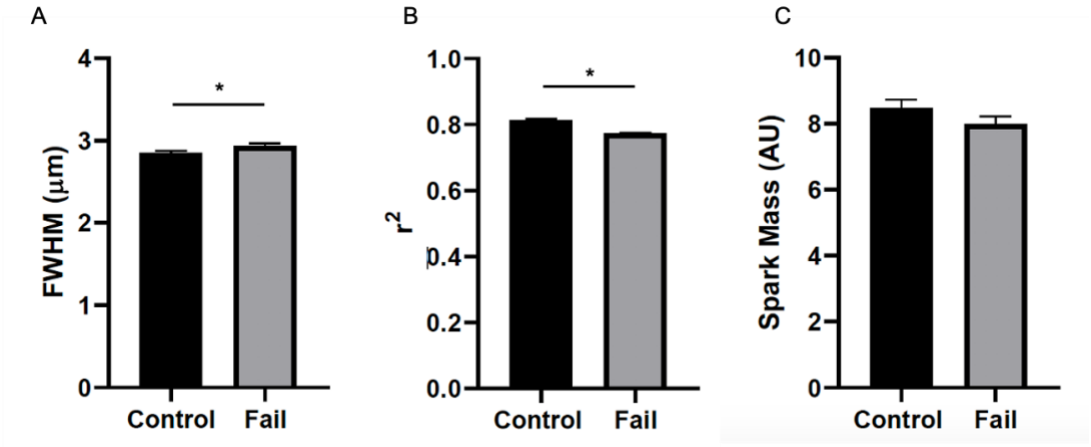

Figure 4.3: Calcium spark activity in right ventricular heart failure. Observation of Ca^{2+} spark activity within right ventricular cardiomyocytes using TIRF microscopy. Cells were isolated from Adult male Wistar rats injected with 60 mg/kg monocrotaline to induce right ventricular heart failure (Fail), or a saline matched Control. (A) There was a significantly wider spatial footprint of a Ca^{2+} spark in Fail animals, as evidenced by FWHM measurements. (B) This was complemented by a significant reduction in a Ca^{2+} sparks r^2 value within Fail animals. (C) No significant difference was recorded in spark mass between Control and Fail animals, but a decreased trend was observed upon the development of right ventricular heart failure. Values are mean±SEM; Fail n=9 animals, n= 2311 Ca^{2+} sparks; Control n=6 animals, n= 1675 Ca^{2+} sparks.

In regard to Ca^{2+} spark morphology, r^2 is a coefficient which determines how aligned a Ca^{2+} spark is to a gaussian profile. Ca^{2+} sparks recorded from the

Fail animals deviated to a greater extent from a gaussian profile, compared to Control animals. This was quantified by a significant reduction in the average r^2 value in Fail-RV compared to Control-RV Ca^{2+} sparks (Control-RV 0.81±0.00; Fail-RV 0.77±0.00 (t-test; $p=9.37x10^{-22}$)). Of note, there was no significant difference in spark mass between Control-RV and Fail-RV (t-test; $p=0.17$). However, there was a 5.6% decrease in spark mass within Fail-RV Ca^{2+} spark profiles compared to the average 8.47±0.26 AU spark mass of Control-RV cardiomyocytes, representing a decreased trend in RV HF.

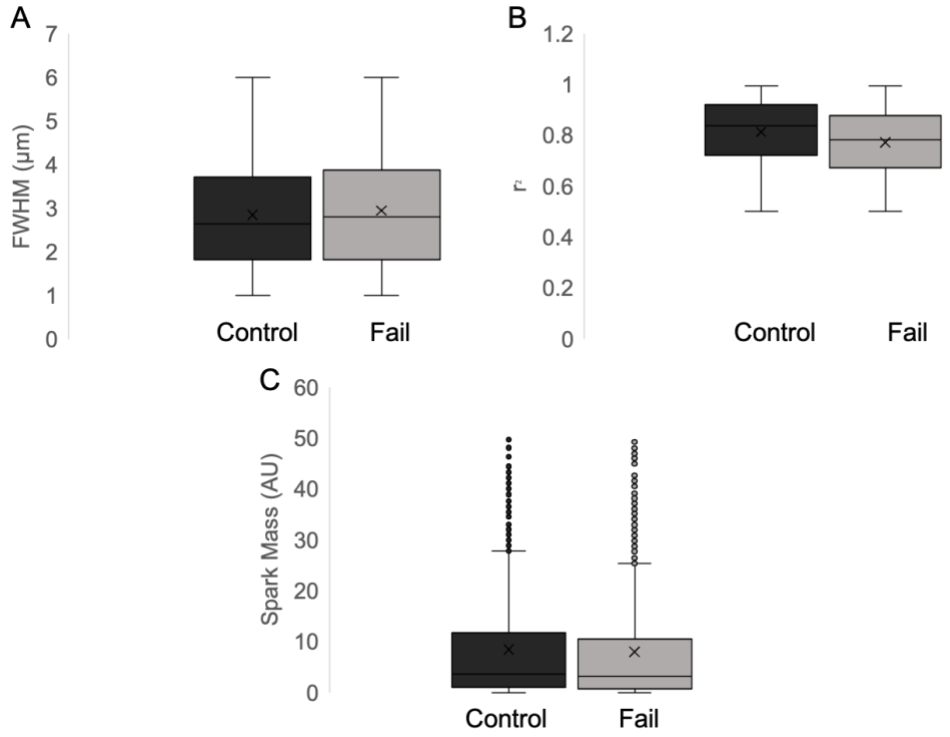

Figure 4.4: Calcium spark activity in right ventricular heart failure. Observation of Ca^{2+} spark activity within right ventricular cardiomyocytes using TIRF microscopy. Cells were isolated from Adult male Wistar rats injected with 60 mg/kg monocrotaline to induce right ventricular heart failure (Fail), or a saline matched Control. Reported Ca spark morphology for the Control and Fail groups in regard to (A) FWHM (B) r^2 and (C) spark mass. Values are median; Fail n=9 animals, n= 2311 Ca^{2+} sparks; Control n=6 animals, n= 1675 Ca^{2+} sparks.

Data was grouped together to account for the heterogeneity that exists within Ca^{2+} spark signalling. The range of Ca^{2+} spark parameters was similar between the Control-RV and Fail-RV groups. Specifically, the range in FWHM (Control 5.0 μm; Fail 5.0 μm), r^2 (Control 0.5; Fail; 0.5) and spark mass (Control 49.68 AU; Fail 49.89 AU) are depicted in Figure 4.4. The increased mean FWHM in Fail animals is reflected in a 0.18 μm greater

median FWHM of 2.81 μm, alongside a decreased median r^2 (Control 0.84; Fail 0.78). The decreased trend in spark mass was also represented within the median value, with Ca^{2+} sparks within Control animals exhibiting a 0.56 AU greater spark mass than the 3.12 AU reported within the Fail group. Combined, this suggests that the significant variations across the mean data are not due to outliers or anomalies within the dataset that may have arisen from combining Ca^{2+} spark data from multiple animals.

4.3.3 Remodelling of the RyR2 and JPH2 ultrastructure within right ventricular heart failure

The cluster pattern of RyR2 and JPH2 within RV cardiomyocytes was analysed from Control and Fail animals (Figure 4.5). Following the puncta threshold detection method and application of a binary mask as outlined previously, a cluster boundary was applied and number of RyR2 and JPH2 per puncta calculated. Data for RyR2 and JPH2 cluster morphology was obtained from the same RV cardiomyocytes, using DNA-PAINT with a localisation accuracy of 12 nm. Cluster areas defined in the puncta threshold process as containing <1 RyR2 or JPH2 were removed from the analysis. Their removal was considered to account for spurious structures which may reflect autofluorescence or weak DNA-PAINT events.

Within each cluster, RyR2 and JPH2 density was quantified (Figure 4.5A), referred to as ‘count’. The significant decrease in RyR2 cluster area upon RV HF was validated by a nearly two-fold reduction in RyR2 count (Control-RV 5.85±0.51 puncta; Fail-RV 3.27±0.22 puncta (one-way ANOVA; *p=0.00*)). There was no significant change in JPH2 count per cluster in Fail-RV compared to Control-RV (one-way ANOVA; *p=0.46*), but a decreased trend was visible. The mean 7.91±0.67 μm^2 area of an RyR2 cluster within Fail-RV was approximately half the size of RV cardiomyocytes in Control-RV, with a significant reduction in RyR2 cluster size within RV HF (one-way ANOVA; *p=0.00*). Of note, RyR2 cluster area within Fail-RV was also significantly smaller than JPH2 cluster size within Fail and Control RV cardiomyocytes (one-way ANOVA; *p=0.02 and p=0.00 respectively*). There was no significant change in JPH2 cluster size between Fail and Control

animals (one-way ANOVA; *p=0.57*), despite an 8.11 μm^2 reduction in mean JPH2 cluster area within Fail-RV compared to Control-RV.

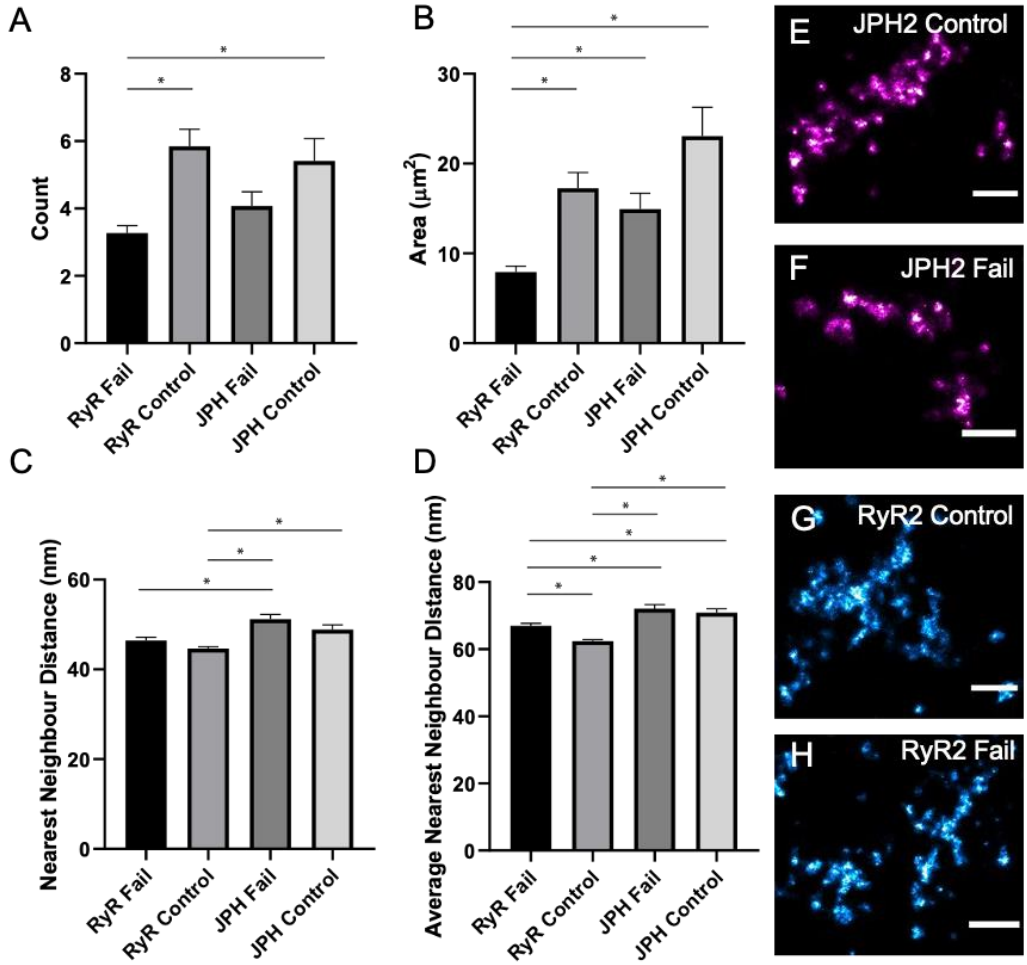

Figure 4.5: Structural remodelling of calcium handling proteins within right ventricular heart failure. Quantitative analysis of peripheral RyR2 and JPH2 cluster pattern within right ventricular cardiomyocytes using DNA-PAINT microscopy. Cells were isolated from adult male Wistar rats injected with 60 mg/kg monocrotaline to induce right ventricular heart failure (Fail), or a saline matched control. Puncta detection analysis was undertaken upon rendered DNA-PAINT data. (A) The protein density per cluster was calculated, with Control animals having a greater cluster density compared to Fail. (B) For each cluster identified, the area was calculated, accounting for any holes or gaps within the structure. Control animals had a greater cluster area than their Fail counterparts for both JPH2 and RyR2. (C) The distance between one punctum and its nearest neighbour was calculated. No significant change between the RyR2 in Control and Fail animals was recorded, similar to JPH2. (D) The average nearest neighbour distance between one punctum and its three nearest neighbours revealed a significantly decreased distance between all variables and the RyR2 Control group. (E-H) Cluster pattern for JPH2 Control, JPH2 Fail, RyR2 Control and RyR2 Fail groups respectively. Values are mean±SEM; Fail n=3 animals, n=285 clusters; Control n=3 animals, n=263 clusters. Scale bars, E-H: 200 nm.

The NND or 3NND was analysed (Figure 4.5C and 4.5D). When comparing RyR2 NND, there was an increased distance between RyR2 in Fail-RV compared to Control-RV (one-way ANOVA; *p=0.12*), however this was not significant until average NND was analysed (one-way ANOVA; *p=0.00*), suggesting fragmentation in RyR2 within HF to be heterogeneous and widespread across the JMC (Control-RV 62.43±0.42 nm; Fail-RV 66.97±0.76 nm average NND). There was no significant change in JPH2 NND (one-way ANOVA; *p=0.28*) or average NND (one-way ANOVA; *p=0.82*) upon the development of RV HF. However, the spatial distribution of RyR2 and JPH2 is suggested to be different. For example, the 44.65±0.40 nm RyR2 NND within Control-RV is significantly less than that of JPH2 in RV Fail (one-way ANOVA; *p=0.00*) or Control-RV (one-way ANOVA; *p=0.00*), with a similar trend quantified in average NND (one-way ANOVA; *p=0.00 and p=0.00 respectively*). This suggests that RyR2 in Control-RV have a denser cluster morphology than JPH2. When RyR2 becomes fragmented within RV HF, to reflect the JPH2 cluster pattern, there is still a significantly reduced average NND present between Fail-RV RyR2 66.97±0.76 nm spaced puncta and JPH2's cluster pattern within Control and Fail RV cardiomyocytes (one-way ANOVA; *p=0.01 and p=0.00 respectively*).

4.3.4 Dual colour imaging of RyR2 and JPH2

Two-colour image acquisition with Exchange-PAINT enabled the co-localisation of two Ca^{2+} handling proteins to be studied, namely RyR2 and JPH2 at the JMC. Within Control-RV and Fail-RV, both groups had a significantly greater proportion of their JPH2 stain that co-localised with the RyR2 puncta (Control-RV 0.73±0.03; Fail-RV 0.70±0.04 (t-test; *p=0.02*)) compared to the fraction of RyR2 stain that co-localised with JPH2 (Control-RV 0.50±0.07; Fail 0.54±0.02 (t-test; *p=0.02*)). This is suggestive of JPH2's role as a regulator of RyR2 (Figure 4.6). Specifically, in Fail-RV, the fraction of JPH2 that co-localised with an RyR2 protein was 3.5% lower than in Control-RV; however, this decrease was not significant (t-test; *p=0.63*). There was a greater 7.05% decrease between Control-RV and Fail-RV recorded in regard to the proportion of RyR2 stain which overlaid JPH2's, but again this change was not significant (t-test; *p=0.63*). One experimental

limitation is the low number of two-colour datasets acquired to analyse the remodelling of JPH2 in relation to RyR2. Heterogeneity across the cell should be considered therefore as single channel analysis of JPH2 and RyR2 suggests that a greater degree of structural remodelling occurs for the RyR Ca^{2+} protein compared to the JPH2 anchor.

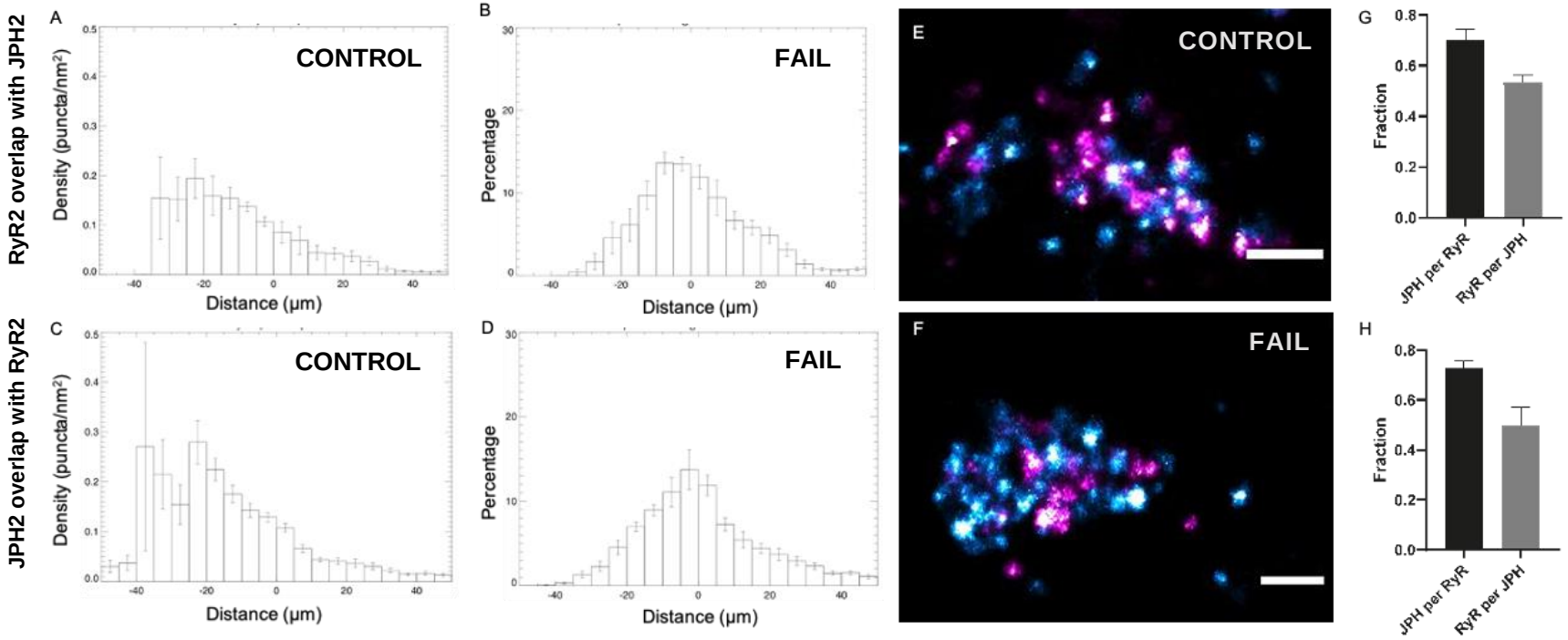

Figure 4.6: Two-colour localisation of RyR2 and JPH2 within right ventricular heart failure. Quantitative analysis of peripheral RyR2 and JPH2 cluster pattern within right ventricular cardiomyocytes using DNA-PAINT microscopy. Cells were isolated from Adult male Wistar rats injected with 60 mg/kg monocrotaline to induce right ventricular heart failure (Fail), or a saline matched control. Puncta detection analysis was undertaken upon rendered DNA-PAINT data. Comparison of (A) Control animals and (C) Fail animals regarding the density by which RyR2 and JPH2 stain overlap. There is minimal change in the percentage of co-localisation for the RyR2 and JPH2 staining pattern between (B) Control and (D) Fail animals. DNA-PAINT acquisition using multiple imager strands was utilised to visualise the structural pattern of the RyR2 (blue) and JPH2 (purple) proteins within (E) Control and (F) Fail animals. The fraction by which JPH2 overlapped with RyR2 and RyR2 was associated with JPH2 was analysed within the (G) Control and (F) Fail animals, with no significant remodelling in protein pattern detected. Values are mean±SEM; Fail n=8 cells; Control n=9 cells. Scale bars, A-E: 200 nm.

4.3.5 Application of the correlative imaging protocol

The spontaneous Ca^{2+} profiles from RV cardiomyocytes from Fail and Control animals were analysed, looking specifically at spark mass, as calculated by *xySpark* (Steele and Steele, 2014). The co-ordinates of each Ca^{2+} spark were evaluated in relation to the underlying RyR2 puncta, visualised using DNA-PAINT. The method of overlay of the Ca^{2+} spark TIRF and RyR2 DNA-PAINT datasets within the correlative imaging protocol has been previously outlined (Section 3.3.6). The footprint of a Ca^{2+} spark is a function of its FWHM. There was no significant change between the mean RyR2 density underneath a Ca^{2+} spark's FWHM spatial footprint in Fail and Control RV cardiomyocytes, with only a 11.5% increase in RyR2 density recorded within Fail-RV compared to Control-RV (Control-RV 33.51±1.40 puncta; Fail-RV 37.36±2.03 puncta (t-test; *p=0.12*)). However, the spark mass (as defined in Section 3.3.6) within Control-RV was 60.43% greater than within Fail-RV (t-test; *p=0.01*).

In the scattergrams of the spark mass plotted against the number of RyR2 underneath each individual spark, we observe a dense points cloud in the spark mass range of 0-10 (AU). This is noticeable in the grey region shown with the point density colour coding. Between Control-RV and Fail-RV (Figure 4.7A&B) we observe very little, if not any, shift in the central portion of this dense points cloud. However, we do observe a rightward shift in the points coloured purple or black in Fail-RV, suggesting that a subset of the larger sparks (spark mass > 10 AU) are more likely to involve a greater number of local RyRs, despite the fact that the spark mass, on average, tends to be depressed (Figure 4.7D). This is reflected by the greater range in RyR2 count within the Fail-RV cells (Figure 4.7C).

There are a number of explanations for this rightward shift. It is likely that Ca^{2+} sparks within the MCT model of RV HF tend to occur preferentially in regions that have a greater number of RyR2. As shown in previous simulations (Sheard et al., 2019), it is likely that a reduced efficiency in RyR2 coupling may implicitly self-select cellular regions which have a higher RyR2 density for the generation of Ca^{2+} spark activity. It is also possible that Ca^{2+}

sparks within these self-selected regions propagate slower, a phenomenon which could be missed by the slow time-sampling that these experiments required to minimise the signal-to-noise ratio.

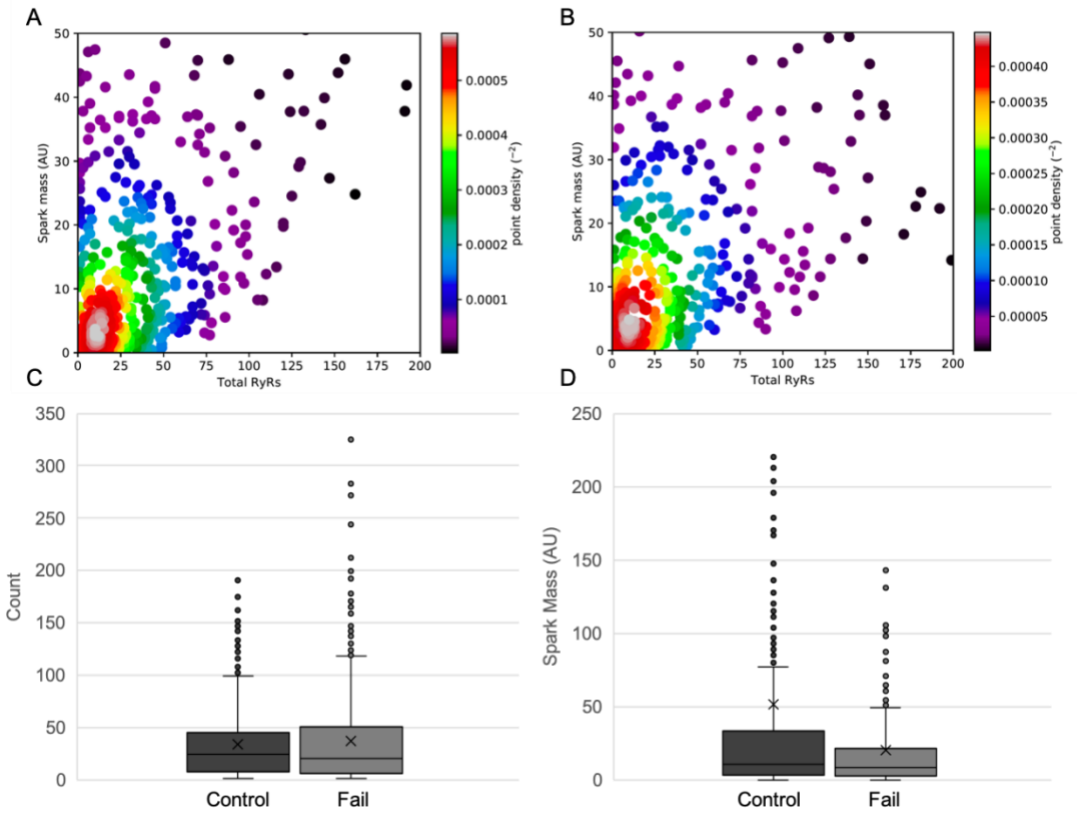

Figure 4.7: Relationship between RyR2 count and calcium spark mass in right ventricular heart failure. Correlative imaging protocol applied to ventricular cardiomyocytes from Adult male Wistar rats injected with 60 mg/kg monocrotaline to induce right ventricular heart failure (Fail), or a saline matched control. Quantitative analysis of RyR2 density underneath a Ca^{2+} spark's spatial footprint according to FWHM was evaluated in regard to that Ca^{2+} spark's mass. Point density scattergram was utilised to represent the shape of the data cloud, with red denoting the greatest density of unitary Ca^{2+} spark events. (A) Spread of point density in Control animals suggested the formation of larger Ca^{2+} sparks in the presence of more RyR2 channels. (B) Within right ventricular heart failure, this projection of point density had a greater fragmentation. (C) Box and whisker plot of RyR2 density revealed a greater variation in RyR2 count underneath a recorded Ca^{2+} spark within the Fail animals. (D) However, the variation within the Ca^{2+} spark profile recorded within the Fail animals was reduced compared to Control. Values are mean±SEM; Fail n=8 cells; Control n=5 cells.

It should be noted that evaluation of RyR2 count underneath a Ca^{2+} sparks footprint is unable to analyse the orientation of each puncta in regard to the pattern by which they cluster. The same spark mass was plotted in a point-density-encoded scattergram in relation to the nearest neighbour distance between each RyR2 puncta underneath a Ca^{2+} spark's spatial footprint. NND, in this analysis, represented a measure of the closeness of the spatial

coupling between the clustered RyRs in locality of a given Ca^{2+} spark. The most striking observation in this analysis is the rightward shift in the densest regions of the points cloud (coloured in dark blue) between Control-RV to Fail-RV.

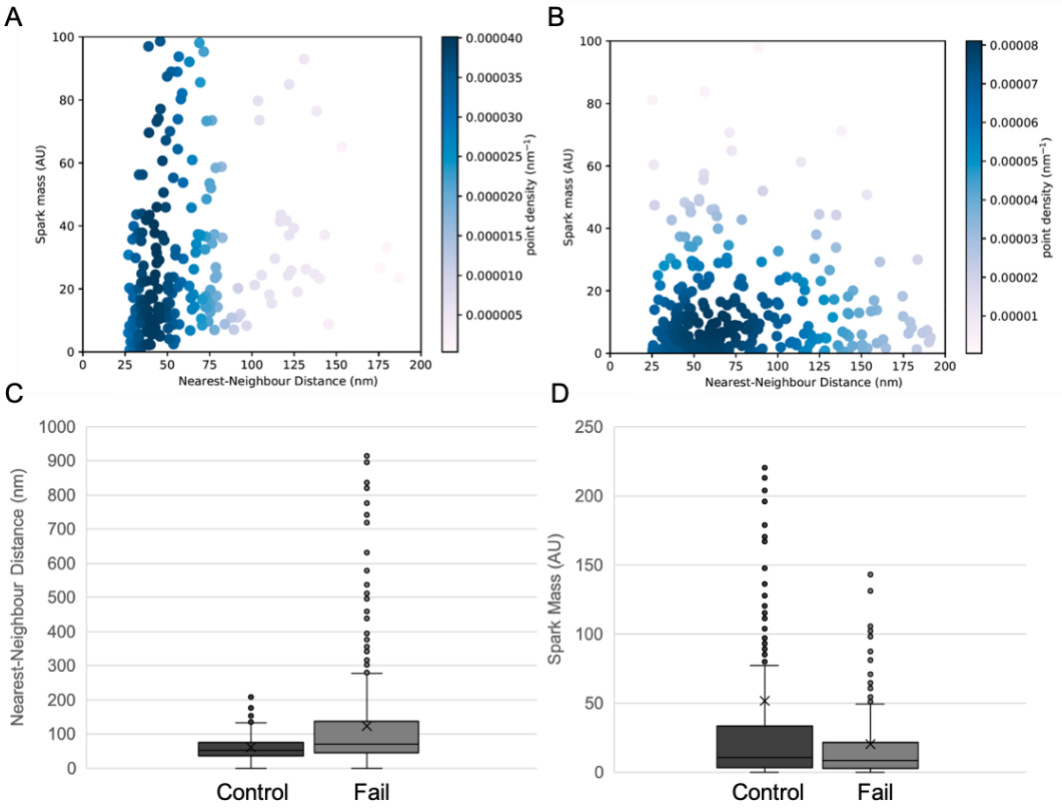

Figure 4.8: Relationship between RyR2 nearest neighbour distance and calcium spark mass in right ventricular heart failure. Correlative imaging protocol applied to ventricular cardiomyocytes from Adult male Wistar rats injected with 60 mg/kg monocrotaline to induce right ventricular heart failure (Fail; grey), or a saline matched control (Control; black). Quantitative analysis of RyR2 nearest neighbour distance underneath a Ca^{2+} spark's spatial footprint was aligned with the respective mass of each Ca^{2+} spark. Point density scattergram was utilised to represent the shape of the data cloud, with dark blue denoting the greatest density of unitary Ca^{2+} spark events. (A) Analysis within Control animals suggests the majority of Ca^{2+} sparks originating from regions where RyR2 has a small nearest neighbour distance. (B) Within Fail animals, there was a greater range in nearest neighbour distance in relation to spark mass. (C) A box and whisker plot visualised an increased range in nearest neighbour distance within Fail animals. (D) This was accompanied by a decreased range in spark mass. Values are mean±SEM; Fail n=8 cells; Control n=5 cells.

When the distribution of the NND alone was analysed, fragmentation of the RyR2 location across a cell was apparent within RV HF, with a significant decrease in spark mass (t-test; *p=0.01*) within Fail-RV being accompanied by a significant 50.29% increase in NND to 123.31±7.18 nm (t-test;

p=1.19x10^{-15}) (Figure 4.8). Point density scattergrams allow spark mass to be evaluated in relation to NND on a spark-by-spark basis. Control-RV exhibited a high density of Ca^{2+} sparks, regardless of size, being generated from regions where NND was 25-50 nm. This suggests that Ca^{2+} sparks within Control-RV had a greater propensity within regions of a cell that had RyR2 puncta closely located. This is unlike Fail-RV, where the point density cloud was broader and depressed, with Ca^{2+} sparks originating from regions where NND was 25-100 nm. This depressed point density cloud reflects the reduced spark mass within Fail-RV and indicates an increased fragmentation within the RyR2 pattern and a disorganisation at the level of the CRU.

The 60.43% decrease in spark mass within Fail-RV was not accompanied by a significant change in average NND (Control-RV 125.60±4.15 nm; Fail-RV 123.31±7.18 nm (t-test; *p=0.78*)). However, there was a greater range of average NND distances between RyR2 puncta within the Fail-RV, suggesting a greater level of heterogeneity within the RyR2 pattern. Specifically, the range in average NND underneath a Ca^{2+} spark's spatial footprint was 310.32 nm in Control-RV compared to the greater 888.21 nm range in Fail-RV (Figure 4.9C). In the point-density-encoded scatter plots of the spark mass against the average of the neighbour distances (a measure of the spacings of the local ensemble of RyRs; Figure 4.9A&B), a clear rightward shift in the densest region of the points cloud (yellow) was observed in Fail-RV compared to Control-RV. In particular within Control-RV, the majority of Ca^{2+} sparks, across a range of sizes in regard to their mass, were recorded from regions which had an average NND of less than 100 nm. This suggests that Ca^{2+} sparks, regardless of size, were generated from cellular regions that had a tightly packed RyR2 array. However, similar to the NND patterning, within Fail-RV the point density cloud was broader and depressed with the majority of Ca^{2+} sparks originating from regions where average NND was 50-200 nm. Taken together Figure 4.8A&B and Figure 4.9A&B suggest that Ca^{2+} sparks observed in Fail-RV cells coincide with regions with looser RyR spacings. It is likely that this observation represents the general fragmentation of the RyR2 patterning observed previously in

Fail-RV (Sheard et al., 2019). Furthermore, the depressed point density cloud is reflective of the reduced mean spark mass recorded overall within Fail-RV.

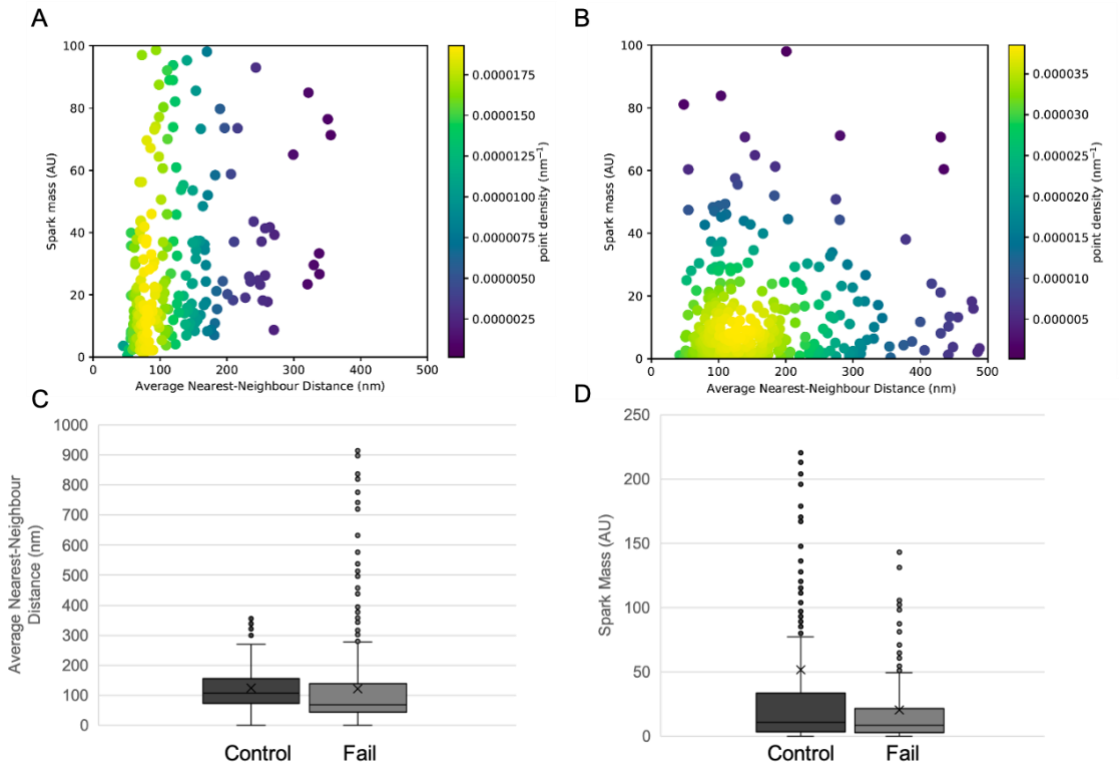

Figure 4.9: Relationship between RyR2 average nearest neighbour distance and calcium spark mass in right ventricular heart failure. Correlative imaging protocol applied to ventricular cardiomyocytes from Adult male Wistar rats injected with 60 mg/kg monocrotaline to induce right ventricular heart failure (Fail; grey), or a saline matched control (Control; black). Quantitative analysis of RyR2 average nearest neighbour distance underneath a Ca^{2+} spark's spatial footprint was aligned with the respective mass of each Ca^{2+} spark. Point density scattergram was utilised to represent the shape of the data cloud, with yellow denoting the greatest density of unitary Ca^{2+} spark events. (A) Analysis within Control animals suggests the majority of Ca^{2+} sparks originating from regions where RyR2 has a small average nearest neighbour distance. (B) There was a rightward shift and flattened relationship between spark mass and RyR2 average nearest neighbour distance in Fail animals. (C) A box and whisker plot visualised a decreased average nearest neighbour distance within Fail animals. (D) This was accompanied by a decreased range in spark mass. Values are mean±SEM; Fail n=8 cells; Control n=5 cells.

4.3.6 Transverse tubule organisation

The T-tubule structure was visualised using confocal microscopy (Figure 4.10). The average branch length in RV cardiomyocytes from Control and Fail animals was 0.51±0.01 μm (t-test; *p=0.97*). The orientation of the T-tubule network was analysed. In RV cardiomyocytes from Control and Fail animals, the majority of T-tubules were orientated at 90° (in the transverse plane), with a second peak visible at 0° representing the longitudinal

branches. A wider peak around 90° was visible within the Fail-RV cardiomyocytes, which could suggest mild remodelling of the T-tubule network from its transverse lineage.

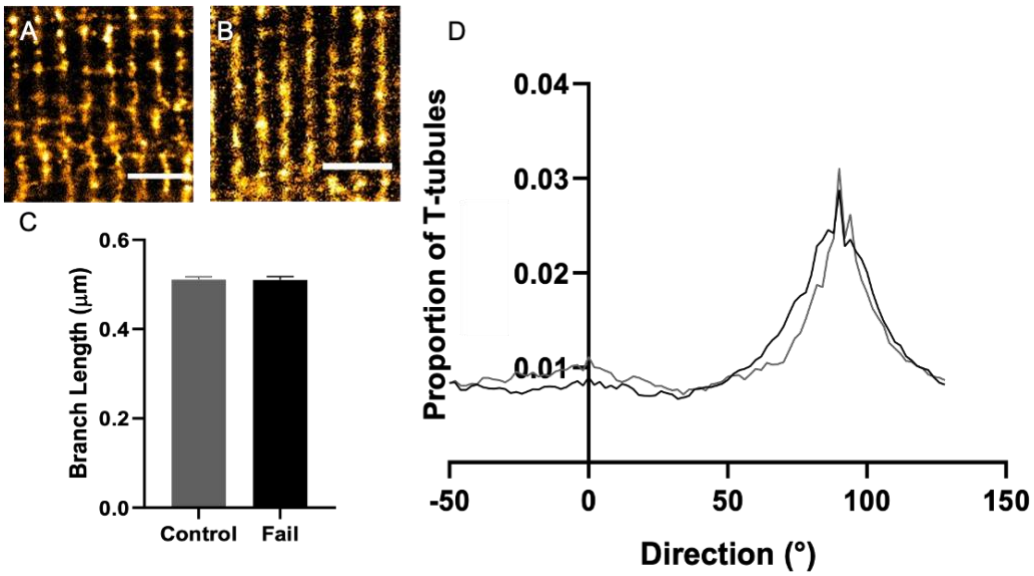

Figure 4.10: Transverse tubule organisation in right ventricular heart failure. Visualisation of the T-tubule structure within right ventricular cardiomyocytes using confocal microscopy. Immunofluorescence staining was undertaken using NCX and Cav3 as a T-tubule marker. Cells were isolated from Adult male Wistar rats injected with 60 mg/kg monocrotaline to induce right ventricular heart failure (Fail; black), or a saline matched control (Control; grey). (A) Visualisation of the T-tubule structure within a saline control. (B) Visualisation of the T-tubule structure within a model of right ventricular heart failure. (C) No significant difference in branch length was detected between the Fail and Control animals. (D) Both Fail and Control animals had a T-tubule structure with directionality orientated in the transverse plane at 90°. However, a wider peak in directionality around 90° within Fail animals suggests that a degree of remodelling within the structure is apparent. Values are mean±SEM; Fail n=3 animals; Control n=4 animals. Scale bars, A-B: 5 μm.

4.4 Discussion

Ventricular cardiomyocytes are one example of an excitable cell. Within disease, such as RV HF, the cardiomyocyte's function can alter and lead to dyssynchronous Ca^{2+} signalling. In this chapter, the established correlative imaging protocol described previously (Chapter 3) was applied to a model of RV HF. The aim was to further the field's understanding of a cell's local relationship between structure and function and how this may alter in disease.

4.4.1 Validation of model

In alignment with previous use of the model, development of hypertrophy and HF was associated with progressive weight loss. This study recorded a deviation in growth from day 10 post MCT administration compared to the saline injected controls. Cardiac cachexia is a known sign of HF (Anker and Sharma, 2002) and was recorded in other MCT induced RV HF studies (Benoist et al., 2014; Fowler et al., 2015; Fowler et al., 2018). Cachexia itself is not commonly due to reduced food intake, but instead it is a metabolic syndrome leading to reduced skeletal muscle mass (Evans et al., 2008; von Haehling et al., 2007). As evidenced within the literature, a significant increase in lung weight was detected, even when body weight was accounted for (Benoist et al., 2014; Fowler et al., 2015; Fowler et al., 2018). This increased weight was not due to pulmonary oedema but from vascular remodelling and increased pulmonary artery muscularisation from MCT administration (Albada et al., 2005; Chen et al., 2012; Schermuly et al., 2004). The decreased liver weight in Fail animals was evidenced in other reports of MCT induced RV HF (Benoist et al., 2014; Fowler et al., 2015). No significant change was noted when body weight was accounted for, indicating that other markers are more critical at marking disease progression (Michael et al., 2007; Xiao et al., 2017). This suggestion is validated by Leach et al. (1975) who discourage the use of liver weight as a marker for disease.

Crucially, RV hypertrophy was evidenced from a significant increase in ventricular weight to body weight ratio within Fail animals. Hypertrophy is known to increase a cell's length, width and volume (Korecky and Rakusan, 1978) which can increase heart weight as measured within the study. This increase aligns with previous data published using the model (Benoist et al., 2014; Fowler et al., 2015; Fowler et al., 2018). Furthermore, the increased trend in RV hypertrophy index reflects that of Schermuly et al. (2004) and is suggestive of no change in LV structure with RV structural remodelling alone (Benoist et al., 2014). Together, these results validate success of the MCT model of RV HF within this study.

4.4.2 Calcium spark analysis with TIRF microscopy

In HF there is a known Ca^{2+} desynchrony at the level of the Ca^{2+} spark. The culmination of Ca^{2+} spark activity can alter the waveform of a Ca^{2+} transient which demonstrates how critical understanding local Ca^{2+} spark activity is when evaluating whole heart function. The frequency of Ca^{2+} transients is known to increase in HF (Louch et al., 2006). One suggestion for this functional change in MCT RV HF is an increased SR Ca^{2+} load due to AP prolongation (Benoist et al., 2012). Overload of the SR with Ca^{2+} can increase the SR Ca^{2+} leak, evidenced by an increase Ca^{2+} spark frequency (Benoist et al., 2012; Fowler et al., 2018). Unlike Benoist et al. (2012) no increase in Ca^{2+} spark mass in Fail animals was found within quiescent cells. This discrepancy could be due to additional mechanisms contributing to SR Ca^{2+} leak aside from Ca^{2+} sparks (Wang et al., 2014). Additional elements of Ca^{2+} signalling therefore require investigation, with RyR2 being critical for SR Ca^{2+} release independent of depolarisation.

Ca^{2+} sensitivity is known to undergo a leftward shift within MCT induced RV HF (Kögler et al., 2003). To understand the degree of RyR2 sensitivity to Ca^{2+}, this study would have benefited from an evaluation of SR Ca^{2+} load within Fail and Control animals. RyR2 open probability was modelled by Fowler et al. (2018) and shown to increase as a result of MCT induced RV HF. The addition of 10 mg/kg/day metoprolol (β_1 receptor inhibitor) to the MCT-induced RV HF model slowed the onset of HF and reduced the increase in RyR2 open probability (Fowler et al., 2018). As a result, in the presence of metoprolol the likelihood of Ca^{2+} spark generation was reduced due to an open probability of 60% compared to the 130% denoted in RV HF in relation to control. The decreased r^2 value in Fail animals reflects a greater degree of deviation in a Ca^{2+} spark's morphology from a true gaussian fit. This finding aligns with the conclusion of Fowler et al. (2018) that the heterogeneity of Ca^{2+} signalling is greater within HF (Fowler et al., 2018).

4.4.3 Role of additional calcium handling proteins in right ventricular heart failure

Alongside changes in RyR2 sensitivity, MCT-induced RV HF is also considered to have an increased NCX current and reduced SERCA activity, elements which will be explored later (Armoundas et al., 2007; Fowler et al., 2018). In regard to Ca^{2+} release from the SR, the IP3R Ca^{2+} channel should also be considered despite its 50-fold lower density than RyR2 (Moschella and Marks, 1993; Perez et al., 1997). Within this study of RV HF the IP3R channel was not investigated. However, the IP3R type 2 isoform is located within the SR membrane of ventricular cardiomyocytes (Foskett et al., 2007; Lipp et al., 2000). Pertinent to the investigation of Ca^{2+} signalling in HF, hypertrophy of cardiomyocytes is thought to lead to an increase in IP3R expression at the JMC (Drawnel et al., 2012; Harzheim et al., 2009). When expressed, the IP3R channel is considered to co-localise with RyR2 to sensitise its neighbouring Ca^{2+} release channel and enhance spontaneous Ca^{2+} release within diastole, contributing towards Ca^{2+} desynchrony (Harzheim et al., 2009). In HF, the IP3R is considered to be independent of CICR, with inhibition of RyR2 having no effect upon its function. Instead, the IP3R is mainly regulated by Ca^{2+} and can sensitise other Ca^{2+} signalling pathways such as the NCX pump to induce depolarisation (Roderick and Knollmann., 2013; Signore et al., 2013). In future studies it would be valuable to investigate the IP3R in more depth in relation to HF.

Future studies would benefit from applying the defined correlative imaging protocol to investigating Ca^{2+} re-uptake pump SERCA2a. A 94% decrease in SERCA2a density has been uncovered in the RV following MCT induced HF (Fowler et al., 2018; Umar et al., 2012). This decreased density has been reported in other models of HF (Kögler et al., 2003; Lyon et al., 2012) and is supported by a simultaneous decrease in PLB expression and increase in NCX activity to maintain Ca^{2+} signalling (Armoundas et al., 2007; Kögler et al., 2003). However, care needs to be taken when evaluating protein changes based upon expression, as they may negate the local changes in regard to JMC remodelling. It would be of interest to study the remodelling of the JMC in 3D. This avenue of research would enable the structure of Ca^{2+}

handling proteins to be studied in greater depth to determine their open and closed state (Peng et al., 2016), but would also provide an opportunity to look more widely at Ca^{2+} diffusion across a cell (Pinali et al., 2013).

4.4.4 Cluster fragmentation of calcium handling proteins

The development of MCT induced RV HF led to a reduction in RyR2 and JPH2 cluster size. This decrease was evidenced to a greater extent within RyR2, suggesting that remodelling of the Ca^{2+} release channel was more notable than that of the membrane tether. The reduction in RyR2 cluster size within HF was also observed by Crossman et al. (2011). Furthermore, the development of RV HF did not coincide with any change in the spatial pattern of JPH2, unlike RyR2 where Fail animals had a more fragmented pattern as evidenced in its average NND measurements. The fragmented pattern of RyR2 was evidenced by the Ca^{2+} release channel having a lower fraction of its staining pattern which overlays with JPH2. This finding was reflected in previous studies, with a ratio of 1.38 JPH2 per RyR2 channel suggested across the cardiomyocyte (Munro et al., 2016; Jayasinghe et al., 2018a). The placement of JPH2 in relation to RyR2 is not considered random. Neither is JPH2 believed to be tightly coupled to RyR2 by the nature that co-localisation is not 100% but is instead heterogenous across the cell (Jayasinghe et al., 2018a). Not all literature reflects this trend. Due to the microscopy technique used and method of analysis, some literature reflects a similar association between JPH2 and RyR2. The importance of this is displayed when a 30 nm degree of error defined within dSTORM microscopy (Baddeley et al., 2009b) is applied to cluster analysis which greatly increases the overlay percentage (Hou et al., 2015; Jayasinghe et al., 2012). This study, through the use of DNA-PAINT, accounts for the gaps and non-uniform cluster pattern within each stain without this degree of error and aligns with previous DNA-PAINT analysis (Jayasinghe et al., 2018a).

4.4.5 Modulatory role of junctophilin in right ventricular heart failure

The modulatory role of JPH2 upon RyR2 is perhaps best described by van Oort et al. (2011) in their JPH2 knock out mouse model. Loss of the membrane tether disrupted the JMC to an extent whereby current of the

voltage gated Ca^{2+} channel was unchanged, but the Ca^{2+} current was not able to elicit CICR due to an uncoupling of the RyR2 channels. Despite a decrease in SR Ca^{2+} load, RyR2 channels had an increased activation within diastole, contributing towards spontaneous Ca^{2+} leak in the form of Ca^{2+} sparks. This finding suggests a role of JPH2 in modulating RyR2 open probability, with a loss of JPH2 contributing towards dyssynchronous Ca^{2+} function. Within this study, despite a decreased trend in the association between JPH2 and RyR2 upon RV HF, there was no significant change in co-localisation. Therefore, care should be taken when comparing JPH2 knock out models to this study. However, RyR2 and JPH2 cluster size decreased upon the development of RV HF, with both proteins known to co-immunoprecipitate (van Oort et al., 2011). This suggests that HF can affect channel interaction to an extent.

A JPH2 knock down model was developed by Beavers et al. (2013). They noted a decreased association between JPH2 and RyR2, as visualised within this study through Exchange-PAINT. This decreased interaction led to an increase in RyR2's open probability and a resultant increase in Ca^{2+} spark frequency that was partially restored by a JPH-mimicking oligopeptide. A similar response was recorded by Wang et al. (2014) when they decreased JPH2 expression. Furthermore, the resultant increased RyR2 open probability led to an enhanced NCX outward current which increased Ca^{2+} spark frequency and FWHM, the latter significantly altered upon RV HF within this study. The correlative imaging protocol did not visualise JPH2 in regard to Ca^{2+} spark activity, but a hypothesis could be presented in relation to JPH2's modulatory role within HF. The modulatory role of JPH2 within Ca^{2+} signalling is supported by the decreased trend in JPH2 and RyR2 interaction within Fail animals in accordance with known changes in Ca^{2+} spark morphology. There was no significant change in RyR2 density underneath the Ca^{2+} spark footprints recorded from Fail and Control animals. However, changes in Ca^{2+} spark morphology could be arising from JPH2-driven modulation of RyR2 instead of a structural remodelling of the Ca^{2+} release channel itself. This suggestion is validated by Munro et al. (2016) who visualised no change in RyR2 cluster size within their JPH2

knock down study but noted a change in Ca^{2+} signalling. Further research is required to expand upon this hypothesis and understand the functional implications of JPH2 and RyR2's interaction at a local level in regard to Ca^{2+} spark generation.

4.4.6 Remodelling of the ryanodine receptor cluster organisation in right ventricular heart failure

Crucially, within the wider DNA-PAINT analysis a reduction in RyR2 cluster size was denoted in Fail animals, similar to Munro et al. (2016). This suggests that multiple factors in addition to JPH2 are underlying the structural remodelling of the JMC within HF. The whole dyadic structure should therefore be studied in regard to maintaining Ca^{2+} homeostasis (Guo et al., 2014; Munro et al., 2016). When drawing conclusions from the application of the correlative imaging protocol, it should be stated that cluster size was not analysed, a feature made apparent when observing total RyR density underneath a Ca^{2+} sparks spatial footprint. The mismatch between the change in spark mass compared to the relative change in RyR2 density upon the onset of RV HF does not support the hypothesis that the RyR2 density underneath a Ca^{2+} spark footprint is a major determinant for a Ca^{2+} sparks size in relation to its mass (Figure 4.7A&B). This warrants further analysis of RyR2 organisation at the level of the JMC. From looking at RyR2 count alone, it is likely that the contribution from the number of RyR2 present to the spark mass evoked is minor, or dependent on other factors such as luminal Ca^{2+} concentration and other regulators of the RyR2 channels that may undergo compensatory change in expression or function.

An alternative analysis to quantify the presence of heterogenous remodelling of RyR2 underneath each Ca^{2+} spark was the measure of NND and average NND. In RV HF, a rightward shift in point density cloud of NND and average NND variables in regard to spark mass was notable. This is suggestive of the functional implications that a reduced RyR2 cluster size and fragmentation of the Ca^{2+} handling protein pattern may have upon the cell in regard to Ca^{2+} spark mass generated. This increased NND and average NND within Fail-RV compared to Control-RV was also identified within

previous widespread DNA-PAINT studies separate to the correlative imaging method. Specifically, this shift in NND within the failing animals was notable by a change in its relationship with spark mass. The relationship between spark mass and NND visible within Control-RV was dampened within the heart failure model. This represents the impact that fragmentation of the RyR2 puncta pattern has upon the generation of Ca^{2+} sparks, with the organisation of RyR2 no longer able to generate a spark mass reflective of the physiological coupled nature of the Ca^{2+} release channel.

In regard to RyR2 organisation, the decreased cluster size and increased fragmentation was in accordance with conclusions from Sheard et al. (2019) in their 10xEEM evaluation of RyR2 remodelling within RV HF. They detected an increased number of orphan RyR2 channels, a phenomenon visualised within this study and previously reported by Song et al. (2006). The functional implications of orphan RyR2 are unknown. However, a reduction in RyR2 functional coupling could arise from an increased fragmentation of the RyR2 cluster pattern. This could lead to a reduction in Ca^{2+} spark fidelity and a decreased release of Ca^{2+} from the SR which is reflective of the decreased Ca^{2+} spark mass recorded within this study (Sheard et al., 2019; Song et al., 2006). When the CRU was modelled (Walker et al., 2014), functional coupling of the RyR2 was regarded as critical for Ca^{2+} spark fidelity. However, this coupling was not determined necessarily by RyR2 cluster size but instead by the orientation of RyR2 within its cluster. This finding could explain why within this study a greater structural determinant of Ca^{2+} signalling was NND and average NND rather than RyR2 count.

The significant reduction in RyR2 cluster size within RV HF is indicative of a physical change in the coupling of RyR2 channels. Uncoupling of the RyR2 can also occur from the biochemical remodelling of the RyR2. Specifically, increased phosphorylation of the RyR2 within HF is known to increase channel open probability and lead to a greater release of SR Ca^{2+} (Sobie et al., 2006). A heightened phosphorylation gradient is known to exist across RyR2 clusters within the MCT induced RV HF model that is not present

within healthy controls (Sheard et al., 2019). When phosphorylated, the RyR2 has reduced binding to FKBP12.6 which decreases the propensity for RyR2 to remain in its closed state. A shift in RyR2's open probability can enhance Ca^{2+} spark fidelity (Marx et al., 2000; Marx et al., 2001; Sheard et al., 2019). The role of FKBP12.6 was assessed by Asghari et al. (2020). When FKBP12.6 was bound to RyR2, the Ca^{2+} spark frequency and FWHM was reduced and RyR2 puncta were arranged in smaller clusters which had a side-by-side orientation. Phosphorylation of RyR2, however, increased SR Ca^{2+} release and led to an increased cluster size. It should be noted that cluster size was calculated using an area-based approach. Therefore, repeat studies are required using a different analysis approach to evaluate whether phosphorylation directly alters cluster size. The reliance of Ca^{2+} spark kinetics upon not only RyR2 cluster orientation but RyR2 channel permeability has been previously evidenced through a series of simulations (Cosi et al., 2019). Further research is required using the correlative imaging protocol to reveal how RyR2 modulation alters within RV HF.

Findings within this study were evaluated in regard to previous research that looked at Ca^{2+} handling proteins in regard to local Ca^{2+} signalling. Kolstad et al. (2018) adopted a post-infarct model of HF. Within HF they noted a nanoscale re-organisation of RyR2 at the near surface which resembled the reported increase in NND within this study's model of RV HF. When Ca^{2+} signalling was modelled, slower Ca^{2+} spark kinetics were attributed to both a decrease in RyR2 cluster size and an increased fragmentation. Using their developed correlative imaging method, RyR2 fragmentation was understood to be the predominant variable driving increased variability of Ca^{2+} spark kinetics. However, any conclusions formed from this study should remember that remodelling is a heterogenous process and their data is only a small snapshot of the Ca^{2+} signalling across a cell. Unlike Kolstad et al. (2018), SR Ca^{2+} release from orphan RyR2 was accounted for within this study. This could explain why there was a noted decrease in spark mass compared to Kolstad et al. (2018) who only modelled Ca^{2+} release from sites with an intact JMC. To circumvent the requirement of a fixed sample for SMLM a series of transgenic mouse studies have recorded Ca^{2+} signalling in regard

to RyR2 activation (Hiess et al., 2015). Studies showed that RyR2 cluster orientation was dynamic depending upon the degree of channel modulation. It was suggested that the positioning of the RyR2 within its cluster could determine a Ca^{2+} spark's point of origin (Hiess et al., 2018; Hou et al., 2020). However, these studies relied upon cultured cells due to the nature of the study. Instead, the developed correlative imaging protocol can be applied to primary cells to understand the structural and functional changes that can occur within pathophysiology.

4.4.7 Transverse tubule remodelling

In this research project, the ease of Ca^{2+} diffusion was evaluated by looking at T-tubule system architecture. This study detected the majority of T-tubules to align with a 90° orientation. There was a noted disparity from this peak within RV HF, but not to a significant extent which suggests only minimal remodelling of the T-tubule system within this HF model. The microscopy technique chosen is critical for observing changes in T-tubule architecture (Crossman et al., 2017). Study data could be limited by the use of confocal microscopy. This is pertinent as T-tubule structure is 50 nm in diameter within rat ventricular cardiomyocytes, with variation in T-tubule diameter noted within HF (Crossman et al., 2017; Kawamura et al., 1976; Soeller and Cannell, 1999; Wagner et al., 2012). Furthermore, confocal microscopy negates the study of local changes at the JMC from T-tubule disruption, an element made apparent within the JPH knock out model of Van Oort et al. (2011) whereby remodelling was only detected when a single JMC was studied.

Previous studies have documented T-tubule remodelling to be most prominent in the shift from transverse to longitudinal orientations, a phenomenon which has the capability to be recorded with diffraction-limited techniques (Crossman et al., 2015; Crossman et al., 2017). It should be noted that the use of NCX and Cav3 within this study to stain the T-tubule system has been suggested to visualise a more extensive T-tubule network than the commonly used WGA stain, which could partially explain the lack of significant remodelling within this study (Crossman et al., 2011). For

example, similar to Crossman et al. (2011), this study did reveal an increase in T-tubule directionality upon HF development. Variation may exist between this study and other HF models because of a differing in the compensatory responses triggered that lead to HF, in our model this being strain upon the RV from PAH. It is important to consider that the extent of T-tubule remodelling could vary depending upon the initial insult to the heart that triggers HF development.

The remodelling of the T-tubule system is considered inherently linked to the expression of JPH2. A knock down which reduced JPH2 expression by 51% led to widespread T-tubule disruption (Wei et al., 2010). Within a thoracic aortic banded (TAB) model of HF, the severity of hypertrophy correlated with a decrease in JPH2 expression and the degree of structural remodelling in regard to the T-tubule system (Wei et al., 2010). The increased ventricular weight to body weight ratio upon the development of heart failure suggested the presence of hypertrophy within the MCT model applied. This was validated by Benoist et al. (2014) concluding increased RV wall stress from MCT induced RV HF and Ca^{2+} dysregulation (Benoist et al., 2011; Benoist et al., 2012). However, the slower progression of HF within a TAB model of 8-12 weeks compared to the 3-4 weeks within the MCT model could enable a greater variation in T-tubule remodelling from the longer disease process, a factor commonly evidenced within human HF (Crossman et al., 2011). Application of the correlative imaging protocol to look at the extent of remodelling within the hypertrophy stage of MCT induced RV HF would be of interest to understand how the relationship between structure and function can change within disease (Benoist et al., 2012; Bidasee et al., 2003). A model of slower disease progression might also reveal greater changes in JPH2 and RyR2 co-localisation, with JPH2 density a suggested driver of T-tubule remodelling. It is important to note, however, that JPH2 expression alone is not indicative of T-tubule architecture. For example, SERCA2a gene therapy within a chronic post-infarct model of HF was able to restore the T-tubule system and Ca^{2+} signalling (Lyon et al., 2012). Another consideration for why this application of the MCT model did not visualise a significant degree of T-tubule remodelling is that cells which have a high degree of T-

tubule disruption are more fragile. These cells are therefore less likely to be retained after enzymatic digestion required for cell isolation with the protocol unintentionally favouring the retention of healthy cells (Hatem, 2004; Heinzel et al., 2008; Houser, 2001). In relation to the data acquired within this study, the alteration within JMC structure and Ca^{2+} spark signalling is unlikely to be evoked from T-tubule disruption. This is due to all data being acquired at the sub-sarcolemma, an area devoid of T-tubules.

4.4.8 Translational value

Before conclusions from this rat model of RV HF are made, the translational value must first be considered. For example, there are species differences in regard to a cardiomyocyte's ultrastructure (Heinzel et al., 2008; Jayasinghe et al., 2011). Within the literature, however, rodents are a favoured model due to accessibility and reproducibility, with previous findings and those within this study being in agreement with the minimal number of human HF studies that have been undertaken (Crossman et al., 2011; Crossman et al., 2015).

4.5 Concluding remarks

Within the literature there are conflicting reports regarding the degree of remodelling within HF. The correlative imaging protocol is a welcomed tool to evaluate the relationship between local Ca^{2+} signalling and the underlying structure of a cell. Within the MCT induced RV HF model, there was a substantial decrease in RyR2 cluster size which was accompanied by a significant change in Ca^{2+} spark kinetics. Notably, there was relationship between RyR2 orientation and Ca^{2+} spark mass, with a rightward shift in NND and average NND values upon the development of RV HF in accordance with a decreased Ca^{2+} spark mass. These findings suggest that a relationship exists between the local Ca^{2+} handling properties of a cell and the structures involved.

The remainder of this research will focus upon the application of the correlative imaging protocol to dorsal root ganglion sensory neurones. A DRG neurone shares similarities with cardiomyocytes in regard to the

machinery that releases Ca^{2+} from the cell's internal store. This secondary application will test the validity of the protocol upon a second cell type whilst uncovering the structural basis of Ca^{2+} sparks within the neuronal cell bodies.

Chapter 5. Correlative imaging in dorsal root ganglion sensory neurones

5.1 Introduction

Dorsal root ganglia consist of sensory neurones. The DRG form the beginning of the somatosensory pathway to relay nociceptive, mechanoreceptive and proprioceptive signals between the peripheral and central nervous system (Hanani, 2005; Nascimento et al., 2018). Sensory neurones within the DRG are a form of excitable cell. The neurones are considered to be reliant upon Ca^{2+} signalling for the initiation of neurotransmitter exocytosis (Haberberger et al., 2019; Park and Luo, 2010). However, the extent of calcium's role within the DRG is widely disputed. Specifically, the prominence of the CICR mechanism is unknown.

Within DRG sensory neurones there are two Ca^{2+} release channels located upon the ER; the IP3R and the RyR3 (Henzi and MacDermott, 1992). The activation of RyR3 is known to be by Ca^{2+} alone. However, IP3R stimulation is reliant upon the stimulation of a metabotropic GPCR, with the activation of IP3R by Ca^{2+} directly being unknown (Finch et al., 1991; Henzi and MacDermott, 1992; Simpson et al., 1995; Thayer et al., 1988). Previous research has focussed upon the application of pharmacological agents to understand the functional changes in Ca^{2+} signalling upon the stimulation and inhibition of IP3R and RyR3 in isolation. These studies revealed an ability of both channels to release Ca^{2+} from the ER and have a role in Ca^{2+} signalling. However, the question of whether IP3R and RyR3 share the same ER Ca^{2+} pool is still unanswered (Liu et al., 1991; Simpson et al., 1995; Thayer et al., 1988). Furthermore, the use of a channel-specific antagonist led to the suggestion that RyR3 has a predominant role within Ca^{2+} spark generation (Ouyang et al., 2005a; Ouyang et al., 2005b). There is however a lack of experimental evidence regarding how the structural positioning of the IP3R and RyR3 channels relate to the functional generation of Ca^{2+} sparks.

This chapter evaluates the role of IP3R and RyR3 Ca^{2+} release channels within DRG sensory neurones in direct relation to the functional role of Ca^{2+}. Specifically, the aim was to understand the extent of each channel's role within Ca^{2+} signalling by combining the use of pharmacological agents in tandem with the developed correlative imaging protocol. This research attempts to demonstrate how the relationship between a cell's Ca^{2+} signalling is revealed further by understanding the local ultrastructure.

5.2 Method

A primary culture of DRG sensory neurones was obtained from neonatal male Wistar rats (aged 6-10 days). The extraction of DRGs from the spine followed a protocol outlined by Kirton et al. (2013), as detailed in the Methods Chapter (Section 2.2.2). Prior to use, DRGs were left at 37°C within a humidified incubator (air supplemented with 5% CO_2).

5.2.1 Live cell calcium imaging

Following the protocol outlined in the Methods Chapter (Section 2.3), the DRG sensory neurones were loaded with 5 μM Fluo4-AM and spontaneous Ca^{2+} spark activity observed. The use of fiducial markers upon the coverslip and TIRF positioning of the beam ensured that Ca^{2+} sparks were recorded from the surface of a cell. Specialised PyME acquire software was used to record Ca^{2+} spark activity, which was analysed using the *xySpark* plug-in for ImageJ (Steele and Steele, 2014), prior to being filtered according to the parameters detailed within the Methods Chapter (Section 2.6.2).

5.2.2 Immunofluorescence staining

The SMLM technique of dSTORM was adopted to visualise the JMC structure within the DRG sensory neurones. Specifically, the Ca^{2+} release channels IP3R and RyR3 along with the Ca^{2+} re-uptake pump SERCA were probed. The typical immunofluorescence protocol and dSTORM image acquisition has been detailed in the Methods Chapter (Section 2.5.2). Each dataset was rendered with a localisation accuracy of 20 nm, following the rendering method previously described (Section 2.6). To undertake two-colour dSTORM, two proteins of interest were individually labelled with either

Alexa 660 or Alexa 647 (Munro et al., 2016). A purpose-built beam splitter divided the emitted light from each fluorophore onto half of the Andor Zyla 5.5 pixel chip, to display a mirror image of each protein staining pattern within the same region of the sample.

When rendered, for two-colour datasets an overlay was formed of the two single channels. These data were stitched together using the composite tool within dh5view. The accuracy of this overlay was verified by how well the outline of the cell aligned within each channel. Within single and two-colour dSTORM, the staining pattern for IP3R, SERCA and RyR3 was quantified using the puncta detection method within dh5view, as explained previously in the Methods Chapter (Section 2.6.1).

5.2.3 Correlative imaging protocol

Functional Ca^{2+} spark activity can be recorded in relation to the underlying JMC structure of a sensory neurone. Experimentally, this was undertaken following the previously outlined correlative imaging protocol (Section 3.4.7). As a result, the local relationship of Ca^{2+} handling was evaluated at a cell's surface.

5.2.4 Pharmacological agents

The activation or inhibition of Ca^{2+} release channels can be modulated by pharmacological agents. Live-cell Ca^{2+} imaging of DRGs was undertaken (Section 2.3). Each pharmacological agent was applied to the DRG culture within a 5 mM Ca^{2+} Tyrode's solution. The cells were left for 10 minutes prior to Ca^{2+} imaging to enable the pharmacological agent to diffuse and the DRG sensory neurones to equilibrate. A 100 μM and 1 mM tetracaine concentration was used in accordance to previous research, which had used the antagonist to bind to RyR3 and reduce Ca^{2+} spark activity (Westcott et al., 2012). A low concentration of 20 μM 2-APB or greater 100 μM was utilised based upon the research of Ouyang et al. (2005a) in DRG sensory neurones. A greater concentration of 2-APB has been known to elicit further Ca^{2+} mediated responses, namely a change in cellular SOCE in addition to its inhibition of IP3R opening (Bootman et al., 2002). To stimulate RyR3

opening, a 5 mM caffeine concentration was used, similar to Ouyang et al. (2005a). The bradykinin concentration (250 nM) was chosen based upon the advice of Dr Gamper's research group at The University of Leeds.

5.3 Results

5.3.1 Structural placement of calcium handling proteins

The Ca^{2+} handling proteins; IP3R, RyR3 and SERCA had a similar cluster pattern at the surface of DRG sensory neurones (Figure 5.1). Although there is a trend with RyR3 exhibiting the smallest number of puncta per cluster and SERCA the largest, this difference was not significant (SERCA 7.21±0.75 puncta; RyR3 5.57±0.50 puncta; IP3R 6.48±1.01 puncta (one-way ANOVA; *p=0.17 for SERCA/RyR; p=0.79 for SERCA/IP3R; p=0.65 RyR3/IP3R*)). Furthermore, this similarity across the staining patterns was verified by there being no significant difference in the cluster area of each protein, despite the similar trend exhibited (SERCA 30.60±3.07 μm^2; RyR3 23.97±2.37 μm^2; IP3R 25.85±4.55 μm^2 (one-way ANOVA; *p=0.26 for SERCA/RyR; p=0.59 for SERCA/IP3R; p=0.93 RyR3/IP3R*)). This similarity within the cluster patterning of Ca^{2+} handling proteins is not unexpected due to the structural nature of the CRU and the ability to enable an optimised release and subsequent reuptake of the Ca^{2+} ion. A positive and negative immunofluorescence staining control counters any suggestion that the structural pattern detected is artefactual.

When the location of each puncta was quantified in relation to its nearest neighbour, using the variable NND, the IP3R puncta had a significantly greater degree of fragmentation across their staining pattern compared to RyR3 and SERCA. However, RyR3 and SERCA puncta had a similar proximity to each other at a local level (SERCA 48.52±0.31 nm; RyR3 48.11±0.42; IP3R 50.64±0.41 nm (one-way ANOVA; *p=0.69 for SERCA/RyR; p=0.00 for SERCA/IP3R; p=0.00*)). When the staining pattern was quantified across a greater surface area, there was no significant difference between the three Ca^{2+} handling channels in regard to their 3NND (SERCA 74.14±0.32 nm; RyR3 74.57±0.47 nm; IP3R 74.71±0.42 nm (one-way ANOVA; *p=0.70 for SERCA/RyR; p=0.59 for SERCA/IP3R; p=0.98*

RyR3/IP3R)). This suggests that at a local level the IP3R has a sparser staining pattern that does not necessarily align with the RyR3 and SERCA positioning within the cell.

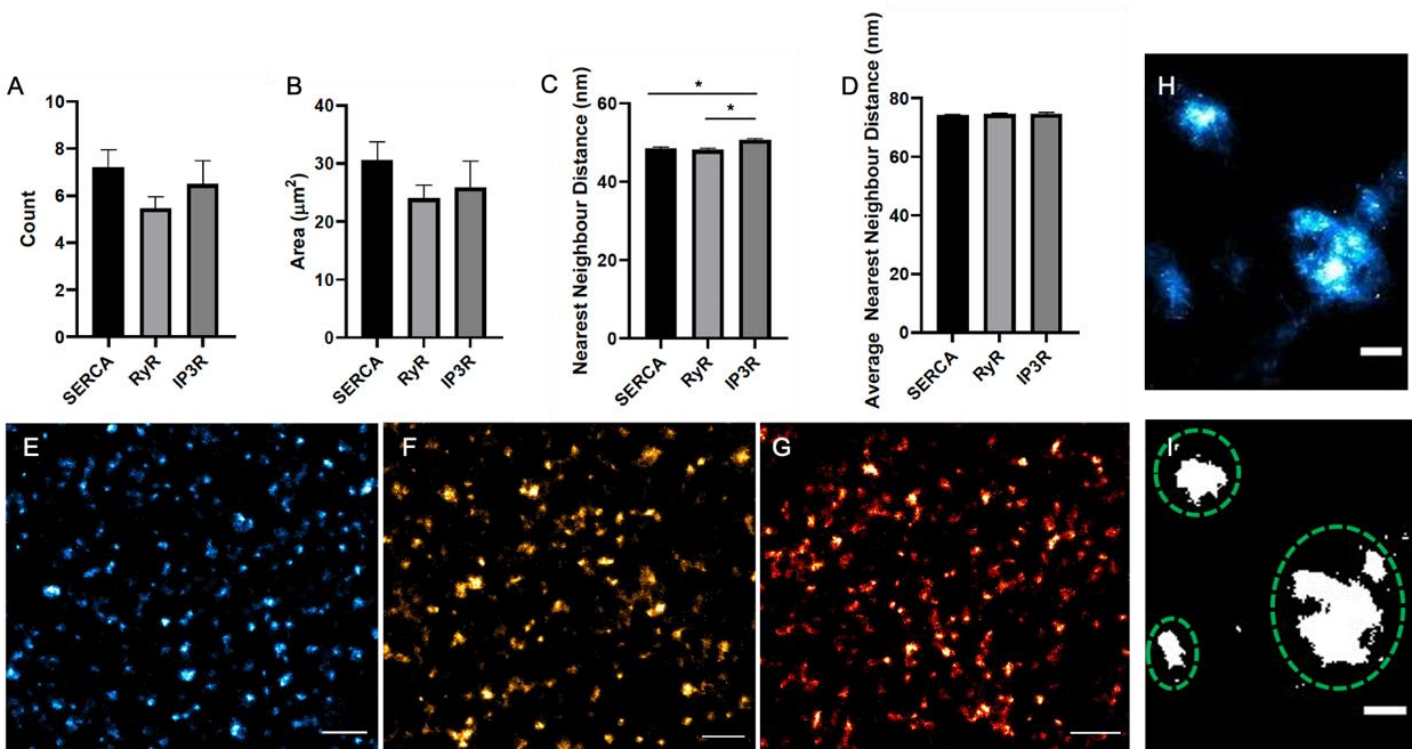

Figure 5.1: Cluster pattern of calcium handling proteins. Quantitative analysis of peripheral RyR3, IP3R and SERCA cluster pattern within dorsal root ganglia sensory neurones using dSTORM microscopy. Cells were extracted from neonatal male Wistar rats. Puncta detection analysis was undertaken upon rendered dSTORM data. (A) The protein density per cluster was calculated, with SERCA having the greatest cluster size. (B) The area of each cluster was quantified, accounting for any holes or gaps within the structure. (C) The distance between one punctum and its nearest neighbour was calculated. The IP3R puncta had a significantly greater distance between puncta then either RyR3 or SERCA. (D) There were no significant differences between calcium handling proteins regarding the average nearest neighbour distance between one protein puncta and it's three neighbours. (E-G) Cluster pattern for SERCA, RyR3 and IP3R puncta. (H-I) Magnified region of SERCA puncta with binary mask of same region with individual clusters defined by dotted green boundary. Values are mean±SEM; SERCA n=13 cells; RyR3 n=7 cells; IP3R n=6 cells. Scale bars, E-G: 500 nm; H-I: 100 nm.

5.3.2 Dual imaging of calcium signalling proteins

The association between the Ca^{2+} re-uptake pump SERCA and the Ca^{2+} release channels IP3R and RyR3 were quantified. Approximately three quarters of the IP3R and RyR3 stain was co-localised with the SERCA pump (IP3R fraction 0.75±0.01; RyR3 fraction 0.77±0.02, IP3R n=6; RyR3 n=7). Conversely, the proportion of SERCA stain which co-localised with either the IP3R or RyR3 stain was significantly less. Specifically, a 0.69±0.02 fraction of the SERCA stain was associated with IP3R puncta (paired t-test; *p=0.00*) and a similar 0.68±0.04 fraction of SERCA co-localised with RyR3 (paired t-test; *p=0.048*) This similarity in RyR3 and IP3R staining pattern in relation to SERCA suggests that both Ca^{2+} release channels associate with the Ca^{2+} re-uptake pump in a similar manner at the level of the JMC.

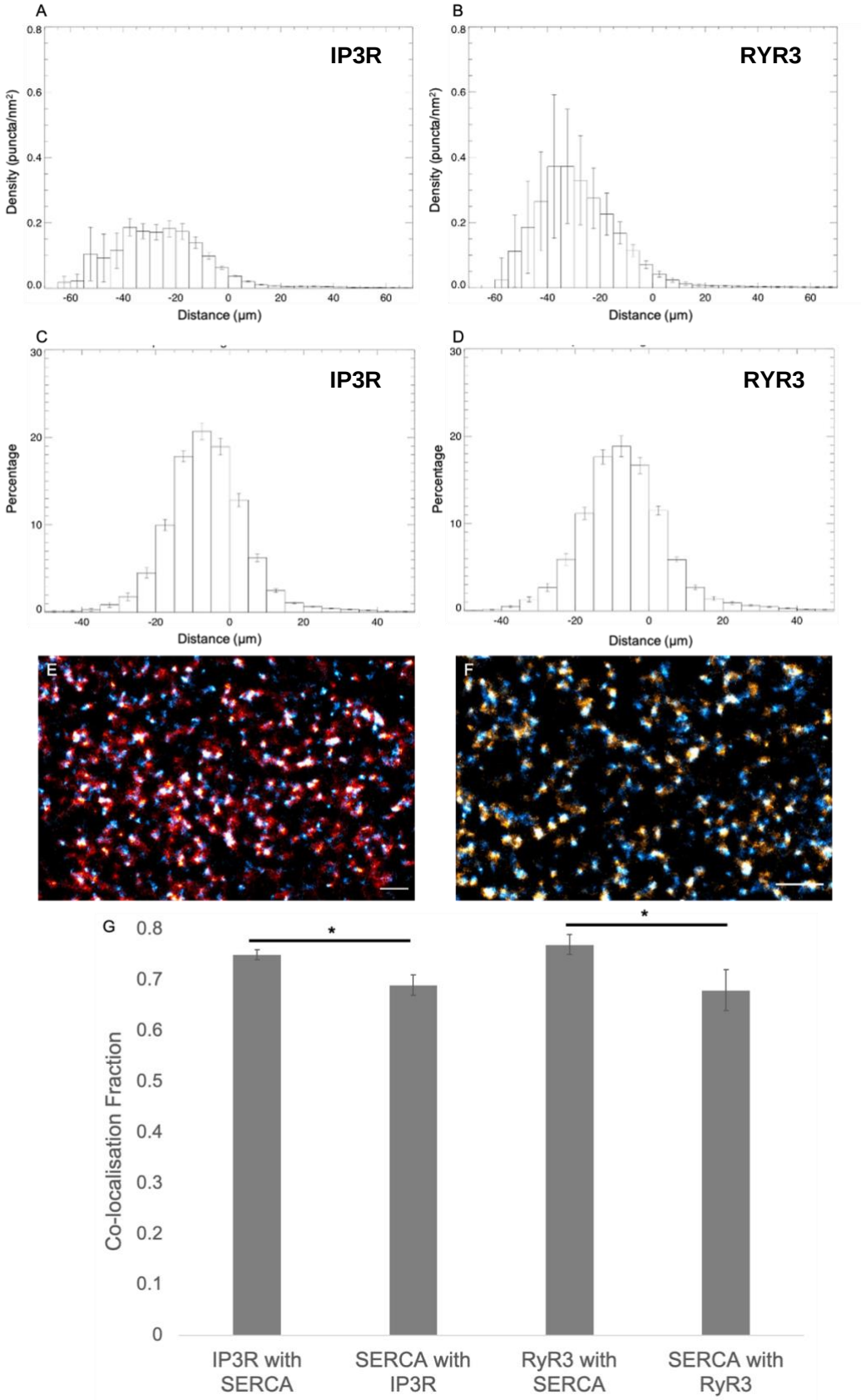

Figure 5.2: Co-localisation of calcium handling proteins. Quantitative analysis of peripheral RyR3 and IP3R with the calcium reuptake channel SERCA within dorsal root ganglia (DRG) sensory neurones using dSTORM microscopy. Cells were extracted from neonatal male Wistar rats. Puncta detection analysis was undertaken upon rendered dSTORM data. The extent by which the (A) IP3R and

(B) RyR3 protein pattern overlaps with SERCA in regard to protein density. The relationship between (C) IP3R and (D) RyR3 staining pattern in regard to SERCA was visualised as a percentage. (E-F) Two-colour dSTORM acquisition of IP3R (red) and RyR3 (orange) respectively with SERCA (blue). (G) Fraction of co-localisation between SERCA and the IP3R and RyR3 and staining pattern. Values are mean±SEM; RyR3 n=7 cells; IP3R n=6 cells. Scale bars, E-F: 500 nm.

5.3.3 Calcium spark morphology

5.3.3.1 Pharmacological stimulation of calcium release channels

Spontaneous Ca^{2+} spark activity was recorded at the surface of sensory neurones within the DRG. It is known that RyR3 and IP3R mediate the release of Ca^{2+} from the ER. Therefore, pharmacological agents were applied to study local Ca^{2+} signalling. Compared to when DRG sensory neurones were exposed to 5 mM Ca^{2+} containing Tyrode's alone, the activation of RyR3 by 5 mM caffeine resulted in a significant decrease in FWHM by 17.42% (calcium 1.32±0.02 μm; caffeine 1.09±0.02 μm (one-way ANOVA; $p=3.70x10^{-26}$)). Similarly, IP3R activation from 250 nM bradykinin resulted in a significant 15.13% decrease in FWHM (calcium 1.19±0.03 μm; bradykinin 1.01±0.02 μm (one-way ANOVA; $p=1.75x10^{-7}$)). The reduced spatial spread in the xy plane, however, did not lead to a corresponding change in spark mass. Instead, the application of caffeine and bradykinin resulted in an increased spark mass compared to basal 5 mM Ca^{2+} Tyrode solution (Figure 5.3). It is important to consider that spark mass is not calculated based upon Ca^{2+} spark FWHM alone, but also a Ca^{2+} spark's amplitude. In the presence of 250 nM bradykinin, a spark mass of 2.40±0.16 AU was analysed (one-way ANOVA; $p=0.78$). However, only the 25.30% increase to 2.49±0.15 AU upon caffeine administration was significant (one-way ANOVA; $p=4.25x10^{-8}$) compared to the 1.86±0.10 AU within 5 mM Ca^{2+} Tyrode conditions.

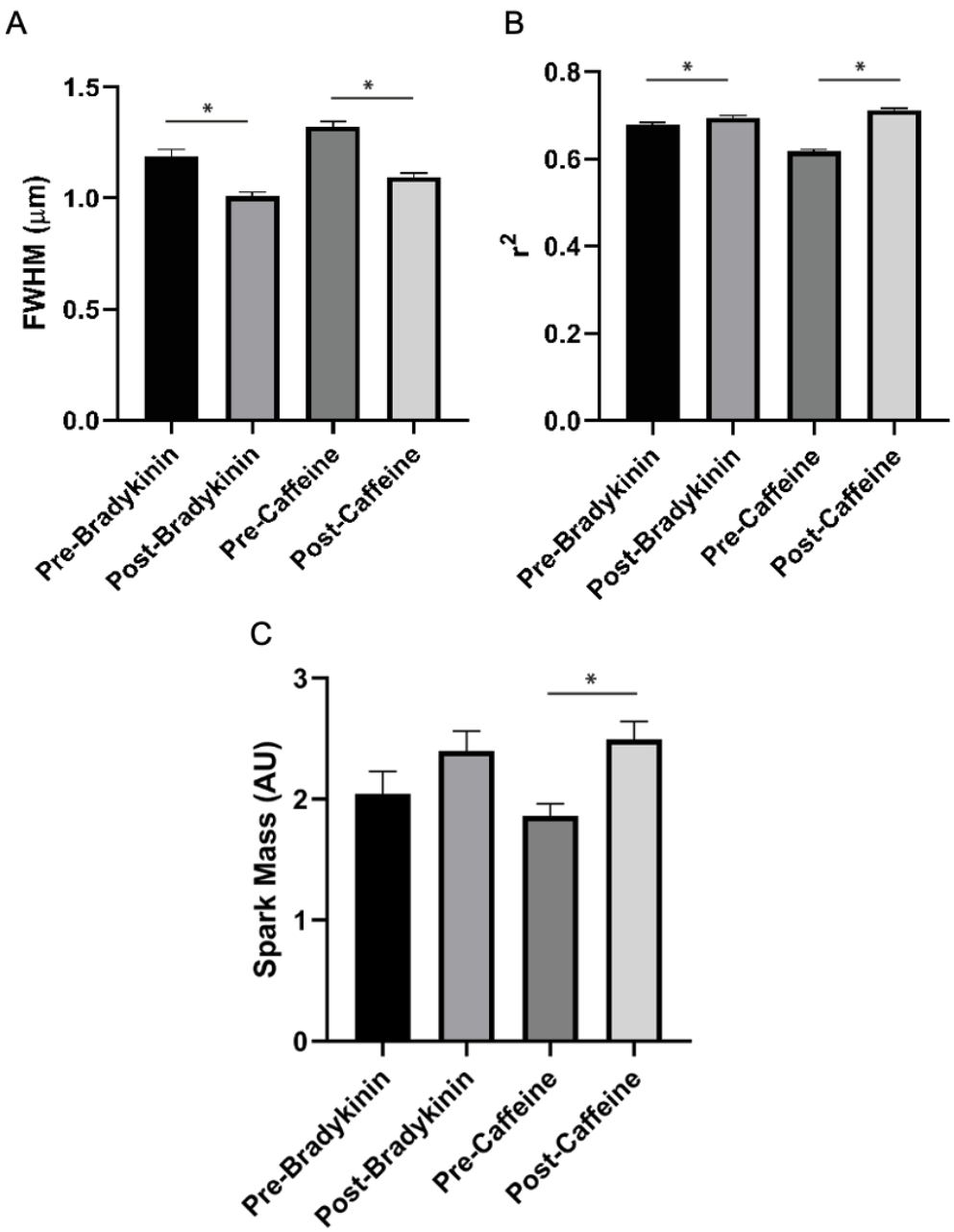

Figure 5.3: Pharmacological stimulation of RyR3 and IP3R. Observation of Ca^{2+} spark activity at the periphery of dorsal root ganglia (DRG) sensory neurones using TIRF microscopy. Cells were extracted from neonatal male Wistar rats. Pre-bradykinin and pre-caffeine recordings were acquired when the DRG's were exposed to 5 mM $CaCl_2$ Tyrode's solution. This was followed by the application of either 250 nM bradykinin or 5 mM caffeine. (A) The application of bradykinin and caffeine decreased FWHM from baseline recordings. (B) Conversely, the r^2 value of a Ca^{2+} spark increased when the IP3R or RyR3 channel was stimulated. (C) This led to an increased trend in Ca^{2+} spark mass, a change which was only significant upon 5 mM caffeine application. Values are mean±SEM; pre-bradykinin n= 269 Ca^{2+} sparks; post-bradykinin n= 284 Ca^{2+} sparks; pre-caffeine n= 934 Ca^{2+} sparks; post-caffeine n= 569 Ca^{2+} sparks.

Upon the administration of caffeine and bradykinin, the Ca^{2+} spark recording had a greater Gaussian fit upon analysis, as represented by a significant increase in r^2 value. Specifically, the r^2 value upon caffeine administration increased 12.68% from the 0.62±0.00 recorded in the presence of 5 mM Ca^{2+} containing Tyrode's alone (one-way ANOVA; $p=3.70x10^{-58}$). The 0.69±0.01 r^2 value upon 250 nM bradykinin administration was less than the effect of caffeine administration, however, it was still significantly greater than the initial 0.68±0.01 in 5 mM Ca^{2+} Tyrode's alone (one-way ANOVA; $p=2.17x10^{-4}$). It is important to note that although caffeine and bradykinin administration resulted in a significant change to FWHM, r^2 and spark mass values compared to 5 mM Ca^{2+} Tyrode's solution, the degree of percentage change was not significantly different (paired t-test; FWHM *p=0.84; r^2 p=0.27; spark mass p=0.52*) (Figure 5.4). This suggests that the response in Ca^{2+} spark morphology was comparable when either RyR3 or IP3R was stimulated.

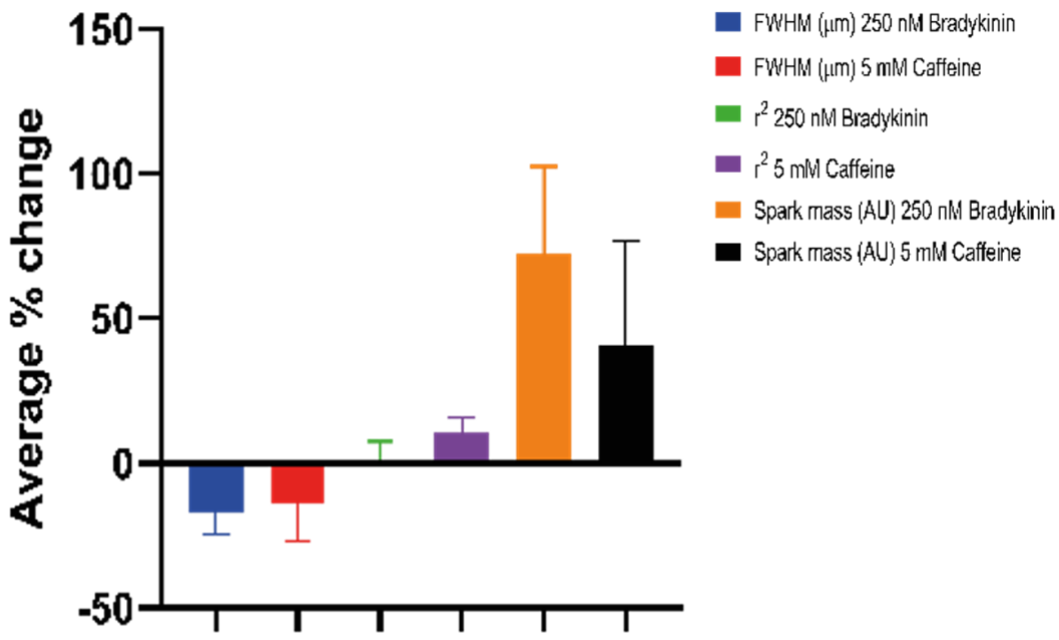

Figure 5.4: Percentage change in calcium spark kinetics from pharmacological stimulation of RyR3 and IP3R. Observation of Ca^{2+} spark activity at the periphery of dorsal root ganglia (DRG) sensory neurones using TIRF microscopy. Cells were extracted from neonatal male Wistar rats. The percentage change in FWHM, r^2 value and spark mass was calculated between the 5 mM $CaCl_2$ Tyrode's solution at baseline and the application of either 250 nM bradykinin or 5 mM caffeine. Upon either IP3R or RyR3 channel pharmacological stimulation, no significant change in any of the Ca^{2+} spark markers analysed was identified.

Values are mean±SEM percentage change; pre-bradykinin n= 269 Ca^{2+} sparks; post-bradykinin n= 284 Ca^{2+} sparks; pre-caffeine n= 934 Ca^{2+} sparks; post-caffeine n= 569 Ca^{2+} sparks.

5.3.3.2 Pharmacological inhibition of calcium release channels

Similar to stimulation of the IP3R and RyR3, upon the application of tetracaine and 2-APB, the FWHM was reduced. From the baseline FWHM recording of 1.56±0.05 μm, there was a significant decrease upon the inhibition of IP3R and RyR3 channels by 100 μM 2-APB and 1 mM tetracaine respectively (1 mM tetracaine 1.35±0.05 μm; 100 μM 2-APB 1.39±0.04 μm (one-way ANOVA; *p=0.03 and p=0.045 respectively*)). Notably, the exposure of DRG sensory neurones to 100 μM tetracaine minimally altered FWHM (one-way ANOVA; *p=0.18*), with an even smaller change upon FWHM upon 20 μM 2-APB administration (one-way ANOVA; *p=1.00*). This led to a significant difference in FWHM between the 1.35±0.05 μm recorded upon 1 mM tetracaine exposure compared to the 1.55±0.05 μm FWHM when only 20 μM of 2-APB was administered (one-way ANOVA; *p=0.04*). This suggests that tetracaine, even at a low concentration, has a greater influence upon a Ca^{2+} spark's FWHM compared to 2-APB.

Regardless of the concentration administered, the 0.67±0.01 r^2 value recorded with 5 mM Ca^{2+} containing Tyrode's was significantly greater then when tetracaine (one-way ANOVA; 100 μM Tetracaine *p=0.043;* 1 mM Tetracaine *p=0.04*) and 2-APB (one-way ANOVA; 20 μM 2-APB *p=0.00;* 100 μM 2-APB *p=0.00*) were present. This suggests that regardless of concentration, the Gaussian fit of a Ca^{2+} spark is weaker upon the inhibition of RyR3 with either 100 μM tetracaine or 1 mM tetracaine which led to a 0.64±0.01 and 0.63±0.01 r^2 value respectively. In addition, the r^2 value of 0.62±0.01 was reduced upon the inhibition of IP3R by the application of either 20 μM 2-APB or 100 μM 2-APB, suggesting a deviation from the standardised Ca^{2+} spark morphology. There was no significant change between the 2.73±0.26 AU spark mass recorded in the presence of 5 mM Ca^{2+} Tyrode's compared to tetracaine (one-way ANOVA; 100 μM Tetracaine *p=0.42;* 1 mM Tetracaine *p=0.42*) or 2-APB application (one-way ANOVA; 20 μM 2-APB *p=1.00;* 100 μM 2-APB *p=0.22*). However, the administration

of 100 μM 2-APB resulted in an average 3.42±0.25 AU spark mass. This was significantly greater than when the RyR3 channel was inhibited by either 100 μM tetracaine or 1 mM tetracaine to result in a 2.17±0.16 AU and 2.07±0.26 AU spark mass respectively (one-way ANOVA; *p=0.00 and p=0.00 respectively*). This is due to a decreased trend within spark mass visible upon the RyR3 inhibition with tetracaine contrary to increased measure of spark mass upon IP3R inhibition with 2-APB.

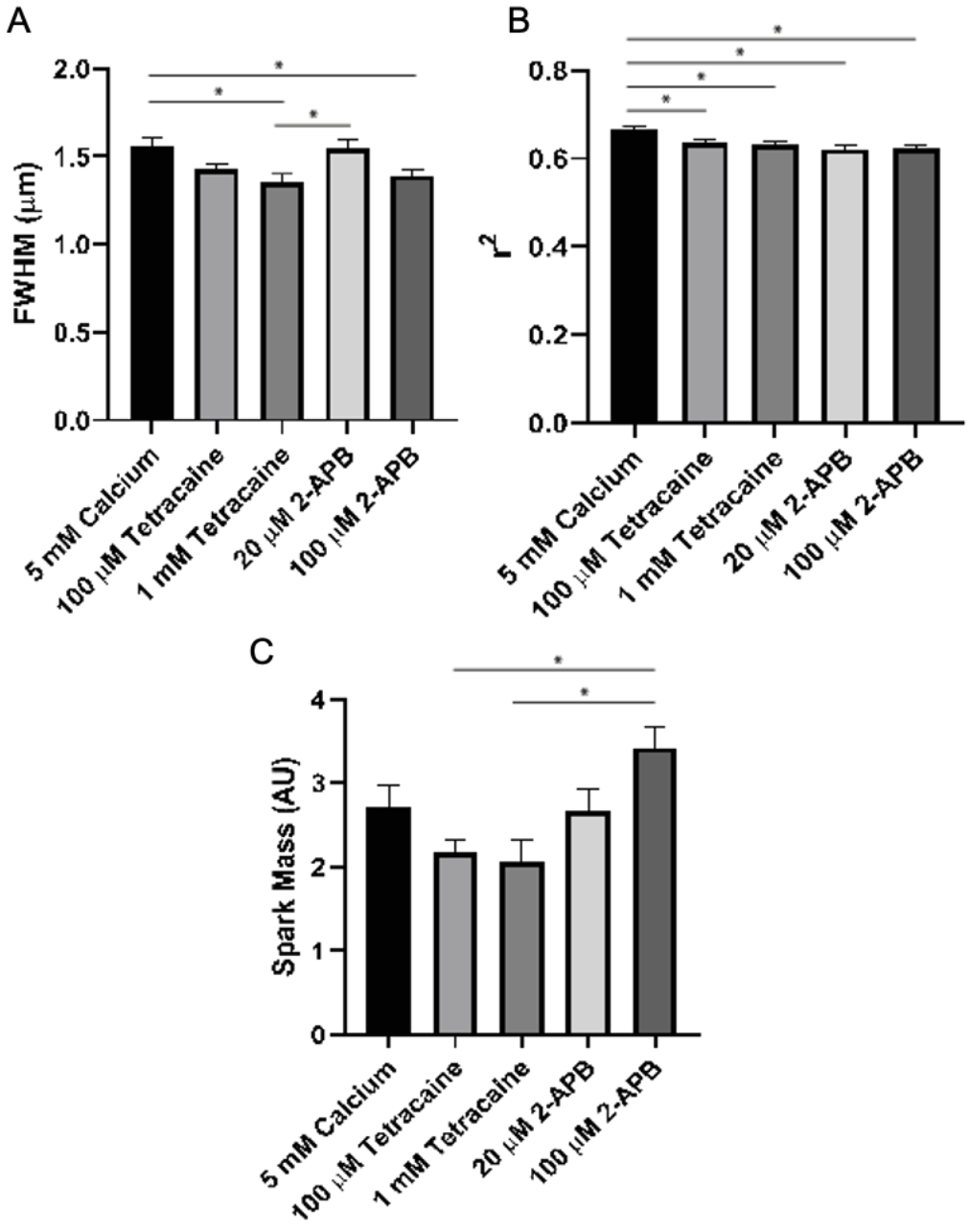

Figure 5.5: Pharmacological inhibition of RyR3 and IP3R. Observation of Ca^{2+} spark activity at the periphery of dorsal root ganglia (DRG) sensory neurones using TIRF microscopy. Cells were extracted from neonatal male Wistar rats. Baseline

Ca^{2+} spark activity was recorded when DRG's were exposed to 5 mM $CaCl_2$ Tyrode's solution. The RyR3 channel was pharmacologically inhibited with 100 μM or 1 mM tetracaine, whilst IP3R was inhibited by 20 μM or 100 μM 2-APB. (A) There was a significant decrease in FWHM upon the inhibition of RyR3 and IP3R at 1 mM tetracaine and 100 μM 2-APB application respectively. (B) The application of all pharmacological agents regardless of dose resulted in a significant decrease in r^2 value from the 5 mM $CaCl_2$ baseline. (C) Spark mass was not significantly different between 5 mM $CaCl_2$ baseline and any pharmacological application; however, an increased mass was quantified upon 100 μM 2-APB application compared to in the presence of tetracaine. Values are mean±SEM; 5 mM Calcium n= 616 Ca^{2+} sparks; 100 μM tetracaine n= 1179 Ca^{2+} sparks; 1 mM tetracaine n= 542 Ca^{2+} sparks; 20 μM 2-APB n= 626 Ca^{2+} sparks; 100 μM 2-APB n= 1046 Ca^{2+} sparks.

5.3.4 Correlative imaging protocol with DRG sensory neurones

The local structures of RyR3 and IP3R were analysed in regard to the local Ca^{2+} spark function within sensory neurones of DRG's at the near surface. From the data acquired using the correlative imaging protocol, we examined the scattergrams of the Ca^{2+} spark mass (integral of the overall spark signal) plotted as a function of the number of puncta of IP3R and RyR3 (Figure 5.6A&B). From the shapes of the points cloud (colour-coding shows local point density), the correlations in both cases were weak, given the number of sparks examined.

Unlike structural and functional experiments which were previously undertaken in isolation within this study, there was a significantly reduced RyR3 count of 8.16±0.77 puncta compared to the 15.37±1.47 puncta identified for IP3R (t-test; $p=1.77x10^{-5}$) underneath the spatial footprint of recorded Ca^{2+} sparks. This was reflected by RyR3 having a median density of 3 puncta underneath a Ca^{2+} sparks spatial footprint, half of that exhibited by the IP3R patterning. Furthermore, IP3R count has a greater range underlying a Ca^{2+} spark being recorded (Figure 5.6C) and a 30.89% larger spark mass (t-test; $p=0.03$) within IP3R associated Ca^{2+} sparks compared to those associated with RyR3 (Figure 5.6D).

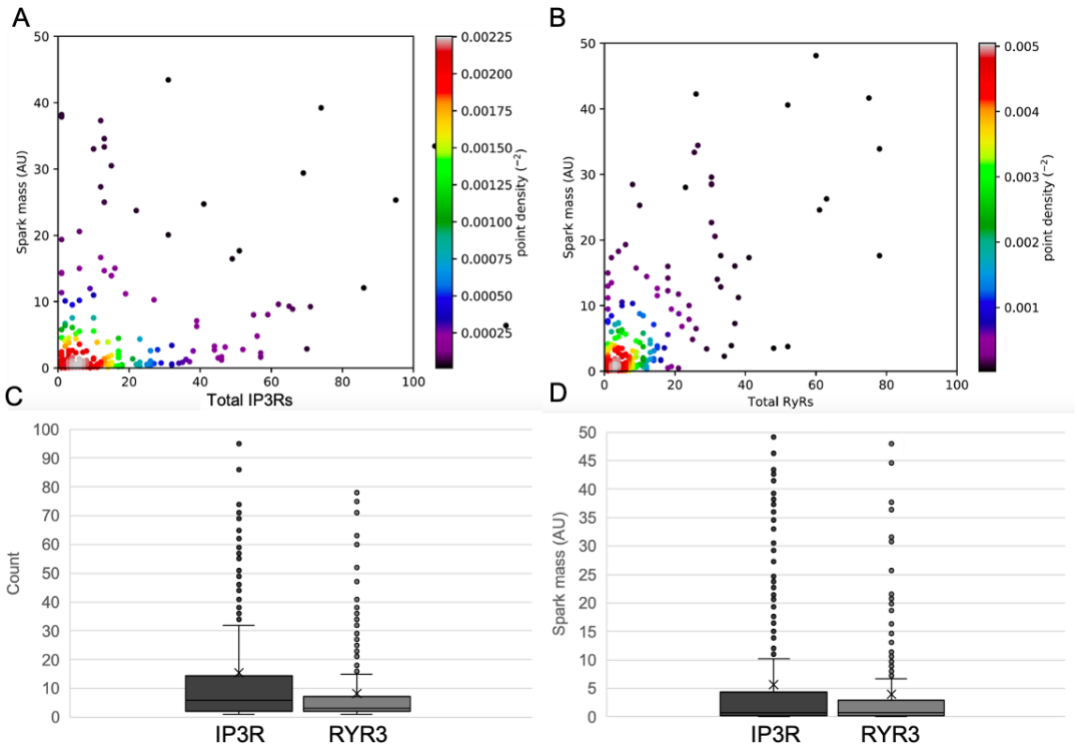

Figure 5.6: Relationship between the density of calcium handling proteins and the mass of locally generated calcium sparks. Correlative imaging protocol applied to dorsal root ganglia (DRG) sensory neurones from neonatal male Wistar rats. Point density scattergram was utilised to represent the shape of the data cloud, with red denoting the greatest density of unitary Ca^{2+} spark events. Quantitative analysis of (A) IP3R density and (B) RyR3 density underneath a Ca^{2+} sparks spatial footprint according to FWHM. This was evaluated in regard to the mass of the same Ca^{2+} spark. When the range of data punctum was evaluated (C) IP3R (black) has a greater range in puncta per Ca^{2+} spark footprint and (D) spark mass values compared to RyR3 (grey). Values are mean±SEM; RyR3 n=7 cells; IP3R n=6 cells.

The distance between an individual Ca^{2+} handling protein can be analysed using the function of NND. Interestingly, there was no significant difference (t-test; *p=0.12*) between the spacing of individual RyR3 and IP3R in regard to their NND (Figure 5.7). However, RyR3 did have an 18% greater mean NND compared to IP3R, reflected perhaps by its 813.12 nm NND range which is twice that of IP3R puncta. When NND was analysed in regard to spark mass, there appeared to be an association between NND and spark mass for both the RyR3 and IP3R structures. Specifically, the densest regions in the scattergram points cloud (coloured in yellow) reflected that a large number of the sparks occurred in regions where the RyR3 NND was between 25 and 50 nm, irrespective of the spark mass. For IP3R, they were spread across a broader range of NNDs (0-75 nm). These contrasting

shapes and the ranges of the points cloud suggest that the Ca^{2+} sparks recorded from these DRGs tend to correlate stronger with regions where there is closer RyR3-RyR3 spatial association. On the other hand, the dependence on IP3R spacings is weak, if at all.

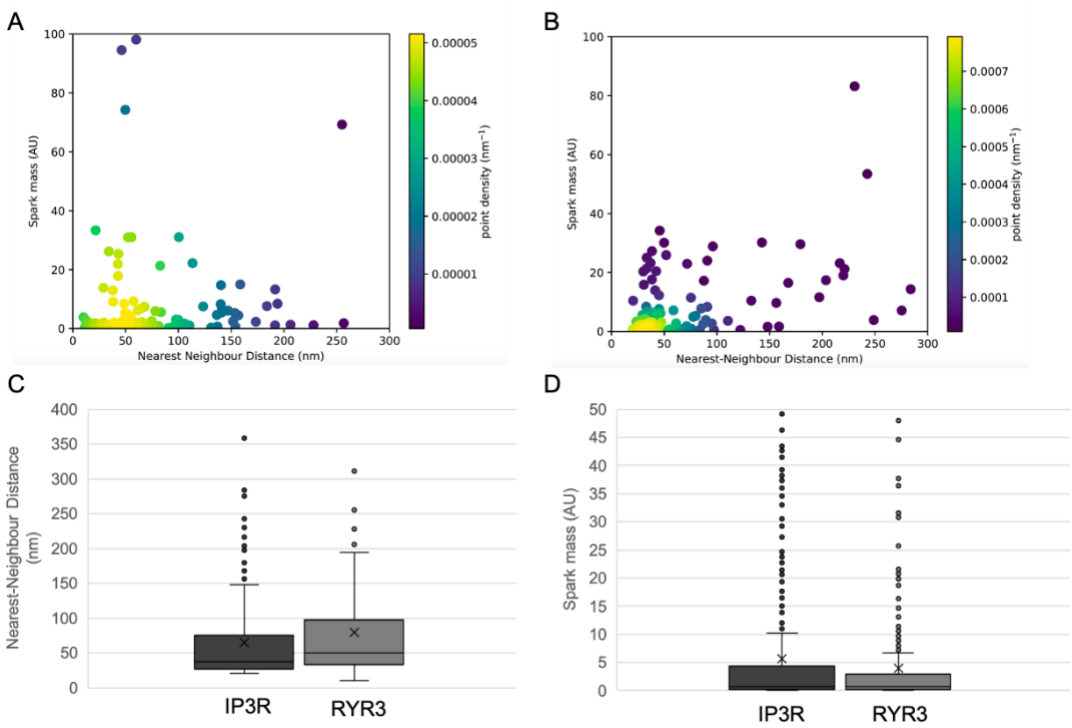

Figure 5.7: Relationship between the nearest neighbour distance of calcium handling proteins and the mass of locally generated calcium sparks. Correlative imaging protocol applied to dorsal root ganglia (DRG) sensory neurones from neonatal male Wistar rats. Point density scattergram was utilised to represent the shape of the data cloud, with yellow denoting the greatest density of unitary Ca^{2+} spark events. Quantitative analysis of (A) IP3R or (B) RyR3 nearest neighbour distance underneath a Ca^{2+} spark's spatial footprint was examined in relation to the respective mass of each Ca^{2+} spark. (C) The mean nearest neighbour distance was greater for RyR3 (grey) values than the IP3R (black) puncta, (D) despite a reduced range in spark mass. Values are mean±SEM; RyR3 n=7 cells; IP3R n=6 cells.

The observation of this relationship was strengthened when average NND was analysed, taking into account the distance between three neighbouring puncta (t-test; *p=0.01*). Specifically, the RyR3 staining pattern had a 26.14% greater average NND than within IP3R (Figure 5.8). This increased average NND within RyR3 was accompanied by a larger 38.40±13.64 AU spark mass, compared to that of 8.03±1.04 AU recorded in IP3R data. It is important to note that RyR3 has a 540 nm greater range in average NND values compared to IP3R puncta. This represents a greater variation in the RyR3 staining pattern. However, this increased variation in structure

morphology within RyR3 appears to be accompanied by an increased variation in spark mass with a 42.10% greater range present from Ca^{2+} sparks generated at the same location as RyR3 staining compared to IP3R staining. When the variation in point density was evaluated between RyR3 and IP3R, the densest regions of the points cloud (yellow) appear in regions that display either IP3R average NND between 50 and 150 nm or RyR3 average NND between 50 and 75 nm. Similar to the analysis in Figure 5.7, these observations suggest that the Ca^{2+} sparks in DRG soma arise more clearly when there is spatial proximity between multiple RyR3s. Their relationship to IP3R spacings may be random, if not weak.

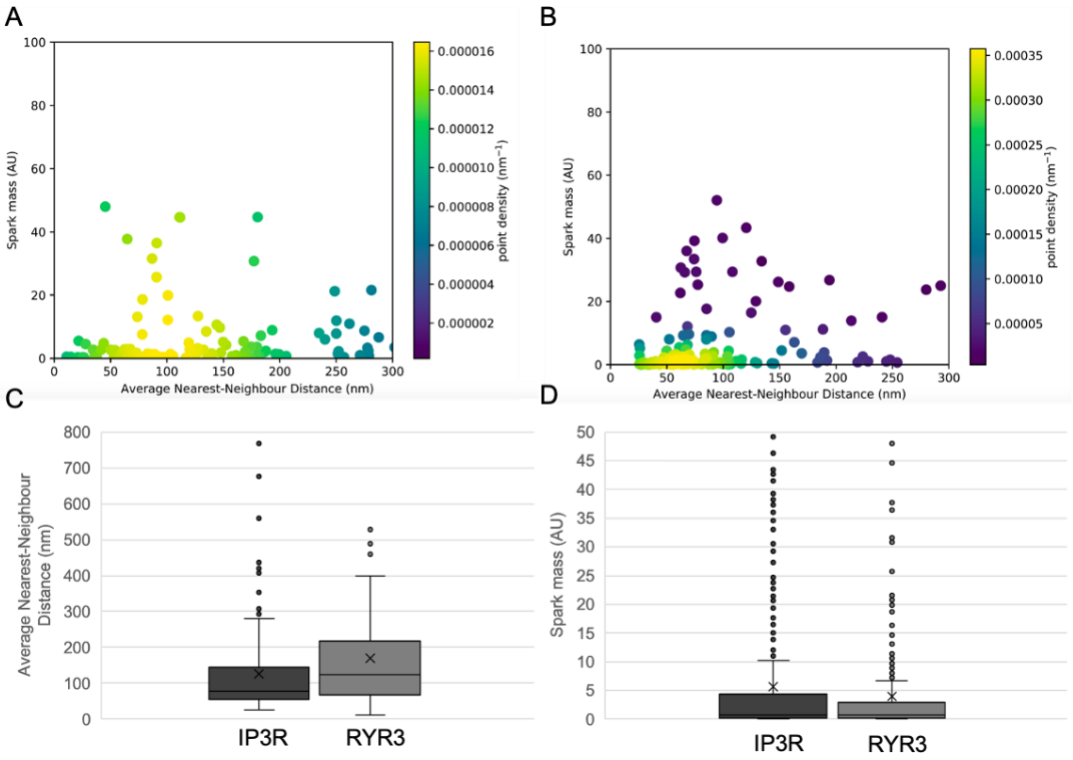

Figure 5.8: Relationship between the average nearest neighbour distance of calcium handling proteins and the mass of locally generated calcium sparks. Correlative imaging protocol applied to dorsal root ganglia (DRG) sensory neurones from neonatal male Wistar rats. Point density scattergram was utilised to represent the shape of the data cloud, with yellow denoting the greatest density of unitary Ca^{2+} spark events. Quantitative analysis of (A) IP3R or (B) RyR3 average nearest neighbour distance underneath a Ca^{2+} spark's spatial footprint was evaluated in regard to the respective mass of each Ca^{2+} spark. (C) The RyR3 (grey) staining pattern had a greater range in average nearest neighbour values compared to the IP3R (black) channel. (D) However, the spark mass was reduced within the Ca^{2+} spark profiles which were aligned with the RyR3 channel compared to the IP3R. Values are mean±SEM; RyR3 n=7 cells; IP3R n=6 cells.

5.4 Discussion

5.4.1 Structural organisation of calcium handling proteins

Literature upon the cluster orientation of Ca^{2+} handling proteins within the DRG sensory neurones is limited. Shah et al. (2020) undertook dSTORM analysis of the IP3R1 channel and identified a widespread punctate staining pattern at the near surface of the neurone, similar to observations within this study. Their analysis found IP3R1 clusters to be compact, with a radius of 50.8±1.4 nm (mean ± SEM). Due to a difference in analysis, this is not directly comparable with the research presented within this study which calculated cluster size based upon area. Specifically, this study based cluster area upon a binary mask created upon signal intensity combined with a puncta detection analysis to individually locate each puncta. Similar to IP3R1, the distribution of RyR3 at the cell periphery is widespread and abundant. RyR3 has a punctate cluster pattern, with puncta spaced an average 1.84±0.10 μm (mean ± SEM) apart (Ouyang et al., 2005b). When the assumption is made that each puncta represents one Ca^{2+} release channel, the study calculated a denser organisation of RyR3, with an average NND of 74.57±0.47 nm (mean ± SEM). Discrepancy within this organisation could be from an overestimation of distancing by Ouyang et al. (2005b) from their use of confocal microscopy compared to the choice of SMLM within this study. However, their alignment of RyR3 spacing with Ca^{2+} release sites supports the rationale of this research to study the structure of the Ca^{2+} release channel in regard to Ca^{2+} signalling. The RyR channel is known to be 30 nm^2 (Chen-Izu et al., 2006), with dSTORM data known to have a 20 nm xy spatial resolution. An assumption was made within this study that each punctum represented one Ca^{2+} handling protein. Further research is however required to ascertain the size of IP3R, RyR3 and SERCA within DRGs when visualised using dSTORM to ensure that small, tightly packed puncta are spatially resolved to avoid an overestimation as with previous dSTORM analyses (Baddeley et al., 2009b).

Previous literature has alluded to the placement of IP3R1 and RyR3 within a DRG sensory neurone based upon the cell's response to pharmacological agents. Specifically, the two Ca^{2+} release channels are suggested to interact

but have a varying distribution across the cell (Berridge, 1993). The research detailed within this study utilises SMLM to visualise the Ca^{2+} handling machinery within the DRGs. It was concluded that IP3R and RyR3 along with the Ca^{2+} re-uptake channel SERCA have a similar cluster pattern across the DRG and both Ca^{2+} release channels co-localise with SERCA to the same extent. Due to a limited choice in antibodies, the direct association between RyR3 and IP3R1 was not studied. At a local level, IP3R1 puncta were more sparse than RyR3 or SERCA. However, this was not noticeable when average NND was accounted for. Use of the correlative imaging protocol is therefore critical in understanding whether Ca^{2+} signalling is affected by the varied coupling of IP3R1 and RyR3 at a single channel level.

5.4.2 Stimulation of calcium spark activity

Within the DRG sensory neurones, Ca^{2+} sparks were detected across the diameter of the soma when imaging was undertaken at the near surface. When evoked, Ca^{2+} sparks occurred locally and did not propagate into Ca^{2+} waves. These characteristics mirror the Ca^{2+} spark recordings made by Ouyang et al. (2005a) and follows the suggestion of how the ER spans across the whole neuronal cell body (Solovyova et al., 2002; Thayer et al., 1988). This structural knowledge is of importance as IP3R and RyR3 activation concluded that channel opening depleted the same ER Ca^{2+} store (Irving et al., 1992).

Within a DRG, there are caffeine-sensitive stores. The application of the pharmacological agent can lead to Ca^{2+} release from the ER (Thayer et al., 1988). Specifically, caffeine is known to activate the RyR Ca^{2+} release channel across multiple cell types, including neurones (Ouyang et al., 2005b; Wu et al., 2013). Caffeine is known to increase RyR3 channel activity (Lokuta et al., 2002) and sensitise the CICR mechanism in a concentration-dependent manner (Usachev et al., 1993). The application of 1 mM caffeine increased Ca^{2+} spark frequency but had a negligible effect upon any other aspect of the Ca^{2+} spark kinetics. The variation by which FWHM decreased and spark mass increased could be due to a 5-fold difference in caffeine concentration used. This variation in concentration response requires further

research as it could suggest that caffeine has the ability to stimulate RyR3 channel activation but not gate the termination of the channel opening (Ouyang et al., 2005a). It should be considered that this study is measuring spontaneous Ca^{2+} spark kinetics from a small cellular region which is exploiting the physiological response which would be evident in vivo (Cheng and Lederer, 2008). To overcome this limitation, a future study could apply KCl to depolarise the neuronal cell and observe the physiological mechanism of CICR (Koizumi et al., 1999).

The sensitivity of a DRG sensory neurone to caffeine can vary in accordance with the density of Ca^{2+} handling proteins present (Shmigol et al., 1995; Shmigol et al., 1996). Within this study the analysis did not differentiate Ca^{2+} spark recordings based upon neuronal class. As a result, the response to pharmacological agents may vary across the sub-types of DRGs which could impact the percentage change recorded in Ca^{2+} spark morphology from 5 mM Ca^{2+} control. The extent of a pharmacological agents role upon RyR3 coupling and their interaction with other modulatory factors needs further investigation to fully elucidate the role of RyR3, IP3R and SERCA in maintaining Ca^{2+} homeostasis within the cytosol. It would be valuable to note that the response to caffeine is transient. Usachev and Thayer (1997) noted a return to basal Ca^{2+} signalling 3-6 minutes after a 5 mM caffeine application. Within this study, repeat applications of caffeine were not undertaken. Therefore, the extent of change in neuronal response to the pharmacological agent over time should be considered.

There is a reliance upon ER Ca^{2+} load to maintain a cell's response to caffeine. This was evidenced upon the administration of thapsigargin. When Ca^{2+} reuptake via SERCA was inhibited by thapsigargin the electrochemical gradient across the ER and cytosol was impaired due to the restoration of the ER Ca^{2+} load via SERCA, resulting in a depletion of the ER Ca^{2+} store. This alteration reduced the phenomenon of CICR and impaired Ca^{2+} signalling (Shmigol et al., 1994; Solovyova et al., 2002). Whilst this study did not analyse SERCA functionality, it did visualise a co-localisation between SERCA and the caffeine-sensitive RyR3 channel which suggests an

association between channel functionality. However, within the study of Solovyova et al. (2002), neither application of caffeine nor thapsigargin completely depleted the ER Ca^{2+} store. It was revealed that SERCA had a similar co-localisation with IP3R. This could suggest that complete ER store depletion could be prevented by a negative feedback loop initiated by the IP3R channel to preserve neuronal function. This feedback loop is possible due to the ability of the IP3R to open in response to changes in local cytosolic Ca^{2+} concentration. To understand the degree of channel interdependence around the ER, further research would benefit from measuring cytosolic and ER Ca^{2+} concentration (Solovyova et al., 2002).

Bradykinin is a nonapeptide and inflammatory mediator which has a role within nociceptive signalling. The binding of bradykinin to the B_1 or B_2 receptors upon the surface of a sensory neurone within the DRG can trigger a signalling cascade pathway. Specifically, the protein kinase C pathway can be activated. This can lead to the synthesis of IP3 and the activation of IP3Rs within the ER to trigger intracellular Ca^{2+} release (Thayer et al., 1988; Vellani et al., 2004). The release of Ca^{2+} mediated from bradykinin administration has been recorded within DRGs upon multiple occasions (Liu et al., 2010; Thayer et al., 1988).

The IP3R channel and B_2 receptor are considered to be tethered within the neurone by actin filaments (Delmas et al., 2002). Application of bradykinin is known to elicit an increase in cytoplasmic Ca^{2+} concentration (Shah et al., 2020). Within this study, the application of 250 nM bradykinin mobilised the ER Ca^{2+} store but caused a marked reduction in FWHM from increased IP3R channel activity. It should be noted that previous research has revealed bradykinin has a less extensive effect across DRG sensory neurones compared to caffeine (Thayer et al., 1988). A study by Koizumi et al. (1999) upon hippocampal neurones revealed that the stimulation of both IP3R and RyR3 channels evoked an ER Ca^{2+} release across the whole neurone. According to Ca^{2+} spark release sites, both channels are in part co-localised, supporting the SMLM findings within this study. It was concluded that the Ca^{2+} spark evoked by either caffeine or bradykinin is similar in

morphology, with the percentage change from 5 mM Ca^{2+} control not being significantly different between the two stimulants. This view is supported by Thayer et al. (1988) who noted no physiological difference in Ca^{2+} transients evoked from bradykinin or caffeine exposure. This research concludes, therefore, that both IP3R and RyR3 are involved within Ca^{2+} spark generation within DRG sensory neurones. However, similar to the data presented within this study, Koizumi et al. (1999) noted that the caffeine response had a shorter spatial spread in regard to FWHM than within bradykinin evoked Ca^{2+} sparks. FWHM can be affected by a range of factors including the local cytoplasmic diffusion of Ca^{2+} and Fluo4-AM dye. In addition, FWHM can also be determined by the number of Ca^{2+} release channels recruited within a cell. The latter variable could be enhanced by bradykinin compared to caffeine application.

Although bradykinin is considered a well-chosen IP3R channel activator (Delmas et al., 2002), caffeine is considered to have an inhibitory role upon the IP3R channel. The application of 5 mM caffeine can decrease IP3R activity 3-fold (Bezprozvanny et al., 1994; Koizumi et al., 1999). This suggests that RyR3 has a more influential role in the generation of spontaneous Ca^{2+} sparks. Such an assumption could explain the greater change in spark mass upon caffeine administration within this study. Similar findings by others (Boittin et al., 1998; Koizumi et al., 1999; Parker et al., 1996a) have even suggested that IP3R has a role in only initiating a Ca^{2+} puff, with the amplification into a Ca^{2+} spark being reliant upon RyR3 activation. Non-specific targets of pharmacological stimulants exemplify the current uncertainties within the literature regarding single channel functionality. For example, responses with bradykinin administration cannot negate the role of RyR3. This provides a rationale for the developed correlative imaging protocol to study the functional and structural properties of a cell in combination.

5.4.3 Inhibition of calcium spark activity

This study utilised varying concentrations of tetracaine and 2-APB to inhibit the RyR3 and IP3R1 channel respectively. The role of 2-APB as an IP3R

inhibitor was first documented by Maruyama et al. (1997). It is well suited for this research due to it having the inability to inhibit the RyR channel (Maruyama et al., 1997). The role of 2-APB in mediating Ca^{2+} release within DRG sensory neurones has been evidenced by several research groups (Bootman et al., 2002; Lu et al., 2006; Ouyang et al., 2005a). The RyR3 channel can be inhibited by tetracaine and lead to the elimination of RyR mediated Ca^{2+} sparks within DRGs (Ouyang et al., 2005a). The activation of RyR was prevented by the presence of tetracaine within DRGs (Lokuta et al., 2002). Specifically, the local anaesthetic is known to reduce the RyR's open probability in a concentration-dependent manner to reduce Ca^{2+} release from the cell's internal store (Csernoch et al., 1999).

Regardless of concentration or pharmacological agent there was a significant decrease in r^2 value recorded. This variable needs to be analysed with caution as it is largely reflective of the signal to noise ratio. Upon the administration of tetracaine, this study recorded a concentration dependent decrease in FWHM, with no change in spark mass. One explanation for a constant spark mass despite a decreased FWHM could be due to a concurrent change in Ca^{2+} spark amplitude. This is in contrast to Ouyang et al. (2005a) and Westcott et al. (2012) who abolished Ca^{2+} sparks with a 1 mM and 100 μM tetracaine dose. However, it is reflective of Curtis et al. (2008) who found a decreasing FWHM in line with an increased tetracaine concentration.

Future studies would benefit from measuring the change in Ca^{2+} spark frequency to evaluate the degree of change in RyR3 channel gating by tetracaine. Care should be taken with the interpretation of tetracaine as an RyR3 inhibitor. At comparable concentrations to those used within this study, the pharmacological agent has been known to simultaneously inhibit the IP3R response and Na^{+} current across the plasmalemma (MacMillan et al., 2005; Sugiyama and Muteki, 1994). Both of these non-specific mechanisms of tetracaine can vary the cellular response across the neuronal population.

The application of 2-APB is considered to inhibit IP3R1-mediated Ca^{2+} release (Maruyama et al., 1997). However, regardless of concentration, within this study 2-APB did not alter spark mass and only decreased FWHM when 100 μM concentration was administered. This minimal response to 2-APB was reflected within the literature whereby 20 μM 2-APB failed to ablate Ca^{2+} spark activity (Ouyang et al., 2005a). The change in Ca^{2+} signalling by 2-APB could be non-specific. Missiaen et al. (2001) suggested that 2-APB can bind to the IP3R in a non-competitive manner to IP3 to inhibit the channel in part. However, they also noted that a 100 μM 2-APB, similar to this study, was responsible for a 50% decrease in ER Ca^{2+} load from a probable non-specific inhibition of SERCA. Therefore, the change in Ca^{2+} spark morphology could be independent of the Ca^{2+} release channel, as reviewed by Bootman et al. (2002) who claimed 2-APB to have a role even in the absence of IP3R (Prakriya and Lewis, 2001). Furthermore, the minimal degree of selectivity to IP3R is believed to vary across receptor isoforms, with IP3R1 channels targeted most (Bootman et al., 2002; Kukkonen et al., 2001). The IP3R inhibitor should therefore be used with caution and any difference in Ca^{2+} spark kinetics should be analysed in regard to the known limitations of the inhibitor (Bootman et al., 2002). Unfortunately, no ideal IP3R antagonist is available (Bootman et al., 2002). This limitation in study design promotes the requirement to study channel placement within a cell in regard to its functional release of Ca^{2+}.

The study of 2-APB further revealed the pharmacological agent to have a non-specific inhibition upon SOCE due to the interaction of IP3R within the Ca^{2+} signalling process (Ma et al., 2000). Specifically, 2-APB is considered to inhibit the CRAC channel current which is part of the SOCE response (Kukkonen et al., 2001). Within the SOCE complex, ANO1 tethers the PM to the ER within DRG sensory neurones and is deemed critical to the Ca^{2+} signalling process from interaction within the B_2 receptor and IP3R channel (Cabrita et al., 2017; Jin et al., 2013; Kunzelmann et al., 2016). It should be remembered, therefore, that additional Ca^{2+} regulatory mechanisms are involved beyond the RyR3 and IP3R channels studied here.

Investigations regarding cellular Ca^{2+} signalling should therefore not just be undertaken at the single channel level but take into account the whole JMC. The work of Hogea et al. (2019) supports this approach. They applied 250 nM bradykinin to DRG sensory neurones. Alongside Ca^{2+} release from the ER via IP3R they also recorded stimulation of the SOCE mechanism. Maintenance of this response was suggested to be due to a tethering of the PM to the ER by the protein JPH4. In particular, the STIM1 and Orai1 regions of the SOCE complex were co-immunoprecipitated with JPH4 and co-localised from dSTORM observations. The extent to which the SOCE complex is reliant upon JPH4's role as a membrane tether was demonstrated in a knock-down study. When JPH4 expression was reduced, the IP3R response and consequent SOCE activation to bradykinin was less apparent. In addition, the NCX should be analysed, with inhibition of the Ca^{2+} efflux pathway known to impair Ca^{2+} signalling across the neurone (Verdru et al., 1997).

5.4.4 Application of the correlative imaging protocol

The use of pharmacological agents is convoluted, as can be evidenced from their application within this study. An additional method for understanding Ca^{2+} signalling based upon the role of Ca^{2+} handling channels is the application of the developed correlative imaging protocol. When applied to DRG sensory neurones, spark mass can be evaluated in relation to RyR3 and IP3R orientation. There was a greater mean mass recorded for Ca^{2+} sparks that originated from regions which had underlying IP3R density compared to RyR3 density. This was accompanied by a greater range in IP3R density being observed underneath detected Ca^{2+} sparks which suggests a differing role of RyR3 and IP3R in the generation of Ca^{2+} sparks. The sensitivity of both IP3R and RyR3 to Ca^{2+} can ensure that channel activity is regulated through feedback loops to maintain Ca^{2+} homeostasis across the neurone (Foskett et al., 2007; Simpson et al., 1995). No variation within cluster morphology was detected at a neuronal level within this immunofluorescence study. However, when the local RyR3 and IP3R structure was evaluated at the initiation site of a Ca^{2+} spark there were apparent differences. Most noticeably, the RyR3 cluster size was

significantly smaller compared to IP3R, suggesting that fewer RyR3 channels need to be functionally coupled to generate a larger Ca^{2+} signal from the ER store compared to IP3R recruitment. This study has visualised the ability of these Ca^{2+} handling proteins to cluster and suggests that RyR3 channel activation has an increased reliance upon channel coupling compared to IP3R. One suggestion could be that the enhanced coupled properties of the RyR3 channel ensure that fewer RyR3 proteins are required to generate Ca^{2+} sparks comparable to those present within the IP3R data.

We have previously suggested that the observation of spark mass in relation to the underlying overall count of a Ca^{2+} release channel can detract from the local relationship between Ca^{2+} spark morphology and the structural organisation of the channels that enable such a function. Due to the diffraction-limited nature of live-cell Ca^{2+} imaging, a more accurate study of structural organisation is the NND which accounts for the placement of Ca^{2+} release channels, regardless of count. When NND and average NND was locally analysed in regard to spark mass, the majority of Ca^{2+} sparks originated from cellular regions which had a nearly 2-fold smaller range in distances between RyR3 puncta compared to IP3R puncta. Therefore, although there was no significant difference between IP3R and RyR3 mean NND values, there was an ability for a tightly clustered RyR3 protein pattern to produce Ca^{2+} sparks of comparable mass to regions where IP3R had a more fragmented patterning. This finding reflects the importance of studying a Ca^{2+} handling proteins coupled functional role.

Crucially, such conclusions can only be made when the local structure and function of the JMC can be studied in relation to each other. Further study is required to understand whether additional modulatory factors, such as phosphorylation, can impact the coupling of RyR3 and IP3R at these sites. Specifically, the coupled nature of IP3R and RyR3 needs to be studied to further understand the role of RyR3 activation in response to IP3R gating, with previous research suggesting that IP3R activation is considered to generate small releases of Ca^{2+} which can trigger RyR3 Ca^{2+} spark

generation (Foskett et al., 2007). The sensitivity of this correlative imaging protocol to this proposed sequential mechanism is unknown.

5.4.5 Concluding remarks

The correlative imaging protocol provided a non-pharmacological approach to analyse the relationship between Ca^{2+} signalling and the structure of Ca^{2+} handling proteins at a local level. Current understanding regarding the role of IP3R and RyR3 within CICR remains largely unknown due to the inability to isolate channel function. However, this study has been able to visualise how the orientation of multiple Ca^{2+} handling proteins can impact the morphology of a Ca^{2+} spark generated.

It is worth remembering that within this study only spontaneous Ca^{2+} sparks were examined under conditions where mechanisms like SOCE and activation of bradykinin-stimulated receptors are unlikely to be naturally active. Therefore, the IP3R channel should not be discounted for its role in Ca^{2+} signalling. A future experiment to further understand the physiological role of RyR3 and IP3R across the ER Ca^{2+} stores could be the examination of electrically evoked Ca^{2+} sparks under varying frequency.

The developed correlative imaging study highlights the role of RyR3 and IP3R as Ca^{2+} release channels upon the ER. Within the soma of DRGs, the generation of a Ca^{2+} spark was clearer when there was a spatial proximity between the RyR3 channel. This suggests that RyR3 and IP3R have a differing role in regard to the generation of Ca^{2+} sparks from the ER. Multiple variables are involved within Ca^{2+} signalling in addition to the two channels studied within this research. Most notably, further investigation regarding the role of SOCE within Ca^{2+} signalling is required to understand how JPH4 can modulate Ca^{2+} release from the ER and exacerbate the initial CICR mechanism. It would be beneficial for future research to also account for DRG sensory neurone classification. This would account for any heterogeneity in Ca^{2+} signalling and density of Ca^{2+} handling proteins across the sub-classes of DRG’s in accordance with their physiological function.

Chapter 6. Broader perspectives

Within cell signalling, Ca^{2+} has a ubiquitous role. The release of Ca^{2+} from its internal store occurs at the level of the JMC, alternatively known as the CRU. The relationship between the ultrastructure of the JMC and local Ca^{2+} signalling has been of great interest within research. However, no experimental methodology has been available to study this Ca^{2+} handling structure and function within a primary cell type. Within this study, a correlative imaging protocol was developed to overcome this limitation within the discipline. Such a protocol has a benefit to the biophysicist in their study of cellular mechanisms in regard to cellular function. Applicable to this study is the benefit to the biologist, through the provision of a protocol which enables the study of protein distribution alongside cellular function. Specifically, the structure of a JMC can be visualised at an xy spatial resolution of <10 nm through application of SMLM, namely DNA-PAINT, and aligned with previously recorded Ca^{2+} spark profiles.

Application of the developed correlative imaging protocol has enabled the heterogeneity of a cell's structure to be studied in relation to cellular function. Specifically, the known decrease in RyR2 cluster size and fragmentation of the protein pattern within RV HF (Crossman et al., 2011; Sheard et al., 2019) was evaluated in relation to Ca^{2+} spark morphology and compared to the saline control. Within Control animals, a relationship was apparent between the orientation of RyR2 and the local functional Ca^{2+} sparks generated. This relationship was dampened within the RV HF model. In alignment with the literature, within RV HF an increased distance between neighbouring RyR2 puncta was detected. Most notably, a rightward dispersal was evidenced within the Fail animals, with an increased density of Ca^{2+} sparks being generated from regions which had a more fragmented RyR2 pattern, compared to within Control animals. The role of RyR2 coupling and modulation of RyR2 gating has been suggested to contribute towards this finding. However, structural remodelling of a cardiomyocyte is varied within HF due to the rate and degree of disease progression.

This correlative imaging protocol does not allow for whole heart function to be examined but instead focusses upon the generation of Ca^{2+} sparks at a local level to the CRU. Implementation of an additional optical mapping stage would allow membrane potential and Ca^{2+} transients across the whole heart to be recorded. This would explore how the ultrastructure and local Ca^{2+} signalling within an isolated cardiomyocyte translates to whole heart function in health and disease. In turn, this would be an invaluable tool to understand whether arrhythmia generation arises from structural remodelling of a heart's specialised conduction system.

Versatility of the correlative imaging protocol was displayed through its application to a second cell type; DRG sensory neurones. Previous research has focussed upon the use of pharmacological agents to study the Ca^{2+} release channels responsible for Ca^{2+} spark generation. However, pharmacological agents have poor selectivity for IP3R and RyR3 leading to their respective role in Ca^{2+} spark fidelity being largely unknown (Bootman et al., 2002; Koizumi et al., 1999; Ma et al., 2000; MacMillan et al., 2005). This study identified involvement of both RyR3 and IP3R in the release of Ca^{2+} from the ER. Further research is required to study the physiological release of Ca^{2+} from the ER in relation to IP3R and RyR3 distribution. Specifically, electrical stimulation of DRGs should next be undertaken to initiate Ca^{2+} sparks in a manner which enables the IP3R-mediated SOCE and B_2 receptor pathway to be active.

Additional application of the correlative imaging protocol would further the understanding of Ca^{2+} signalling within biological processes. For example, INS1 cells are a cell-line of the pancreatic β-cell. Its role of insulin secretion is mediated by the activation of voltage gated Ca^{2+} channels upon the detection of glucose (Choi et al., 2011; Gilon et al., 1993; Wollheim and Sharp, 1981; Yang and Berggren, 2006). The mechanism of CICR has been reported within INS1 cells, with IP3R and RyR known to release Ca^{2+} from the ER in response to voltage gated Ca^{2+} channel activation (Choi et al., 2011). Application of the correlative imaging protocol would reveal the degree by which protein organisation of a cell and channel function can

control the release of insulin in response to changing blood glucose concentrations. Ultimately, this could further understanding within the research community of how the mechanism of blood glucose sensitivity alters within diabetes.

Regardless of application, the correlative imaging protocol would benefit from being able to study Ca^{2+} channel opening in real-time. This has been undertaken by Hiess et al. (2018) with the use of GFP-tagged RyR2 channels within cardiomyocytes. They visualised RyR2 channel opening simultaneous to Ca^{2+} spark generation. However, the structural and functional xy spatial resolution of this study was limited to 250 nm. The ability to specifically probe Ca^{2+} release channels which are active within primary wild-type cells at an xy spatial resolution <10 nm would enable the proteins responsible for Ca^{2+} spark generation to be studied directly. This is unlike the current protocol which investigates all channels underneath a Ca^{2+} spark's spatial footprint. One approach to target active RyR2 channels has been the use of the peptide ligand imperacalcin and DPc10 (Valdivia et al., 1992; Yamamoto and Ikemoto, 2002); however, so far this approach has lacked specificity. Development of a specific ligand which can competitively bind to and activate Ca^{2+} handling proteins would enable specific channels to be visualised simultaneous to Ca^{2+} movement. Alternatively, recent advancement in super-resolution microscopy have enabled cells to be imaged for their structure in real-time at an xy spatial resolution beyond the diffraction limit of light (Jones et al., 2011). This continual development would enable Ca^{2+} signalling and JMC structure to be visualised sequentially within live cells and remove many of the limitations that arise from a separate immunofluorescence protocol. However, currently DNA-PAINT remains the most suitable method to study proteins at <10 nm spatial scale.

As discussed within this research, Ca^{2+} sparks are not only a product of RyR or IP3R organisation. Activation of the Ca^{2+} release channel can be modulated by multiple processes, including; luminal and cytosolic Ca^{2+} concentration, phosphorylation of the channel itself or the role of membrane tethers such as JPH. In addition, surrounding ion channels and pumps such

as NCX and SERCA can also modulate the propensity by which an RyR and IP3R gate their Ca^{2+} release. Any future application of the correlative imaging protocol would therefore benefit from further understanding of Ca^{2+} channel activity.

In summary, the aims of this study were to develop an alternative protocol which could be used as a tool to experimentally study the ultrastructure and local Ca^{2+} signalling of a cell in relation to each other. This aim has been achieved. So far, application of the correlative imaging protocol has enabled the structural and functional remodelling within RV HF to be studied in regard to each other. Furthermore, the role of Ca^{2+} release channels in regard to the CICR mechanism have been evaluated within DRG sensory neurones. This displays the protocol's versatility and potential for multiple applications to further understanding of Ca^{2+} signalling within systems biology.

Appendix A

Oligonucleotide	K_{on} (M^{-1}/s^{-1})	K_{off} (s^{-1})	K_D (μM)
P1	701,253 ± 105,011	0.189 ± 0.01	0.274 ± 0.05
P2	676,667 ± 381,389	0.204 ± 0.02	0.377 ± 0.21
P3	768,000 ± 218,625	0.182 ± 0.04	0.261 ± 0.13

Appendix A 1: Affinity of DNA-PAINT imager probes. Association rate (K_{On}), Dissociation rate (K_{Off}) and Dissociation constant (K_D) of oligonucleotide strands; P1, P2 and P3. Values are calculated from surface plasmon resonance and interactions applied 1:1 to a Langmuir Isotherm binding model. Data collected and analysed by Ashlea Rowley at The University of Leeds. Values are mean±SD; n=3.

Reference List

Abbe, E., (1873) Beiträge zur Theorie des Mikroskops und der mikroskopischen Wahrnehmung. Archiv f. mikrosk. Anatomie 9, 413–468.

Agasti, S.S. et al. (2017) DNA-barcoded labeling probes for highly multiplexed Exchange-PAINT imaging. Chem. Sci. 8, 3080–3091.

Albada, M.E. et al. (2005) The role of increased pulmonary blood flow in pulmonary arterial hypertension. European Respiratory Journal 26, 487–493.

Ambrosy, A.P. et al. (2014) The Global Health and Economic Burden of Hospitalizations for Heart Failure: Lessons Learned From Hospitalized Heart Failure Registries. Journal of the American College of Cardiology 63, 1123–1133.

Anker, S.D. and Sharma, R. (2002) The syndrome of cardiac cachexia. Int. J. Cardiol. 85, 51–66.

Armoundas, A.A. et al. (2007) Cellular and Molecular Determinants of Altered Ca2+ Handling in the Failing Rabbit Heart. Am J Physiol Heart Circ Physiol 292, H1607–H1618.

Asghari, P. et al. (2020) Cardiac ryanodine receptor distribution is dynamic and changed by auxiliary proteins and post-translational modification. eLife 9, e51602.

Asghari, P. et al. (2014) Nonuniform and variable arrangements of ryanodine receptors within mammalian ventricular couplons. Circ. Res. 115, 252–262.

Auer, A. et al. (2017) Fast, Background-Free DNA-PAINT Imaging Using FRET-Based Probes. Nano Lett. 17, 6428–6434.

Baddeley, D. et al. (2011) 4D Super-Resolution Microscopy with Conventional Fluorophores and Single Wavelength Excitation in Optically Thick Cells and Tissues. PLoS One 6.

Baddeley, D. et al. (2009a) Light-Induced Dark States of Organic Fluochromes Enable 30 nm Resolution Imaging in Standard Media. Biophysical Journal 96, L22–L24.

Baddeley, D. et al. (2009b) Optical single-channel resolution imaging of the ryanodine receptor distribution in rat cardiac myocytes. PNAS 106, 22275–22280.

Beavers, D.L. et al. (2013) Mutation E169K in junctophilin-2 causes atrial fibrillation due to impaired RyR2 stabilization. J Am Coll Cardiol 62.

Benoist, D. et al. (2014) Systems approach to the study of stretch and arrhythmias in right ventricular failure induced in rats by monocrotaline. Prog Biophys Mol Biol 115, 162–172.

Benoist, D. et al. (2011) Arrhythmogenic substrate in hearts of rats with monocrotaline-induced pulmonary hypertension and right ventricular hypertrophy. Am J Physiol Heart Circ Physiol 300, H2230–H2237.

Benoist, D. et al. (2012) Cardiac arrhythmia mechanisms in rats with heart failure induced by pulmonary hypertension. Am J Physiol Heart Circ Physiol 302, H2381–H2395.

Berlier, J.E. et al. (2003) Quantitative comparison of long-wavelength Alexa Fluor dyes to Cy dyes: fluorescence of the dyes and their bioconjugates. J. Histochem. Cytochem. 51, 1699–1712.

Berridge, M.J. (1998) Neuronal Calcium Signaling. Neuron 21, 13–26.

Berridge, M.J. (1993) Inositol trisphosphate and calcium signalling. Nature 361, 315–325.

Berridge, M.J. et al. (2000) The versatility and universality of calcium signalling. Nature Reviews Molecular Cell Biology 1, 11–21.

Bers, D. (2001) Excitation-Contraction Coupling and Cardiac Contractile Force. Springer Science & Business Media.

Bers, D.M. (2002) Cardiac excitation-contraction coupling. Nature 415 (6868), 198-205.

Bers, D.M. (2008) Calcium Cycling and Signaling in Cardiac Myocytes. Annu. Rev. Physiol. 70, 23–49.

Bers, D.M. and Stiffel, V.M. (1993) Ratio of ryanodine to dihydropyridine receptors in cardiac and skeletal muscle and implications for E-C coupling. American Journal of Physiology-Cell Physiology.

Bers D.M. et al. (2003) Sarcoplasmic Reticulum Ca2+ and Heart Failure. Circulation Research 93, 487–490.

Betzig, E. et al. (2006) Imaging Intracellular Fluorescent Proteins at Nanometer Resolution. Science 313, 1642–1645.

Bezprozvanny, I. et al. (1994) Caffeine-induced inhibition of inositol(1,4,5)-trisphosphate-gated calcium channels from cerebellum. Mol Biol Cell 5, 97–103.

Bidasee, K.R. et al. (2003) Streptozotocin-Induced Diabetes Increases Disulfide Bond Formation on Cardiac Ryanodine Receptor (RyR2). J Pharmacol Exp Ther 305, 989–998.

Blumhardt, P. et al. (2018) Photo-Induced Depletion of Binding Sites in DNA-PAINT Microscopy. Molecules 23, 3165.

Boittin, F.X. et al. (1998) Inositol 1,4,5-trisphosphatem and ryanodine sensitive Ca2+ release channel-dependent Ca2+ signalling in rat portal vein myocytes. Cell Calcium 23, 303–311.

Bootman, M.D. et al. (2002) 2-Aminoethoxydiphenyl borate (2-APB) is a reliable blocker of store-operated Ca2+ entry but an inconsistent inhibitor of InsP3-induced Ca2+ release. The FASEB Journal 16, 1145–1150.

Breitwieser, G.E. (2008) Extracellular calcium as an integrator of tissue function. Int J Biochem Cell Biol 40, 1467–1480.

Brette, F. and Orchard, C. (2003) T-Tubule Function in Mammalian Cardiac Myocytes. Circulation Research 92, 1182–1192.

Bridge, J.H.B. et al. (1999) Properties of Ca2+ sparks evoked by action potentials in mouse ventricular myocytes. J Physiol 518, 469–478.

Brochet, D.X.P. et al. (2011) Quarky Calcium Release in the Heart. Circ Res 108, 210–218.

Cabrita, I. et al. (2017) Differential effects of anoctamins on intracellular calcium signals. The FASEB Journal 31, 2123–2134.

Cannell, M.B. et al. (1994) Spatial non-uniformities in [Ca2+]i during excitation-contraction coupling in cardiac myocytes. Biophys J 67, 1942–1956.

Cannell, M.B. and Soeller, C. (1997) Numerical analysis of ryanodine receptor activation by L-type channel activity in the cardiac muscle diad. Biophys J 73, 112–122.

Chacko, J.V. et al. (2013) Sub-Diffraction Nano Manipulation Using STED AFM. PLoS One 8.

Chen, Y. et al. (2012) Left ventricular failure produces profound lung remodeling and pulmonary hypertension in mice: heart failure causes severe lung disease. Hypertension 59, 1170–1178.

Cheng, H. and Lederer, W.J. (2008) Calcium Sparks. Physiological Reviews 88, 1491–1545.

Cheng, H. et al. (1993) Calcium sparks: elementary events underlying excitation-contraction coupling in heart muscle. Science 262, 740–744.

Chen-Izu, Y. et al. (2006) Three-Dimensional Distribution of Ryanodine Receptor Clusters in Cardiac Myocytes. Biophys J 91, 1–13.

Choi, K.J. et al. (2011) Ca2+-induced Ca2+ Release from Internal Stores in INS-1 Rat Insulinoma Cells. Korean J Physiol Pharmacol 15, 53–59.

Clapham, D.E. (1995) Calcium signaling. Cell 80, 259–268.

Clowsley, A.H. et al. (2020) Repeat DNA-PAINT suppresses background and non-specific signals in optical nanoscopy. bioRxiv 2020.04.24.059410.

Cohn, J.N. et al. (2000) Cardiac remodeling--concepts and clinical implications: a consensus paper from an international forum on cardiac remodeling. Behalf of an International Forum on Cardiac Remodeling. J. Am. Coll. Cardiol. 35, 569–582.

Cole, R.W. et al. (2011) Measuring and interpreting point spread functions to determine confocal microscope resolution and ensure quality control. Nature Protocols. 6, 1929-1941.

Croix, C.M. et al. (2005) Confocal microscopy: comparisons, applications, and problems. BioTechniques 39, S2–S5.

Cosentino, M. et al. (2019) AFM-STED correlative nanoscopy reveals a dark side in fluorescence microscopy imaging. Sci Adv 5.

Cosi, F.G. et al. (2019) Multiscale Modeling of Dyadic Structure-Function Relation in Ventricular Cardiac Myocytes. Biophysical Journal 117, 2409–2419.

Crossman, D.J. et al. (2015) Combining confocal and single molecule localisation microscopy: A correlative approach to multi-scale tissue imaging. Methods, Super-resolution Light Microscopy 88, 98–108.

Crossman, D.J. et al. (2017) Transverse tubule remodelling: a cellular pathology driven by both sides of the plasmalemma? Biophys Rev 9, 919–929.

Crossman, D.J. et al. (2011) Changes in the Organization of Excitation-Contraction Coupling Structures in Failing Human Heart. PLOS ONE 6, e17901.

Csernoch, L. et al. (1999) Effects of tetracaine on sarcoplasmic calcium release in mammalian skeletal muscle fibres. J Physiol 515, 843–857.

Curtis, T.M. et al. (2008) Modification of smooth muscle Ca2+-sparks by tetracaine: Evidence for sequential RyR activation. Cell Calcium 43, 142–154.

Delmas, P. et al. (2002) Signaling Microdomains Define the Specificity of Receptor-Mediated InsP3 Pathways in Neurons. Neuron 34, 209–220.

Dickson, R.M. et al. (1997) On/off blinking and switching behaviour of single molecules of green fluorescent protein. Nature 388, 355–358.

Drawnel, F.M. et al. (2012) Mutual antagonism between IP3RII and miRNA-133a regulates calcium signals and cardiac hypertrophy. J Cell Biol 199, 783–798.

Elbaz, Y. and Schuldiner, M. (2011) Staying in touch: the molecular era of organelle contact sites. Trends in Biochemical Sciences 36 (11), 616-623.

Endo, M. (2009) Calcium-Induced Calcium Release in Skeletal Muscle. Physiological Reviews 89, 1153–1176.

Evans, W.J. et al. (2008) Cachexia: a new definition. Clin Nutr 27, 793–799.

Fabiato, A. (1983) Calcium-induced release of calcium from the cardiac sarcoplasmic reticulum. Am. J. Physiol. 245, C1-14.

Fabiato, A. and Fabiato, F. (1972) Excitation-Contraction Coupling of Isolated Cardiac Fibers with Disrupted or Closed Sarcolemmas: Calcium dependent cyclic and tonic contractions. Circulation Research 31, 293–307.

Fearnley, C.J. et al. (2011) Calcium Signaling in Cardiac Myocytes. Cold Spring Harb Perspect Biol 3, a004242.

Finch, E.A. et al. (1991) Calcium as a coagonist of inositol 1,4,5-trisphosphate-induced calcium release. Science 252, 443–446.

Fish, K.N. (2009) Total internal reflection fluorescence (TIRF) microscopy. Current protocols in cytometry, Unit 12.8

Foskett, J.K. et al. (2007) Inositol Trisphosphate Receptor Ca2+ Release Channels. Physiological Reviews 87, 593–658.

Fowler, E.D. et al. (2015) Decreased creatine kinase is linked to diastolic dysfunction in rats with right heart failure induced by pulmonary artery hypertension. J Mol Cell Cardiol 86, 1–8.

Fowler, E.D. et al. (2018) Beta1-adrenoceptor antagonist, metoprolol attenuates cardiac myocyte Ca2+ handling dysfunction in rats with pulmonary artery hypertension. J Mol Cell Cardiol 120, 74–83.

Franzini-Armstrong, C. (1994) Unraveling the ryanodine receptor. Biophys J 67, 2135–2136.

Franzini-Armstrong, C. et al. (1999) Shape, size, and distribution of Ca(2+) release units and couplons in skeletal and cardiac muscles. Biophys J 77, 1528–1539.

Friedberg, M.K. and Redington, A.N. (2014) Right Versus Left Ventricular Failure. Circulation 129, 1033–1044.

Friel, D.D. and Tsien, R.W. (1992) A caffeine- and ryanodine-sensitive Ca2+ store in bullfrog sympathetic neurones modulates effects of Ca2+ entry on [Ca2+]i. J Physiol 450, 217–246.

Galice, S. et al. (2018) Size Matters: Ryanodine Receptor Cluster Size Affects Arrhythmogenic Sarcoplasmic Reticulum Calcium Release. Journal of the American Heart Association 7, e008724.

Gallo, A. et al. (2016) Endoplasmic reticulum-plasma membrane associations: structures and functions. Annual Review of Cell and Developmental Biology 32(1), 279-301.

Garbino, A. et al. (2009) Molecular evolution of the junctophilin gene family. Physiological Genomics 37 (3), 175-186.

Garbino, A. and Wehrens, X.H. (2010) Emerging role of junctophilin-2 as a regulator of calcium handling in the heart. Acta Pharmacol Sin 31, 1019–1021.

Gibson, K.H. et al. (2014) Chapter 2 - Fluorescing the Electron: Strategies in Correlative Experimental Design, in: Müller-Reichert, T., Verkade, P. (Eds.), Methods in Cell Biology, Correlative Light and Electron Microscopy II. Academic Press, pp. 23–54.

Gilon, P. et al. (1993) Oscillations of secretion driven by oscillations of cytoplasmic Ca2+ as evidences in single pancreatic islets. J. Biol. Chem. 268, 22265–22268.

Gómez, A.M. et al. (1996) Defective excitation-contraction coupling in experimental cardiac hypertropy and heart failure. Science 276 (5313), 800-806.

Gomez-Arroyo, J.G. et al. (2012) The monocrotaline model of pulmonary hypertension in perspective. American Journal of Physiology – Lung Cellular and Molecular Physiology 302 (4), L363.

Gómez-Varela, A.I. et al. (2020) Simultaneous co-localized super-resolution fluorescence microscopy and atomic force microscopy: combined SIM and AFM platform for the life sciences. Scientific Reports 10, 1122.

Gong, H. et al. (2016) Simple Method To Prepare Oligonucleotide-Conjugated Antibodies and Its Application in Multiplex Protein Detection in Single Cells. Bioconjug. Chem. 27, 217–225.

Graefe, S. and Mohiuddin, S.S. (2020) Biochemistry, Substance P, in: StatPearls. StatPearls Publishing, Treasure Island (FL).

Guo, A. et al. (2014) Overexpression of junctophilin-2 does not enhance baseline function but attenuates heart failure development after cardiac stress. Proc Natl Acad Sci U S A 111, 12240–12245.

Gwathmey, J. K. et al. (1991) Contractile deactivation and uncoupling of crossbridges. Effects of 2,3-butanedione monoxime on mammalian myocardium. Circulation Research 69, 1280–1292.

Haberberger, R.V. et al. (2019) Human Dorsal Root Ganglia. Front. Cell. Neurosci. 13.

Hamel, V. et al. (2014) Correlative multicolor 3D SIM and STORM microscopy. Biomed. Opt. Express, BOE 5, 3326–3336.

Hampton, C.M. et al. (2017) Correlated fluorescence microscopy and cryo-electron tomography of virus-infected or transfected mammalian cells. Nat Protoc 12, 150–167.

Hanani, M. (2005) Satellite glial cells in sensory ganglia: from form to function. Brain Research Reviews 48, 457–476.

Harjola, V.P. et al. (2016) Contemporary management of acute right ventricular failure: a statement from the Heart Failure Association and the Working Group on Pulmonary Circulation and Right Ventricular Function of the European Society of Cardiology. European Journal of Heart Failure 18, 226–241.

Harzheim, D. et al. (2009) Increased InsP3Rs in the junctional sarcoplasmic reticulum augment Ca2+ transients and arrhythmias associated with cardiac hypertrophy. PNAS 106, 11406–11411.

Hatem, S. (2004) Does the loss of transverse tubules contribute to dyssynchronous Ca2+ release during heart failure? Cardiovasc Res 62, 1–3.

Hayashi, T. et al. (2009) Three-dimensional electron microscopy reveals new details of membrane systems for Ca^{2+} signalling in the heart. Journal of Cell Science 122 (Pt 7), 1005-1013.

Heilemann, M. et al. (2008) Subdiffraction-resolution fluorescence imaging with conventional fluorescent probes. Angew Chem Int Ed Engl 47 (33), 6172-6176.

Heinzel, F.R. et al. (2008) Remodeling of T-Tubules and Reduced Synchrony of Ca2+ Release in Myocytes From Chronically Ischemic Myocardium. Circulation Research 102, 338–346.

Helle, S.C.J. et al. (2013) Organization and function of membrane contact sites. Biochemica et Biophysica Acta- Molecular Cell Research 1833 (11), 2526-2541.

Henzi, V. and MacDermott, A.B. (1992) Characteristics and function of Ca2+ — and inositol 1,4,5-trisphosphate-releasable stores of Ca2+ in neurons. Neuroscience 46, 251–273.

Henne, W.M. et al. (2015) Molecular mechanisms of inter-organelle ER-PM contact sites. Current Opinion in Cell Biology 35, 123-130.

Hiess, F. et al. (2018) Dynamic and Irregular Distribution of RyR2 Clusters in the Periphery of Live Ventricular Myocytes. Biophysical Journal 114, 343–354.

Hiess, F. et al. (2015) Distribution and Function of Cardiac Ryanodine Receptor Clusters in Live Ventricular Myocytes. J. Biol. Chem. 290, 20477–20487.

Hirvonen, L.M. and Cox, S. (2018) STORM without enzymatic oxygen scavenging for correlative atomic force and fluorescence superresolution microscopy. Methods Appl Fluoresc 6, 045002.

Hobro, A.J. and Smith, N.I. (2017) An evaluation of fixation methods: Spatial and compositional cellular changes observed by Raman imaging. Vibrational Spectroscopy, Prominent Young Vibrational Spectroscopists 91, 31–45.

Hogea, A. et al. (2019) Junctophilin-4 is essential for signalling at plasma membrane-endoplasmic reticulum junctions in sensory neurons. bioRxiv 842476.

Hollingworth, S. (2001) Calcium sparks in intact skeletal muscle fibres of the frog. J Gen Physiol 118 (6), 653-678.

Hoshijima, M. et al. (2006) Reversal of Calcium Cycling Defects in Advanced Heart Failure: Toward Molecular Therapy. Journal of the American College of Cardiology, Critical Issues in Cardiovascular Research 48, A15–A23.

Hou, Y. et al. (2015) Nanoscale analysis of ryanodine receptor clusters in dyadic couplings of rat cardiac myocytes. Journal of Molecular and Cellular Cardiology 80, 45–55.

Hou, Y. et al. (2020) Correlating Calcium Sparks and Ryanodine Receptor Localization in Live Cardiomyocytes. Biophysical Journal 118, 567a.

Houser, S.R. (2001) Reduced abundance of transverse tubules and L-type calcium channels: another cause of defective contractility in failing ventricular myocytes. Cardiovasc Res 49, 253–256.

Houser, S.R. and Margulies, K.B. (2003) Is depressed myocyte contractility centrally involved in heart failure? Circulation Research 92 (4), 350.

Huang, L.Y. and Neher, E. (1996) Ca(2+)-dependent exocytosis in the somata of dorsal root ganglion neurons. Neuron 17, 135–145.

Huff, J. (2015) The Airyscan detector from ZEISS: confocal imaging with improved signal-to-noise ratio and super-resolution. Nature Methods 12, i–ii.

Huff, J. et al. (2017) The new 2D superresolution mode for ZEISS Airyscan. Nature Methods. 14, 1223.

Hurley, M.E. et al. (2020) A correlative super-resolution protocol to visualise structural underpinnings of fast second-messenger signalling in primary cell types. Methods. In Press

Ibrahim, M. et al. (2011) The structure and function of cardiac t-tubules in health and disease. Proc Biol Sci 278, 2714–2723.

Irving, A.J. et al. (1992) Interactions between Ca2+ mobilizing mechanisms in cultured rat cerebellar granule cells. The Journal of Physiology 456, 667–680.

Janeway, J. et al. (2001) The structure of a typical antibody molecule. Immunobiology: The Immune System in Health and Disease. 5th edition.

James, W.P.J. (1999) Ca2+ Signaling. Basic Neurochemistry: Molecular, Cellular and Medical Aspects. 6th edition.

Jayasinghe, I. et al. (2018a) True Molecular Scale Visualization of Variable Clustering Properties of Ryanodine Receptors. Cell Reports 22, 557–567.

Jayasinghe, I. et al. (2018b) Shining New Light on the Structural Determinants of Cardiac Couplon Function: Insights From Ten Years of Nanoscale Microscopy. Front. Physiol. 9.

Jayasinghe, I.D. et al. (2015) Revealing t-tubules in striated muscle with new optical super-resolution microscopy techniques. Eur J Transl Myol - Basic Appl Myol 25, 15-26.

Jayasinghe, I.D. et al. (2012) Nanoscale Organization of Junctophilin-2 and Ryanodine Receptors within Peripheral Couplings of Rat Ventricular Cardiomyocytes. Biophys J 102, L19–L21.

Jayasinghe, I.D. et al. (2009) Organization of Ryanodine Receptors, Transverse Tubules, and Sodium-Calcium Exchanger in Rat Myocytes. Biophysical Journal 97, 2664–2673.

Jin, X. et al. (2013) Activation of the Cl− Channel ANO1 by Localized Calcium Signals in Nociceptive Sensory Neurons Requires Coupling with the IP3 Receptor. Sci Signal 6, ra73.

Jones, S.A. et al. (2011) Fast three-dimensional super-resolution imaging of live cells. Nat Methods 8, 499–508.

Jungmann, R. et al. (2010) Single-molecule kinetics and super-resolution microscopy by fluorescence imaging of transient binding on DNA origami. Nano Lett. 10, 4756–4761.

Jungmann, R. et al. (2014) Multiplexed 3D cellular super-resolution imaging with DNA-PAINT and Exchange-PAINT. Nature Methods 11 (3), 313-318.

Jungmann, R. et al. (2016) Quantitative super-resolution imaging with qPAINT. Nat Meth 13 (5), 439-442.

Kane, C. and Terracciano, C.M.N. (2017) Concise Review: Criteria for Chamber-Specific Categorization of Human Cardiac Myocytes Derived from Pluripotent Stem Cells. Stem Cells 35, 1881–1897.

Kawai, M. et al. (1999) Excitation-contraction coupling in rat ventricular myocytes after formamide-induced detubulation. American Journal of Physiology-Heart and Circulatory Physiology 277, H603–H609.

Kawamura, K. et al. (1976) Ultrastructural changes in hypertrophied myocardium of spontaneously hypertensive rats. Jpn. Circ. J. 40, 1119–1145.

Kay, J.M. and Heath, D. (1966) Observations on the pulmonary arteries and heart weight of rats fed on Crotalaria spectabilis seeds. J Pathol Bacteriol 92, 385–394.

Kemp, C.D. and Conte, J.V. (2012) The pathophysiology of heart failure. Cardiovascular Pathology 21 (5), 365-371.

Khomula, E.V. and Voitenko, N.V. (2006) Dynamics of calcium release and uptake by the internal calcium stores in rat sensory neurons. Neurophysiology 38, 305–307.

Kirton, H.M. (2013) Transient overexpression of genes in neurones using nucleofection. Ion Channels, Methods in Molecular Biology.

Klabunde, R.E. (2012) Cardiovascular Physiology Concepts. Lippincott Williams & Wilkins

Klein, T. et al. (2014) Eight years of single-molecule localisation microscopy. Histochem Cell Biol 141 (6), 561-575.

Koizumi, S. et al. (1999) Characterization of Elementary Ca2+ Release Signals in NGF-Differentiated PC12 Cells and Hippocampal Neurons. Neuron 22, 125–137.

Kögler, H. et al. (2003) Mechanical load-dependent regulation of gene expression in monocrotaline-induced right ventricular hypertrophy in the rat. Circulation Research.

Kolb, H.C. et al. (2001) Click Chemistry: Diverse Chemical Function from a Few Good Reactions. Angewandte Chemie International Edition 40, 2004–2021.

Kolstad, T.R. et al. (2018) Ryanodine receptor dispersion disrupts Ca2+ release in failing cardiac myocytes. eLife 7, e39427.

Korecky, B. and Rakusan, K. (1978) Normal and hypertrophic growth of the rat heart: changes in cell dimensions and number. American Journal of Physiology-Heart and Circulatory Physiology 234, H123–H128.

Kukkonen, J.P. et al. (2001) 2-aminoethoxydiphenyl borate reveals heterogeneity in receptor-activated Ca(2+) discharge and store-operated Ca(2+) influx. Cell Calcium 30, 117–129.

Kukulski, W. et al. (2012) Precise, correlated fluorescence microscopy and electron tomography of lowicryl sections using fluorescent fiducial markers. Methods Cell Biol. 111, 235–257.

Kunzelmann, K. et al. (2016) Modulating Ca^{2+} signals: a common theme for TMEM16, Ist2, and TMC. Pflugers Arch. 468, 475–490.

Lanner, J.T. et al. (2010) Ryanodine Receptors: Structure, Expression, Molecular Details, and Function in Calcium Release. Cold Spring Harb Perspect Biol 2.

Lawson, S.N. (1992) Morphological and biochemical cell types of sensory neurones. Sensory Neurones: Diversity, Development and Plasticity. New York: Oxford University Press.

Leach, K.G. et al. (1975) In vivo assessment of liver size in the rat. Journal of Nuclear Medicine. 16, 380-385.

Lederer, W.J. et al. (1990) Sodium-calcium exchange in excitable cells: fuzzy space. Science 248, 283–283.

Levy, D. et al. (1990) Prognostic Implications of Echocardiographically Determined Left Ventricular Mass in the Framingham Heart Study.

Lindner, E. (1957) Submicroscopic morphology of the cardiac muscle. Z Zellforsch Mikrosk Anat 45, 702–746.

Lipp, P. et al. (2000) Functional InsP3 receptors that may modulate excitation-contraction coupling in the heart. Curr. Biol. 10, 939–942.

Lipp, P. and Niggli, E. (1996) A hierarchical concept of cellular and subcellular Ca2+-signalling. Progress in Biophysics and Molecular Biology 65, 265–296.

Liu, B. et al. (2010) The acute nociceptive signals induced by bradykinin in rat sensory neurons are mediated by inhibition of M-type K^+ channels and activation of Ca^{2+}-activated Cl^- channels. J Clin Invest 120, 1240–1252.

Liu, P.-S. et al. (1991) Caffeine-Sensitive Calcium Stores in Bovine Adrenal Chromaffin Cells. Journal of Neurochemistry 56, 172–177.

Llano, I. et al. (1994) Calcium-induced calcium release in cerebellar Purkinje cells. Neuron 12, 663–673.

Lokuta, A.J. et al. (2002) Functional properties of ryanodine receptors from rat dorsal root ganglia. FEBS Letters 511, 90–96.

Louch, W.E. et al. (2004) Reduced synchrony of Ca2+ release with loss of T-tubules—a comparison to Ca2+ release in human failing cardiomyocytes. Cardiovasc Res 62, 63–73.

Louch, W.E. et al. (2006) T-tubule disorganization and reduced synchrony of Ca2+ release in murine cardiomyocytes following myocardial infarction. J Physiol 574, 519–533.

Lu, S.-G. et al. (2006) Intracellular calcium regulation among subpopulations of rat dorsal root ganglion neurons. J Physiol 577, 169–190.

Lukyanenko, V. et al. (2009) Mitochondria in cardiomyocyte Ca2+ signaling. Int J Biochem Cell Biol 41, 1957–1971.

Lutz, T. et al. (2018) Versatile multiplexed super-resolution imaging of nanostructures by Quencher-Exchange-PAINT. Nano Res. 11, 6141–6154.

Lyon, A.R. et al. (2012) Plasticity of surface structures and β2-adrenergic receptor localization in failing ventricular cardiomyocytes during recovery from heart failure. Circ Heart Fail 5, 357–365.

Ma, H.-T. et al. (2000) Requirement of the Inositol Trisphosphate Receptor for Activation of Store-Operated Ca2+ Channels. Science 287, 1647–1651.

MacMillan, D. et al. (2005) IP3-mediated Ca2+ increases do not involve the ryanodine receptor, but ryanodine receptor antagonists reduce IP3-mediated Ca2+ increases in guinea-pig colonic smooth muscle cells. J Physiol 569, 533–544.

Markram, H. et al. (1995) Dendritic calcium transients evoked by single back-propagating action potentials in rat neocortical pyramidal neurons. The Journal of Physiology 485, 1–20.

Martini, F.H. et al. (2012) Fundamentals of Anatomy and Physiology. Pearson.

Maruyama, T. et al. (1997) 2APB, 2-Aminoethoxydiphenyl Borate, a Membrane-Penetrable Modulator of Ins(1,4,5)P3-Induced Ca2+ Release. J Biochem 122, 498–505.

Marx, S.O. et al. (2000) PKA Phosphorylation Dissociates FKBP12.6 from the Calcium Release Channel (Ryanodine Receptor): Defective Regulation in Failing Hearts. Cell 101, 365–376.

Marx S.O. et al. (2001) Coupled Gating Between Cardiac Calcium Release Channels (Ryanodine Receptors). Circulation Research 88, 1151–1158.

Mathers, D.A. and Barker, J.L. (1984) Spontaneous voltage and current fluctuations in tissue cultured mouse dorsal root ganglion cells. Brain Research 293, 35–47.

Mattheyses, A.L. et al. (2010) Imaging with total internal reflection fluorescence microscopy for the cell biologist. J Cell Sci 123, 3621–3628.

McCall, E. et al. (1996) Effects of FK-506 on Contraction and Ca2+ Transients in Rat Cardiac Myocytes. Circulation Research 79, 1110–1121.

McDonough, S.I. et al. (2000) Origin Sites of Calcium Release and Calcium Oscillations in Frog Sympathetic Neurons. J. Neurosci. 20, 9059–9070.

Michael, B. et al. (2007) Evaluation of Organ Weights for Rodent and Non-Rodent Toxicity Studies: A Review of Regulatory Guidelines and a Survey of Current Practices. Toxicol Pathol 35, 742–750.

Missiaen, L. et al. (2001) 2-Aminoethoxydiphenyl borate affects the inositol 1,4,5-trisphosphate receptor, the intracellular Ca2+ pump and the non-specific Ca2+ leak from the non-mitochondrial Ca2+ stores in permeabilized A7r5 cells. Cell Calcium 29, 111–116.

Möckl, L. et al. (2014) Super-resolved Fluorescence Microscopy: Nobel Prize in Chemistry 2014 for Eric Betzig, Stefan Hell, and William E. Moerner. Angewandte Chemie International Edition 53, 13972–13977.

Moerner, and Kador (1989) Optical detection and spectroscopy of single molecules in a solid. Phys. Rev. Lett. 62, 2535–2538.

Molkentin, J.D. (2006) Dichotomy of Ca2+ in the heart: contraction versus intracellular signaling. J Clin Invest 116, 623–626.

Mortensen, K.I. et al. (2010) Optimized localization-analysis for single-molecule tracking and super-resolution microscopy. Nat Methods 7, 377–381.

Moschella, M.C. and Marks, A.R. (1993) Inositol 1,4,5-trisphosphate receptor expression in cardiac myocytes. J Cell Biol 120, 1137–1146.

Munro, M.L. et al. (2016) Junctophilin-2 in the nanoscale organisation and functional signalling of ryanodine receptor clusters in cardiomyocytes. J Cell Sci 129, 4388–4398.

Nahidiazar, L. et al. (2016) Optimizing Imaging Conditions for Demanding Multi-Color Super Resolution Localization Microscopy. PLOS ONE 11, e0158884.

Nascimento, A.I. et al. (2018) The intriguing nature of dorsal root ganglion neurons: Linking structure with polarity and function. Progress in Neurobiology 168, 86–103.

Nieuwenhuizen, R.P.J. et al. (2015) Quantitative Localization Microscopy: Effects of Photophysics and Labeling Stoichiometry. PLoS One 10.

Opazo, F. et al. (2012) Aptamers as potential tools for super-resolution microscopy. Nat. Methods 9, 938–939.

Orchard, C. and Brette, F. (2008) t-tubules and sarcoplasmic reticulum function in cardiac ventricular myocytes. Cardiovasc Res 77, 237–244.

Orchard, C.H. et al. (2009) The role of mammalian cardiac t-tubules in excitation–contraction coupling: experimental and computational approaches. Experimental Physiology 94, 509–519.

Ouldridge, T.E. et al. (2013) DNA hybridization kinetics: zippering, internal displacement and sequence dependence. Nucleic Acids Res 41, 8886–8895.

Ouyang, K. et al. (2005a) Ca2+ sparks and secretion in dorsal root ganglion neurons. PNAS 102, 12259–12264.

Ouyang, K. et al. (2005b) Ca2+-induced Ca2+ Release in Sensory Neurons low gain amplification confers intrinsic stability. J. Biol. Chem. 280, 15898–15902.

Park, J. and Luo, Z.D. (2010) Calcium channel functions in pain processing. Channels 4, 510–517.

Parker, I. et al. (1996a) Elementary events of InsP3-induced Ca2+ liberation in Xenopus oocytes: hot spots, puffs and blips. Cell Calcium, Microdomains and elemental events in calcium signalling 20, 105–121.

Parker, I. et al. (1996b) Ca2+ sparks involving multiple Ca2+ release sites along Z-lines in rat heart cells. The Journal of Physiology 497, 31–38.

Pawley, J.B. (1991) Fundamental and practical limits in confocal light microscopy. Scanning 13, 184–198.

Peng, W. et al. (2016) Structural basis for the gating mechanism of the type 2 ryanodine receptor RyR2. Science 354.

Perez, P.J. et al. (1997) Identification and Functional Reconstitution of the Type 2 Inositol 1,4,5-Trisphosphate Receptor from Ventricular Cardiac Myocytes. J. Biol. Chem. 272, 23961–23969.

Periasamy, M. et al. (2008) Regulation of sarcoplasmic reticulum Ca2+ ATPase pump expression and its relevance to cardiac muscle physiology and pathology. Cardiovasc Res 77, 265–273.

Pinali, C. et al. (2013) Three-dimensional reconstruction of cardiac sarcoplasmic reticulum reveals a continuous network linking transverse-tubules: this organization is perturbed in heart failure. Circ. Res. 113, 1219–1230.

Poulet, C. et al. (2020) Junctophilin-2 tethers T-tubules and recruits functional L-type calcium channels to lipid rafts in adult cardiomyocytes. Cardiovasc Res.

Prakriya, M. and Lewis, R.S. (2001) Potentiation and inhibition of Ca2+ release-activated Ca2+ channels by 2-aminoethyldiphenyl borate (2-APB) occurs independently of IP3 receptors. J Physiol 536, 3–19.

Prasad, A.M. and Inesi, G. (2012) Analysis of Calcium Transients in Cardiac Myocytes and Assessment of the Sarcoplasmic Reticulum Ca2+-ATPase Contribution, in: DiMario, J.X. (Ed.), Myogenesis: Methods and Protocols, Methods in Molecular Biology. Humana Press, Totowa, NJ, pp. 411–421.

Putney, J.W. (1999) Ca2+ Signalling. Basic Neurochemistry: Molecular, Cellular and Medical Aspects.

Ries, J. et al. (2012) A simple, versatile method for GFP-based super-resolution microscopy via nanobodies. Nature Methods 9, 582–584.

Ridler, T.W. and Calvard, S. (1978) "Picture Thresholding Using an Iterative Selection Method," in IEEE Transactions on Systems, Man, and Cybernetics, 8 (8), 630-632.

Rocchetti, M. et al. (2014) Ranolazine prevents INaL enhancement and blunts myocardial remodelling in a model of pulmonary hypertension. Cardiovascular Research 104 (1), 37-48.

Roderick H.L. and Knollmann, B.C. (2013) Inositol 1,4,5-Trisphosphate Receptors. Circulation 128, 1273–1275.

Roderick, H.L. et al. (2007) Calcium in the heart: when it’s good, it’s very very good, but when it’s bad, it’s horrid. Biochem. Soc. Trans. 35, 957–961.

Rosenbluth, J. (1962) Subsurface cisterns and their relationship to the neuronal plasma membrane. J. Cell Biol. 13, 405–421.

Rüegg, J.C. (1986) Principles of Calcium Signalling in Muscle, in: Rüegg, J.C. (Ed.), Calcium in Muscle Activation: A Comparative Approach, Zoophysiology. Springer, Berlin, Heidelberg, pp. 239–248.

Sandler, V.M. and Barbara, J.-G. (1999) Calcium-Induced Calcium Release Contributes to Action Potential-Evoked Calcium Transients in Hippocampal CA1 Pyramidal Neurons. J. Neurosci. 19, 4325–4336.

Sato, D. and Bers, D.M. (2011) How Does Stochastic Ryanodine Receptor-Mediated Ca Leak Fail to Initiate a Ca Spark? Biophysical Journal 101, 2370–2379.

Savio-Galimberti, E. et al. (2008) Novel Features of the Rabbit Transverse Tubular System Revealed by Quantitative Analysis of Three-Dimensional Reconstructions from Confocal Images. Biophys J 95, 2053–2062.

Schermuly, R.T. et al. (2004) Chronic sildenafil treatment inhibits monocrotaline-induced pulmonary hypertension in rats. Am. J. Respir. Crit. Care Med. 169, 39–45.

Schnitzbauer, J. et al. (2017) Super-resolution microscopy with DNA-PAINT. Nature Protocols 12, 1198-1228.

Scriven, D.R.L. et al. (2010) Analysis of Cav1.2 and Ryanodine Receptor Clusters in Rat Ventricular Myocytes. Biophysical Journal 99, 3923–3929.

Scriven, D.R.L. et al. (2000) Distribution of Proteins Implicated in Excitation-Contraction Coupling in Rat Ventricular Myocytes. Biophysical Journal 79, 2682–2691.

Shah, S. et al. (2020) Local Ca^{2+} signals couple activation of TRPV1 and ANO1 sensory ion channels. Science Signaling 13, eaaw7963.

Sheard, T.M.D. et al. (2019) Three-Dimensional and Chemical Mapping of Intracellular Signaling Nanodomains in Health and Disease with Enhanced Expansion Microscopy. ACS Nano 13, 2143–2157.

Shen, J.-X. et al. (2004) Polymorphism of Ca2+ Sparks Evoked from In-Focus Ca2+ Release Units in Cardiac Myocytes. Biophys J 86, 182–190.

Shimozawa, T. et al. (2013) Improving spinning disk confocal microscopy by preventing pinhole cross-talk for intravital imaging. PNAS 110, 3399–3404.

Shmigol, A. et al. (1994) Role of caffeine-sensitive Ca2+ stores in Ca2+ signal termination in adult mouse DRG neurones. Neuroreport 5, 2073–2076.

Shmigol, A. et al. (1996) Gradual caffeine-induced Ca2+ release in mouse dorsal root ganglion neurons is controlled by cytoplasmic and luminal Ca2+. Neuroscience 73, 1061–1067.

Shmigol, A. et al. (1995) Calcium-induced calcium release in rat sensory neurons. The Journal of Physiology 489, 627–636.

Signore, S. et al. (2013) Inositol 1, 4, 5-trisphosphate receptors and human left ventricular myocytes. Circulation 128, 1286–1297.

Simpson, P.B. et al. (1995) Neuronal Ca2+ stores: activation and function. Trends in Neurosciences 18, 299–306.

Smyrnias, I. et al. (2010) Comparison of the T-tubule system in adult rat ventricular and atrial myocytes, and its role in excitation–contraction coupling and inotropic stimulation. Cell Calcium 47, 210–223.

Sobie, E.A. et al. (2006) The Ca2+ leak paradox and “rogue ryanodine receptors”: SR Ca2+ efflux theory and practice. Prog Biophys Mol Biol 90, 172–185.

Soeller C. and Cannell M. B. (1999) Examination of the Transverse Tubular System in Living Cardiac Rat Myocytes by 2-Photon Microscopy and Digital Image–Processing Techniques. Circulation Research 84, 266–275.

Soeller, C. and Cannell, M.B. (2002) Estimation of the sarcoplasmic reticulum Ca^{2+} release flux underlying Ca^{2+} sparks. Biophysical Journal 82 (5), 2396-2414.

Soeller, C. et al. (2007) Analysis of ryanodine receptor clusters in rat and human cardiac myocytes. PNAS 104, 14958–14963.

Soeller, C. et al. (2009) Three-dimensional high-resolution imaging of cardiac proteins to construct models of intracellular Ca2+ signalling in rat ventricular myocytes. Experimental Physiology 94, 496–508.

Solovyova, N. et al. (2002) Ca2+ dynamics in the lumen of the endoplasmic reticulum in sensory neurons: direct visualization of Ca2+-induced Ca2+ release triggered by physiological Ca2+ entry. The EMBO Journal 21, 622–630.

Sommer, E.W. et al. (1985) Neuronal subpopulations in the dorsal root ganglion of the mouse as characterized by combination of ultrastructural and cytochemical features. Brain Research 346, 310–326.

Song, L.S. et al. (2005) Calcium Biology of the Transverse Tubules in Heart. Ann N Y Acad Sci 1047, 99–111.

Song, L.S. et al. (2006) Orphaned ryanodine receptors in the failing heart. PNAS 103, 4305–4310.

Steele, E.M. and Steele, D.S. (2014) Automated detection and analysis of Ca^{2+} sparks in xy image stacks using a thresholding algorithm implemented within the open-source image analysis platform ImageJ. Biophysical Journal 106 (3), 566-576.

Stehbens, S. et al. (2012) Imaging intracellular protein dynamics by spinning disk confocal microscopy. Methods in enzymology 504, 293.

Stemmer, A. et al. (2008) Widefield fluorescence microscopy with extended resolution. Histochemistry and Cell Biology 130 (5), 807.

Subramanian, S. et al. (2001) Underlying mechanisms of symmetric calcium wave propagation in rat ventricular myocytes. Biophys J 80, 1–11.

Sugiyama, K. and Muteki, T. (1994) Local anesthetics depress the calcium current of rat sensory neurons in culture. Anesthesiology 80, 1369–1378.

Sun, X.H. et al. (1995) Molecular architecture of membranes involved in excitation-contraction coupling of cardiac muscle. J Cell Biol 129, 659–671.

Tada, M. et al. (1983) Effects of phospholamban phosphorylation catalyzed by adenosine 3′:5′-monophosphate- and calmodulin-dependent protein kinases on calcium transport ATPase of cardiac sarcoplasmic reticulum. Journal of Molecular and Cellular Cardiology 15, 335–346.

Tanaami, T. et al. (2002) High-speed 1-frame/ms scanning confocal microscope with a microlens and Nipkow disks. Appl. Opt., AO 41, 4704–4708. https://doi.org/10.1364/AO.41.004704

Takeshima, H. et al. (2000) Junctophilins: A novel family of junctional membrane complex proteins. Molecular Cell 6 (1), 11-22.

Thayer, S. et al. (1988) Regulation of calcium homeostasis in sensory neurons by bradykinin. J Neurosci 8, 4089–4097.

Thompson, R.E. et al. (2002) Precise nanometer localization analysis for individual fluorescent probes. Biophys J 82, 2775–2783.

Tokunaga, M. et al. (2008) Highly inclined thin illumination enables clear single-molecule imaging in cells. Nature Methods 5, 159–161.

Turkowyd, B. et al. (2016) From single molecules to life: microscopy at the nanoscale. Analytical and Bioanalytical Chemistry 408 (25), 6885-6911.

Umar, S. et al. (2012) Spontaneous Ventricular Fibrillation in Right Ventricular Failure Secondary to Chronic Pulmonary Hypertension. Circ Arrhythm Electrophysiol 5, 181–190.

Usachev, Y. et al. (1993) Caffeine-induced calcium release from internal stores in cultured rat sensory neurons. Neuroscience 57, 845–859.

Usachev, Y.M. and Thayer, S.A. (1997) All-or-None Ca2+ Release from Intracellular Stores Triggered by Ca2+ Influx through Voltage-Gated Ca2+ Channels in Rat Sensory Neurons. J. Neurosci. 17, 7404–7414.

Valdivia, H.H. et al. (1992) Scorpion toxins targeted against the sarcoplasmic reticulum Ca(2+)-release channel of skeletal and cardiac muscle. Proc Natl Acad Sci U S A 89, 12185–12189.

Van de Linde, S. et al. (2011) Direct stochastic optical reconstruction microscopy with standard fluorescent probes. Nat Protoc 6 (7), 991-1009.

van Oort, R.J. et al. (2011) Disrupted Junctional Membrane Complexes and Hyperactive Ryanodine Receptors Following Acute Junctophilin Knockdown in Mice. Circulation 123, 979–988.

Vellani, V. et al. (2004) Functional bradykinin B1 receptors are expressed in nociceptive neurones and are upregulated by the neurotrophin GDNF. The Journal of Physiology 560, 391–401.

Verdru, P. et al. (1997) Na+-Ca2+ Exchange in Rat Dorsal Root Ganglion Neurons. Journal of Neurophysiology 77, 484–490.

Vogelsang, J. et al. (2008) A Reducing and Oxidizing System Minimizes Photobleaching and Blinking of Fluorescent Dyes. Angewandte Chemie International Edition 47, 5465–5469.

von Haehling, S. et al. (2007) Nutrition, metabolism, and the complex pathophysiology of cachexia in chronic heart failure. Cardiovasc Res 73, 298–309.

Wagner, E. et al. (2012) Stimulated Emission Depletion Live-Cell Super-Resolution Imaging Shows Proliferative Remodeling of T-Tubule Membrane Structures After Myocardial Infarction. Circ Res 111, 402–414.

Walker, M.A. et al. (2015) On the Adjacency Matrix of RyR2 Cluster Structures. PLoS Comput Biol 11.

Walker, M.A. et al. (2014) Superresolution Modeling of Calcium Release in the Heart. Biophysical Journal 107, 3018–3029.

Wang, E. et al. (2005) Performance comparison between the high-speed Yokogawa spinning disc confocal system and single-point scanning confocal systems. J Microsc 218, 148–159.

Wang, S.Q. et al. (2001) Ca 2+ signalling between single L-type Ca 2+ channels and ryanodine receptors in heart cells. Nature 410, 592–596.

Wang, S.Q. et al. (2004) The quantal nature of Ca2+ sparks and in situ operation of the ryanodine receptor array in cardiac cells. Proc Natl Acad Sci U S A 101, 3979–3984.

Wang, W. et al. (2014) Reduced junctional Na+/Ca2+-exchanger activity contributes to sarcoplasmic reticulum Ca2+ leak in junctophilin-2-deficient mice. Am J Physiol Heart Circ Physiol 307, H1317–H1326.

Wei, S. et al. (2010) T-tubule remodeling during transition from hypertrophy to heart failure. Circ Res 107, 520–531.

Westcott, E.B. et al. (2012) Function and expression of ryanodine receptors and inositol 1,4,5-trisphosphate receptors in smooth muscle cells of murine feed arteries and arterioles. The Journal of Physiology 590, 1849–1869.

Williams, A.J. et al. (2018) The ryanodine receptor: advances in structure and organization. Current Opinion in Physiology, Cardiac physiology from inside to out 1, 1–6.

Wilmot, I. et al. (2017) Chapter 5 - Dilated Cardiomyopathy and Cardioskeletal Involvement, in: Jefferies, John Lynn, Blaxall, B.C., Robbins, J., Towbin, J.A. (Eds.), Cardioskeletal Myopathies in Children and Young Adults. Academic Press, Boston, pp. 85–111.

Wilson, D.W. et al. (1992) Mechanisms and pathology of monocrotaline pulmonary toxicity. Critical Reviews in Toxicology 22 (5-6), 307-325.

Wollheim, C.B. and Sharp, G.W. (1981) Regulation of insulin release by calcium. Physiological Reviews.

Wu, B. et al. (2013) Presenilins regulate calcium homeostasis and presynaptic function via ryanodine receptors in hippocampal neurons. Proc Natl Acad Sci U S A 110, 15091–15096.

Wu, C.C. et al. (2014) Calpain-Dependent Cleavage of Junctophilin-2 and T-Tubule Remodeling in a Mouse Model of Reversible Heart Failure. J Am Heart Assoc

Xiao, R. et al. (2017). Monocrotaline Induces Endothelial Injury and Pulmonary Hypertension by Targeting the Extracellular Calcium–Sensing Receptor. Journal of the American Heart Association 6, e004865.

Xie, W. et al. (2010) Deciphering ryanodine receptor array operation in cardiac myocytes. J Gen Physiol 136, 129–133.

Xie, Y.P. et al. (2012) Sildenafil prevents and reverses transverse-tubule remodelling and Ca^{2+} handling dysfunction in right ventricle failure induced

by pulmonary artery hypertension. Hypertension 59 (2), 355-362.

Xu, J. et al. (2017) Stochastic optical reconstruction microscopy (STORM). Curr Protoc Cytom 81, 12.46.1-12.46.27.

Yamamoto, T. and Ikemoto, N. (2002) Peptide Probe Study of the Critical Regulatory Domain of the Cardiac Ryanodine Receptor. Biochemical and Biophysical Research Communications 291, 1102–1108.

Yang, S.N. and Berggren, P.O. (2006) The Role of Voltage-Gated Calcium Channels in Pancreatic β-Cell Physiology and Pathophysiology. Endocr Rev 27, 621–676.

Yano, M. et al. (2000) Altered stochiometry of FKBP12.6 versus ryanodine receptor as a cause of abnormal Ca^{2+} leak through ryanodine receptor in heart failure. Circulation 102 (17), 2131-2136.

Zhang, J.X. et al. (2018) Predicting DNA Hybridization Kinetics from Sequence. Nat Chem 10, 91–98.